Department of Electrical & Electronic Engineering
Melbourne School of Engineering
The University of Melbourne

National ICT Australia (NICTA)

Reevaluating Electroencephalography for Epileptic Seizure Prediction

Elma O'Sullivan-Greene

Submitted in total fulfilment of
the requirements of the degree of

Doctor of Philosophy

`Produced on archival quality paper`

April, 2011

Abstract

Prediction of epileptic seizures would greatly reduce the burden of epilepsy for over 50 million people worldwide. Seizure events are typically characterised by a loss of consciousness and much of the burden of this disease for patients is due to the advent of seizures without any prior warning. Reliable seizure prediction would, in the first instance, offer patients the ability to prepare for seizure events by reducing locational safety hazards and providing choice in avoiding situations of social stigma. In the second instance, the long term aspiration for seizure prediction would be the incorporation of prediction into a closed loop device, to not only predict but ultimately prevent seizures.

Despite 35 years of research, analysis of brainwaves (EEG) has failed to reliably predict seizures. This thesis re-evaluates the current system of acquiring EEG measurements of brain dynamics. It is argued that conventional EEG contains insufficient information for seizure prediction, using theoretical methods from linear systems, stochastic estimation and non-linear systems.

This thesis frames the task of inferring brain activity from EEG measurements as an observability problem for coupled oscillator dynamics. Observability is analysed *(i)* under the classical linear systems theory definition using minimal data, *(ii)* as a stochastic estimator problem using linear Kalman filtering techniques and *(iii)* under a non-linear framework of measure preserving maps using entropy estimates. All these analyses con-

clude that conventional EEG signals will not reveal the secrets of brain dynamics to the extent of predicting epileptic seizures. Instead, actively evoked EEG (recordings follow an input stimulus) provides an opportunity to enrich the brainwaves so as to enable prediction. This active measurement paradigm offers hope for a clinical solution in the future.

The contributions of this thesis are two-fold: Firstly, to mathematically demonstrate that current passive EEG acquisition is an inherently unsuitable measurement for epileptic seizure prediction, theoretically explaining 35 years of unsuccessful research in the field. Secondly, to advocate the adoption of active EEG acquisition as a viable alternative for future work in seizure prediction from EEG data.

Declaration

This is to certify that

1. The thesis comprises only my original work towards the PhD,
2. due acknowledgement has been made in the text to all other material used,
3. the thesis is less than 100,000 words in length, exclusive of tables, maps, bibliographies and appendices.

Signature

Date

Acknowledgements

It is my pleasure to thank those who made this thesis possible:

I owe my deepest gratitude to Iven Mareels for his unwavering enthusiasm, knowledge, vision and fantastic support. I sincerely thank Levin Kuhlmann for always finding time and for his generous guidance from the perspective of neuroscience. I would like to show my gratitude to Anthony Burkitt for his constant support and knowledge in neural physics.

This thesis was greatly enriched by the expertise of the epilepsy group at The University of Melbourne and St Vincent's Hospital, Melbourne, in particular Mark Cook, Karen Fuller, David Grayden, Simon Vogrin and Alan Lai. The discussions amongst this group contributed greatly to my transition into the bio-medical field and are greatly appreciated.

I am indebted to so many friends and colleagues at the Dept. of Electrical & Electronic Engineering for their interest in neuroengineering and for friendly faces along the way: Jennifer Chee, Michelle Chong, Dean Freestone, Colin Hales, Kelvin Layton, Rahil Garnavi, Matthieu Gilson, Tania Kameneva, Brian Krongold, Stephan Lau, Nick Opie, Emily O'Brien, Girish Nair, Andre Peterson, Craig Savage, Martin Spencer, Paulius Stepanas, Daniel Taft, Bahman Tahayori, Tuyet Vu, Byron Wicks, Wave Yang and especially Andrea Varsavsky for the invaluable guidance from one who'd been on the seizure prediction path before.

Thank you to NICTA for the financial support of my study and especially to Tracy Painter and David Strover for assisting in many different ways to make administration matters run exceptionally smoothly.

To my family: Colin, I thank you for your support and patience over this PhD journey to Australia. My parents, I thank you for the educational start, without which, this thesis would likely never have been completed.

Contents

List of Figures

List of Tables

List of Abbreviations

AED	Antiepileptic drugs
CMRR	Common Mode Rejection Ratio
DSI	Dynamical Similarity Index
EEG	Electroencephalography \Electroencephalograph
EPSP	Excitatory Post Synaptic Potential
FPR	False Positive Rate
ICA	Independent Component Analysis
IPSP	Inhibitory Post Synaptic Potential
LED	Light Emitting Diode
MLE	Maximum Lyapunov Exponent
STLmax	Maximum Short Term Lyapunov Exponent
MDLM	Minimum Description Length Model
RMS	Root Mean Squared
RNS	Responsive Neuro-Stimulation
SNR	Signal to noise ratio
UV	Ultra-Violet
VNS	Vagus Nerve Stimulation

List of Symbols and Notation

$\mathbb{R}$	The set of real numbers
$\mathbb{C}$	The set of complex numbers
$\lambda(\mathbf{A})$	The eigenvalues of matrix $\mathbf{A}$
$det(\mathbf{A})$	The determinant of matrix $\mathbf{A}$
$\mathbf{A}'$	The transpose of matrix $\mathbf{A}$
$\sigma(\mathbf{A})$	The singular values of matrix $\mathbf{A}$
$\mathbf{x}$	A vector of states $\mathbf{x}$
x	A scalar state x
$E\left[x\right]$	The expected value of x
$Cov\left[x\right]$	The covariance of x
$Var\left[x\right]$	The variance of x
$x \in N(\bar{x}, \sigma^2)$	x is a normally distributed variable with mean $\bar{x}$ and variance σ^2
$\because$	Denotes *because* or *since* within mathematical text
$:=$	Denotes *is defined as* within mathematical text
$ker(\mathbf{A})$	The kernel of matrix $\mathbf{A}$

Glossary of Mathematical Terminology

Companion Form	Canonical format of system matrices $(\mathbf{A}, \mathbf{B}, \mathbf{C})$ where the system structure is readily visible allowing for ease of controllability/ observability
Coprime	$P(s)$ & $Q(s)$ are coprime polynomials if they have no common roots
Full rank	A matrix is full rank if all rows (or equivalently columns) are linearly independent
Kernel	The kernel of a matrix, $\mathbf{A}$ is all x vectors such that $\mathbf{A}x = 0$
Lebesgue Measure	Lebesgue measures correspond to the standard measures of space in Euclidean geometry (e.g. length in $\mathbb{R}^1$, area in $\mathbb{R}^2$)
Trace	The trace of a square matrix is the sum of the elements along the diagonal
Unimodular Matrix	A polynomial matrix, $P(s)$, whose determinant is not a function of s

Introduction

On the topic of obstacles to seizure prediction, a summary of informal discussions at the 3rd International Seizure Prediction Workshop in Freiburg, Zaveri, Frei and Osario noted that, *"put bluntly, $\cdots$ it is not necessarily possible to predict states of a dynamical system on the basis of a limited amount of measurements"* [2]. This thesis seeks to formally investigate what it is we can expect to glean from electroencephalographic recordings of electrical brain activity towards the effort of seizure prediction in epilepsy.

Epilepsy is a neurological disorder characterised by recurrent "seizures"and is associated with abnormal neuronal activity in the brain. Seizure events manifest clinically in a variety of ways including loss of consciousness and involuntary muscle contraction.

The World Health Organisation (WHO) estimates that worldwide over 50 million people suffer from epilepsy [3], while over the course of a lifetime, 100 million people will experience an epileptic episode [4]. This makes epilepsy the single most common serious neurological condition in the world today. A study by the WHO [3] reported that the prevalence of epilepsy varies across geographical regions within the range of 0.5% to 4% of the total population. In Australia, it is estimated that 2% of the population is affected by epilepsy [5].

Current treatments for epilepsy predominantly rely on anti-epileptic drugs (AEDs) [6]. Unfortunately these AEDs have a large number of side-effects, the more serious of which are cognitive changes such as sedation, aggression, depression and withdrawal [7]. Furthermore, the long-term use of AEDs *may*[1] be problematic due to the development of tolerance [8, 9]. Tolerance is the reduction of response following prolonged use of a drug, resulting in the controllability of seizures to become refractory to treatment with

---

[1] The author notes that the existence of tolerance to AEDs is a contentious issue

time. There also exists an estimated 9% - 25% [10, 11] of patients for which a successful AED or combination of AEDs cannot be found. For these patients, the surgical removal or “resection” of the epileptic brain volume may be an option.

In addition to the unsavoury side-effects of AEDs, people with epilepsy suffer from social stigma and vocational obstacles. Another burden is the risk of status epilepticus. This is the condition of continuous seizure activity without a recovery of consciousness between seizures which is a life-threatening emergency.

The ability to predict seizures would have a profound impact on the quality of life of epilepsy sufferers [12]. In the first instance, seizure prediction with a portable warning system [13] would dramatically reduce the risks associated with injury due to untimely loss of consciousness. With such a warning system, reliable seizure prediction may also enable people to hold a drivers license, who are currently ineligible due to incompliance with the necessary seizure-free time period. However, the long term objective of seizure prediction would be to prevent imminent seizures from occurring through direct intervention.

Seizure prevention might be achieved through either automated drug therapy or electrical stimulation. Automated drug therapy could operate through direct short-acting anti-epileptic drug delivery to the epileptic brain volume following seizure prediction [13]. This would be preferable over the current continuous drug treatment as it has the potential to dramatically reduce the average amount of drugs taken over time. Reduction of drug intake would not only reduce the side effects but may also extend the useful lifetime of the drug by slowing the build up of tolerance. An alternate and more ideal solution to drug therapy, would be the development of an electric stimulation treatment that could prevent a seizure from occurring once an imminent seizure is predicted [13]. If such an electric stimulation treatment was developed then an implantable device with both prediction and seizure “quenching” capabilities could be envisaged. Such an implantable device would be particularly beneficial for the 9%-25% [10, 11] of patients that have medically refractory (unresponsive to drug therapy) epilepsy - in Australia this is up to 100,000 persons[2].

In economic terms, it was estimated in 1990 that over AU$238 million was spent per annum on the direct costs of epilepsy treatment in Australia [14]. For comparison

---

[2] For a population of 20 million, with an epilepsy prevalence of 2%[5] and 25%[11] of epilepsy patients presenting medically refractory epilepsy

purposes, this is on a par with the early 1990 figures for the direct economic burden of diabetes (type 2) at AU$216.7 million per annum [15]. The indirect costs of epilepsy, that is the productivity related costs, are also significant although more difficult to estimate [16]. Furthermore, the existence of the intangible costs associated with the emotional issues of the condition are generally acknowledged. Undoubtedly, better epilepsy treatment, particularly prediction and subsequent prevention of epileptic seizures, would have a marked impact on both the indirect and emotional costs. While treatment in the form of an implantable device may not decrease the direct treatment costs of epilepsy, the benefits in terms of quality of life are immeasurable.

With this motivation for seizure prediction, this thesis examines what we can expect to learn about the underlying state of the brain from electroencephalographic data. The important contribution of this work is providing theoretical limits for the amount of information about brain dynamics that can be gleaned from data of this form. These theoretical limits are stringent, putting the viability of current approaches to seizure prediction based on these data in serious doubt. These results do however point to theoretically viable avenues for seizure prediction in implantable devices of the future.

Outline of Thesis

Background and Motivation

This thesis begins with an introduction to neurophysiology in Chapter 1, which details the structure of the brain, the condition of epilepsy and the methods of Electroencephalography (EEG) recording. A literary review is presented in Chapter 2, which provides an overview of existing research in the area of epileptic seizure prediction based on EEG data.

Main Research Findings

Chapter 3 provides a snapshot of typical time-frequency behaviour found in EEG signals as motivation to investigate observability of EEG measurements from the brain. The observability problem is considered using an abstraction, a coupled oscillator model for brain dynamics, this model is presented in Chapter 4. Chapters 5 and 6 explore observability issues with the coupled oscillator model which provides theoretical boundaries for the task for predicting epileptic seizures from EEG. Chapter 5 focuses on a linear, deterministic observability argument followed in Chapter 6 by both a stochastic argument (based on a Kalman filtering approach) and a non-linear entropy argument (based on entropy of measure preserving maps). Chapter 7 presents a paradigm for seizure prediction that may overcome the theoretical limitations elucidated in Chapter 5 and 6 through the addition of an active probing signal.

Conclusion

A discussion of the main thesis results is found in Chapter 8, together with a list of thesis contributions. A number of fruitful avenues for potential future investigations form part of this discussion.

Publications List

Invited Book Chapter

E. O'Sullivan-Greene, L. Kuhlmann, A. Varsavsky, D. B. Grayden, A. N. Burkitt and I. M. Y. Mareels. *Seizure Prediction and Observability of EEG Sources.* In Epilepsy: The Intersection of Neurosciences, Biology, Mathematics, Engineering and Physics, Ed. Osorio, I. and Zaveri, H. and Frei, M. G. and Arthurs, S. CRC Press, 2011.

Fully Refereed Conference Papers

E. O'Sullivan-Greene, I. Mareels, A. Burkitt and L. Kuhlmann. Observability issues in networked clocks with applications to epilepsy. *Proceedings of the* 48^{th} *IEEE Conference on Decision and Control (IEEE CDC)*, p 3527–3532, 2009.

E. O'Sullivan-Greene, I. Mareels, D. Freestone, L. Kuhlmann and A. Burkitt. A paradigm for epileptic seizure prediction using a coupled oscillator model of the brain. *Proceedings of the* 31^{st} *IEEE Engineering in Medicine and Biology Conference (IEEE EMBC)*, p 6428–6431, 2009.

C. Savage and E. O'Sullivan-Greene, Epileptic Seizure Prediction using Random Projections, *Proceedings of IEEE Intl. Conference on Intelligence Sensors, Sensor Networks and Information Processing (ISSNIP)*, p 647 - 650, 2007.

Conference Presentations

A. Peterson, E. O'Sullivan-Greene, A. Burkitt, I. Mareels, D. Grayden, M. Cook, L. Kuhlmann and K. Fuller, Modelling for Understanding and Prediction of Epileptic Seizures, *The Inaugural Medical Bionics Conference*, Lorne, Victoria, Australia, Nov 2008.

E. O'Sullivan-Greene, L. Kuhlmann and I. Mareels, A Coupled Oscillator Model model for EEG: towards synchrony based epileptic seizure prediction, *3rd Australian Workshop on Mathematical and Computational Neuroscience*, Melbourne, Nov 2008.

E O'Sullivan-Greene, I. Mareels and L. Kuhlmann. Modifications of the EEG signal for delay reconstruction based seizure prediction methods,*3rd International Workshop on Epileptic Seizure Prediction*, Freiburg, Germany, 2007.

Chapter 1

Epilepsy and the EEG

This chapter provides an introduction into the anatomy and electrodynamics of the brain. The neurological disorder of epilepsy is discussed together with the measurement of brain dynamics through Electroencephalography (EEG) recordings.

1.1 Structure of the Brain

The brain together with the spinal cord make up the central nervous system, the body's sensory analysis and decision making system. [17, 18, 1] provide the following information regarding the anatomy of the brain. The brain can be subdivided into two main regions, the brainstem and cerebrum. The cerebrum is structurally divided into two main regions each called a cerebral hemisphere. The outer layer of the hemispheres is known as the cerebral cortex. The cortex is a much folded structure which is estimated to contain in the order of 10^{10} nerve cells or *neurons* [1, Ch. 1]. The cortex contains both *grey matter* and *white matter*. Grey matter is a layer containing a high density of neuron cell bodies while, the white matter, located underneath the grey matter, is largely composed of nerve fibers or *axons*. The cortex is further divided into four main lobes, each with its own function specification, see Figure 1.1. The brain stem connects the spinal cord to the cerebral cortex, via the thalamus, a deep brain structure which gates the information flow from the brainstem to the cortex, see Figure 1.2.

The fundamental unit of the nervous system is the *neuron* or nerve cell. Neurons convey information by firing electrical impulses known as action potentials. Each neu-

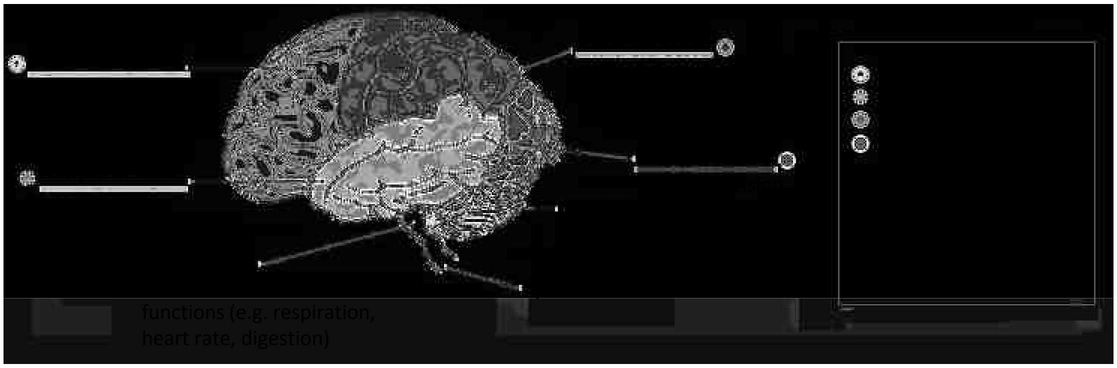

Figure 1.1: Surface view of the brain, illustrating the main lobes of the cerebral cortex and their basic functions, taken in part from [19]

ron consists structurally of a cell body, *soma*, input nerve fibers, *dendrites*, and output nerve fibers, the *axons*. Neurons connect to each other via synapses. Cortical neurons are strongly interconnected with a single neuron connecting with up to 10^5 synapses that transmit inputs from other neurons [1, Ch 1]. Pyramid cells are one such cortical neuron, named after their pyramid shaped soma, see Figure 1.3. Pyramid neurons exhibit a columnar organisation, where each column acts as a highly connected functional unit. Columns are orientated perpendicular to the cortical surface, and have diameters in the order of 300-600μm [17, Ch. 23].

Connections between neurons at synapses are generally regulated via chemical neurotransmitters. The resulting input signal to a neuron is either *excitatory*, in that it encourages the output of the neuron to fire, or *inhibitory*, which has the opposite effect. These input signals are referred to as excitatory post synaptic potentials (EPSPs) and inhibitory post synaptic potentials (IPSPs) named after their effect on subsequent neurons [1, Ch. 1]. A neuron will fire an output action potential if the sum of the EPSPs and IPSPs is above a certain threshold.

The molecular basis for the occurrence of action potentials is due to ions such as sodium and potassium [17]. Neurons have a resting cell potential of approximately -70mV across their cell membrane [20, Ch. 4]. This resting potential arises from the distribution of ions inside and outside of the cell. The cell membrane is however permeable to these ions. The flow of ions across the membrane through voltage gated channels causes the relative ion concentration to change, leading to an action potential. The voltage gated ion channels receive their control voltage from the post synaptic potentials (both EPSP and

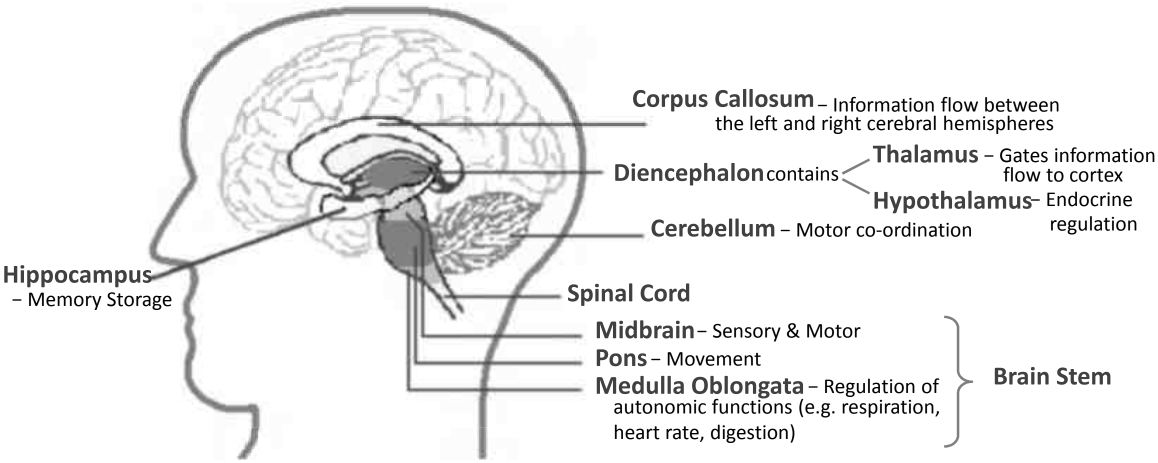

Figure 1.2: Midline cross-section between the cerebral hemispheres of the brain, illustrating the brain stem, deep brain structures and their basic functions. Taken in part from [19]

IPSP) of the synapses of connecting neurons. Figure 1.4 shows an intracellular recording similar to that 1^{st} recorded by Cole and Curtis with the giant neuron of a squid in 1938, illustrating an action potential.

1.2 Epilepsy

The International League Against Epilepsy (ILAE) defines an epileptic event as “a transient occurrence of signs and symptoms due to abnormally excessive or synchronous neuronal activity in the brain”[21]. Epilepsy is defined as “a disorder of the brain characterised by an enduring predisposition to generate epileptic seizures”[21], and is usually not diagnosed until more than one epileptic event has occurred.

The time during a seizure is commonly referred to as the *ictal* period, while the times between seizures are referred to as the *inter-ictal* periods. The time just before a seizure is referred to as the *pre-ictal* period. Prediction of epileptic seizures is dependent on the existence of a definitive and identifiable pre-ictal stage. The time period following a seizure but before normal neurological function has returned is called the *post-ictal* period.

While much advancement has been made in the field of human neurophysiology and

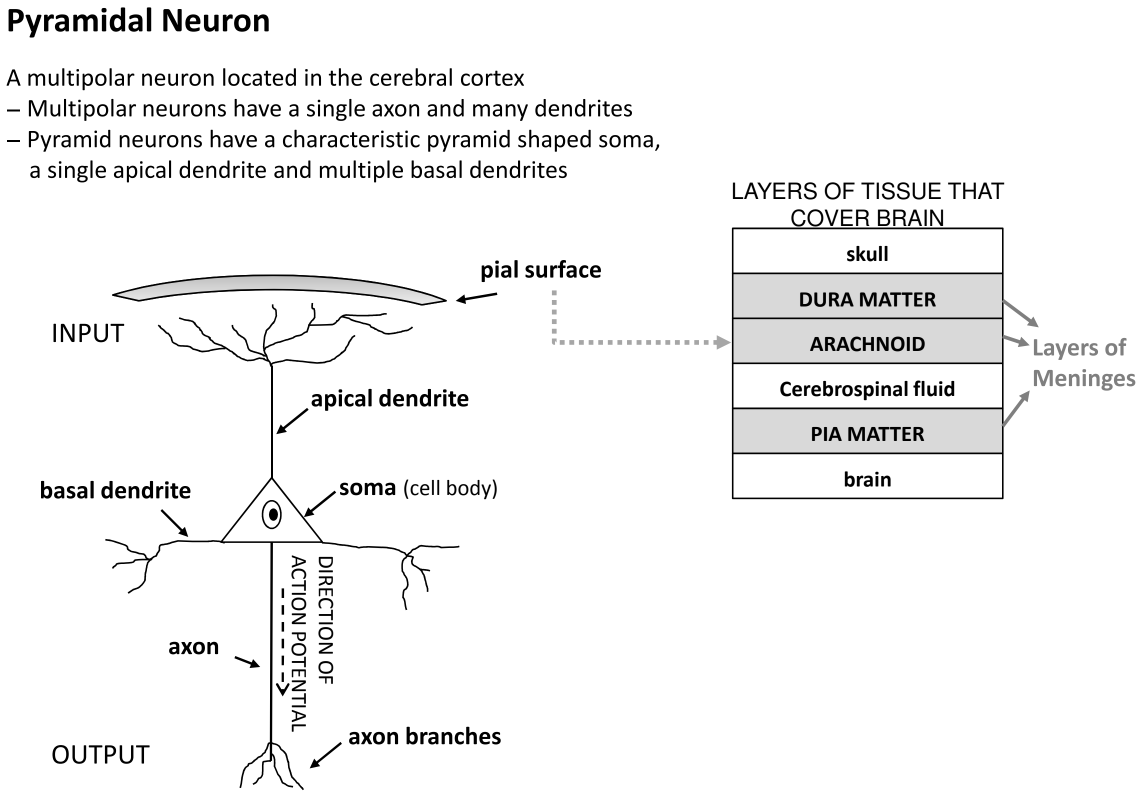
Pyramidal Neuron

A multipolar neuron located in the cerebral cortex
– Multipolar neurons have a single axon and many dendrites
– Pyramid neurons have a characteristic pyramid shaped soma, a single apical dendrite and multiple basal dendrites

Figure 1.3: Diagram of a pyramid neuron showing its anatomical parts and its orientation perpendicular to the cortex surface

epileptogenesis in recent years, knowledge of physiological processes remains largely inferential and speculative, with much of the current understanding based on comparison with animal models [22]. A common viewpoint is that local epileptiform discharges (a small group of neurons that begin to fire in a synchronous manner), can somehow recruit and entrain other nearby neurons leading to large scale synchronised epileptiform oscillation [10]. It is generally thought however, that the normal connectivity and function of the cortex, hippocampus and thalamus gives rise to the ability to generate both local and large scale synchronised neuronal discharges [23]. These networks of brain structures have mass recurrent excitatory connections [23] and one candidate for the mechanism of synchronisation is a reduction of inhibition in these networks [10, Ch. 3]. However, this is not the only candidate for the mechanism of synchronisation - a more general hypothesis is that mass synchronisation of neurons can occur due to an imbalance between inhibition and excitation in networks. With this more general hypothesis, synchronisation could be

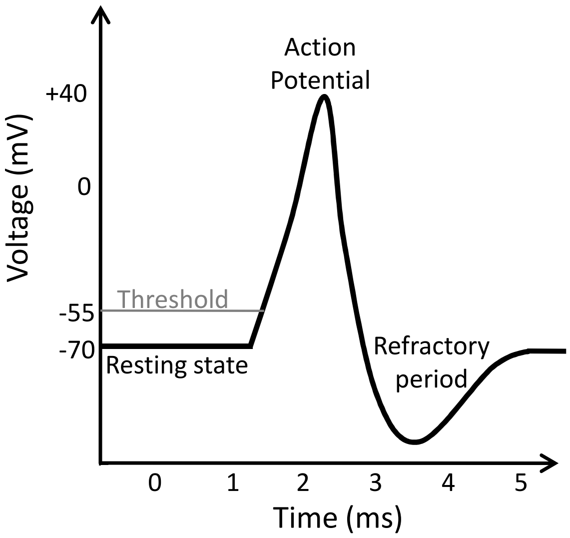

Figure 1.4: Intracellular recording of a neuron

a result of not only the aforementioned reduction of inhibition, but also a reduction in excitation or indeed an increase in either inhibition and/or excitation [24].

An increase in inhibition is believed to be the mechanism by which some antiepileptic drugs work. Antiepileptic drugs are the current standard practice in clinical epilepsy treatment[6, 25]. Drugs commonly prescribed include phenytoin, carbamazepine and benzodiazepines. In more recent times, a new generation of AEDs have materialised including tiagabine and vigabatrin. The primary action of tiagabine, vigabatrin and benzodiazepines is to promote GABAergic inhibition, where GABA is the main inhibitory neurotransmitter in the brain [25]. The action mechanism of phenytoin and carbamazepine is that of blockage of the voltage-dependent sodium channels [25].

With the mechanisms of epileptic seizure generation (and consequently the action of anti-epileptic drugs) poorly understood, epileptic seizures are classified according to their clinical manifestations. [17, 26] define the two main classification groups as *partial onset* or *focal onset* seizures and *generalised onset* seizures. Partial onset seizures originate in a small group of neurons that form the seizure focus. Such seizure focuses are often at the site of a lesion in the brain tissue. Partial onset seizures can be further segmented into simple partial seizures and complex partial seizures. Simple partial seizures, do not involve a loss of consciousness, and may manifest in sensory, psychic and repetitive motor phenomena. Complex partial seizures, however, do involve a loss of consciousness. Generalised onset seizures entrain neuron populations in both hemispheres from the onset. Partial onset seizures can often progress to become generalised seizures, such seizures are labelled as secondary generalised seizures. Generalised seizures themselves can be further streamed into *tonic clonic* seizures (formerly grand mal) and *absence seizures* (formerly petit mal). Tonic clonic seizures are characterised by a convulsive state followed by a definable post-ictal period, while absence seizures are associated with a non-convulsive seizure state and no post-ictal period.

Epilepsy can be further classified as *idiopathic* or *symptomatic* epilepsy. Idiopathic epilepsy is that with an unknown cause, while symptomatic epilepsy has an identifiable cause. Idiopathic epilepsy is presumed to be linked with genetic inheritance [27, Ch. 27]. Some of the diverse causes of symptomatic epilepsy include damage to neural tissue due to, for example, infections of the central nervous system such as meningitis, severe head trauma, intracranial tumors, strokes or a structural lesion [27, Ch. 27].

1.3 Electroencephalography

Electroencephalography (EEG) is a record of the temporal fluctuations of electrical potentials recorded from electrodes placed on or inside the human brain.

The electric field that is measured during the EEG is not due to the action potentials in the neuron cells but instead it arises from the ionic current outside neurons [20, 28]. Essentially the EEG *"detects the same information that neurons access when they "decide" whether or not to fire impulses, but an EEG records that information for thousands of cells at once"*, Walter J. Freeman [29]. The extracellular current that is measured by the EEG results from both the ionic current at the synapses and the excitatory and inhibitory fluctuations in the neuron cell membrane. The extracellular electric field that corresponds to such an extracellular current can be modelled by means of a classic charge dipole [20, 1]. The pyramidal cells are the main neurons that contribute to EEG signal, because these pyramid cells are orientated perpendicular to the cortical surface. The charge dipole model corresponding to such a pyramid neuron is aligned in the same direction as the neuron itself - perpendicular to the cortex surface, see Figure 1.5. The ordered orientation of the pyramid cells allows the electrical fields generated by individual neurons to superimpose in an additive manner. Since this combined electric field is generated in a conducting medium, the field is conducted to both the cortical surface and the scalp surface by volume conduction, where it can be recorded as the EEG signal. The tendency of the cortical neurons to synchronise their activity in time further enhances the electrical field from which the EEG signal is recorded [20]. Thus the EEG recorded at both cortex and scalp level records the *"fluctuating, volume conducted electrical field generated by synaptic currents in large numbers of synchronously active cortical pyramid neurons"* [20].

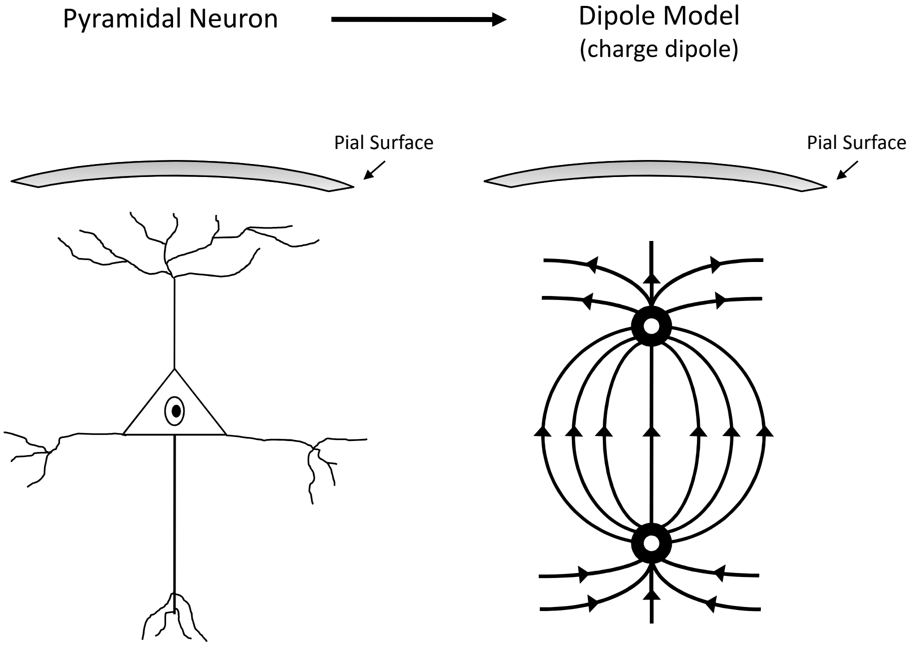

Figure 1.5: Dipole model of a pyramid neuron

Extracranial or "scalp" EEG is recorded from the scalp surface, while intracranial EEG is invasively recorded from the surface of the cortex. Recordings of potential are also taken from deep brain structures and deep into the cortex tissue - such deep invasive measurements are termed depth recordings. The amplitudes recorded in all cases depends on size of electrode: intracranical electrodes are generally of the order of 1mm [27, Ch38]; scalp electrode size is of the order of 1cm [27, Ch7]; depth electrodes are often "micro-electrodes" on scale of 1μm. The spatial scale of cortical matter that contributes to these recordings ranges from 100μm for intracranical electrodes to 10cm for scalp electrodes [1, Ch. 4]. Thus, intracranial EEG and depth recordings can provide detailed local information, while the scalp EEG, with contributions from an estimated 100-1000 million neurons averaged over large tissue masses, provides “big picture” data [1].

1.3.1 Interpretation of the EEG

Considering the large numbers of neurons, whose signals are space averaged and volume conducted through the several layers of tissue before being recorded at the scalp, it is amazing that any coherent information can be derived from scalp EEG. However, the scalp EEG signal reveals observable patterns related to specific states of consciousness such as attention, concentration, agitation and relaxation [27, 30, 1]. Furthermore, EEG recordings can reveal sleep stages, alcoholism, drug addiction, depth of anesthesia, seizures as well as other neurological disorders [27, 1]. Simply by placing a pair of electrodes on a scalp, the unprocessed differential recordings clearly shows several characteristic oscillations or *rhythms* that are associated with various states of cognitive function. See Table 1.3.1 for a list of such rhythms and their associated cognitive states. It is thought that these oscillations or rhythms can be attributed to the feedback loops that exist between the cortex and the thalamus, *thalamocortical* feedback, and the feedback loops that exist between different parts of the cortex itself, *corticocortical* feedback [20]. This attribution is due to the inverse linkage between the time delays that exist (due to the different distances travelled by signals) along these feedback routes and the characteristic frequencies that appear in the EEG [1, Ch. 11]. Therefore, the association between certain frequencies in the EEG and certain cognitive states could be due to the specific feedback loops engaged in that cognitive task. However, it has also been shown that the frequency ranges in the EEG correspond to the resonance frequencies that would be supported by a sphere of size similar to the average skull [1, Ch. 3].

Name	Frequency Range	Association
delta, δ	0.1-3.5 Hz	unconsciousness, deep sleep,see Fig. 1.6(b)
theta, θ	4-7.5 Hz	reduced consciousness, sleep,see Fig. 1.6(d)
alpha, α	8-13 Hz	awake, relaxed, (clinically: awake, eyes closed),see Fig. 1.6(a)
beta, β	14-30 Hz	consciously alert, agitated, tense,see Fig. 1.6(c)
gamma, γ	30 Hz +	attention, sensory stimulation

Table 1.3.1: Rhythms of the EEG [1]

From an epilepsy viewpoint, visual analysis of the EEG provides useful clinical information [27]. Seizures themselves are often accompanied by synchronous behavior across many of the recorded channels, followed by a post-ictal period of slow activity, see Figures 1.7(a) & 1.7(b). This can be interpreted as an increase in the synchronisation of discharging neurons in a large cortical region during the ictal period accompanied by a loss of inhibition. Absence seizures often manifest as a 3Hz spike and wave pattern in the EEG, see Figure 1.7(c). The inter-ictal epileptiform EEG is also likely to exhibit characteristic *spikes* which can aid in epilepsy diagnosis. These spikes are short lasting, sharp peaks that are clearly distinct from the surrounding background activity, see Figure 1.7(d).

It is thought that the origin of epileptiform spikes is due to the temporal summation of abnormally discharging neurons. Although indicative of epilepsy, these epileptiform discharges can be associated with a region of cortex that is in fact distinct from the epileptogenic zone (the brain region where the seizures are generated). Thus, it is probably incorrect to interpret the spikes as “mini-seizures”. It is thought that spikes may in fact reflect a process that prevents seizures from occurring, due to the increase of spikes under the influence of some anti-epileptic drugs, e.g. carbamazepin [20, Ch. 13]. As the presence of spikes in the inter-ictal EEG is used to aid epilepsy diagnosis, the probability of such spikes occurring in the normal non-epileptic brain is of concern. An American study [31] investigating the probability of spikes and other inter-ictal epileptiform discharges in the general non-epileptic population found that 12.3% of the EEG recorded from normal patients exhibited such phenonema. However, the study was biased in that the normal patients in the study had been referred for EEG analysis due to suspected neurological conditions. Consequently, the study concluded that although epileptiform discharges are not uncommon in patients without epilepsy, the “majority [exhibiting such phemomena] have underlying acute or progressive cerebral disorders”. An earlier study in Italian children [32] found that, given activity regarded as epileptiform in the EEG of normal children, the probability of subsequently developing epilepsy in the following 8-9 year period was only 0.077. It could be concluded that, while epileptiform EEG activity, such as spikes, are often present in the EEG of epileptic individuals, such activity is also not uncommon in the non-epileptic population.

While the EEG signal contains much useful clinical and diagnostic information, the signal also contains noise elements or *artefact* which obscure the clinically useful signal. Artefacts commonly found in the EEG include muscle artefact, cardiac artefact and mains pick-up artefact. Muscle artefact can be caused by movement of the scalp muscles and also by eye-blinks. Such muscle movement results in large amplitude alterations to the EEG. Cardiac artefact is that which is correlated with the timing of the heart beat. Such cardiac artefact is caused by the pulsing of the entire cortex in sync with the heart beat. Mains pick-up artefact is interference that is picked up from the mains power source. This artefact oscillates at the mains frequency (50Hz ±0.5% in Australia [33]). Software filtering, applied post-recording, can dramatically reduce some forms of interference, however care must be taken as the filtering process not only removes artefact but also alters the nature of the remaining signal. Intracranical EEG provides a much cleaner signal when compared to scalp EEG as muscle artefact is absent.

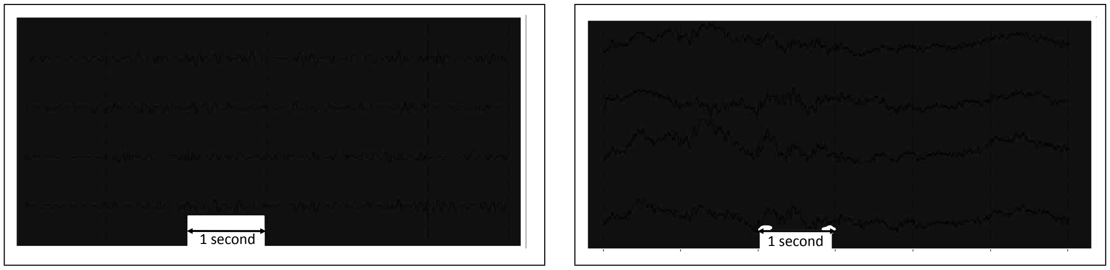

(a) alpha (b) delta

(c) beta (d) theta

Figure 1.6: Example of EEG segments showing normal adult rhythms, taken from scalp dataset in Table 1.3.2

1.3.2 Instrumentation

The EEG data acquisition system used in the recording of the majority of EEG data under analysis for this thesis is the *Compumedics E-series*™ hardware with *Profusion EEG*™ software [1]. The Compumedics user guide [34] provides the following system specifications.

---

[1] Compumedics Ltd.,30-40 Flockhart Street, Abbotsford 3067, Victoria

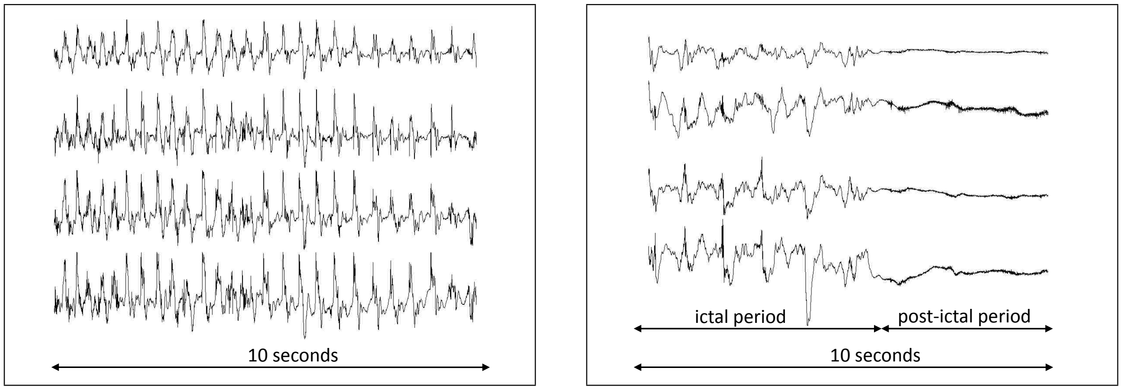

(a) Example of an EEG segment showing the synchronisation between channels during a seizure event

(b) Example of an EEG segment showing the transition from seizure event to a post-ictal period with slow activity

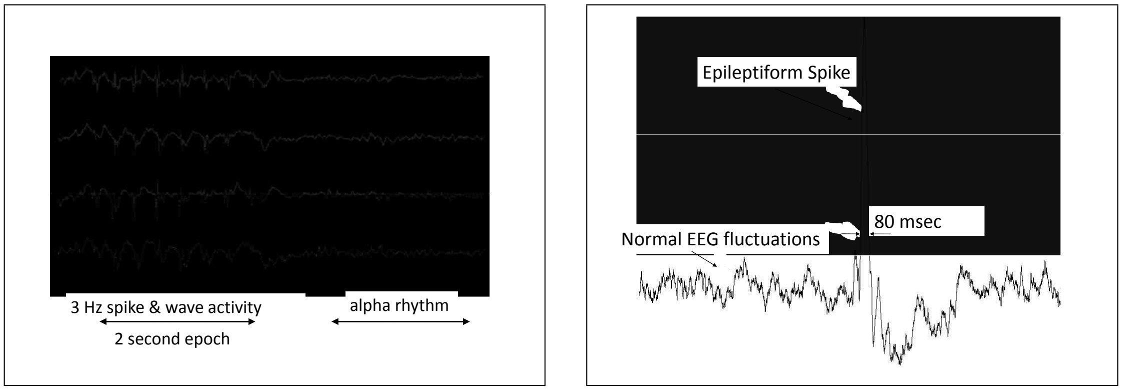

(c) Example of an EEG segment showing 3 Hz spike and wave activity during an absence seizure, followed by a period of alpha rhythm

(d) Example of an EEG segment showing an epileptiform spike

Figure 1.7: Examples of Epileptiform EEG activity, taken from scalp dataset in Table 1.3.2

The system records from up to 64 channels with a choice in sampling rate of 256 Hz or 512 Hz. This system hardware filters the signals such that only data in the range 0.15 Hz - 105Hz is recorded. The Compumedics machine amplifies the signals with a gain accuracy of ±1% and a CMRR[2] of >110dB. The output noise in the recorded signal is expected to be typically 2μVp-p in the range 0.16Hz - 70Hz. The system allows a user configerable input range of 1mVp-p - 16mVp-p, and an electrode dc offset of up to ±350mV. The signal is digitised with a resolution of 14 bits. Each channel is recorded with reference to a single electrode, "REF". The Compumedics user-guide [34] suggest that this REF electrode is placed "centrally on the patient's head near electode Fz, Cz or Pz", see Figure 1.8.

There exists an international standard for the placement of electrodes in scalp EEG recordings, this is known as the *10/20* electrode system [35]. This system relies on taking measurements between certain fixed points on the head, namely the *nasion*, which lies at the bridge of the nose, and the *inion*, which is the notch at the base of the skull at the back of the head. The electrodes are then placed at points that are 10% and 20% of these distances, see Figure 1.8. This standard provides a reasonably robust manner of enabling meaningful comparison between recordings of EEG across patients and recording sites.

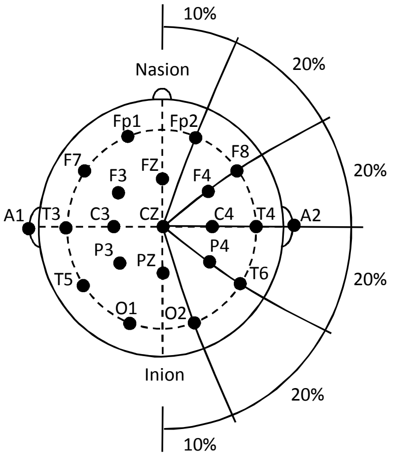

Figure 1.8: Electrode position and labelling of the international 10/20 system

Intracranial electrode placement is typically in the form of a grid, where the electrodes are uniformly spaced and embedded in a transparent silastic material [27, Ch. 41]. An illustration of a possible grid array on the cortex surface is provided in Figure 1.9.

---

[2] Common Mode Rejection Ratio

The exact number of electrodes on the grid and their precise location on the cortex varies depending on the clinical purpose of the recording. The grid recordings available for this research were recorded in patients with medically refractory epilepsy who were possible candidates for surgical removal of the seizure focus. The recordings were for the purpose of localising the seizure focus and ensuring that this focus was unimportant in the patient's cognitive function. Also available to this research are some depth intracranial recordings, where electrodes are surgically inserted into both the cortical tissue and the deep brain structures.

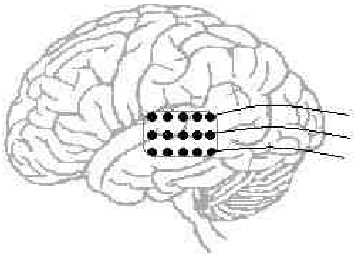

Figure 1.9: Example of electrode position with a intracranial grid, taken in part from [19]

For both scalp and intracranial EEG recordings, the signal recorded from different amplifiers can be displayed and analysed post-recording using various electrode referencing systems called *montages* [30]. In bipolar montages, consecutive pairs of electrodes are linked. The bipolar chains of electrodes may be connected going from front to back (longitudinal) or from left to right (transverse). Another type of montage is the unipolar or referential montage. In this montage, each of the electrodes are tied to a common reference electrode. Ideally, an inactive electrode, that is uninvolved in the electrical field under observation, is chosen as the common reference. As such an ideal electrode does not exist, an average of all the channels or the aural (ear) electrode can be used as reference. The database acquired for the purpose of this research is recorded using a reference electrode placed as follows: for scalp recordings the reference electrode is placed centrally on the patient's head near electrode Fz, Cz or Pz", see Figure 1.8; for intracranial recordings, the electrodes are referenced to an external scalp reference, located at the back of the head.

1.3.3 Research Dataset

The set of recordings available for use over the course of this thesis are detailed in Table 1.3.2.

EEG type	Recording length	Number of Patients	Origin
Scalp	Continuous, longterm	15	St Vincent's Hospital, Melbourne
Intracranial	Continuous, longterm	6	St Vincent's Hospital, Melbourne
Intracranial	Interictal & ictal segments	21	University Hospital of Freiburg, Germany (*)
Intracranial	Continuous, longterm	3	Competition dataset from (*) as part of the 3rd International seizure prediction workshop 2007, Freiburg, Germany

Table 1.3.2: EEG Database

Chapter 2

Literature Review

This chapter begins with an overview of existing research in epileptic seizure prediction from EEG measurements. Section 2.6 discusses the current state of seizure prediction internationally, leading to the key contributions of this Thesis in Section 2.7.

2.1 Can Seizures be Predicted?

Until the 1970s, it was believed that the transition from inter-ictal periods to ictal phenomenon was instantaneous, and occurred without warning. However, mounting evidence had lead to the postulation that this 2-stage model could be expanded to include a third state, that of the pre-ictal period. The prospects for development of reliable epileptic seizure prediction relies on the existence of a definable pre-ictal period. The evidence for the existence of such a definable pre-ictal period is discussed in this section.

It is clinically undisputed that prodromal or indicative symptomatic changes exist in certain patients prior to seizure onset [11, 36, 37]. The existence of this qualitative phenomenon, commonly referred to as an "aura", indicates that a quantitatively definable pre-ictal period is likely. While it can be argued that auras which immediately proceed a seizure could in fact be the beginning part of the seizure itself, it is well known clinically that prodromal changes, as reported by both patients and their families, can exist from several hours to days in advance. These premonitory changes involve alterations of the nervous system and include mood changes, nausea, headache and psychic symptoms. Such prodromal changes even allow some people to apply a self control seizure prevention strategy with varying degrees of success [36, 37]. The success of such a strategy could be explained as the prevention of neural networks from being recruited into epileptogenic synchronisation by the person consciously pulling those networks into some other physiological processing task. It follows from this knowledge of aura existence and self control techniques that the possibility of seizure prediction and subsequent prevention via means of a quantitative engineering analysis is plausible.

Several studies indicate that the application of engineering analysis techniques to EEG data may allow a pre-ictal state to be defined [38, 39, 40, 41, 42, 43, 44]. Methods employed include approaches from nonlinear dynamics, such as pre-ictal changes in the largest Lyaponov exponent, a pre-ictal decrease of synchronisation between EEG channels and the use of dimensional analysis to find a pre-seizure decrease in EEG complexity. Other methods employed looked at changes to the frequency and energy of the EEG signal prior to seizure onset. The results and validity of these methods will be further discussed in the subsequent sections.

2.2 Introduction to Approaches of EEG Analysis

The EEG signal appears at first glance to be a multi-frequency stochastic or "noisy" signal. Indeed, Fourier analysis reveals that the EEG signal contains several distinct frequency bands in the range 0.5 - 30(and higher) Hz. This has lead to a multitude of linear analysis techniques [1] being applied to the EEG. However, the EEG may also be considered to be a time series measured from a dynamical system, where this dynamical system is non-linear and represents the activity of the brain. With this non-linear view, the variability of the

---

[1] Linear systems can be defined as dynamical systems $\dot{x} = f(x, u)$, with some initial state $x = x_0$ and input u, characterised by the function f, for which the family of all possible time trajectories that the system can produce, $\mathbb{B}$:

$$\mathbb{B} = \{x : \exists u \Rightarrow \dot{x} = f(x, u)\} \tag{2.2.1}$$

is a linear subspace of $\mathbb{R}^n$ [45]. For linear systems, $f(x, u) = \mathbf{A}x + \mathbf{B}u$, where the entries of matrices $\mathbf{A}, \mathbf{B}$ are real. Such systems obey the principal of superposition:

$$\{x_1, x_2 \in \mathbb{B}; \alpha, \beta \in \mathbb{R}\} \Rightarrow \{\alpha x_1 + \beta x_2 \in \mathbb{B}\}. \tag{2.2.2}$$

Systems which do not obey the above are classified as non-linear. Linear analysis methods such as linear transforms, T, (including the Fourier transform) obey

$$T(x_1 + x_2) = T(x_1) + T(x_2) \tag{2.2.3}$$

and for a scalar $\lambda \in \mathbb{R}$

$$T(\lambda x) = \lambda T(x) \tag{2.2.4}$$

signal may be attributed to the presence of an attractor rather than to noise (or both) [46, 20, 47]. The brain as a non-linear dynamical system can be represented as being input-driven, or alternatively as having no inputs. Both of these approaches, linear and non-linear, will be considered in further detail in sections 2.3 & 2.4 respectively. Additionally, it is possible that the brain function may be neither linear nor non-linear and instead *stochastic* in nature, where stochastic noise may be intrinsic to brain function. An underlying stochastic brain is however not generally assumed in the existing seizure prediction algorithms.

Much of the current literature has adopted the following conventions in statistical performance indicators for both seizure prediction and detection algorithms [28]:

- *Sensitivity* refers to the ratio of correct predictions (*true positives*) out of the total number of seizures, both predicted and unpredicted seizures (*false negative*).

$$\text{Sensitivity} = \frac{\#\text{ true positives}}{\#\text{ true positives} + \#\text{ false negatives}} \tag{2.2.5}$$

- *False positive rate, FPR,* is a measure of the number of *false positives* (predictions made at times when no seizure subsequently occurred) per unit time, T, (usually per hour).

$$\text{FPR} = \frac{\#\text{ false positives}}{\text{T}} \tag{2.2.6}$$

- *Specitivity* refers to the ratio of non seizure epochs that are correctly predicted (*true negatives*) to the total number of non seizure epochs. This definition of specificity, for the purpose of seizure prediction, requires that the EEG data to be discretised into epochs of a fixed duration.

$$\text{Specificity} = \frac{\#\text{ true negatives}}{\#\text{ true negatives} + \#\text{ false positives}} \tag{2.2.7}$$

Although these statistics provide a means of comparing seizure prediction algorithms, the methodology used for testing the performance of each algorithm must be considered alongside the reported statistics. Many studies, especially earlier ones before large data storage facilities became available, do not consider much, if any, control data in the sense of large inter-ictal periods or EEG from a non-epileptic population. Therefore, these studies focus on sensitivity while ignoring specificity and false positive rate. Although intracranial EEG from a non-epileptic population is unavailable on ethical grounds, inter-ictal intracranial data can easily be considered for control purposes. Another aspect to be considered when interpreting these statistical indicators, is that most of the literature to date is not predictive in the sense of predicting the onset of a seizure at an exact time. Instead a pre-ictal period is identified for time periods of increased likelihood of seizure onset. The latter concept of "prediction" may prove sufficient however for adequate control of seizures with either an on-demand drug delivery treatment or perhaps preventative electrical stimulation therapy.

2.3 Linear Approaches

As early as 1975 linear approaches of EEG analysis were attempted in an effort to predict epileptic seizures. The advantage of linear analysis techniques is that they are both well-established and powerful tools for quantification and prediction of signals and systems. Linear techniques are less computationally intensive when compared to non-linear techniques when dealing with the same "dimensionality" and were therefore the tool of choice historically before the advent of modern computer processing power.

Several linear approaches to seizure prediction will be discussed in the remainder of this section. It was found however, that the success of these methods was minimal. This general lack of success may be attributed to the idea that the brain and its function are most likely non-linear in nature and hense that linear measures are ultimately unsuitable for quantifying the changes in non-linear brain state that lead to a seizure.

2.3.1 Selected Linear Measures: Performance and Scepticism

Spectral Analysis

In 1975 Viglione *et al.* [48] investigated the ability of pattern recognition applied to the spectral analysis of a limited number of scalp EEG channels to predict generalised tonic-clonic seizures. However this approach was soon abandoned due to poor results [9, 11].

Power spectral analysis was again applied to scalp EEG in an effort to predict epileptic seizures in 1982, when Siegel *et al.* [49] showed that the pre-ictal period before absence seizures could be distinguished with some seizures, in some patients (64%-83% of the time in 4 of the 5 patients studied). The findings of Inouye *et al.* [50] in 1994 were similar in that they *"suggested structural changes in EEG frequency composition just before SWCs* [spike and wave complexes of absence seizures] *because of an epileptogenic process"*, but in this case such changes were found in each of the 10 patients they studied. The structural change they found was an increase in "arrhythmic slow activity" [10, Ch. 13].

Such early seizure prediction attempts prompted preliminary spectral investigation with the scalp EEG database of the University of Melbourne epilepsy research group. This investigation has shown the frequency content of ictal EEG and the EEG immediately prior to seizure onset to contain frequencies predominately in the range 5-25 Hz. However, a subset of these "seizure frequencies" are also common in the normal waking "alpha" brain state, rendering any useful spectral analysis for seizure prediction difficult. This overlap of alpha (8- 13 Hz) and seizure frequencies (3-25 Hz) was also noted by Saab and Gotman in their seizure detection work [51].

However, with the advent of increased computational power and data storage ability, EEG recordings with a high sampling frequency have been possible. Such intracranial and deep brain structure recordings in both animal models and human patients show that increased spectral power at higher frequencies (80-500Hz) may relate to epileptogenesis [52, 53]. Further investigation into the possibilities of seizure prediction with high frequency oscillations is needed.

Linear Modelling

Linear modelling approaches have been applied to the EEG signal in an attempt to use the resulting models for prediction. An example of this is the 15-coefficent autoregressive modelling attempt of Rogowski *et al.* in 1981 on the scalp EEG of epileptic patients with absence epilepsy [54]. This resulted in prediction horizons of only a few seconds. Such short prediction horizons could be classed as detection due to the time period of a few seconds that can exist between the onset of a seizure electrographically and clinically [10, Ch. 12]. However it is worth noting that such short prediction horizons could be sufficient for therapeutic intervention by means of electrical stimulation, especially if the prediction/detection occurred before the patient experienced any clinical symptoms.

Linear Statistics: Variance, Skewness, Kurtosis & Cross-correlation

More recently, basic linear statistics have been investigated as seizure prediction candidates. In 2003, McSharry *et al.* investigated the use of variance as a predictor with intracranial data [55]. Although there was a marked decrease in variance during seizures, it was concluded that this basic linear statistic failed to show any alteration during the pre-ictal period. In 2005, Mormann *et al.* [13] considered the ability of several linear measures to predict epileptic seizures with intracranial data. These measures included variance and other univariate (analysed on a single channel) measures such as the skewness, kurtosis and the relative power in different spectral bands. A bivariate measure (multichannel analysis), that of a cross-correlation estimate, was also considered. However these measures showed "no global effect in the sense of a uniform and similar change found in all channels for all seizures of a patient". Furthermore these linear measures either failed to show significant pre-ictal changes or showed contradicting changes, such as a pre-ictal increase in some channels and yet decrease in other channels for a single measure.

Accumulated Energy

Energy measures have also been considered in recent years for seizure prediction. In 2001 Litt, Esteller et al [42] found that accumulated energy increased in the 50 minute epoch before seizure onset, when compared to a baseline of 1 hour at least 3 hours before any ictal period. Their method was based on the premise that increases in accumulated energy are associated with oncoming seizures. Accumulated energy was defined as the "running sum of the square of the EEG voltage sampled at 200Hz". Their method showed remarkable results with a sensitivity of 90% and a specificity of 88% which corresponded to a FPR (False positive rate) of 0.089. However, later studies by both this group and other groups questioned these initial findings.

In 2005, Esteller *et al.* [56] again attempted to quantify the pre-ictal state using estimates of energy. This study was designed to be causal by comparing the accumulated energy measure of a 1 minute segment to a randomly chosen baseline of 20 minutes taken from at least 4 hours prior to a seizure. Accumulated energy was defined as,

$$E[n] = \frac{1}{N_1} \sum_{i=1+(n-1)(N_1-D)}^{n(N_1-D)+D} x(i)^2, \tag{2.3.1}$$

where N_1 is the number of samples in an observation window, D is the window shifting, $x(i)$ is the EEG recording at time i, and n is the time index of the energy measure. If an adaptive decision threshold, based on a long term baseline energy measure of 20 minutes, was greater than a short term energy computed over 1 minute, a warning of imminent seizure was declared. However the expected pre-ictal energy increases only occurred in 50% of cases, and thus "no statistically significant results were found". The results presented indicated that pre-ictal energy showed not only increases, but also "bursts" and "quiet periods". Furthermore, increases in energy are also indicative of post-ictal, sleep states and of course of ictal events themselves. Therefore it appears that, while energy would be a quantity especially suited to an implantable device with its low computational requirements, pre-ictal energy increase is not a viable indicator for seizure prediction. A second paper by Harrison *et al.* [57] on the application of accumulated energy to EEG data in 2005, supported this conclusion in that no pre-ictal energy indicator could be found. With energy sensitive to amplitude levels, one notable limitation of this work is the absence of data normalisation before the energy measure was applied, although this is somewhat handily compensated for through the use of the baseline energy calibration step.

Measures of Synchronisation

It has been observed that epileptic seizures occur with a synchronisation of neural activity across different brain regions. This observation has been exploited by seizure prediction methods that aim to test for an increase in synchronisation of neuron activity before seizure onset.

In 2003, Mormann *et al.* investigated synchronisation measures for "detection of a preseizure state" with intracranical data [41, 40]. To compute the instantaneous phase, $\phi(t)$ of each channel for comparison, the authors employed the Hilbert transform. The analytical signal is represented as

$$\psi(t) = s(t) + j\tilde{s}(t) = A(t)e^{j\phi(t)}, \tag{2.3.2}$$

where s(t) is the EEG time-series and $\tilde{s}(t)$ is the Hilbert transform of the time series,

$$\tilde{s}(t) = \pi^{-1}.PV. \int_{-\infty}^{+\infty} \frac{s(\tau)}{t-\tau} d\tau, \tag{2.3.3}$$

where PV is the Cauchy principal value [20]. It follows from Equation 2.3.2 that the instantaneous phase, $\phi(t)$ can be computed as

$$\phi(t) = \tan^{-1}\left(\frac{\tilde{s}(t)}{s(t)}\right). \tag{2.3.4}$$

To consider the instantaneous phase difference, $\Delta\phi(t)$ between channels in a statistical sense the concept of *phase coherence*, introduced by Mormann *et al.* in 2002 [58], is utilised. Phase coherence, R, essentially projects the instantaneous phase differences onto the unit circle, and computes the average length vector.

$$R = \left|\frac{1}{N}\sum_{t=0}^{N-1} e^{j\Delta\phi t}\right|, \tag{2.3.5}$$

where R values are in the range [0:1]. Surprisingly the results of Mormann *et al.* find that a decrease, rather than the expected increase, in synchronisation occurs before seizure onset. The sensitivity published was 81% for a database of 32 analysed seizures [41] and 86% for a database of 14 analysed seizures [40]. In both cases a specificity of 100% (i.e no false positives) was declared. However, prediction was allowed for lengthy time periods up to 3 hours and 41 minutes in advance of clinical ictal onset and only short lengths of EEG recordings were available (average length 6.5hr/patient hours) for analysis. These two factors indicate that the false positive analysis may not be meaningful.

In 2005, Le Van Quyen *et al.* [59] published work on synchronisation, again using Equations (2.3.2 - 2.3.5) with an intracranial dataset. In contrast to the findings of Mormann *et al.* as both increases and decreases of "synchronisation" were found in pre-ictal periods. By classifying the possible inter-ictal synchronisation profiles in a reference library and comparing the pre-ictal synchronisation profiles to this library, a sensitivity of 70% (out of 72 seizures) was found, with anticipation times hours in advance of seizure onset. However no conclusions can really be drawn from this study as only 5 patients were analysed, from which 5 different reference templates had to be considered. Perhaps a patient-specific seizure prediction method could develop from this approach, but a much larger data base would need to be considered first.

The Hilbert transform has some limitations when applied to noisy datasets due to the nature of the transform. The Hilbert transform can give rise to large differences between the instantaneous phase of a function $f(t)$, $\phi(f(t))$ and the instantaneous phase of the same function with small noise δ, $\phi(f(t) + \delta)$. Considering that the EEG contains significant levels of measurement noise, the Hilbert transform is most likely unsuitable for the robust tracking of underlying synchronisation between brain regions. This may explain why both increases and decreases in synchronisation prior to seizures are seen in the literature using the Hilbert transform. Furthermore, as a linear transform, the Hilbert transform is likely to fail to capture the complex synchronisation activity present in the brain. Alternative non-linear synchronisation measures are considered in Section 2.4.1.

2.4 Non-linear Approaches

The brain is a complicated system where the interaction of billions of neurons give rise to spatially and partially synchronised functional behaviour. Neurons themselves and small networks of neurons are non-linear in nature, so it can be inferred that the brain system as a whole is a non-linear dynamical system. This has lead to a range of theoretical methods and measures in the field of non-linear dynamics to be applied to the EEG. The hope being that somehow a low dimensional, but perhaps complex, non-linear attractor may be sufficient to describe the brain's behaviour.

The hope in a non-linear system approach is that the underlying dynamics are rather simple to describe, for example by way of a set of non-linear differential equations, however the time evolution of the corresponding states exhibits “chaotic” (noisy, erratic) behaviour. The *state* of a system provides all the information necessary, besides the input, to predict the future of the system [60], where the future of the system is determined by integrating the system equations. *State space* refers to the vector space or manifold, within which, the time evolving state of a dynamical system resides. The main non-linear approaches consider the brain as an autonomous system, i.e. without input, or consider the input as a “white noise”.

Non-linear analysis of recorded time series data, such as the EEG, usually calls for a state space reconstruction to allow the underlying dynamics to be analysed. But given a single time series recording of one of the states of the system, or indeed an arbitrary function of several states of the system, it is less than intuitive that meaningful information about the system as a whole can be derived. However, in 1981 Takens and Aeyels independently proposed a remarkable delay embedding theorem which allows a model of the dynamical system to be reconstructed directly from time series data [61, 62]. Let the mapping f describe the evolution of the state vector $\mathbf{x}$ over time. Let y be an output measurement from the system defined by some arbitrary function ϕ. For simplicity y is a scalar here.

$$\dot{\mathbf{x}}(t) = f(\mathbf{x}(t)) \tag{2.4.1}$$

$$y(t) = \phi(\mathbf{x}(t)) \tag{2.4.2}$$

The goal is to reconstruct the unknown state vector $\mathbf{x}$ given the measurement time-series $y(t)$. In embedding, the dynamics are reconstructed by allowing the system states to be represented as vectors of delayed measurement signals. For example take a time-series of measurements observed every τ seconds,

$$\begin{aligned}[y(t-n\tau),\dots,y(t-2\tau),y(t-\tau),y(t)] &= [\phi(\mathbf{x}(t-n\tau)),\dots,\phi(\mathbf{x}(t-2\tau)),\phi(\mathbf{x}(t-\tau)),\phi(\mathbf{x}(t))] \\ &:= \widetilde{\Phi}(\mathbf{x}(t))\end{aligned} \tag{2.4.3}$$

where $\mathbf{x}(t-n\tau)$ are the states $\mathbf{x} = [x_1, x_2, x_3 ... x_m]$ at time $t - n\tau$. An example of a measurement vector $\widetilde{\Phi}(\mathbf{x}(t))$, in the context of the brain system, could be the EEG time-series recording from one electrode, see Figure 2.1 for an illustration of this. The measurement vector $\widetilde{\Phi}(\mathbf{x}(t))$ can be used to create $\mathbf{z} = [z_1, z_2 ... z_d]$, a d-dimensional reconstruction of the m-dimensional system with states $\mathbf{x} = [x_1, x_2 ... x_m]$. These reconstructed states $\mathbf{z}$ are found by representing the states as delayed versions of $\widetilde{\Phi}(\mathbf{x})$, e.g $z_1 = \widetilde{\Phi}(\mathbf{x}(t))$, $z_2 = \widetilde{\Phi}(\mathbf{x}(t-\tau))$, and $z_d = \widetilde{\Phi}(\mathbf{x}(t-(d-1)\tau))$. While $\widetilde{\Phi}$ is a mapping from $\mathbb{R}^m \to \mathbb{R}^1$, more generally, this co-ordinate change from $\mathbf{x}$ to $\mathbf{z}$ can be represented by the delay map $\Phi : \mathbb{R}^m \to \mathbb{R}^d$ where $\mathbf{z}(t) = \Phi(\mathbf{x}(t))$ and conversely $\mathbf{x}(t) = \Phi^{-1}(\mathbf{z}(t))$. Reconstruction is only guaranteed, however, under certain conditions including that the dimension $d \geq 2m+1$. Further details of the limiting conditions attached to reconstruction and their impact are discussed later in this section.

While such a reconstructed system is not equivalent to the original system, it can be interpreted as the same system with the co-ordinate system rescaled. More precisely, for an underlying system f and a reconstructed system $\dot{\mathbf{z}}(t) = F(\mathbf{z}(t))$, the following holds $F = \Phi \circ f \circ \Phi^{-1}$ [63].

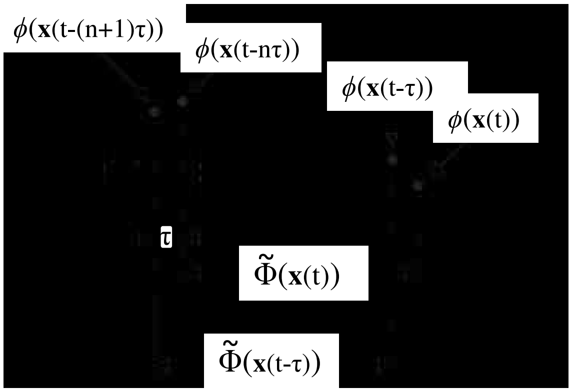

Figure 2.1: Illustration of delay reconstruction from a single electrode time series EEG measurement

$$
\begin{aligned}
\Phi \circ f \circ \Phi^{-1}\left(\mathbf{z}\left(t\right)\right) &= \Phi\Big(f\Big(\Phi^{-1}\big(\mathbf{z}\left(t\right)\big)\Big)\Big); \\
&= \Phi\Big(f\big(\mathbf{x}\left(t\right)\big)\Big); \\
&= \Phi\big(\dot{\mathbf{x}}\left(t\right)\big); \\
&= \dot{\mathbf{z}}\left(t\right) \\
&= F\big(\mathbf{z}\left(t\right)\big) \qquad (2.4.4)
\end{aligned}
$$

As an illustrative example, consider the classic Lorenz model, which has states $\mathbf{x} = [x_1, x_2, x_3]$ and is described by the coupled non-linear differential equations:

$$\dot{x_1} = 10(x_2 - x_1), \qquad (2.4.5)$$

$$\dot{x_2} = -x_1 x_3 + 28 x_1 - x_2, \qquad (2.4.6)$$

$$\dot{x_3} = x_1 x_2 - \frac{8}{3} x_3. \qquad (2.4.7)$$

Each state itself looks like a stochastic (noisy) signal, see Figure 2.2(a), however a plot of the state space of x_1 vs x_2 projected onto the x_3 plane, as illustrated in Figure 2.2(c) shows that the system has an underlying deterministic structure. This phase space structure, in this case a characteristic figure of eight, is referred to as the *attractor* of the model. If however, access to each of the states was unavailable, but instead a measurement $\phi(\mathbf{x}) = 3x_1 - 2x_2$ could be observed, see Figure 2.2(b). By reconstructing the state space as $\mathbf{z} = [z_1, z_2, z_3] = [\widetilde{\Phi}(\mathbf{x}(t)), \widetilde{\Phi}(\mathbf{x}(t-\tau), \widetilde{\Phi}(\mathbf{x}(t-2\tau))]$ and then plotting z_1 vs z_2 projected onto the z_3 plane, the attractor in Figure 2.2(d) can be found. This reconstructed attractor in Figure 2.2(d) is equivalent to the system attractor in Figure 2.2(c) under a rescaling transformation of the plot axes. Therefore, scale independent measures computed on the reconstructed system can be considered equivalent to the measures on the original system. Such scale independent measures include measures of entropy, dimension and Lyapunov exponents. The significance of these measures will be discussed later in this chapter.

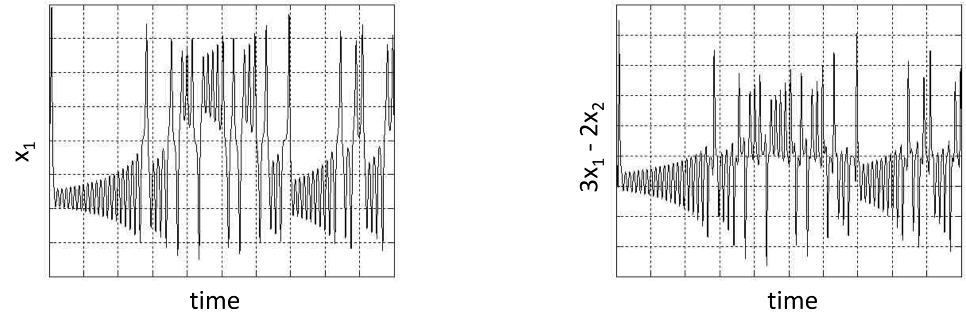

(a) Time evolution of the system state x_1

(b) Time series measurement on the system,$3x_1 - 2x_2$

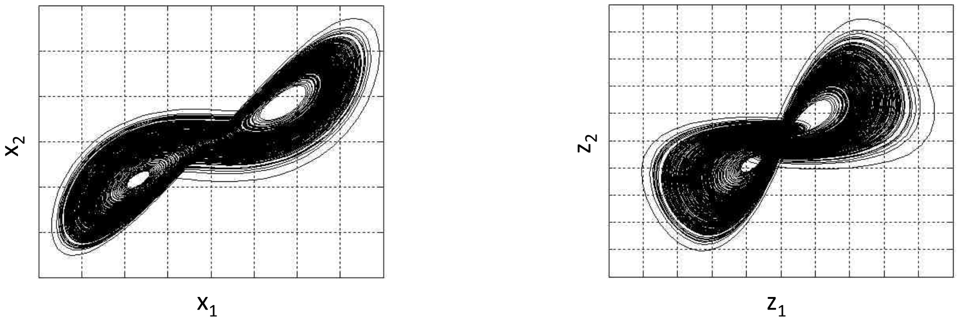

(c) Lorenz system attractor

(d) Reconstructed system attractor

Figure 2.2: Example of delay reconstruction with the Lorenz model

Attractors of brain dynamics created from delay embedding of EEG data resulting from computer simulations of the brain were published in 1991 by W. J. Freeman [29], and in 2003 by Lopes da Silva *et al.* [64]. In Freeman's simulations the phase portraits illustrate the differences between attractors representing simulated olfactory brain dynamics, where one attractor represents a resting state (Figure 2.3(a)) and the other represents a state during perception of a familiar scent (Figure 2.3(b)). These phase portraits suggest a more ordered, almost periodic, brain state during scent perception than at rest. Lopes da Silva's simulated phase portraits represent a thalmo-cortical network of a normal brain (Figure 2.4(a)) and an epileptic brain (Figure 2.4(b)). These state space diagrams illustrate the idea that the brain has two attractors, representing the inter-ictal state and the seizure state. In the normal brain these attactors are well separated such that a transition from normal to seizure will, in all likelihood, never occur. However, in the epileptic brain the borders between these attractors are blurred, facilitating easy input driven transition between seizure and non-seizure states. The transition between seizure and non-seizure states is a key question for non-linear dynamics. While the input driven transition between two strange attractors as illustrated in Figure 2.4 is one possibility, another possibility is that of a *bifurcation*. A bifurcation is a change in the stability property of a system depending on the value of a *bifurcation parameter*. If a bifurcation existed, as suggested in brain models such as the Robinson model [65], there would exist a parameter μ which would indicate the seizure/non-seizure status of the brain system. If the trajectory of such a parameter μ could be tracked, any changes in the system from a non-seizure state towards a seizure state could be predicted, see Figure 2.5.

(a) Resting

(b) Perception of familiar scent

Figure 2.3: Phase portraits from computer models of the brains olfactory system, published in [29]

While these models present interesting paradigms for the nature of non-linear brain dynamics, there are however, serious theoretical limitations associated with practical delay reconstruction on any real-world dynamical system [63]. Firstly Takens' theorem is valid only in the realm of autonomous systems, that is time invariant systems, that are independent of any external inputs. Consequently, Takens' theorem is limited to systems that are stationary. Furthermore, delay reconstruction is only valid when working with noise-

(a) Normal (b) Epileptic

Figure 2.4: Phase portraits from computer models of the brains thalamo-cortical network, published in [64]

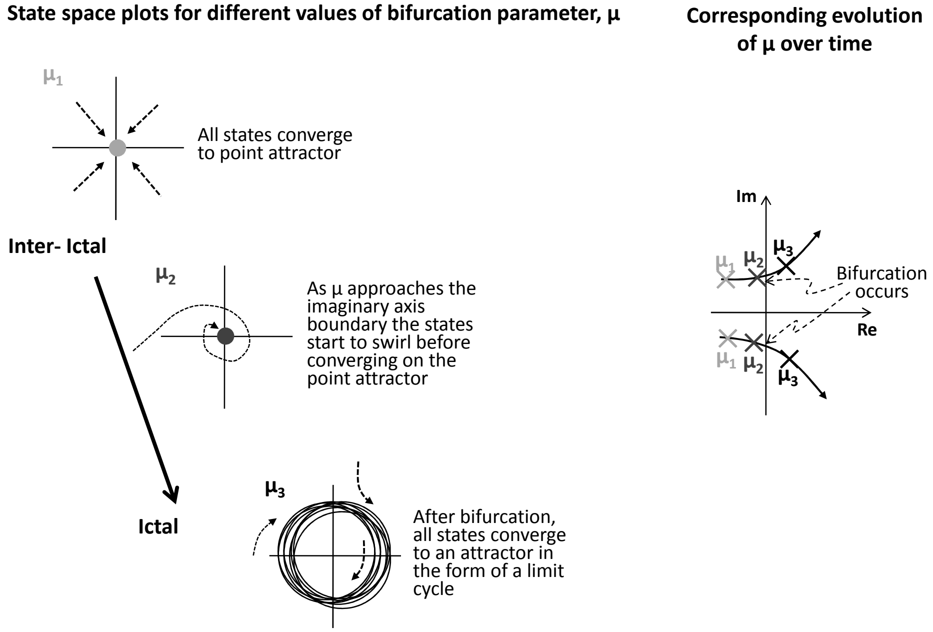

Figure 2.5: Illustration of a bifurcation. The transition from normal inter-ictal brain state to seizure state may be some form of bifurcation phenomenon.

free time series measurement. There are also constraints regarding adequate amounts of data for the reconstruction to be valid. Takens originally specified that the embedding dimension, d must be greater than twice the dimension of the system under observation ($d \geqslant 2m + 1$). Such constraints imply that serious caution must be taken when applying reconstruction method to any real world data, and in the interpretation of any results.

Although work applying delay construction techniques to the EEG time series is common, within the current framework of theoretical understanding the EEG is ultimately an unsuitable signal for such analysis on many fronts. Firstly, the brain is not an autonomous system, our brains undoubtedly process external inputs and the EEG signal is clearly non-stationary (for a overview of stationarity, or lack thereof, in the EEG signal, see the end of this section). Secondly, to reconstruct low-dimensional systems in the order of 5 dimensions would still require over 1 million data points to reliably reconstruct the system [66]. Considering the structural and functional complexity in the brain, it is not unreasonable to imagine that a model of the brain would be high dimensional. This would imply that much data is required to reconstruct the brain's system. Furthermore, the EEG is non-stationary, and may only be considered quasi-stationary (as required for reconstruction) for short periods of time. Such short periods of time are most likely too short to provide adequate data for reconstruction. Thirdly, reconstruction is only valid for purely deterministic systems. As the EEG is a signal with a considerable amount of measurement noise, there is a stochastic element to the time series which disqualifies it for analysis within Takens' original framework. However, even if the reconstruction from the EEG time series is not a true representation of the underlying dynamics, relative measures may still be useful indicators of changes in the dynamics of the underlying system. For instance, rather than taking measures as precisely defining the brain dynamics at a given time, changes in such measures over time may correlate with changes in the underlying dynamics [20, Ch. 3].

Another consideration for delay reconstruction on the EEG is that it is a measure on a spatially distributed dynamical system. Such a spatially distributed system can be viewed as a collection of locally distinct systems which interact with each other. Then, for a given EEG recording at one channel, the reconstruction would have to consider the inputs coming into the system from the remote spatial locations. This of course would make the local system under analysis non-autonomous and as such, unsuited to reconstruction techniques. However Stark discussed a preliminary framework for reconstructing such *spatio-temporal* systems in [63, 67], which effectively replaces the remote interactions of the local system by noise. Stark's framework extends Takens' original theorem to account for noise in the system. Stark argues that reconstructing a high-dimensional spatio-temporal system is too complicated, in that for most real world cases, there would not be sufficient time series data available for the reconstruction. Instead, Stark argues that reconstructing a local system may provide more useful information. Perhaps reconstruction of the underlying brain dynamics would be somewhat sensible from this viewpoint. It may not be unreasonable to apply reconstruction techniques to an EEG time series derived from the difference in signals recorded from two closely spaced cortical regions. In this manner it could be hypothesised that the majority of the "noise input" to the local system, from other spatially distant systems, would be "cancelled out". Meaningful reconstruction could then be applied to the remaining difference signal, where any further noise elements in that signal would be considered within the framework of Stark's theorem for reconstruction for systems with stochastic forcing.

Stationarity

The methods usually employed in both non-linear and linear time series analysis require the stationarity of the data set. A data set or time-series is considered stationary in a linear systems sense if its statistical properties and spectral characteristics are constant over time. From a non-linear or dynamical systems point of view, stationarity essentially implies that the dynamical law describing the system does not change (over long time scales) [68, 69]. The clear differences in the EEG of different states (e.g. sleep, awake, alpha rhythm, and also in the epileptic brain: ictal, pre-ictal and post-ictal), with the mean, variance and frequency components differing between states, imply that the EEG is undeniably a non-stationary time series. Particularly from the viewpoint of non-linear systems measures, the criterion of stationarity in EEG time-series of sufficient length for analysis is almost impossible to satisfy in practice.

However many methods theoretically requiring stationarity have been applied to the EEG data with mixed success, see Section 2.4.1 of this document. Much of this literature on applying non-linear dynamic theory to the EEG data relies on the assumption of "weak stationarity". Weak stationarity, or wide sense stationarity can be defined for linear systems as requiring statistical quantities up to the second order to be shift invariant. For non-linear systems this essentially equates to the assumption that the dynamical changes during an EEG recording are sufficiently slow in time to allow short segments of EEG data to be considered approximately stationary or “quasi-stationary”.

Much research has been focused on the stationarity (or rather non-stationarity) of EEG time series, with particular emphasis on the estimated times during which EEG segments can be regarded “quasi-stationary” for analysis. Blanco *et al.* [47] isolated segments of the EEG, in the order of 20 seconds during which “weak stationary criteria” (or wide-sense stationary) were satisfied in an empirical observation of the low order statistics of the signal. They propose that reliable dynamic measures can be computed within these 20 sec segments. Observations of a similar nature led Lopes Da Silva and Niedermeyer to conservatively conclude that short epochs of the EEG signal, ∼10 sec, recorded while the patient’s behavioural conditions were unchanging, could be considered stationary for analysis [27, pg 1200]. However, Kantz and Schreiber [70, 71] see the linear systems notion of weak stationarity, as used by both Blanco *et al.* and Lopes Da Silva *et al.* to be inadequate in a non-linear setting. Alternative stationary analysis from a non-linear systems viewpoint has been conducted by Reike *et al.* [69, 72]. This non-linear analysis was based on the quantification of recurrence of vectors in state space. Dikanev *et al.* compared both statistical (linear) and dynamical (non-linear) analysis of EEG segments, where the dynamical analysis was centered around quantifying changes in the distances between vectors in state space [68]. Dikanev *et al.* concluded that their non-linear stationarity analysis segmented the EEG signal into a greater number of quasi-stationary segments than the statistical linear stationarity analysis. The dynamically stationary epochs were found to be in the range ∼10-12 seconds for the pre-ictal, ictal and post-ictal EEG data considered. In addition, regarding seizure prediction, both Reike [72] and Dikanev [68] suggest that segmentation of the various dynamical states in the EEG through stationarity analysis may be useful in quantifying a pre-ictal state, however this has not been attempted with any reasonable EEG database as yet.

In conclusion, non-stationarity is undoubtedly inherent in the EEG signal and analyses of this signal that require stationarity must be applied to suitably qualified quasi-stationary segments. Such quasi-stationary segments are most likely to be in the order of 10s as determined by non-linear stationarity analyses.

2.4.1 Selected Non-Linear Measures: Performance and Scepticism

Despite the obvious limitations with delay reconstruction, including non-stationarity, a number of non-linear statistics based on this method have been used with varying success. These statistics, estimated by analysing the distances between points in an appropriate embedding space, include the classic non-linear systems measures of correlation dimension, Lyapunov exponents and entropy and also measures attempting to quantify underlying dynamical changes.

Dimension

The dimension of an attractor is related to the number of degrees of freedom in the system dynamics and can be regarded as an indicator of system complexity. One type of dimension measure is the *correlation dimension, D*, this is calculated as

$$D_2 = \lim_{r \to 0} \frac{d \log(C_r)}{d \log(r)}, \tag{2.4.8}$$

where C_r is the *correlation integral*:

$$C_r = \frac{2}{N(N-w)} \sum_{i=1}^{N-w} \sum_{j=i+1}^{N} \theta(r - |X_i - X_j|). \tag{2.4.9}$$

N is the number of vectors, w is the Theiler correction, θ is the heaviside function and |...| indicates the vector norm [20, Ch. 3]. The correlation integral computes the likihood that any two points on the attractor will be closer than a certain distance, r. The slope of $\frac{\log(C_r)}{\log(r)}$, as r tends to zero is the classic "Grassberger and Procaccia" estimate of the correlation dimension. The Theiler correction excludes data point pairs which are close together in state space due to being close together in time. As a distance measurement, the correlation integral is sensitive to amplitude levels and thus normalisation of the EEG signal is essential; however, normalisation of the data was not considered in this work.

It has been postulated that epileptic events should lead to a reduction in the complexity of the brain's dynamical system. Such a complexity reduction is thought to occur due to the increase in synchronisation between recording channels (and therefore brain regions) that is visually observed in ictal EEG. It follows then that finding a decrease in complexity in the brain activity, as computed from the EEG, could indicate a pre-ictal state [44]. Estimation of the system dimension has been used as a complexity indicator in an effort to predict seizures, with a reduction in the dimensional measure expected to indicate a complexity reduced pre-ictal state.

In 1998 Lehnertz and Elger [43] estimated the effective correlation dimension D_2^{eff} from a 30-dimensional embedding of intracranical EEG data, with a database of 16 patients. The measure was computed on channels individually, and can therefore be classified as a univariate measure. The authors defined an estimator D^* for D_2^{eff}, based on the average slope of the correlation integral,

$$D^* = \frac{1}{N_r} \sum_{r=r_l}^{r_u} \frac{d \log(C_r)}{d \log(r)}, \tag{2.4.10}$$

where N_r specified the number of r values in the range $[r_l, r_u]$. The authors specified that,

$$D_2^{eff} = \begin{cases} D^* & \text{if } D^* \leq D_{max} \text{ and } N_r \geq 5 \\ D_u & \text{otherwise} \end{cases}, \tag{2.4.11}$$

where D_{max} is a maximum unresolvable dimension and D_u is an arbitrary fixed threshold of 10. Pre-ictal states were declared when D_2^{eff} fell below a threshold for a particular duration. The threshold was taken as the mean inter-ictal level of D_2^{eff}, while the duration was taken to be the maximum duration that D_2^{eff} remained below the threshold value in the inter-ictal data-set. The authors were careful to note that this estimate for the correlation dimension should be regarded as an empirical quantity and not one with a precise theoretical significance. Results with this method were highly promising with sensitivity of 94% and prediction times (defined as the time between seizure onset and declaration time of a pre-ictal state) of 4.25 - 25 min. However, no indication of the specificity was given. In 2001 Lehnertz tested their work on a larger number of 59 patients with 95 seizures [73]. This study resulted in a lower sensitivity of 47% and a mean prediction time of 19 sec. Again, specificity or the number of false positives was ignored. Furthermore, in both studies the statistical significance of the results was not discussed. This highlights the need for analysis with a large data set, particularly one containing a significant interictal control element, as well as statistical significance measures, to validate the method.

The promising findings of Lehnertz *et al.* were later disputed when further analysis was conducted by two other research groups: Aschenbrenner-Scheibe, Maiwald *et al.* [74, 75] and Harrison *et al.* [76]. Aschenbrenner-Scheibe, Maiwald *et al.* [74] found that by replicating Lehnertz's method with a lengthy inter-ictal dataset, analysis of the pre-ictal data showed "only 1 out of the 88 seizures [in their data set] was preceded by a significant pre-ictal dimension drop". This corresponds to a sensitivity of only 1.13%. In an effort to improve sensitivity Aschenbrenner-Scheibe, Maiwald *et al.* adapted the threshold and duration levels for prediction and evaluated the corresponding trade off between sensitivity and false positives per hour. They found that for reasonable false positive rate of 0.1 FP/hr, the sensitivity ranged from 8.3 - 38.3% corresponding to assigned maximum prediction length windows of 20 min and 50 min respectivly. In a later paper, Aschenbrenner-Scheibe, Maiwald *et al.* [75] again evaluated Lehnertz's method as part of a review of several prediction methods with a database of 21 patients and 88 seizures. They found similar results as before with a low sensitivity of 20% corresponding to a false positive rates of 0.1 FP/hr given a maximum prediction length windows of 30 min.

A second group, that of Harrison *et al.* [76] sharply disputed Lehnertz's findings and claimed that the correlation dimension has "no predictive power for epileptic seizures" when tested on their database of 20 patients. The authors showed that the correlation integral (equation 2.4.9), central to Lehnertz's algorithm, is sensitive to changes in the energy of the signal, through investigation of both the effects of amplitude normalisation and surrogate data testing. The authors argued that any *"seizure detection ability of the correlation-integral based measures is directly linked to the signals variation in the time-frequency-energy characteristics rather than to any non-linear dynamics present"* in the data. These findings and the findings of Aschenbrenner-Scheibe, Maiwald *et al.* combine to support the conclusion that any seizure predicting ability of the correlation dimension is unlikely. The inability of this method can be attributed to both the limitations of delay reconstruction for the EEG as discussed earlier in Section 2.4 and the further difficulties associated with the correlation integral as highlighted by Harrison *et al.*

The dimension limitations of delay reconstruction deserves careful consideration in the context of embedding EEG data. Leaving aside for the moment the theoretical requirement that the embedding dimension, d, should be over twice the underlying system dimension, m, consider the number of datapoints available to populate a reconstructed state space of arbitrary dimension. This is limited by stationarity. Earlier in this Section 2.4 stationarity was determined to be in the order of 10 seconds. At typical EEG sampling rates of 512Hz this gives us approximately 5000 data points to populate the embedding space. For $d = 2$ an embedding plane, and $d = 3$, a 3-dimensional object, this offers a reasonably dense population of points. For higher dimensions, whether or not there would be enough points to adequately populate the embedding space in order to distinguish an attractor (should it exist) is questionable. By $d = 30$, the embedding dimension used in Lehnertz and Elger's study [43], 5120 points (effectively 170 points per dimension) could only populate the space in such a sparse fashion that any measures based on distance between points would be highly illposed. Figure 2.6 provides some illustrative insight into this showing the spareness of 170 points per dimension in both 2-dimensional and 3 dimensional embedding spaces (341 and 512 datapoints respectively) for the Lorenz system previously introduced at the start of Section 2.4. This issue of sparely populated embeddings is equally problematic for the other measures in embedding space, including Lyapunov exponents, entropy and dynamical similarity index each discussed in the forthcoming sections. The case of doubling the data and halving the embedding dimension ($d = 16$, 10240 datapoints), later utilised as the embedding space for dynamic similarity index, is also illustrated in Figure 2.6 to show the case of 640 data points per dimension (1920 datapoints for 3-dimensions and 1280 datapoints for 2-dimentions). Note these plots are highly simplistic in that they ignore the time considerations - rather than embedding a short segment of the time-series which would only provide very localised attractor information, it was assumed that our data samples are spread in time such that the all areas of the attractor are represented. Certainly for real EEG, presuming our brains have more complex dynamics than the three state Lorenz system, it would be impossible to extract enough datapoints from stationary segments of EEG to adequately populate a low dimensional embedding space (d in the range of 10-30 dimensions). Moreover, there are additional realities impeding reconstruction:(i) $d = [10, 30]$ is far less that the anticipated underlying order of m (ii) the effect of noise further disorganising those few embedding points that are available.

Lyapunov Exponents

A second non-linear measure used is that of Lyapunov exponents. These describe the exponential divergence (or convergence) of nearby trajectories in state space, providing an indication of the stability of solutions to small perturbations in the dynamical system. Dynamical systems, that are both non-linear and deterministic, are classified as *chaotic* if the long term behaviour of the system is highly unpredictable due to sensitivity to

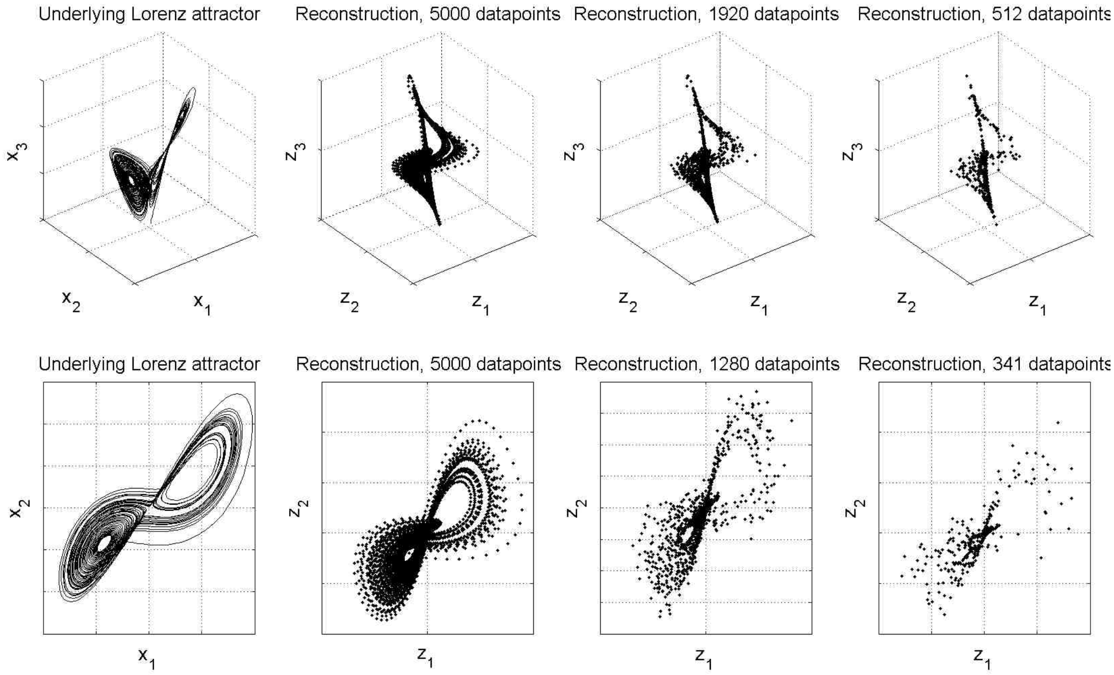

Figure 2.6: Illustrative example of the impact of data quantity in embedding space for the Lorenz System with 3 states, $\mathbf{x}$. The reconstructed states after data embedding, $\mathbf{z}$ are shown for various amounts of data (*i*)5000 datapoints (*ii*) 640 datapoints per dimension (1920 points for 3-D upper plot,1280 points for 2-D lower plot) (*iii*) 170 data points per dimension (512 points for 3-D upper plot, 341 points for 2-D lower plot)

initial conditions. Lyapunov exponents, as a measure of exponential divergence of nearby trajectories in state space, provide a measure for how "chaotic" a dynamical system is. For two points in state space with an initial separation, δx_0 the Lyapunov exponent, λ, that characterises the evolution of the separation between the points in time is

$$\delta x(t) = e^{\lambda t} \delta x_0. \tag{2.4.12}$$

There is a whole spectrum of Lyapunov exponents to characterise a system, one for each dimension in state space, since the rate of divergence of nearby trajectories can differ for each possible orientation of the initial separation vector between the trajectories. The largest or maximum Lyapunov exponent, MLE, is of particular interest, as it can be used as a measure of predictability of the dynamical system. A positive MLE implies an exponential rate of divergence, which indicates that the underlying system may be chaotic and therefore highly unpredictable. A positive MLE does not however imply the system is definitely chaotic: chaotic systems require not only a positive Lyapunov exponent but also other conditions including overall system stability. The MLE is essentially the 1^{st} Lyapunov exponent, λ_1, which measures the exponential expansion/ contraction of adjacent points in state space. (Note the 2^{nd} Lyapunov exponent, λ_2, measures the exponential expansion/ contraction of an area element in state space, while the 3^{rd} Lyapunov exponent, λ_3, measures the exponential expansion/ contraction of a volume element in state space, *etc* ...)

In 1990 Iasemidis *et al.* first suggested the use of Lyapunov exponents for seizure detection [77], finding in intracranial EEG that the value of the MLE decreases at seizure onset, indicative of a decrease of system complexity during ictal periods. They also found that the pre-ictal EEG exhibited "several abrupt drops" which could perhaps be exploited for predictive purposes. To find the Lyapunov exponent the authors attempted the reconstruction of the brains dynamical system with an embedding dimension, d = 7, on 12 seconds of EEG data recorded at 500Hz. An adaptation of Wolf's method [78] was applied to the resulting attractor reconstructed for each channel recorded. Wolf's method was based on computing the distance, $L(t_{k-1})$, between two nearby points in state space at a time t_{k-1}, and comparing this to the evolved distance between the two points at a later time t_k, $L'(t_k)$. The MLE was defined as

$$\lambda_1 = \frac{1}{t_M - t_0} \sum_{k=1}^{M} log_2 \frac{L'(t_k)}{L(t_{k-1})}. \tag{2.4.13}$$

However, as highlighted by Kantz and Schreiber, Wolf's method can easily obtain the wrong results as the algorithm "does not allow one to test for the presence of exponential divergence, but just assumes its existence and thus yields a finite component for stochastic data also, where the true exponent is infinite" [70].

Despite this limitation of Wolf's method, in 2003 Iasemidis *et al.* developed their initial findings in an effort to predict epileptic seizures, based on a short-term MLE [9]. The authors note that since the brain system is highly non-stationary, only estimates of short term maximum Lyapunov exponents, STLmax, from EEG segments in the order of 10 sec, are to be considered. These univariate (single channel) measures are then combined to create a multivariate measure, called "spatio-temporal dynamical entrainment". The authors noticed that the STLmax profiles for each individual recording channel converged to similar values in the pre-ictal period. Dynamical entrainment is a measure of this similarity and is computed as

$$D_{ij}^{t} = STLmax_{i}^{t} - STLmax_{i}^{t}, \tag{2.4.14}$$

where t indicates a particular 10 minute time window, and $STLmax_{i}^{t}$ denotes a vector of 60 STLmax values for recording channel i (one STLmax value for every 10 sec recording). A pre-ictal state was declared when the dynamical entrainment, D_{ij}^{t}, corresponded to a value between a pair T-statistic. Results were promising with a sensitivity of 82%, a false positive rate of 0.16 FP/hr and a mean seizure prediction horizon of 71.7 min before ictal onset.

However, later studies by Lai, Harrison *et al.* questioned the suitability of Lyapunov exponents for non-stationary, high-dimensional and noisy time series analysis [79, 80]. In [79] the authors analysed the time-series from several non-linear models and found Lyapunov exponents to be unsuitable for detection and prediction of underlying changes in these models. The authors then extrapolated these findings to claim that "Lyapunov exponents do no appear to have any predictive or detective powers for epileptic seizures". In [80] the authors expanded their claims on the basis of illustrative models and also tests using intracranial data. However, Iasimidis *et al.* replied to this claim by providing evidence that the methods of Lai, Harrison *et al.* contained several faults, from inadequate computation of Lyapunov exponents to misinterpretation of their models [81]. Iasimidis *et al.* also highlighted that Lai, Harrison *et al.* did not consider dynamical entrainment. Although Iasimidis *et al.*'s critisism of Lai, Harrison *et al.*'s work appears to have substance, their work in highlighting the unsuitability of Lyapunov exponents raises valid concerns about the application of delay reconstruction methods to non-stationary, high-dimensional and noisy time series such as the EEG.

Entropy

The concept of entropy has many interpretations in varied scientific fields. In physical thermodynamics systems, entropy, S, quantifies the amount of disorder of the system at a molecular level, where the higher the entropy the greater the disorder. The second law of thermodynamics states that, for isolated systems, entropy will always stay constant or increase. This implies that systems will always tend towards a state of increased disorder, which corresponds to tending towards a state of thermodynamic equilibrium. From a statistical thermodynamics viewpoint, assuming that the dynamics of a system can be captured by a Markovian process of microscopic states with probability, p_i, entropy can be expressed as,

$$S = -k \sum_i p_i \ln p_i \tag{2.4.15}$$

where k is Boltzmann's constant and p_i is the probability of the i^{th} system microscopic state, where this microstate is associated with the i^{th} quantum energy level E_i.

A similar expression to equation 2.4.15 exists for entropy, H, as applied to information theory. Shannon's entropy equation, provides a measure for the average information content of a system with information symbols x_i,

$$H = E[I(x_i)] = \sum_i p(x_i) I(x_i) = -\sum_i p(x_i) \log_2(p(x_i)) \tag{2.4.16}$$

where E[...] denotes expected value, $p(x_i)$ is the probability of symbol x_i occurring. $I(x_i)$ is the information content of symbol x_i, with

$$I(x_i) = \log_2 \left(\frac{1}{p(x_i)} \right) \tag{2.4.17}$$

for binary information. Information content of a symbol is related to the probability, $p(x_1)$, of a symbol in the sense that if the probability of a symbol x_1, is 1, then the information gained by receiving that symbol is zero, while if probability, $p(x_2)$ of a symbol x_2 is 0.2, then the information gained by receiving that symbol is $\sim$0.7. In this way the less likely a symbol is, the more valuable its information content on a scale of 0 (no information) to 1 (complete information). Entropy, H, is measured in units of bits/ symbol and can accordingly also be defined as the rate of information transfer in a system.

The expansion of the entropy concept to dynamical systems is discussed next. The aforementioned definitions specify that the system space is segmented and probabilities are assigned to each segment - for dynamical systems the phase space of the dynamical systems can be divided into cells, with probabilities then assigned for the likelihood of a trajectory being in a given cell[2]. With this segmentation, the entropy becomes

$$S_n = -k \sum_r p_r \ln(p_r) \tag{2.4.18}$$

where k is a constant and p_r is the probability that a trajectory which started in a particular initial cell will be located in the r^{th} cell after n units of time [82]. The implications of this formula are: If all the trajectories starting in a particular cell end up in cell r after N time steps, then the probability p_r is 1, and $S_n = 0$ for all n. This constant change in entropy as time evolves may occur, for example, in the case of a deterministic non-linear system with an attractor in the form of a limit cycle (regular motion). If however, the trajectories starting in a particular cell end up in N different cells after x time steps, with equi-probability of ending up in any given cell r, then the probability p_r is $\frac{1}{N}$, and $S_n = -k\ln(\frac{1}{N})$. Therefore, the entropy is larger for a higher number of possible cells where the trajectory could be. As N increases (or entropy increases), the ability to predict future system behaviour decreases. Thus, an increase in the rate of change of entropy over time implies that the system is becoming more “chaotic”. Entropy for dynamical systems is generally computed as a change in entropy ΔS_n. This change in entropy, known as Kolmogorov (or Kolmogorov-Sinai) entropy, K, is defined as

$$K_n = \frac{1}{\tau}(S_{n+1} - S_n) \tag{2.4.19}$$

where τ represents one time step, and S_n is that described in Equation 2.4.18.

Kolmogorov entropy can be shown to be closely related to Lyapunov exponents. This is unsurprising considering that both entropy and Lyapunov exponents are measures for the level of chaos and hence unpredictability, in the system. In some cases, a mathematical

---

[2] Implicitly we have assumed that the state space and the dynamics are such that a Markovian symbolic process may be inferred.

relationship between the two can be expressed with entropy equal to the sum of the positive Lyapunov exponents. One method for computation of Kolmogorov entropy from time-series data, as proposed by Grassberger and Procaccia, is

$$K_2 = \frac{1}{\Delta t} log_2 \frac{C_m(r)}{C_{m+1}(r)} \tag{2.4.20}$$

where C_m is the correlation integral (which computes the likelihood of trajectories occurring within a cell of radius r, see 2.4.10), with an embedding dimension m and an original time-series sample time Δt [20]. This method computes entropy by considering the change in correlation integral for a small value of r, for two high values of the embedding dimension m, and m+1. The reliance of this method on delay reconstruction indicates that it is unlikely to be a suitable measure for application to non-stationary, noisy, high-dimensional EEG data.

This unsuitability of entropy measures based on delay reconstruction may indicate the lack of success found when the method was applied to the EEG. In 2003, Van Drongelen *et al.* [83] investigated the ability of Kolmogorov entropy (with Equation 2.4.20) as a seizure prediction candidate in the simultaneously recorded intracranial and scalp EEG of children. The method used for entropy calculation was that described by Grassberger and Procaccia, see equation 2.4.20. The results revealed that prediction was more successful with intracranical data rather than scalp data, with a sensitivity of 60% (3 out of 5 patients) for intracranial data and a sensitivity of 40% (2 out of 5 patients) for scalp data. However, both these sensitivity results are quite low. Prediction times ranged from 2-40 min in advance of seizure onset. Insufficient control (non-seizure) data was considered to evaluate the specificity or false positive rate.

Dynamical Similarity Index

In 1999 Le Van Quyen *et al.* proposed a “dynamical similarity index”, DSI, algorithm for seizure “anticipation” which compared the dynamics of a reference window with the dynamics of a test period [44]. Le Van Quyen *et al.* showed results which indicated that the dynamics are altered in the pre-ictal period, thus providing a warning sign for seizure anticipation. Their method was based on creating a m-dimensional embedding of a vector which was composed of the time intervals between positive going zero crossings computed from a 25-30 second window of the EEG data series (m=10 or 16). Singular value decomposition was applied to this embedding, resulting in a linear reduction to a r-dimensional model (r=3 or 4) which acted as a template for the dynamics. Templates for both reference and test dynamics were cross-correlated, using the correlation integral, to find the DSI measure. The cross-correlation integral was defined as $C(S_{ref}, S_t)$, where

$$C(S_{ref}, S_t) = \frac{1}{N_{ref} N_t} \sum_{i}^{N_{ref}} \sum_{j=1}^{N_t} \theta(r - |Y_i(S_{ref}) - X_j(S_t)|). \tag{2.4.21}$$

N_{ref} and N_t are the number of vectors in the reference and test templates respectively, θ is the heaviside function and $|...|$ indicates the euclidean vector norm. The Correlation integral computes the likelihood that any two vectors, X and Y, between the test template, S_t, and the reference template, S_{ref} respectively, will be closer than a certain distance, r. A seizure is anticipated, or equivalently, pre-ictal dynamics are found, if the statistical significance of the DSI measure, Σ, is greater than k (where k is chosen to be 5) over a time period D. By the Chebyshev inequality, the probability of the significance, Σ, being greater than k is bounded as follows

$$P(|\Sigma| \geq k) \leq 1/k^2, \tag{2.4.22}$$

where $1/k^2 = 0.04$. In their original algorithm [44] D was set to 150s, however in a later paper Le Van Quyen *et al.* [84] stipulated that the inequality $|\Sigma| \geq 5$ must hold continuously up until the seizure occurs. Seizure anticipation is determined by the earliest anticipation found across all recorded EEG channels.

The Le Van Quyen group published promising preliminary results using intracranical data in 1999 with a sensitivity of 83% and a mean anticipation time ~6 min [44]. Futher studies on scalp EEG resulting in a sensitivity of 96% and a mean anticipation time of 7 min [84]. However in both cases the number of false positives was not considered. In 2002, Navarro and Le Van Quyen extended their study to include control data and thereby find an estimate for the false positive rate. Through analysing both intracranical and scalp EEG they found a sensitivity of 83%, a false positive rate of 0.21 ± 0.2 FP/hr and mean anticipation time of 7.5 mins [85].

However later analysis of the dynamical similarity method raised doubts when several groups failed to replicate this with other data sets (including preliminary analysis with our own group's scalp data set), given the requirement that the DSI remains below the threshold continuously up until the event occurs. Maiwald *et al.* found only a sensitivity of 21-42% for a false positive rate of 0.14-0.15 FP/hr with an intracranial data set [75]. De Clercq *et al.* found that none of the seizures in their scalp data set were predicted [86]. Note that Le Van Quyen *et al.* provided one patient's data from their data set to De Clercq *et al.*. Using this data De Clercq found anticipation to be 20 minutes in advance of seizure - showing DeClercq's interpretation of the method to be correct.

These contradicting findings can be in part explained by some of the shortcomings of the DSI approach. Firstly, the reduction of the dynamics templates via SVD essentially reduces the reconstructed dynamics to a 3 or 4 dimensional linear model. This is certainly inadequate in the non-linear brain dynamics realm. Secondly, artefacts are likely to strongly contribute to these 3-4 dimensions available in the reduced linear model. Thirdly, an analysis that attempts time series delay reconstruction of the brain dynamics the data contained in a 25-30 second window is undoubtedly insufficient for reasons explained earlier in Section 2.4 with Figure 2.6. Fourthly, as highlighted previously in the case of the correlation dimension, Harrison *et al.* showed that the correlation integral, central to the DSI algorithm, is sensitive to changes in the energy of the signal without suitable amplitude normalisation. Harrison *et al.* suggest that any "seizure detection ability of the correlation-integral based measures is directly linked to the signals variation in the time-frequency-energy characteristics rather than to any non-linear dynamics present" in the data [76].

However, the reduction of the raw EEG data by taking only the zero-crossing time intervals reduces 10-fold the data for processing, and thus allows the possibility of causal online EEG analysis. The algorithm does seem to provide a rather robust, seizure detection ability with our data, as also found by the De Clercq group, *"At the start of the epileptic seizure the similarity measure suddenly dropped"*[86]. Although, relative to other detection methods, DSI is rather computationally intensive. In addition, comparing test windows with a reference window more than 1 hour away shows the dynamics are quite uncorrelated. Rather than showing seizure anticipation this clearly shows that the EEG is not stationary. As suggested by Le Van Quyen *et al.* 1999 [44], perhaps DSI can be used as an indicator of which periods the EEG can be considered quasi-stationary for analysis.

Measures of Synchronisation

Linear measures of synchronisation were discussed in Section 2.3.1, however non-linear synchronisation measures are also available. From a dynamical systems viewpoint this synchronisation in the brain can be considered as the synchronisation of coupled non-linear sub-systems from different brain regions.

While some preliminary work has been conducted in the application of non-linear measures of synchronisation or *generalised synchronisation* to the EEG [87, 88], to the authors knowledge no seizure prediction or anticipation algorithms have been published using these methods. However non-linear synchronisation analysis has been applied to the EEG in an effort to locate the seizure focus and also to investigate synchronisation between different brain regions. In [88] a measure of *nonlinear mutual predictability* was proposed to localise the seizure focus. This measure was based on the detection of the interdependence between delay reconstructed dynamics from two brain regions via investigating if short term predictions of trajectories from one system can be improved with information from the other system. In [87] a measure of *synchronisation likelihood* was employed. This synchronisation between reconstructed dynamics from two electrodes was computed as the likelihood that Y_j will be close to Y_i given that X_j is close to X_i, where Y and X are the attractors resulting from a reconstruction of EEG data from two different electrodes.

A Note on Normalisation

Surprisingly, a major consideration, that seems to be absent from the reviewed literature, is a discussion of the nature of the EEG data. Dynamical systems measures would benefit greatly from normalisation of the EEG data prior to processing, as highlighted throughout this literary review and therefore it is the current practice within our group to normalise [28]. Normalisation could take the following form: for each processed segment, the mean should be removed and the data should be normalised by the root mean squared (RMS) value of that segment. The signal to be processed $s(i)$ should be:

$$s(i) = \frac{x_{zm}(i)}{\sqrt{\frac{1}{N}\sum_{i=1}^{N} x_{zm}^2(i)}}, \tag{2.4.23}$$

where

$$x_{zm}(i) = x(i) - \frac{1}{N}\sum_{i=1}^{N} x(i), \tag{2.4.24}$$

where x is the raw EEG signal, x_{zm} is the zero-mean (mean removed) signal, and N is the number of data points in the segment to be processed. The removal of the mean can be assumed to have no effect on the information content of the data since the mean or DC value is meaningless when the data has been hardware DC filtered during the acquisition stage. Additionally, the data represent voltages; there is no meaning that can be attached to a DC voltage in the context of brain dynamics.

2.5 Conclusions on Seizure Prediction Algorithms

The overriding conclusion resulting from the literature, is that, seizure prediction remains unsolved. Throughout the review it was found that initial results promising a prediction algorithm failed to be replicated on other datasets, and are therefore unsuited for clinical applications. Given the variety of epilepsy etiologies and clinical manifestations, it would be wise to expect that a range of patient-specific algorithms could be required, with each patient suiting a particular method from a database of possible algorithm choices. However, such a patient-specific approach has also yet to be achieved for a sufficiently large patient cohort to allow for clinical use.

The algorithms reviewed in this chapter that did result in initial promising results, but failed to reproduce such results on larger databases or when tested by other research groups, were based on delay reconstruction /delay embedding. The limitations of delay reconstruction (stationary, noiseless data recorded on a low-dimensional, autonomous system) imply that the EEG is ultimately an unsuitable signal within the current reconstruction framework. This conclusion follows from the knowledge that the EEG is a highly non-stationary data set, with high levels of measurement noise in EEG recordings. In addition, the brain is not an autonomous system since our brains undoubtedly process external inputs. Moreover, there exists no conclusive evidence that the brain (or indeed epileptic events themselves) are low dimensional. These theoretical realisations correlate with the lack of practical success in published methods based on delay reconstruction approaches. The conclusion is simple: to date no prediction algorithm that can work in a clinical setting has been discovered. This conclusion is now shared by the international community [89].

2.6 The Current State of Seizure Prediction Internationally

The 3^{rd} international workshop on Seizure Prediction in Epilepsy was held in Freiburg, Germany in 2007 bringing together interdisciplinary teams of researchers to discuss the progress made and future directions of the field of seizure prediction [90]. Attendance at this meeting early in the research journey of this thesis provided an excellent opportunity to assess the state of the field prior to formulating specific research questions. A follow up 4^{th} meeting of this group was held in Kansas, USA in 2009 where the research findings detailed in later chapters were presented. At these international think-tanks there was consensus on what issues have progressed and what remained to be achieved, see Section 2.6.1. Furthermore, these meetings showed marked shift in research focus from the 1995-2005 decade of time-series analysis of EEG for clinical prediction applications as discussed in this Chapter thus far. These new directions are discussed in Section 2.6.2.

2.6.1 Issues Solved and Outstanding

Solved: The Statistics of Seizure Prediction

There has been a successful focus on statistical evaluation of seizure prediction results. The approaches of Schelter *et al.* [91], based on an analytical random predictor and those of Andrzejak *et al.* [92], based on numerical monte-carlo simulation with seizure time surragates, have been strongly adopted by the seizure prediction community to evaluate existing methods and as a minimum criteria for the evaluation of future algorithms. Under these frameworks, all the aforementioned approaches to EEG signal analysis, both linear and non-linear, have failed to reliably predict seizures better than a random predictor [89]. Therefore, it is the conclusion of the international seizure prediction community that, to date, *"it has not been possible to report a successful prospective prediction of epileptic seizures including a sound statistical analysis"* [90, Ch 2].

Solved: Data

Control data, in the form of lengthy inter-ictal recordings, is needed to ensure a true indication of specificity and false positive rate. Progress has been made with the compilation of two large collaborative databases: (1) A European Union funded project, Epilepsiae (2) An American project co-ordinated by the University of Pennsylvania.

Outstanding: Is Epilepsy Predictable?

Testing of the hypothesis "Is epilepsy predictable?" remains inconclusive. Although engineering analysis measures have claimed to be able to find pre-ictal indicators, such predictions/anticipations are questionable in that they failed to be replicated on large databases and to stand up to statistical scrutiny. The other argument put forward for the existence of a pre-ictal period at the beginning of this chapter was that, clinically, prodromal symptoms exist for some patients. A complementary question to "Is epilepsy predictable?", is "Does a pre-ictal period exist?". Of particular interest is the time window over which a pre-ictal period may exist. A suitable order of pre-ictal time period is currently undecided in the field, with engineering analyses in the reviewed literature claiming to find pre-ictal periods from minutes [43] to hours [41].

A physiologically motivated indication of pre-ictal time window would be particularly useful to estimate a ball-park pre-ictal time window that future prediction techniques should focus on. To estimate such a time window from a physiological point of view, data from input-driven epilepsy could be employed. An example of input driven epilepsy is photosensitive epilepsy, where seizures are triggered by visual light stimuli. The time delay between stimuli and seizure onset could be considered to be a pre-ictal time window, for a least some types of epilepsy. Therefore the pre-ictal stage could be expected to be quite short, in which case, early seizure *detection* may be just as useful as prediction, particularly if a rapid seizure-stopping intervention method can be found.

In a general sense it is difficult to make meaningful inferences regarding the nature of epilepsy between patients. As discussed in Section 1.2, epilepsy is the manifesting symptom of many underlying brain malfunctions. Patients with input driven epilepsy are very likely to have entirely different seizure pre-ictal time frames (should a pre-ictal period exist) to those with partial epilepsy or generalised absence seizures. It follows that for seizure prediction, a patient-specific predictor is most likely to find success. Therefore the question of whether epilepsy is predictable can be split into these two issues: predictability that is independent of the patient? (no); predictability that does relate to a specific patient? (perhaps). This thesis will examine the latter case, where a specific model is known.

2.6.2 Current Directions

There has been marked decline in EEG timeseries analysis for seizure prediction reported in the recent literature owing to the lack of success in this pursuit. Instead, the focus of established seizure prediction research hubs has shifted towards (1) Epileptogenesis, the physiological understanding of seizure generation through modelling studies and (2) Intervention methods for seizure abatement.

Understanding Seizures

There is currently a flurry of activity in computational modelling of the neurological networks involved in epilepsy based on both anatomical and electrical data from animal models.

Lopes da Silva *et al.* have developed multiple dynamical model theories based on the assumption of attractor existence and transitions between seizure/normal attractor based on inputs [90, Ch 7]. They have shown that absence type seizures can be modelled by a thalmo-cortical computational model which exhibits bifurcating behaviour where the "jump" from one attractor to the other (normal to seizure activity) occurs due to stochastic fluctuation of any input (rather than tweaking of model parameters). This would imply these seizures are unpredictable and may be more suited to early detection strategies. In contrast, the same group investigated hippocampal spiking in brain slices. When applying probe stimuli to these brain slices, they found increased phase clustering behaviour in the gamma band (> 40Hz) when seizures subsequently occurred. This phenomenon was best modelled with a gradual transition to seizure state, perhaps due to slow parametric shifts caused by inputs. This model would be suited to prediction, however, in discussions at the workshop Lopes da Silva indicated that perhaps the preictal state existence was due only to the microscopic scale.

There were also several other studies analysing brain electrodynamics on a microscopic scale probing into seizure genesis. Trevelyan investigated the existence of intrinsic cortical mechanisms which oppose epileptiform activity. He found that high frequency neuron firing (100-300Hz) may trigger inhibition to prevent recruitment of seizure activity [90, Ch 11]. This led to passionately argued debate amongst workshop participants on whether high frequency oscillations were indeed (1) a "last ditch" attempt to stop seizure spread, or whether they were (2) part of common epileptiform activity and (3) not routinely observed to increase or decrease prior to seizure onset. On a separate interesting topic, Carney *et al.* found, using Granger Causality, that synchronisation during seizures in rat brains was the result of highly directional interactions between cortical regions and deep brain structures including the hippocampus [90, Ch 4].

It is hoped that a greater understanding of seizure phenomenon will provide insights enabling seizure prediction.

Seizure Abatement

While the ability to have just a simple warning prior to seizure onset would be a dramatic improvement for epilepsy sufferers, ideally successful prediction would combine with a prevention technique. Proposals for intervention include electrical stimulation, cooling and UV light.

Electrical stimulation to terminate seizure activity is an area of current active research. Vagus Nerve Stimulation (VNS), the most widespread technique, employs regular pulsed stimulation to a nerve located in the neck in a continuous fashion independent of any prediction warning. After widespread study, the effectiveness of VNS remains unclear. Some patients report a 50% reduction of seizure frequency, however, similar rates were found as a placebo effect with trials where implanted VNS devices were never switched on to stimulate. What has been invaluable however, is the safety record exhibition over 20 years with over 50,000 Cyberonics®VNS devices implanted worldwide [90, Ch 22]. Central nervous system side effects, associated with anti-epileptic drugs, have not been found. Reported side effects are limited to mild or moderate hoarseness, coughing and shortness of breath [90, Ch 22]. Chronic deep brain stimulation, in structures such as the hippocampus, is an alternative stimulation option. Boon *et al.* report that initial hippocampal stimulation trials with 10 patients, showed percentage reductions in seizure frequency over 1 year of 100% (1 patient), 90% (1 patient), 50% (5 patients), 30%-40% (2 patients) with no benefit to the single remaining patient [93]. These chronic stimulation strategies may reduce numbers of seizures for isolated patients but ultimately full seizure control was not achieved. Electrical stimulation that holds the promise of control is *responsive* in nature. Trials with a Neuropace®responsive neuro-stimulation (RNS) device, which stimulates only after seizure warnings, are currently ongoing [90, Ch 23].

Rothman has proposed fascinating alternatives to electrical stimulation using either cooling or light therapy to quickly terminate seizure activity in cortical tissue [90, Ch 21]. Localised cooling of brain tissue has been shown to have anti-epileptic effects and UV light induces robust GABAergic currents (these are neurotransmitter currents that inhibit electrical activity). Modern thermoelectric devices such as Peltier coolers could be a candidate for a rapid response implantable seizure preventions system. Light could be administered through an implantable device with small UV LEDs. Light and cooling therapy have potential for advantage over electrical stimulation in terms of side-effect minimisation as cooling and light rely on mechanisms not intrinsic to normal brain activity and they may be more localised interventions.

Is Prediction Strictly Necessary?

The recent innovations in seizure abatement methods have rapid response times in comparison to the traditionally slow-acting anti-epileptic drugs. In the light of this, seizure prediction, that is warning of imminent seizure *prior* to its onset, may not be a necessary condition for effective treatment. Early onset seizure detection may suffice. The advantage of detection of epileptic seizures over prediction is that it has had much more success in the literature, and it is well known that medical doctors can detect seizures from the EEG record.

Early seizure detection algorithms from the 1980s-1990s have good detection success rates of 70-80% however false alarms are too frequent for therapeutic intervention [94, 95]. More recent detectors have had near perfect detection rates of 94% with a reasonable false positive rate of 0.7 FP/hr [96] and 100% detection rate with false positives under 0.175 FP/hr [97]. Until recently, detection was pursued primarily to retrospectively automate clinical diagnostics.

For prospective use of detection to be useful in an epilepsy intervention solution, there would be an additional requirement for *early onset* detection. That is, there would need to be at most a small latency time between seizure onset and subsequent detection. Ideally, we would require intervention prior to the clinical manifestation of a seizure in patients so a maximum detection latency less than 0.5s would be desirable. Published detection algorithms, where latency figures are specified, have rather more lengthy average detection delays following seizure onset of 5s [97] to 9.6s [98].

In conclusion, current detection algorithms are too slow to enable effective intervention. However, for the ultimate goal of an implantable closed loop seizure prevention device, either prediction or early detection (prior to clinical manifestation) are equally suitable.

In this thesis we explore models of coupled oscillators for the epileptic brain. Here, notions of *prediction* of forthcoming epileptic events, as modelled by synchronous network behaviour, are taken to be functionally synonymous with *early detection* of very localised synchrony prior to large scale synchrony spread.

Obstacles to Seizure Prediction/ Early Onset Detection

On current obstacles to advancement of seizure prediction, discussion among the participants at the 2007 seizure prediction workshop led to *"The first concern, stated bluntly, is that it is not necessarily possible to predict future states of a dynamical system on the basis of a limited amount of measurements"* [90, Ch. 26]. The limited measurement here speaks of intracranical EEG. There are concerns that intracranial EEG provides information only at a single-scale, while the generation of seizures (the phenomenon we wish to predict) is most likely a multi-scale phenomenom. The seizure prediction community is also concerned that even multiscale EEG recordings would still be based on one modality - could more information be gleaned from multiple modalities such as neurochemicals, ionic currents, PH and temperature.

This thesis seeks to examine the limits of our ability to predict seizures with these thoughts in mind.

2.7 Thesis Contributions

- Mathematical evidence, using the notion of observability, that current passive EEG acquisition is an inherently unsuitable measurement for epileptic seizure prediction in that it contains insufficient information to track seizure generation.
    - Evidence is provided from three separate angles:
        1. Deterministic linear systems theory (Linear observability), *Chapter 5.*
        2. Stochastic linear system theory (Kalman filtering), *Chapter 6*
        3. Non-linear system theory (Entropy of measure-preserving maps), *Chapter 6*
    - This provides theoretical explanation for 35 years of unsuccessful research in the field of epileptic seizure prediction.

- Demonstrated via simulation that active EEG acquisition, using brain stimulation techniques, offers a viable alternative for developing clinical seizure prediction technology in the near future, *Chapter 7.*

2.7.1 Selected Publication List

Invited Book Chapter

E. O'Sullivan-Greene, L. Kuhlmann, A. Varsavsky, D. B. Grayden, A. N. Burkitt and I. M. Y. Mareels. *Seizure Prediction and Observability of EEG Sources.* In Epilepsy: The Intersection of Neurosciences, Biology, Mathematics, Engineering and Physics, Ed. Osorio, I. and Zaveri, H. and Frei, M. G. and Arthurs, S. CRC Press, 2011.

Corresponding thesis Chapter: 5

Fully Refereed Conference Papers

E. O'Sullivan-Greene, I. Mareels, A. Burkitt and L. Kuhlmann. Observability issues in networked clocks with applications to epilepsy. *Proceedings of the* 48^{th} *IEEE Conference on Decision and Control (IEEE CDC)*, p 3527–3532, 2009.

Corresponding thesis Chapter: 5

E. O'Sullivan-Greene, I. Mareels, D. Freestone, L. Kuhlmann and A. Burkitt. A paradigm for epileptic seizure prediction using a coupled oscillator model of the brain. *Proceedings of the* 31^{st} *IEEE Engineering in Medicine and Biology Conference (IEEE EMBC)*, p 6428–6431, 2009.

Corresponding thesis Chapter: 7

Chapter 3

Information in Intracranial EEG

Intracranial EEG, avoiding the dispersion effects of the skull, offers the best information about brain activity. This Chapter explores intracranical EEG from a time-frequency perspective, leading to a question of how much of the information we observe relates to the true underlying dynamics. This in turn leads to a question of *observability* which is further explored in Chapter 5.

3.1 Time & Frequency Information in Intracranial EEG

The EEG appears to exhibit oscillations in the range of 0-50Hz with a spectrum that varies over time. In an effort to determine the rate at which this spectral information changes over time and if it may have a use in extracting seizure prediction information from the brain system, various time & frequency analyses are considered. Techniques such as the spectrogram, the periodogram, the Wigner-Ville spectrum and the wavelet scalogram are trialled.

The biological origin of these EEG oscillations is of importance in determining what sort of information may be useful for seizure prediction. The electric field that is measured during the EEG recording, at the cortex level, is the *"fluctuating, volume conducted electrical field generated by synaptic currents in large numbers of synchronously active cortical pyramid neurons"* [20]. However, the origin of the spectral content in these fluctuating EEG fields, is the subject of much debate and speculation within the community of neurologists and bio-scientists [99].

One theory for the origin of these frequencies in this debate is a pacemaker theory. Pacemaker theories are those which centre on the idea that cortical or sub-cortical populations of neurons modulate the activity of populations of cortical neurons. In this case, it is thought that these oscillations or rhythms can be attributed to the feedback loops that exist between the cortex and the thalamus, *thalamocortical* feedback, and the feedback loops that exists between different parts of the cortex itself, *cortiocortical* feedback [20]. This attribution is due to the inverse linkage between the time delays that exist (due the different distances travelled by signals) along these feedback routes and the characteristic frequencies that appear in the EEG [1, Ch. 11]. Therefore, the association between certain frequencies in the EEG and certain cognitive states could be directly due to the specific feedback loops engaged in that cognitive task. A computational model, developed by Robinson et al. [65] shows that thalamo-cortical feedback could result in the appearance of the typical "alpha" frequency (8-12Hz) from populations of cortical neurons.

However, in contrast to the pacemaker theory, it has also been shown that the frequency ranges in the EEG correspond to the resonance frequencies that would be supported by a sphere of size similar to the average skull [1, Ch. 3].

3.2 Spectrogram of EEG

This section examines the spectral content of EEG from patient 2 of the Freiburg data set through the use of classic Fourier decomposition:

$$|X(f)| = \frac{1}{N}\left|\sum_{n=0}^{N-1} x(n)e^{-j2\pi fn}\right|, \tag{3.2.1}$$

where $X(f)$ is the Fourier transform of the signal x at frequency f. Only the magnitude information is considered here. Changes in the Fourier decomposition over time are visualised through use of the spectrogram. A spectrogram shows the magnitude of several Fourier decompositions at different times in the EEG recording with the magnitude or power of the frequencies shown by colour coding.

An example of EEG from this patient is shown in Figure 3.1. This EEG segment is for channel 5 of an intracranial grid placed over the temporal lobe and has been pre-processed using a common average montage (to remove common mode mains artefact). The segment is 47 seconds long and contains a 21 second seizure (between seconds 15 to 36). Prior to the seizure the patient was at rest. Details of the montage choice and the location of the electrodes in question are discussed in Appendix A.1.

Initially it was expected that the spectrogram of EEG would exhibit some continuity across frequency bands, however, it appears that the frequency content of the EEG is highly "discontinuous" in time. A spectrogram of the EEG segment in Figure 3.1, computed using non-overlapping windows of 1 second, is shown in Figure 3.3. The power in a particular frequency band is colour coded as shown in Figure 3.2, with red denoting high power and blue indicating low power. It is "discontinuous" in the sense that the frequency content is dramatically different from one second to the next. To obtain any continuity of frequency power across time, a window with a 90% overlap must be employed as shown in Figure 3.4. A window overlap of 90% for a one second window corresponds to a time update of 100ms for each Fourier decomposition, or equivalently a sliding window update of just 51 new sample points (this EEG has a sampling frequency of 512 Hz). Such a small number of new samples means that a 90% overlapping window is creating visual continuity in a very artificial sense. The necessity of such a large overlap to obtain a spectrogram signal that is reasonably continuous over time leads to the conclusion that the spectrogram of the EEG is particularly non-continuous over time, consistent with an active brain.

Continuity of frequency content over shorter time windows is also considered, to show that, for higher frequencies, the spectrogram is certainly discontinuous and that the visual discontinuity is not a by-product of under-sampling in the case of the one second windowing used earlier. For example a time window of 0.2 sec can allow examination of frequency content greater than 10Hz. The spectrogram for this 0.2 sec window size is shown in Figure 3.5, with a zoomed in image showing the first 10 seconds in Figure 3.6. Clearly the frequency content remains discontinuous over time even in the 10-40Hz band. The strong 45-50Hz frequency content is due to the strong mains pick up artefact present in this dataset. Although the presence of this artefact was reduced though a common average reference, some 50Hz artefact does remain. See Appendix A.1 for a comparison of various montages for this data segment.

The analysis in this section shows that the frequency content of the EEG, extracted

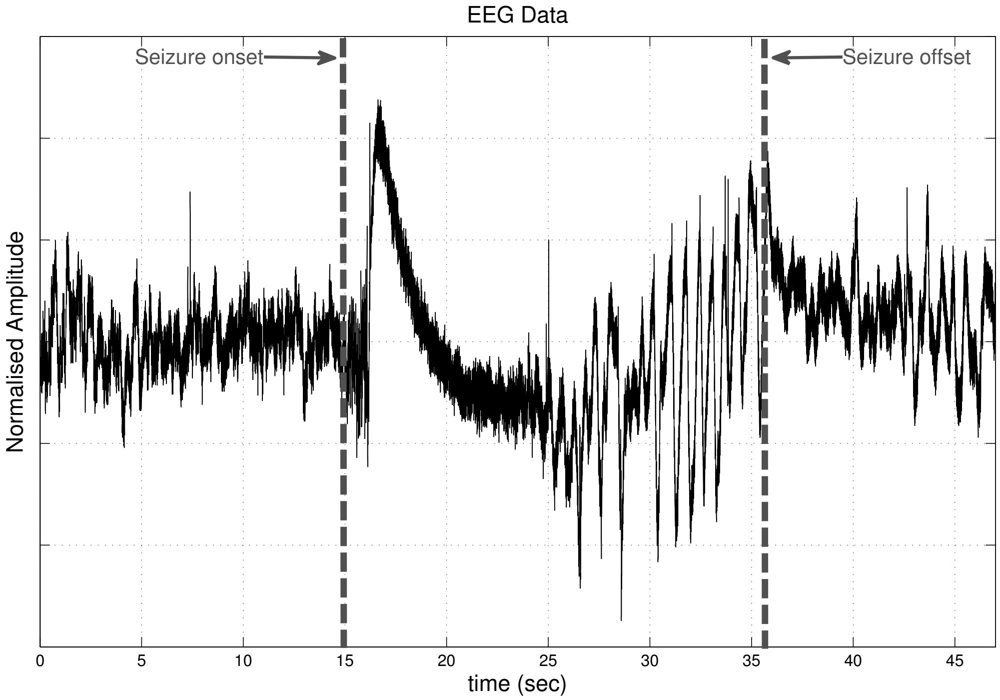

Figure 3.1: Example of EEG data

Figure 3.2: Colour coding used in all the time-frequency information plots of this chapter

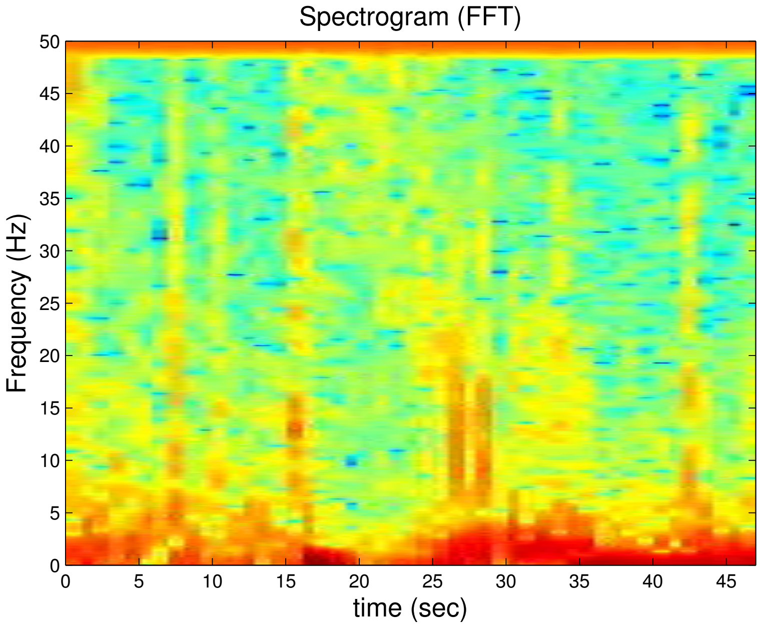

Figure 3.3: Spectrogram of the EEG segment in Figure 3.1, computed in non-overlapping windows of 1 second

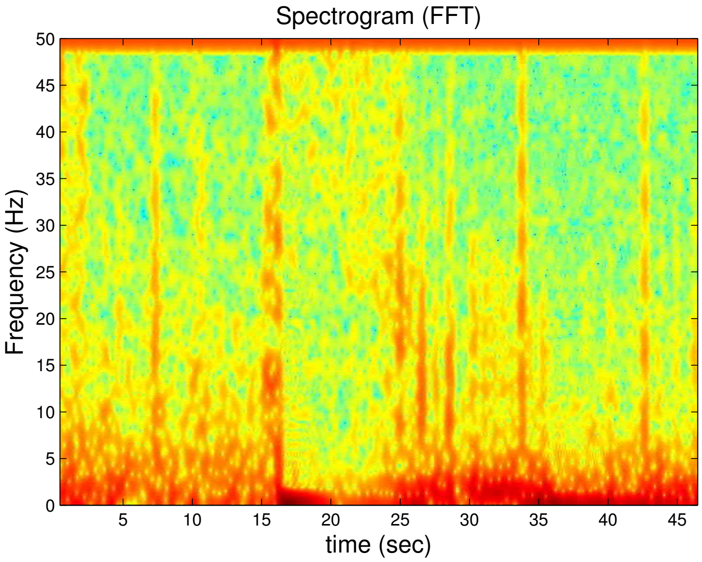

Figure 3.4: Spectrogram of the EEG segment in Figure 3.1, computed with 90% overlapping windows of 1 second

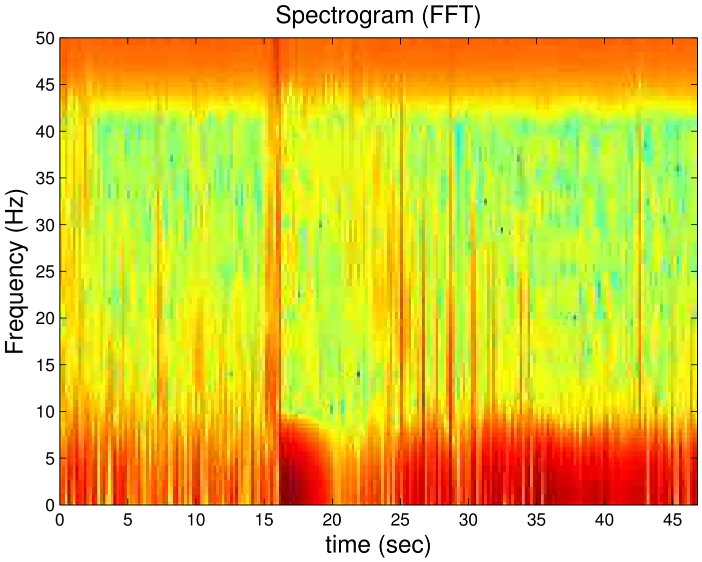

Figure 3.5: Spectrogram of the EEG segment in Figure 3.1, computed in non-overlapping windows of 0.2 seconds

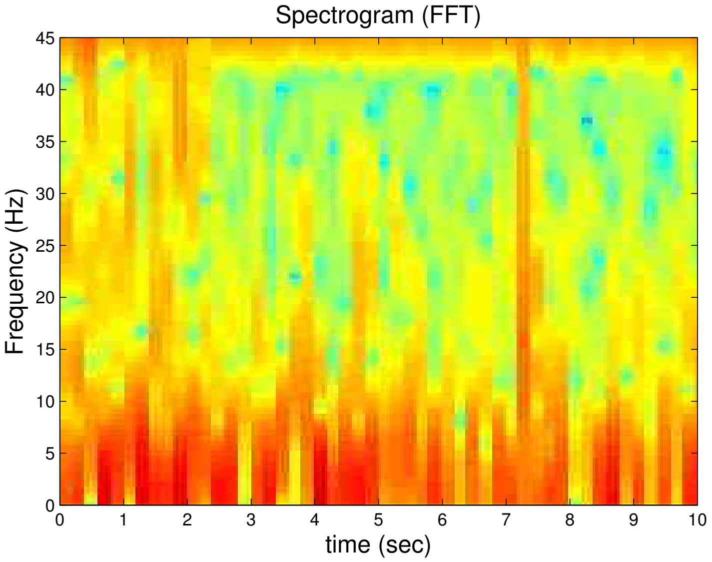

Figure 3.6: 1st 10 seconds of the Spectrogram in Figure 3.5, computed in non-overlapping windows of 0.2 seconds

with a spectrogram, is a rather nebulous concept with which to track information about the underlying system over time. The spectrogram plots in this section almost appear to be randomly generated at each time slice, therefore providing no useful clues about the evolution of the underlying system over time. In principal, no information is lost in the Fourier Transform (the inverse transform of Fourier magnitude & phase will give us an exact replica of the original signal). Note that the plots here concentrate on the amplitude information leaving the phase information out. Although the Fourier transform does give us all the available information, in effect the information is too muddled to be informative. The following section will look at some other commonly used time/frequency portraits of signals to see if a more suitable representation aligned with time-varying dynamics may be found.

3.3 Periodogram

The periodogram of a signal is computed as the Fourier transform of the estimate of autocorrelation of the signal. It is effectively a method used for estimating the power spectrum (spectrogram) of a random process. The Periodogram for a signal x at frequency f is

$$\widehat{P}_{per}(f) = \sum_{m=-(N-1)}^{N-1} \widehat{r}_{xx} e^{-j2\pi fm}. \tag{3.3.1}$$

$\widehat{r}_{xx}$ is the autocorrelation of the signal x,

$$\widehat{r}_{xx}(k) = \frac{1}{N} \sum_{n=0}^{N-1-|k|} x^*(n)x(n+k), |k| = 0, 1, 2, ..., N-1. \tag{3.3.2}$$

An alternative and equivalent form of the magnitude component of the periodogram equation is:

$$\widehat{P}_{per}(f) = \frac{1}{N} \left| \sum_{n=0}^{N-1} x(n)e^{-j2\pi fn} \right|^2 = \frac{1}{N}|X(f)|^2, \tag{3.3.3}$$

where $X(f)$ is the Fourier transform of the signal x. As an alternative estimate of the spectrogram it would be expected that the periodogram would exhibit similar non-continuous frequency content over time.

Figures 3.7 to 3.10 show the periodogram results for the EEG segment in Figure

3.1. They shown similar discontinuity of frequency content across seizures to that of the spectrogram in Section 3.2 as expected. Note that the visual continuity in Figure 3.8 is artificially created by using a large overlap between consecutive windows as discussed in Section 3.2.

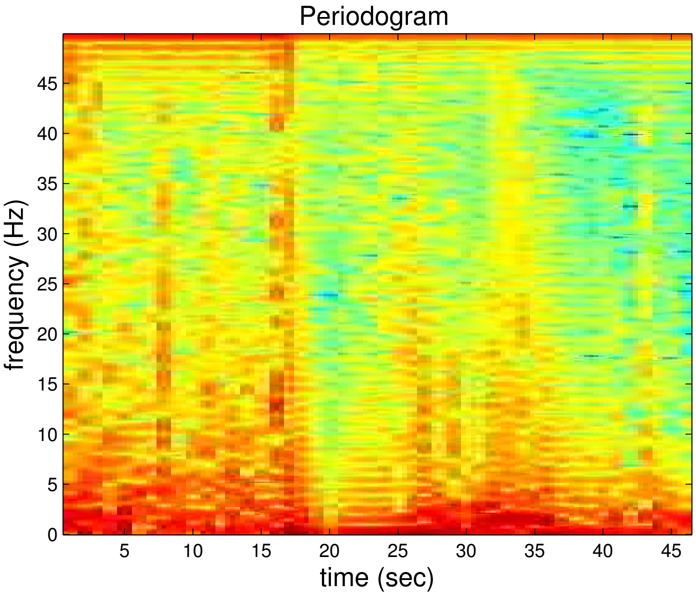

Figure 3.7: Periodogram of the EEG segment in Figure 3.1, computed in non-overlapping windows of 1 second

3.4 Wigner-Ville Distribution

The Wigner-Ville Distribution (or "Wigner-Ville Spectrum") is a time frequency portrait tool that allows a time dependent frequency estimate. This spectrum is computed according to:

$$W_x(t,f) = \int_{-\infty}^{\infty} x(t+\frac{\tau}{2})x^*(t-\frac{\tau}{2})e^{-j2\pi f\tau}d\tau, \tag{3.4.1}$$

for a signal x at time t and frequency f. The advantage of this distribution is that it offers a combined temporal and frequency representation (without windowing), however, this is at the expense of the introduction of "half-frequency" artefacts.

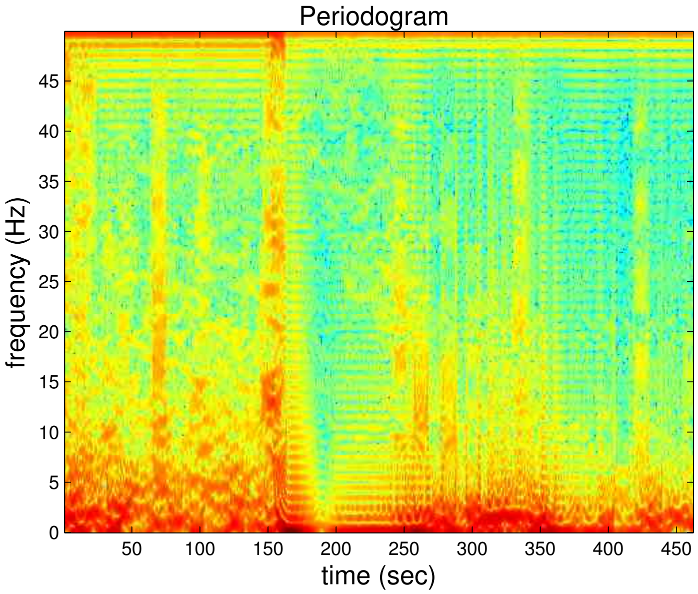

Figure 3.8: Periodogram of the EEG segment in Figure 3.1, computed with 90% overlapping windows of 1 second

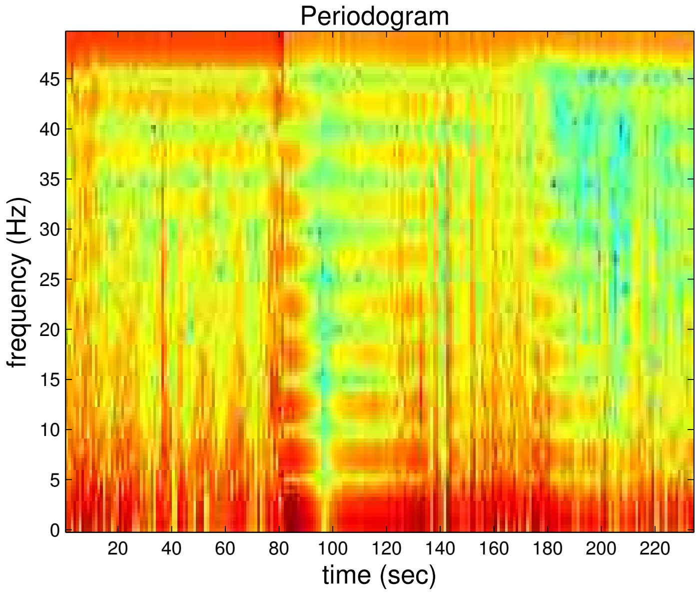

Figure 3.9: Periodogram of the EEG segment in Figure 3.1, computed in non-overlapping windows of 0.2 seconds

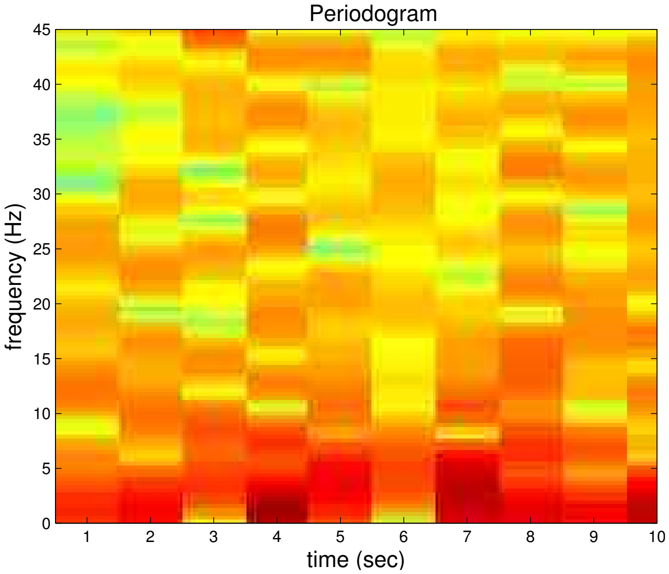

Figure 3.10: 1st 10 seconds of the Periodogram in Figure 3.9, computed in non-overlapping windows of 0.2 seconds

A Wigner-Ville distribution for the EEG segment in Figure 3.1 is shown in Figure 3.11. The problem of the half frequency artefact is clear at 25 Hz. While the strong power in the 50Hz band is a true signal - the 50Hz mains artefact picked up during recording - the power at half that frequency (25Hz) is an artefact of the Wigner-Ville spectrum itself. To clearly illustrate this half frequency problem, a spectrogram and a Wigner-Ville spectrum are shown for a chirp signal in Figure 3.12. The advantage of the Wigner-Ville distribution is also evident in this chirp example with much improved "time" resolution of frequency (narrow high-power line) over the spectrogram.

This problem of half frequency artefacts makes it difficult to determine true EEG frequencies from the Wigner-Ville Distribution. Furthermore, the Wigner-Ville distribution of EEG is similar to the other time frequency methods investigated in that it fails to show frequency changes smoothly over time. Therefore the conclusion is that the Wigner-Ville method is also not well suited to tracking frequency information over time in the EEG.

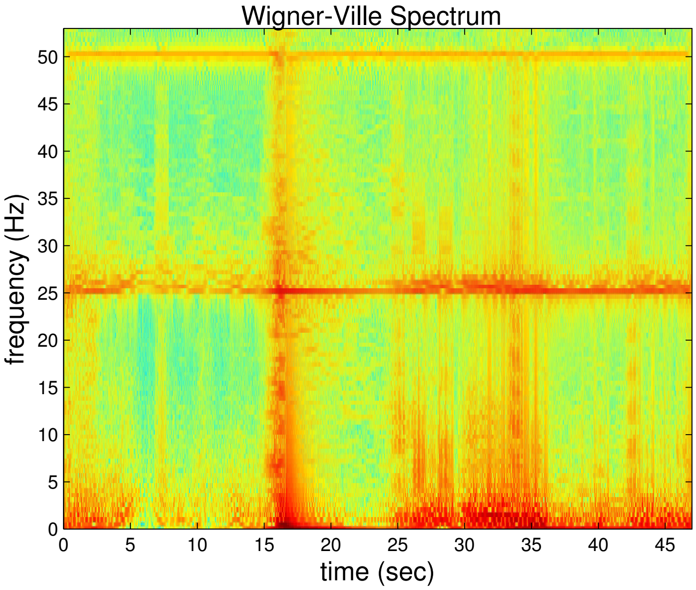

Figure 3.11: Wigner-Ville spectrum of the EEG segment in Figure 3.1

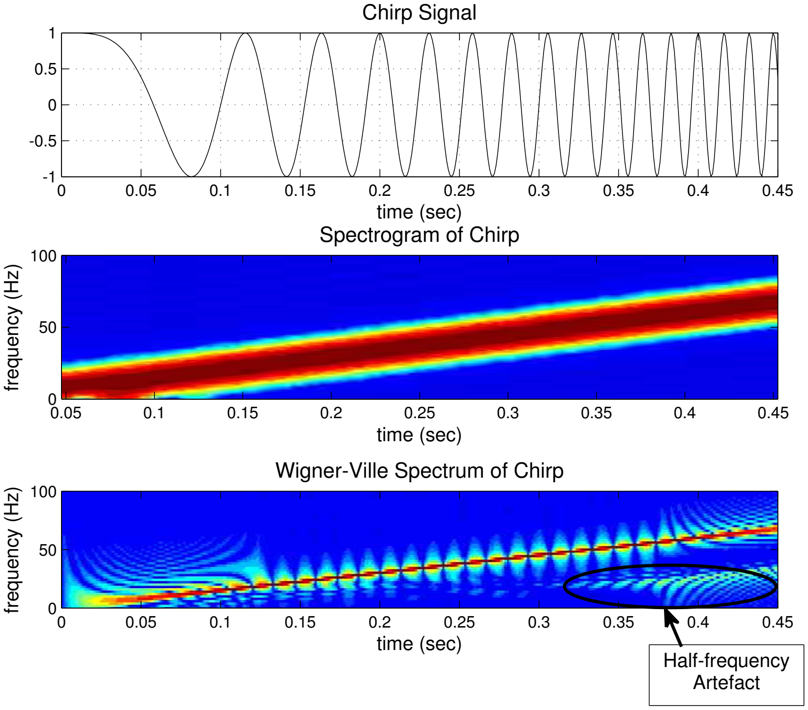

Figure 3.12: Spectrogram and Wigner-Ville Spectrum of a Chirp signal

3.5 Wavelet Transform

Wavelet transforms are similar to Wigner-Ville decompositions in that they combine frequency and temporal aspects in the one transform. Wavelets allow decomposition of a function into different frequency components (or *scales*), with a different temporal resolution for each scale that is suited to that frequency. For the analysis in this section a continuous wavelet transform was chosen:

$$T(s,\tau) = \frac{1}{\sqrt{s}} \int_{-\inf}^{\inf} x(t)\psi^*(\frac{t-\tau}{s})dt, \tag{3.5.1}$$

where τ is the time *translation* and s is the time *scale*. The translation maps the time position in the timeseries $x(t)$ that is under analysis, and the scale can be mapped to a particular frequency for a given wavelet ψ. In this analysis the wavelet type chosen was the morlet wavelet:

$$\phi(t) = e^{-t^2}\cos(5t). \tag{3.5.2}$$

The resulting wavelet spectrogram for the EEG segment in Figure 3.1 is shown in Figure 3.13.

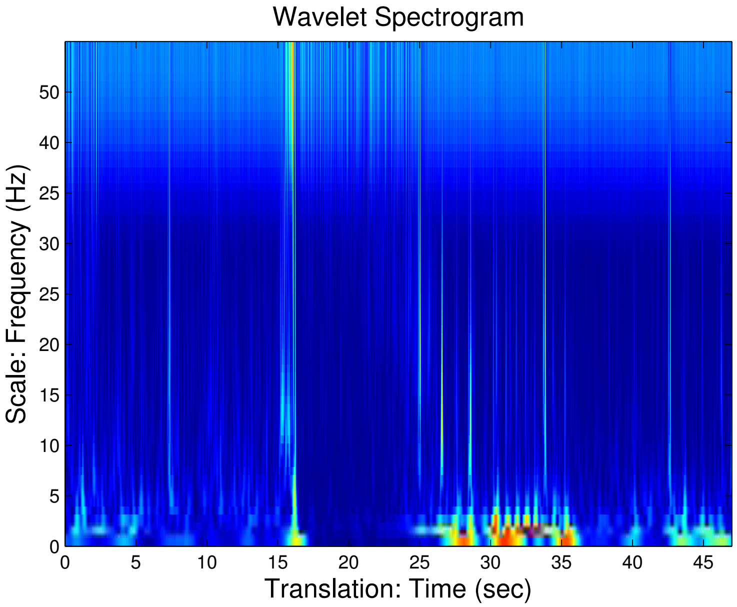

Figure 3.13: Wavelet spectrogram of the EEG segment in Figure 3.1

What is clear from the high temporal resolution of the wavelet spectrum, in contrast to the earlier spectra, is that high-power frequency content is sparsely represented over time. In Figure 3.1, there are just four main frequency events, (*i*) low frequency content (< 5Hz) at time 0 to 5 seconds, (*ii*) activity in the broad frequency band 35-50Hz at time 16 seconds at the seizure onset, (*iii*) further low frequency content (< 5Hz) at time 25 to 35 seconds during the seizure activity and (*iv*) further low frequency content (< 5Hz) at time 43 to 47 seconds. Similar to the Wigner-Ville spectrum, for the Morlet continuous wavelet there is again no apparent smooth transition in the power level of a given frequency or frequency band across time. Furthermore, the high temporal resolution but poorer frequency resolution in the higher frequency ranges lead to very broad band filters that fail to clearly show frequency-specific strong high frequencies in the EEG.

Other wavelets, including the continuous Mexican hat, the digital Haar wavelet and Daubachies 8 wavelet, were trialled with similar outcomes to the Morlet wavelet. In addition, various windowing segment lengths were experimented. The results in all cases generated similar plots to that of the Morlet wavelet, therefore only the Morlet results are shown in the figures here.

3.6 Conclusion

To investigate what features of EEG data may be useful in a seizure prediction algorithm various time & frequency analyses tools have been considered. These analyses: Spectrograms, Periodograms, Wigner-Ville transforms and wavelet transforms, all use linear transforms to pick out frequency and/or time-varying components of the EEG signal over time. Although only results of one 47 second data segment are illustrated in this chapter, the results presented here were found to be repeated for other EEG segments and across patients. The main result of this investigation is that there is no clear continuity in time that is visually evident using these measures, on any timescale. This is most likely due to the fact that these linear measures cannot extract or track underlying brain activity from the EEG signal. This implies that the manner in which the EEG signal changes is not regular enough (periodic enough) to be tracked by such linear measures. This is not surprising when one considers how highly complex the brain system is - an EEG recording of this brain system is a representation of the spatially & temporally averaged fluctuations of the electrical activity of a large tissue area in the order 100μm [1, Ch. 4]. Given this tissue area contains millions of neurons it is undoubtedly complex. It is therefore to be expected that the EEG signal is itself rapidly changing over time, most likely in a non-periodic manner, too irregular for traditional spectral methods.

The analysis in this chapter was undertaken to find a more suitable time-frequency representation to track the state of the underlying brain system over time. The lack of continuity in the results, as extracted using classic time-frequency analysis tools, leads to a conclusion that the "frequency" information as evident in the EEG means little and reveals little about underlining feedback loops in the brain. Certainly, even if these feedback loops existed in the brain system, these classical tools fail to adequately track the time-evolution of the loop activities.

These observations lead to the fundamental question: What can be inferred from the EEG signal about the underlying brain dynamics? Is it possible that some of the observed results can be explained because the EEG signal is simply too poor to represent the intricate transitions in the underlying brain activity? This raises the fundamental question of observability. It is quite possible that there is no visible continuity in EEG frequency information because the EEG allows us to only observe a small fraction of the underlying dynamics.

Chapter 4

A Coupled Oscillator Model for Synchronisation in EEG

It follows from Chapter 2 that decades of research have failed to reliably predict epileptic seizures. In light of this failure the work of this thesis is to investigate what we can expect to achieve toward seizure prediction through analysis of EEG signals. Chapter 3 indicates fundamental complexities that are not easily unravelled by classical signal processing tools. Model based signal analysis may be a better approach. In this chapter we explore suitable model paradigms to address such an investigation.

4.1 Review of Existing Models

There is a plethora of existing models for the epileptic brain that offer fascinating insights into how the brain *may* transition to a seizure state. We are most interested here in the *mesoscopic* level of model which bridges the *microscopic* neuron level dynamics and *macroscopic* brain dynamics which generate large scale EEG measures. These mesoscopic models are *phenomenological models* that describe the local field potentials in subsections of brain matter.

4.1.1 Microscopic Models

Microscopic models characterise small-scale brain activity, typically modelling neuron firing at the level of ion channels. Hodgkin and Huxley's 1952 equations model the membrane potential, $V(t)$, as a capacitive circuit with currents I_i based on various ion concentrations [100].

$$C\frac{dV(t)}{dt} = -\sum_i I_i. \tag{4.1.1}$$

Neurons generate an action potential based on the membrane potential, $V(t)$ (refer to Figure 1.4 in Chapter 1).

This model provided detailed dynamics of individual neurons and small networks of neurons, allowing the investigation of ionic concentration imbalances that lead to localised epileptiform firing behaviour. Additionally, spatial dynamics can be incorporated using multi-compartmental models to account for the branching structure of individual neurons (NEURON software has been developed for this). Attempts to extrapolate Hodgkin and Huxley dynamics & compartmental models to large scale networks quickly become computationally intractable.

The integrate and fire (IF) formalism was developed to enable tractable modelling of neural networks on a neuron population level rather than individual level. The IF model considers spatially homogeneous populations of neurons. Rather than considering the membrane potential $V(t)$ of each neuron, instead for computational tractability we consider the probability density of the membrane potential $P\left(V\left(t\right)\right)$ and consider population level parameters such as the mean spiking rate of action potentials in the network. IF models exhibit behaviour that is consistent with in-vivo recordings of neural spiking activity.

For epilepsy, however, it is as yet unclear how the localised activity, modelled by IF networks, is related to large scale epileptic seizures [28]. An attempt to bridge between the microscopic neuron level and macroscopic EEG activity is made with mesoscopic mean field models.

4.1.2 Mesoscopic Models

Mesoscopic models characterising medium-scale brain activity, typically modelling substructures in the brain, for example a cortical column and the local field potentials that they generate. By contrast, macroscopic models, characterising large-scale brain activity typically model the intracranial EEG signals and generally involve interconnecting mesoscopic models of various brain substructures.

Mesoscopic scale modelling attempts to bridge neuron level activity with large-scale EEG using the *mean field* formalism adopted from statistical physics. The pioneering Wilson-Cowan equations [101] consider two populations of neurons: excitatory and inhibitory. This model reduces the number of equations to describe many thousands of neurons to just two: one for the excitatory population and one for the inhibitory population. The spatio-temporal mean field is used to describe the mass activity of inhibitory and excitatory sub-populations at any given time. Under the assumption that local field potential recordings are proportional to the dendritic fields of the excitatory neurons in the cortex, the model can be used to infer the brain state that *may* generate *in-vivo* recordings. The use of the word *may* is important here as data-fitting to these models is an inverse problem with many potential solutions. With any oscillatory model of N^{th} order, any recorded signal with $N/2$ frequencies can be accurately generated.

The Wilson and Cowan model has spawned many extensions. Jansen & Rit considered the effects of coupled cortical columns, where each individual column was Wilson-Cowan based, to find that alpha and beta EEG-like activity resulted [102]. Wendling *et. al.* used a Wilson-Cowan type model to investigate mesial temporal lobe epilepsy (MTLE) in the hippocampus [103, 104, 105]. A three population model was employed. Two populations of inhibitory neurons were interconnected with (the soma and dendrites respectively of) a single excitatory population. The disruption to the regular balanced ratio of excitatory to inhibitory inputs to the model resulting in localised epileptiform activity similar to that of experimental data.

Suffczynski *et. al.* developed a similar model [106], fitting Wilson-Cowan style model parameters to absence seizure data. This work also built on the earlier work by the same group where Lopes Da Silva *et. al.* used a mean field approach to neuron modelling to replicate the common "alpha" rhythm in local field potentials [107]. The interesting extension of Suffczynski to these earlier works was the incorporation of the corticothalamic relay network with four sub-populations of neurons: inhibitory and excitatory populations in both the cortex and the thalamus. The Robinson model [108, 109, 65] similarly considered the dynamics between thalamus and cortical brain regions for epilepsy. This model can replicate many of the common frequencies of EEG (alpha, delta, theta and beta), absence epilepsies and seizure activation by input stimuli.

The beauty of these mean field models is the reduction in computational complexity they offer. They can be compactly simulated in state space providing us with a neat mapping where various sections of the state-space correspond to distinct brain activities such as alpha activity and seizure activity. The transitions across various regions on route to a seizure are of particular interest. Unfortunately the simplicity of these models is two-fold, in that, it is difficult to infer the exact underlying dynamics that generate a seizure from such reduced models. In effect, mean field models are somewhat agnostic regarding the exact underlying dynamics at both the ionic level and the network structure level. While these models provide many interesting theories of how seizures *may* occur, certainly these models are not yet at the level of sophistication to allow us to fit EEG data and accurately access the true brain state. The future development in this area has great potential for understanding of epilepsy in the brain, but currently these models are not suitable for seizure prediction.

4.2 Proposing a Generic Coupled Oscillator Model

There is much speculation about the phenomenon of seizure generation and the mechanisms of brain dynamics. The overriding conclusion, given the current state of this research, is that while we have many interesting theories, the dynamics of epilepsy are at this stage, unresolved. We do however *observe* in the time domain, across multiple channels, some degree of synchronisation associated with seizures.

Indeed, much of the seizure detection and prediction work to date (discussed in Chapter 2) has involved applying linear and non-linear techniques to both scalp and intracranial EEG data in attempts to track synchrony across brain regions. Linear methods have included cross-correlation [13] and phase analysis based on the Hilbert transform [58, 59]. Several non-linear techniques have utilised the Takens/Aeyels Embedding Theorem [110] in an effort to reconstruct the state space, with “low” embedding dimensions of 7-16. Measures, including correlation dimension [43] and Lyapunov exponents [77], were applied to these reconstructed state-spaces to investigate if there were a predictable transition to a lower-dimensional (more synchronised) brain state. All the approaches to seizure prediction have failed to reliably predict seizures better than a random predictor [89]. Although seizure detection algorithms have been successfully implemented [96], the very early detection required to allow sufficient warning time prior to clinical effects of seizures is yet to be achieved. In light of this failure to find either a prediction or early-onset detection method for EEG, we investigate the extent to which it is possible to observe brain synchrony from the EEG.

We present a “synthetic” brain-like situation, fully under our control, within which we can investigate the limits of a brain like EEG recording. While the exact nature of how this synchronisation may arise or evolve is unknown, we do know how the EEG *measurement* observations are made. Therefore, here we propose a top-down approach to EEG modelling using a coupled oscillator model - this approach is centred on modelling the EEG *measurement* rather than the specific underlying dynamics. It is important to highlight that this it not a model which can tell us anything about the nature of epilepsy. Certainly, the modelling efforts in brain dynamics discussed in Section 4.1 need to continue in order to evolve our understanding of normal brain function, seizure generation and abatement. This top down modelling approach is suited, however, to the specific task of investigating what we may expect from the EEG measurement.

The phenomenon of synchronization in coupled oscillators has cultivated much research interest. Mathematical modelling of such systems, in particular the Kuromoto model [111], has provided fascinating insights into the ability of individual coupled oscillators to merge into collective behaviour without the need for a pacemaker. Synchronization of coupled oscillators has been used to explain diverse natural phenomena from the interaction between brain oscillations and heartbeat [112] to the rhythmic activity of an ant colony between populations inside and outside the nest [113].

Our biological object of interest is the brain. Mathematical modelling of small-scale neuron to neuron interaction has shown coupled oscillator behaviour [114, Ch 5,6]. However, here our focus is on brain dynamics of a larger scale as measured by the oscillating electric fields of the brain, the EEG. Our model abstracts the seizure prediction problem to the study of a simple network of second order oscillators with linear interconnection. Such a model neglects the complexities of biologically realistic neuron-dynamics and instead formulates the observability problem as a generic network of oscillators where an EEG-like measurement is made.

To represent seizure dynamics in terms of synchronisation events, each oscillator in the network represents a region of brain tissue that is oscillating at a certain frequency. As the EEG is the weighted sum of oscillating potentials in the brain, the output in this model is the weighted sum of many pendulum oscillations. This is quite a generic and scalable model. On a microscopic scale, each pendulum represents only a small group of neurons and the output would model depth electric potential recording from a micro-electrode (in the order of 1μm). This model could equally apply right up to the global mesoscopic and macroscopic scales, where each pendulum represents a large area of brain tissue. In these cases, the output measure could model both scalp and intracranial EEG recorded from a macro-electrode (in the order of 1mm [27, Ch38] and 0.8cm [27, Ch7] respectively).

Also available in the model is an input probe stimulus. The inclusion of an input probe stimulus follows recent developments in epileptic seizure prediction that have focused on an active response model rather than the traditional passive manner of EEG measurement [115]. The active response paradigm involves measuring the EEG following an active stimulus (e.g. electric pulse) to a brain region.

A very similar coupled-oscillator model was described by Wright et al. in 1985 to model state changes in the brain [116]. Their motivation for a generic model was that the existing brain models of the time were constrained by *"simplified neuronal relationships and laws of interaction"*, whose *"ideas are difficult to put to critical test, and each [model] necessarily ignores certain problems treated in the others"*. Mathematical models have developed considerably since this work, however, Wright's comments still stand, in that, these models are not yet at a level of sophistication suitable for parameter fitting to EEG for the specific purpose of seizure prediction and it may follow from the analysis as presented here in this thesis, that such models may *never* be rightfully linked to EEG alone.

4.3 A Coupled Oscillator Model

EEG recordings from brain tissue are modelled as the output measurement from a system of networked clocks. Each individual oscillator is modelled as a pendulum clock with the oscillatory motion of the pendulum described as

$$\ddot{x}_i + 2\zeta_i\omega_i\dot{x}_i + \omega_i^2\sin(x_i) = F_i,\ i = 1\ldots N, \tag{4.3.1}$$

where x_i is the angular position of the i^{th} pendulum, ζ is the damping parameter, ω is the natural frequency of oscillation and F is the forcing term. F could take the form $\sin(\omega_{in,i}t)$ for each of any external inputs with input frequency $\omega_{in,i}$ and $\sum_j \alpha_{ij}(x_j - x_i)$ for coupling of the position state from other pendulums. α_{ij} denotes the coupling strength between oscillators i and j.

The behaviour of coupled pendulum oscillators is quite fascinating. The first pendulum clock was constructed by Christiaan Huygens in 1657. While experimenting to find a clock suited to use in a maritime environment Huygens discovered *"..an odd kind of sympathy perceived by him in these watches* [two pendulum clocks] *suspended by the side of each other"* [117]. When two pendulums were suspended from the same table, the pendulums became synchronised in antiphase. When the pendulums were disturbed, the antiphase state was restored within a half-hour and persisted indefinitely. Huygens deduced that the crucial interaction for this effect came from *"imperceptible movements"* of the common frame supporting the two clocks. This was the 1^{st} recorded synchronising coupled oscillator system. The equations governing the dynamics of pendulum motion came about after Huygens time and these imperceptible movements are modelled in the coupling terms of Equation 4.3.1. Synchronisation for quite small "imperceptible" coupling magnitudes occurs provided the initial frequencies are sufficiently close.

The pendulum equation in Equation 4.3.1 can be linearised to:

$$\ddot{x}_i + 2\zeta_i\omega_i\dot{x}_i + {\omega_i}^2 x_i = F_i,\ i = 1\ldots N, \tag{4.3.2}$$

This linear system is a good approximation for small angles of oscillation. While the linear system no longer has the capability to spontaneously synchronise, it still exhibits clock behaviour, but more importantly allows investigation of the system with a range of powerful linear systems tools.

To convert the characteristic equation (Equation 7.1.1) into a state space format, the states for clock system 1 can be labelled as x_{11} and x_{12} which are defined as follows: $x_{11} = x_1$ and $x_{12} = \dot{x}_1$. The time derivatives of the states are then $\dot{x}_{11} = x_{12}$ and $\dot{x}_{12} = \ddot{x}_1 = -2\zeta_1\omega_1 x_{12} - (\omega_1^2 + \alpha_{12})x_{11} + \alpha_{12}x_{21} + \sin(\omega_{in,1}t)$, where x_{21} is the 1^{st} state of system 2 and the forcing is comprised of one input at frequency $\omega_{in,1}$ and the difference between the angles of oscillation of both clocks: $F_i = \sin(\omega_{in,1}t) + \alpha_{12}(x_{11} - x_{21})$.

The resulting state space model for an interacting system of two pendulums is $\dot{\mathbf{x}} = \mathbf{A}\mathbf{x} + \mathbf{B}u$, where u is the input signal and the $\mathbf{A}$ and $\mathbf{B}$ matrices are as follows:

$$\mathbf{A} = \begin{bmatrix} 0 & 1 & 0 & 0 \\ -\omega_1^2 - \alpha_{12} & -2\zeta_1\omega_1 & +\alpha_{12} & 0 \\ 0 & 0 & 0 & 1 \\ +\alpha_{21} & 0 & -\omega_2^2 - \alpha_{21} & -2\zeta_2\omega_2 \end{bmatrix} \tag{4.3.3}$$

$$\mathbf{B} = \begin{bmatrix} 1 & 0 & 1 & 0 \end{bmatrix}', \tag{4.3.4}$$

$$u = \sin(\omega_{in,1}t), \tag{4.3.5}$$

where prime($'$) denotes transpose.

This can be extended to a $2N$ state system, where there are N interconnected pendulum clock subsystems as shown by the following $\mathbf{A}$ with a corresponding illustration in Fig. 4.1:

$$\mathbf{A} = \begin{bmatrix} 0 & 1 & 0 & 0 & \cdots & 0 & 0 \\ -\omega_1 - \widetilde{\alpha}_{1k} & -2\zeta\omega_1 & \alpha_{12} & 0 & \cdots & \alpha_{1N} & 0 \\ 0 & 0 & 0 & 1 & \cdots & 0 & 0 \\ \alpha_{21} & 0 & -\omega_2 - \widetilde{\alpha}_{2k} & -2\zeta\omega_2 & \cdots & \alpha_{2N} & 0 \\ 0 & 0 & 0 & 0 & \cdots & 0 & 0 \\ \alpha_{31} & 0 & \alpha_{32} & 0 & \cdots & -\alpha_{3N} & 0 \\ 0 & 0 & 0 & 0 & \cdots & 0 & 0 \\ \alpha_{41} & 0 & \alpha_{42} & 0 & \cdots & -\alpha_{4N} & 0 \\ \vdots & \vdots & \vdots & \vdots & \ddots & \vdots & \vdots \\ 0 & 0 & 0 & 0 & \cdots & 0 & 1 \\ \alpha_{N1} & 0 & \alpha_{N2} & 0 & \cdots & -\omega_N - \widetilde{\alpha}_{Nk} & -2\zeta\omega_N \end{bmatrix} \tag{4.3.6}$$

where $\widetilde{\alpha}_{ik}$ denotes $\sum_{k=1}^{N} \alpha_{ik}$. Each subsystem is allowed to connect to all the others and $\alpha_{ij} \equiv \alpha_{ji}$ (symmetric coupling). Random interconnections can be constructed by choosing $\alpha_{ij} \geq 0$ from a distribution of values.

The output state for a single recorded EEG channel can be described by $\mathbf{y} = \mathbf{C}\mathbf{x}$, where

$$\mathbf{C} = \begin{bmatrix} 0 & -1 & 0 & -1 \ldots & 0 & -1 \end{bmatrix}. \tag{4.3.7}$$

This generic output vector $\mathbf{C}_i = [0, -1]$ is chosen together with $\mathbf{B}_i = [0, 1]'$ such that the transfer function, $G(s) = \mathbf{C}_i(s\mathbf{I} - \mathbf{A}_i)^{-1}\mathbf{B}_i$, is normalised to 1 at DC for each of the individual uncoupled sub-systems. Equation 4.3.7 is a measurement vector that sums the velocity states of each sub-system equally, however the output can also be a weighted combination. For example, the output may be a convex combination of the angular acceleration states in the system,

$$\mathbf{C} = \begin{bmatrix} 0 & -\delta_1 & 0 & -\delta_2 \ldots & 0 & -\delta_N \end{bmatrix}. \tag{4.3.8}$$

where $(\delta_i \geq 0, \sum_i \delta_i = 1)$. $\delta_i \geq 0$ indicates the relative contribution clock i makes in the “EEG” output signal.

4.4 Conclusion

The model introduced in this Chapter is a very simple *behavioural* description of EEG-like signals. The underlying physiological mechanism governing the oscillations is not considered at all. Nevertheless simulations shown in Figure 4.2 reveal behaviour that could

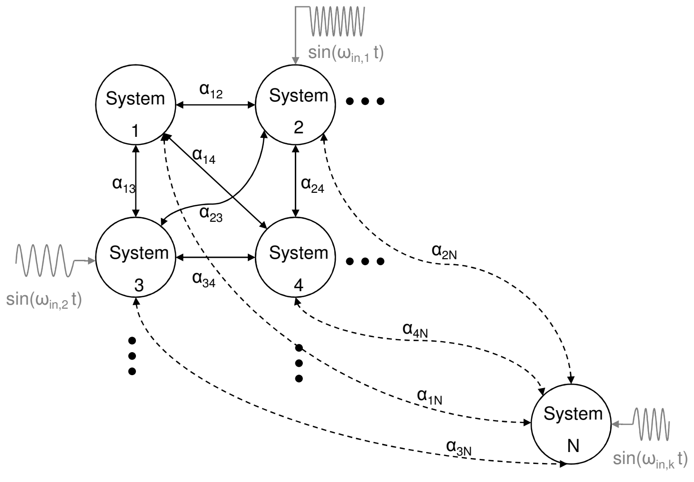

Figure 4.1: The interconnection of N pendulum clock subsystems. α_{ij} is the coupling strength between sub-system i and j. The grey signals are inputs to the system.

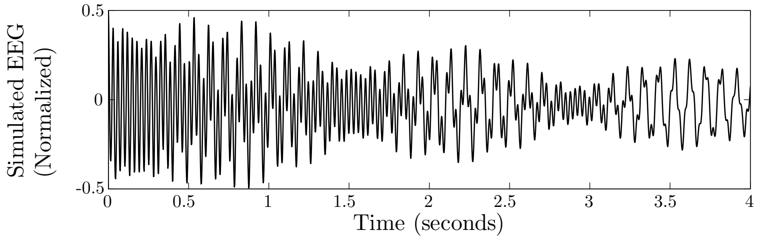

(a) Simulation with $N = 4$ clocks

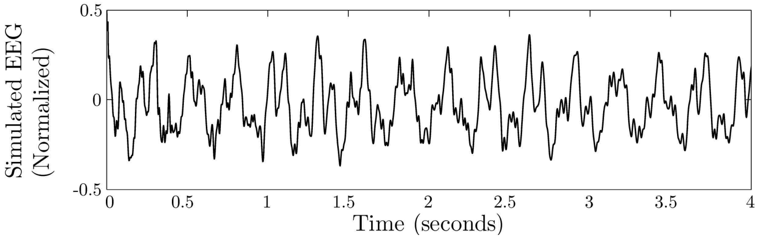

(b) Simulation with $N = 25$ clocks

Figure 4.2: EEG simulations using the coupled oscillator model show waveforms that are consistent with typical EEG sequences, even with relatively few clocks in the network.

easily be part of a real EEG sequence. This is unsurprising given that, in principal, any signal $f(t)$ over any window $t \in [0, T]$ can be approximated as $f(t) = \sum_{i=1}^{N} a_i \sin(\omega_i t + \varphi_i)$. It follows that, for any EEG signal measured, there is a networked clock model that will exhibit as its output a signal consisting of summed sinusoids, $f(t)$, where that $f(t)$ approximates the specific EEG segment well. As indicated, this does not imply that the model is a realistic representation of actual brain dynamics, however, this model can replicate realistic behaviour. In the next chapter we investigate the level of information about the states x that can be recovered from the EEG signal.

Chapter 5

Observability Issues in Networked Clocks

This chapter investigates what we can expect to observe from electroencephalography (EEG) measurements of brain dynamics. Earlier research efforts, as discussed in Chapter 2, have unsuccessfully attempted to track synchrony from EEG, viewing the brain matter as a coupled oscillator with the seizure state resulting from global synchronization. Using the model of networked pendulum clocks, introduced in Chapter 4, we find that observing sufficient information to track the build up of synchrony is an ill-posed problem unless measurements are taken from a very localised region of brain tissue.

5.1 Introduction

The question of what we can expect to *observe* from EEG recordings leads us to the classical systems theory notion of observability. For a linear system with state mapping matrix $\mathbf{A}$, an output measurement determined by $\mathbf{C}$ and an input determined by $\mathbf{B}$ the system $(\dot{\mathbf{x}} = \mathbf{A}\mathbf{x} + \mathbf{B}u, y = \mathbf{C}\mathbf{x})$ is observable, in the sense that we can recover the states $\mathbf{x}$ from the output y, under the following conditions on the pair $(\mathbf{C}, \mathbf{A})$.

The pair $(\mathbf{C}, \mathbf{A})$, $\mathbf{C} \in \mathbb{R}^{p\times N}$, $\mathbf{A} \in \mathbb{R}^{N\times N}$ is observable if and only if any of the following equivalent statements are true [118]:

- The Observability Matrix, $\mathcal{O}(\mathbf{C},\mathbf{A}) = \left[\mathbf{C}', (\mathbf{CA})', (\mathbf{CA}^2)', \ldots, (\mathbf{CA}^{N-1})'\right]'$, is full rank (prime $'$ denotes transpose)
- Popov-Belevitch-Hautus (PBH) test: $rank\left(\begin{bmatrix} \mathbf{A}-\lambda I \\ ---- \\ \mathbf{C} \end{bmatrix}\right) = N, \forall\lambda \in \mathbb{C}$
- The polynomial matrices $\lambda I - \mathbf{A}$ and $\mathbf{C}$ are right coprime.

These definitions of observability consider an idealised situation absent of noise. However, EEG signals do contain considerable noise, including quantisation noise due to the digital nature of EEG recording equipment. In this Chapter we reduced the question of what we can observe from an EEG record to the generalised question of how quantisation of an output, from a large-scale system, effects the observability. This effect of quantisation has implications beyond the epilepsy prediction problem for the observability of any practical system. Given the pervasive nature of this problem across all systems where digital measurements are made, it is not surprising that previous research has touched on the topic.

Koplan and Sontag [119] investigated problems of this nature where the *"outputs reflect various limitations of measuring devices"* resulting in $y = \sigma(\mathbf{Cx})$ rather than the ideal output of $y = \mathbf{Cx}$. They found in particular for the extreme quantisation case of $\sigma(\mathbf{x}) = sign(\mathbf{x})$, where the output was +1 or -1, that the theoretical observability is maintained provided (loosely speaking, see [119] for further details):

(i) The non-quantised system was observable: $(\mathbf{A},\mathbf{C})$ is an observably pair

(ii) For the set of matrices $\mathbf{CA}^{i-1}\mathbf{B}$ for $i = 1, 2 \ldots N$ there are a sufficient number of non-zero rows.

For a single output ($\mathbf{C}$ is a row vector) condition (ii) is satisfied for any $\mathbf{B}$ not equal to the zero vector. In the multidimensional output case, condition (ii) is satisfied provided there are sufficient rows of $\mathbf{C}$, denoted $\mathbf{C}_j$ such that for all i=1-N, $ker(\mathbf{C}_j\mathbf{A}^{i-1}) = 0$[1]. Satisfying these conditions means that the quantised system is observable in the sense that for any $\mathbf{B}$ vector we will always be able to find an input u(t) such that we can distinguish between two states at the output. While this indicates theoretical observability, finding the various u(t) signals that can provide this distinction is not particularly practical in general and furthermore is not available as an option in standard EEG. What are the

---

[1] $ker(\mathbf{A})$, the kernel of a matrix $\mathbf{A}$, that is collection of all $\mathbf{x}$ vectors such that $\mathbf{Ax} = 0$.

theoretical limits of observability for a practical EEG set-up?

Despite over 34 years of research, where many methods have been unsuccessfully applied to the EEG for seizure prediction [89], the issue of observability of the brain system from measurements of EEG has surprisingly not been explored. Instead, observability has been simply assumed to variable extents, with EEG data analysed for seizure precursors in the absence of any real consideration for whether the chosen analysis method was mathematically suitable given the brain system and EEG measurement [77, 43, 40, 44]. Here we attempt a first investigation of what we may expect the EEG to reveal about the underlying brain. The investigation makes use of a highly simplified situation, where we assume to know the underlying dynamics, but only observe a low dimensional signal extracted from a high dimensional state. The question we want to explore is how observable is a large scale system, in particular in the light of finite precision measurements?

We abstract the problem to the study of a simple network of linear oscillators with linear interconnection. Such a model neglects the complexities of biologically realistic neuron-dynamics and instead formulates the problem as one of a generic network of oscillators upon which an EEG-like measurement is made. While synchrony of coupled oscillators is undoubtedly a non-linear process here we limit a first analysis to the linear case and investigate observability using linear methods. If the extent of information that an EEG-like output can reveal is limited in the simple linear case, more complex and realistic non-linear models are unlikely to be more successful. In this context the problem essentially involves: *scale*, the number of individual oscillators in the system, *coupling strength* between oscillators and *measurement resolution*, the accuracy of the EEG measurement.

In the remainder of this Chapter we show that in the most ideal abstraction of the underlying problem, practical observability (assuming a finite precision measurement instrument) is not an obvious property even when the underlying system is observable in the normal sense (i.e. for ideal measurements). The scope of the problem explored in this chapter is defined in Section 5.2. Theoretical analysis is presented in Section 5.3 and supporting simulations can be found in Sections 5.4 and 5.5. Sections 7.4 and 5.7 follow with discussion and conclusions.

5.2 Problem Formulation

5.2.1 Hypothesis

Seizure prediction from EEG has been unsuccessful because the measurement is a poor observer of brain dynamics, in that, information from only a very limited number of the underlying oscillations in the brain are available at the measurement electrode.

5.2.2 Assumptions

With the dynamics of the real brain unknown, the hypothesis is tested by considering the observability of a known model. This model for EEG measurement from the brain is based on a networked clock model, which is the linearised form of the coupled oscillator model as described in detail in Chapter 4.

This problem formulation acts to investigate the limits of information that can be observed from the brain in the scenario of best possible conditions because the networked clock model is very much an over-simplification of the real-world problem. The model has been reduced to a fully-known, linear time invariant system. All dynamical uncertainty, measurement noise and non-stationarity are neglected. These assumptions of the model are listed in Table 5.2.1.

Model	**Real Case**
Dynamics known	Dynamics unknown
No Noise[2]	Noise
Stationary	Non-stationary
time-invariant	time-varying
System dimension[3] known	System dimension unknown
Pure Clocks[4], linear	Non-linear oscillations
Clock interconnections: Regular(homogeneous) & irregular(inhomogeneous)	Unknown

Table 5.2.1: Assumptions of Networked Clock Model

---

[2] The effect of quantisation measurement noise is later considered, but all other noise is neglected

[3] System dimension in number of states, each oscillation requires two states.

[4] Pure clocks have a constant frequency.

5.2.3 Aspects for Exploration

Observability is explored in this Chapter under each of the following aspects:

1. **Representation**
   (a) Continuous-time, damped clocks
   (b) Discrete-time, undamped clocks
2. **Coupling geometry**
   (a) Regular(homogeneous), coupling strength geometrically decaying with distance between clocks
   (b) irregular(inhomogeneous), probabilistic connection between clocks independent of spatial configuration
3. **Measurement resolution**

   Bit length of digital measurement (10 bits, 14 bits, 24 bits)
4. **Scale**

   The number of individual clocks in the networked system

The system structure is explored next in Section 5.3, showing that networked clocks are theoretically observable. An analysis of the impact of coupling geometry, bit length and scale follows in Section 5.5 showing that, under real-world considerations, observability is an illusion.

5.3 Networked Clocks are Observable in Theory

Here observability is considered based purely on the system and measurement matrices **A** and **C** as per the definition of observability in Section 5.1. This definition provided the following equivalent tests for showing observability from **A** and **C**: (*i*) Observability matrix rank test, $\mathcal{O}$, (*ii*) PBH test and (*iii*) Coprime matrix test. For the coupled pendulum clock system introduced in Chapter 4, the relevant **C** and **A** matrices for an N^{th} order system are:

$$\mathbf{C} = \begin{bmatrix} 0 & -\delta_1 & 0 & -\delta_2 \ldots & 0 & -\delta_N \end{bmatrix}. \tag{5.3.1}$$

where δ_i indicates the relative weight clock i makes in the EEG output signal ($\delta_i \geq 0$ and $\sum_i \delta_i = 1$).

$$A = \begin{bmatrix} \mathbf{A}_1 + \varepsilon_{11} & \varepsilon_{12} & \ldots & \varepsilon_{1N} \\ \varepsilon_{21} & \mathbf{A}_2 + \varepsilon_{22} & \ldots & \varepsilon_{2N} \\ \vdots & \vdots & \ddots & \vdots \\ \varepsilon_{N1} & \varepsilon_{N2} & \ldots & \mathbf{A}_N + \varepsilon_{NN} \end{bmatrix}, \tag{5.3.2}$$

where

$$\mathbf{A}_i = \begin{pmatrix} 0 & 1 \\ -\omega_i^2 & -2\zeta_i\omega_i \end{pmatrix}, \tag{5.3.3}$$

$$\varepsilon_{ij} = \begin{pmatrix} 0 & 0 \\ +\alpha_{ij} & 0 \end{pmatrix} \text{for i} \neq \text{j}, \tag{5.3.4}$$

$$\varepsilon_{ij} = \begin{pmatrix} 0 & 0 \\ -\sum_{k=1}^{N} \alpha_{ik} & 0 \end{pmatrix} \text{for i} = \text{j}. \tag{5.3.5}$$

For a pair $(\mathbf{C}, \mathbf{A})$ of this form, testing for an observability matrix with full rank is not practical for networks with more than a few clocks. Instead the PBH test and coprime matrices test provide a more tractable option. The PBH test [120, Ch 2] can be used to show that a system with an $\mathbf{A}$ matrix of form (5.3.7) is observable for our choice of output matrix, $\mathbf{C}$, in certain cases under the condition that the clocks oscillate at distinct frequencies. Firstly, the case of no coupling and, secondly, the case of an upper triangular structure of coupling. For the general cases of global coupling or indeed symmetric coupling ($\alpha_{ij} = \alpha_{ji}$) a polynomial approach to establishing theoretical observability provides a more elegant solution.

5.3.1 Observability with PBH test: case of no coupling

The case of no coupling between clocks can be created by setting $\alpha_{ij} = 0, \forall i, j$. The definition of the PBH test given in Section 5.1 required the matrix,

$$\begin{bmatrix} \mathbf{A} - \lambda\mathbf{I} \\ ---- \\ \mathbf{C} \end{bmatrix}, \tag{5.3.6}$$

to have rank N for for all possible λ in the set of complex numbers. This effectively collapses to only requiring rank N for all λ equal to the eigenvalues of $\mathbf{A}$ (henceforth denoted $\lambda(\mathbf{A})$) as the condition of rank N will clearly be met for all $\lambda \notin \lambda(\mathbf{A})$[2].

For the specific case of no coupling the PBH test matrix (5.3.6) has the following structure, with the 1^{st} N rows forming a block diagonal matrix:

$$\begin{bmatrix} \begin{pmatrix} \mathbf{A_1}+\varepsilon_{\mathbf{11}} & \varepsilon_{\mathbf{12}} & \cdots & \varepsilon_{\mathbf{1N}} \\ \varepsilon_{\mathbf{21}} & \mathbf{A_2}+\varepsilon_{\mathbf{22}} & \cdots & \varepsilon_{\mathbf{2N}} \\ \vdots & \vdots & \ddots & \vdots \\ \varepsilon_{\mathbf{N1}} & \varepsilon_{\mathbf{N2}} & \cdots & \mathbf{A_N}+\varepsilon_{\mathbf{NN}} \end{pmatrix} - \lambda \mathbf{I_{2N}} \\ 0 \quad -\delta_1 \quad 0 \quad -\delta_2 \quad \ldots \quad 0 \quad -\delta_N \end{bmatrix} \tag{5.3.7}$$

where all ε terms are set to zero. The eigenvalues of a block diagonal matrix are simply equal to the eigenvalue of the block diagonal elements:

$$\lambda\left(\begin{bmatrix} \mathbf{A}_1 & \mathbf{0} \\ \mathbf{0} & \mathbf{A}_2 \end{bmatrix}\right) = \{\lambda(\mathbf{A}_1), \lambda(\mathbf{A}_2)\} \tag{5.3.8}$$

It follows that the system eigenvalues can be found by solving the characteristic polynomials of each individual clock, $\lambda^2 + 2\zeta_i\omega_i + \omega_i^2 = 0$. The $2N$ eigenvalues, λ of the N uncoupled systems are

$$\lambda_{i\pm} = -\zeta_i\omega_i \pm \omega_i\sqrt{\zeta_i^2 - 1}, \text{ for } i = 1 \ldots N. \tag{5.3.9}$$

The block diagonal structure, through its stepped placement of non-zero matrix elements ensures that each row pair of 5.3.6 (row k and row $k+1$, for k odd) are guaranteed to be linearly independent of all others row pairs. Row rank can however be lost if the row pairs themselves are linearly dependent i.e. if,

$$\frac{-\lambda}{-\omega_k^2} = \frac{1}{-2\zeta_k\omega_k - \lambda}. \tag{5.3.10}$$

As highlighted at the start of this section, we only need test 5.3.10 for $\lambda \notin \lambda(\mathbf{A})$ which are given in 5.3.9. Solving 5.3.10 for such λ finds that the row pairs are linearly dependent only when $\omega_k = \omega_i$ and $\zeta_k = \zeta_i$ (refer to Appendix A.2). The requirement of having rank N in the $(N+1) \times (N)$ matrix 5.3.6 is satisfied for all λ, therefore the system is observable via the PBH test, provided the systems natural frequencies and damping

---

[2] Since $\lambda \notin \lambda(\mathbf{A})$ is such that $det(\lambda I - \mathbf{A}) \neq 0$ and thus the 1st N rows of (5.3.6) are linearly independent.

parameters do not overlap $\omega_i \neq \omega_j, \zeta_i \neq \zeta_j \; \forall i, j$. For mutually distinct frequencies and damping parameters, testing with the i^{th} eigenvalue, $\lambda_i = -\zeta_i\omega_i \pm \omega_i\sqrt{\zeta_i^2 - 1}$, only results in the loss of 1 row rank (between the i^{th} and $i+1^{th}$ rows), and the extra $\mathbf{C}$ row of the PBH test matrix ensures rank N remains provided $\delta_i \neq 0 \; \forall \; i = 1 \cdots N$. This requirement of distinct frequencies follows intuitively when considering the expected frequency response of the network. Here we expect peaks in the spectrum at the resonant frequencies ω_i. Should these frequencies overlap we cannot expect to tell from the frequency response whether a single oscillator exists, or rather, if multiple oscillators exist at the same frequency, each masking the distinct existence of the other.

Furthermore, it is not unreasonable to assume that a biological network would indeed have all ω_i and all δ_i distinct.

5.3.2 Observability with PBH test: Case of Upper Triangular Coupling

A second interesting matrix structure where the PBH test can be used to prove observability is the case of upper triangular coupling. Here, $\alpha_{ij} = 0 \; \forall \; i < j$ and thus $\varepsilon_{ij} = \mathbf{0} \; \forall \; i < j$.

The eigenvalues of such a matrix are equal to the eigenvalues of the block diagonal sub-matrices.

$$\lambda\left(\left[\begin{array}{cc} \mathbf{A}_1 & \mathbf{X} \\ \mathbf{0} & \mathbf{A}_2 \end{array}\right]\right) = \left\{\lambda(\mathbf{A}_1), \lambda(\mathbf{A}_2)\right\}, \tag{5.3.11}$$

where $\mathbf{X}$ can take any form.

For the network of clocks, an upper triangular structure of coupling means that the eigenvalues of the networked system are identical to those of the subsystems (individual clocks). Each subsystem is observable, therefore, it follows that the $N+1$ rows of (5.3.6) are linearly independent for all λ and the networked system is observable, provided the clocks oscillate at i distinct frequencies following the same argument as given in the previous uncoupled case.

5.3.3 Theoretical Observability: a Polynomial Approach

The eigenvalues of the $\mathbf{A}$ matrix are not so easily found for the general case of symmetric coupling over all scales of system order. The eigenvalues could be approximated by the Gershgorian circle theorem for block diagonal matrices [121], however this would lead to somewhat of a fudged solution to theoretical observability as it is difficult to establish full rank with the PBH test when the eigenvalues are only known within a certain radius.

A system with $(\mathbf{A}, \mathbf{C})$ of the form (5.3.7) and (5.3.1) respectively is observable if the polynomial matrices $\mathbf{D}(\lambda) = \mathbf{A} - \lambda\mathbf{I}$ and $\mathbf{N}(\lambda) = \mathbf{C}$ are right coprime [118]. The Bezout identity [120, Ch 6] can be used to show that for our system $\mathbf{D}(\lambda)$ and $\mathbf{N}(\lambda)$ are indeed right coprime and the system is theoretically observable for most choices of system parameters.

By the Bezout Identity, polynomial matrices $\mathbf{D}(\lambda)$ and $\mathbf{N}(\lambda)$, will be right coprime if and only if there exists polynomial matrices $\mathbf{X}(\lambda)$ and $\mathbf{Y}(\lambda)$, such that,

$$\mathbf{X}(\lambda)\mathbf{N}(\lambda) + \mathbf{Y}(\lambda)\mathbf{D}(\lambda) = I, \tag{5.3.12}$$

where I is the Identity. If we can find successive elementary row operations[3] $U_1, U_2, \ldots U_n$ to reduce $[\mathbf{D}(\lambda), \mathbf{N}(\lambda)]'$, to $[I, \underline{0}]'$, then we have,

$$\mathbf{U}(\lambda) = U_n \ldots U_2 U_1 : \begin{bmatrix} \mathbf{U}_{11} & \mathbf{U}_{12} \\ \mathbf{U}_{21} & \mathbf{U}_{22} \end{bmatrix} \begin{bmatrix} \mathbf{D}(\lambda) \\ \mathbf{N}(\lambda) \end{bmatrix} = \begin{bmatrix} I \\ \underline{0} \end{bmatrix}. \tag{5.3.13}$$

It follows that to satisfy (5.3.12), $\mathbf{U}_{11} = \mathbf{X}(\lambda)$ and $\mathbf{U}_{12} = \mathbf{Y}(\lambda)$. The system is observable provided that such a $\mathbf{U}$ can be found with the necessary condition that $\mathbf{U}$ is a unimodular matrix. A polynomial matrix is unimodular if its inverse is also a polynomial. This is the case if $det(\mathbf{U})$ equals a constant (i.e. $det(\mathbf{U}(\lambda)) \neq 0$ and $det(\mathbf{U}(\lambda))$ is not a function of λ.

Here, the structure of our coupled network has sufficient zero entries across $\mathbf{A} - \lambda I$ and $\mathbf{C}$ such that each column of $[\mathbf{A}' - \lambda I, \mathbf{C}']'$ is generically independent of all the others. Therefore, elementary row operations can be found to transform $[\mathbf{A}' - \lambda I, \mathbf{C}']' \rightarrow [I, \underline{0}]'$

---

[3] Elementary row operations include either (1) Interchanging any 2 rows, (2) Adding to a row, a polynomial multiple of another row or (3) Scaling a row by any real or complex number

and the networked system is observable, except in some non-generic cases when the parameters (ω, ζ, α) combinations satisfy some polynomial equations.

An example of such a non-generic parameter set, for a network of 3 clocks, is detailed in Appendix A.2. It shows the calculation of conditions where observability is lost under the algebra simplifying conditions of uniform connection strength, α, uniform damping, ζ, and a simple measurement vector $\mathbf{C} = [0, 1, 0, 0, \cdots, 0, 0]$. The non-generic set under these conditions was:

$$\begin{aligned} \alpha \in \{ \quad & - \quad \frac{1}{3}\omega_1^2, \\ & + \quad \frac{\zeta^2}{24(-\omega_3+\omega_2)}\left(-f_1(\omega_1,\omega_2,\omega_3,\zeta)+\sqrt{f_2(\omega_1,\omega_2,\omega_3,\zeta)}\right), \\ & + \quad \frac{\zeta^2}{24(-\omega_3+\omega_2)}\left(-f_1(\omega_1,\omega_2,\omega_3,\zeta)-\sqrt{f_2(\omega_1,\omega_2,\omega_3,\zeta)}\right)\}, \end{aligned} \tag{5.3.14}$$

where f_1 and f_2 are functions described in Appendix A.2. For the undamped case $(\zeta_i = 0 \; \forall \; i)$, the set in equation A.3.3 simply reduces to the condition where $\alpha \in \; 1/3\omega_1^2, 0$. The case of non-observability for $\alpha = 0$ is obvious, remembering that for this example we are measuring only from the 1^{st} oscillator. If that oscillator is not connected to the remainder of the network $(\alpha = 0)$ then we would not expect any oscillations to be visible apart from that of the 1^{st} oscillator and thus expect the system to be unobservable.

It is important to note that the smallest perturbation to any of the parameters $(\alpha_{ij}, \zeta_i, \omega_i)$ will restore the condition of full observability. The probability of finding a non-generic set when the system parameters are assigned at random is quite low. Therefore, the effect of the existence of non-generic sets can be considered negligible *on average* for simulations with many trials of randomly assigned parameters. We expect the mean observable percentage over multiple trials to be near 100%. Any significant deviation from 100% observability must be due to factors beyond the coincidence of random parameter choice lying in the non-generic set.

5.4 Non-Observable for all Practical Purposes

Even when the system is observable in the normal sense of the word, it turns out that the simple limitation of a finite precision measurement reduces our ability to distinguish all states drastically.

Observability is computed in this section using the 1^{st} condition defined in Section 5.1, that is, the rank condition on the observability matrix, $\mathcal{O}(\mathbf{C}, \mathbf{A})$. This rank condition requires that $\mathcal{O}(\mathbf{C}, \mathbf{A})$ contains $2N$ (N is the number of clocks) *sufficiently* independent simultaneous equations such that we can solve for the initial state vector x, given the output measurement over time. $\mathcal{O}(\mathbf{C}, \mathbf{A})$ is full rank if it has $2N$ non-zero singular values. In practical computation, the number of singular values of $\mathcal{O}(\mathbf{C}, \mathbf{A})$ that are larger than some tolerance value indicate sufficient independence. That tolerance value is found based on the smallest number we can represent with the number of bits in the measurement.

5.4.1 Continuous Representation

The continuous companion-format state space representation of each individual pendulum system presented thus far is numerically ill-conditioned. The singular values of the observability matrix, $\sigma\big(\mathcal{O}\left(\mathbf{C}, \mathbf{A}\right)\big)$, are proportional to the spectral information in the system matrix $\mathbf{A}$,

$$\sigma\big(\mathcal{O}\left(\mathbf{C}, \mathbf{A}\right)\big) \propto \omega^{(2N-1)}, \tag{5.4.1}$$

where ω is the natural frequency of one of the N clocks in the network. Even for modest network orders ($N \approx 100$), with $\omega \in \{0.5Hz, 200Hz\}$ we can expect to suffer numerical ill-conditioning with very large numerical range for the singular values. To readdress these numerical issues a state space transformation with time-scaling is proposed. This enables us to consider fundamental observability limitations in this system isolated from issues of numerical illposedness.

For each individual pendulum, with a companion format $\mathbf{A_i}, \mathbf{B_i}, \mathbf{C_i}$:

$$\mathbf{A}_i = \begin{pmatrix} 0 & 1 \\ -\omega_i^2 & -2\zeta_i\omega_i \end{pmatrix}, \mathbf{B}_i = \begin{pmatrix} 1 \\ 0 \end{pmatrix}, \mathbf{C}_i = \left(0, -\delta_i\right), \tag{5.4.2}$$

the transformation,

$$\mathbf{T} = \begin{pmatrix} \omega_i & \zeta_i \\ 0 & -\sqrt{1-\zeta^2} \end{pmatrix} \tag{5.4.3}$$

is used. The transformed system becomes:

$$\mathbf{A}_i = \begin{pmatrix} -\zeta_i\omega_i & -\omega_i\sqrt{1-\zeta_i^2} \\ \omega_i\sqrt{1-\zeta_i^2} & -\zeta_i\omega_i \end{pmatrix} \tag{5.4.4}$$

$$\mathbf{B}_i = \begin{pmatrix} \omega_i \\ 0 \end{pmatrix}, \mathbf{C}_i = \left(0, \frac{\delta_i}{\sqrt{1-\zeta_i^2}}\right). \tag{5.4.5}$$

The networked system after transformation becomes,

$$\mathbf{A} = \begin{pmatrix} \mathbf{A}_1 + \varepsilon_{11} & \varepsilon_{12} & \dots & \varepsilon_{1N} \\ \varepsilon_{21} & \mathbf{A}_2 + \varepsilon_{22} & \dots & \varepsilon_{2N} \\ \vdots & \vdots & \ddots & \vdots \\ \varepsilon_{N1} & \varepsilon_{N2} & \dots & \mathbf{A}_N + \varepsilon_{NN} \end{pmatrix}, \tag{5.4.6}$$

$$\mathbf{B} = (\mathbf{B}_1, \mathbf{B}_2 \dots \mathbf{B}_N)', \mathbf{C} = (\mathbf{C}_1, \mathbf{C}_2 \dots \mathbf{C}_N), \tag{5.4.7}$$

where the coupling terms (ε) are transformed from 5.3.4 and 5.3.5 to:

$$\varepsilon_{ij} = T_i \begin{pmatrix} 0 & 0 \\ \alpha_{ij} & 0 \end{pmatrix} T_j^{-1} \ \forall \text{ i}\neq\text{j} \tag{5.4.8}$$

$$\varepsilon_{ii} = T_i \begin{pmatrix} 0 & 0 \\ -\sum_j \alpha_{ij} & 0 \end{pmatrix} T_i^{-1}. \tag{5.4.9}$$

Time-scaling

The transformed system representation, $\dot{\mathbf{x}} = \mathbf{A}\mathbf{x} + \mathbf{B}u$ for the networked clock model, allows for time-scaling the frequency dependency out of the state equation as shown in Equation 5.4.10:

$$\begin{array}{l} \dot{\mathbf{x}} = \frac{d\mathbf{x}}{dt} = \omega\hat{\mathbf{A}}\mathbf{x} + \omega\hat{\mathbf{B}}u \\ \frac{d\mathbf{x}}{d\omega t} = \frac{d\mathbf{x}}{d\tau} = \hat{\mathbf{A}}\mathbf{x} + \hat{\mathbf{B}}u \end{array} \tag{5.4.10}$$

The results of numerical analysis shown in the remainder of this chapter where found using the time-scaled model (simulating in τ time). The large scale networked system was time-scaled using the largest resonance frequency for time normalisation. The results of these simulations can be translated back to the original system with non-normalised frequencies through reverse time-scaling so no information is lost here.

Singular Values of Networked Model

Using the time-scaled system matrices for the networked system, $\{\hat{\mathbf{A}}, \mathbf{C}\}$, the singular values of the observability matrix,

$$\mathcal{O} = \left[\mathbf{C}', (\mathbf{CA})', (\mathbf{CA}^2)', \ldots, (\mathbf{CA}^{N-1})'\right]' \tag{5.4.11}$$

were found for a globally coupled network of 50 pendulum clocks (coupling parameter $\alpha_{ij} = 0.01 \ \forall \ i, j$). The damping parameter ζ was set to 0.001 for all clocks and the normalised frequencies of each clock were uniformly distributed across several frequency ranges. These frequency ranges are a narrow range of 0.98-1 Hz/Hz, a mid-range of 0.6-1 Hz/Hz and a wide range of 0.0025-1 Hz/Hz. Results with each frequency range are shown in Fig. (5.1). As expected, the narrower the frequency range, the more difficult it is to distinguish the various states. The singular value decomposition indicates that less than half the states are identifiable even in a well scaled system using normal machine precision in Matlab.

Through timescaling, we have constrained the growth towards infinity of singular values of the observability matrix, as illustrated in Figure 5.1. In effect, we have avoided machine *overflow*[4]in numerical simulation. However, we also need to consider that the magnitude of singular values become arbitrarily small as the order of the network, N, increases.

---

[4] *Overflow* occurs when numerical values are too large to be represented given a certain number of machine bits. The opposite condition *underflow* describes occurrences for numerical values less than the minimum numerical representation for a given number of machine bits.

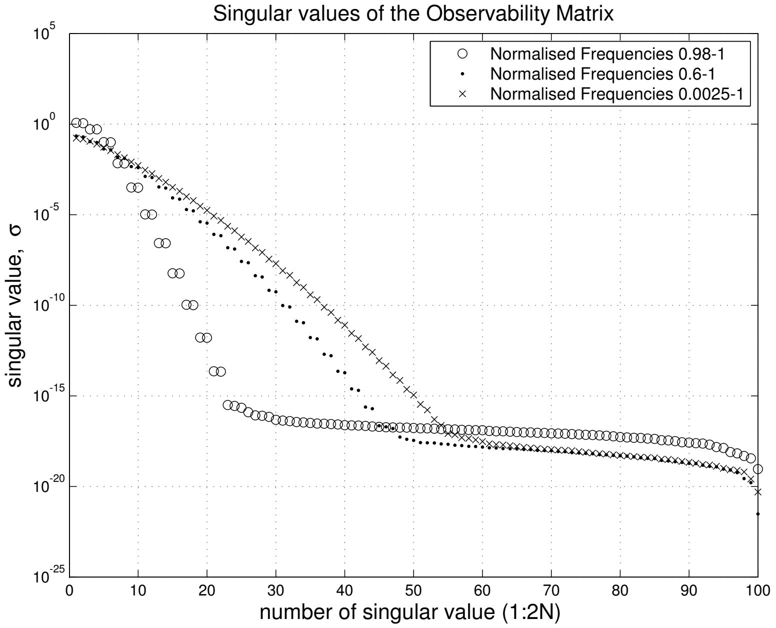

Figure 5.1: The Singular values of the observability matrix, $\mathcal{O} = \left[\mathbf{C}', (\mathbf{CA})', (\mathbf{CA}^2)', \ldots, (\mathbf{CA}^{N-1})'\right]'$, are plotted for a network of $N = 50$ clocks (100 states) whose natural frequencies were uniformly chosen from the normalised frequency range of either 0.98-1 (plotted as symbol o), 0.6-1 (plotted as symbol .) or 0.0025-1 (plotted as symbol x).

The singular value magnitude is a function of the numerical size of the entries in the observability matrix (5.4.11). As N grows the entries of $(\mathcal{O} : CA^N)$ become increasingly small when the eigenvalues of A are less than 1, as we have explicitly timescaled them to be there. While the machine overflow problem has been circumvented, our observability is still dramatically limited effectively due to a machine *underflow* problem. Furthermore, simulation shows the change in shape and magnitude of the curve in Figure 5.1 is negligible for changes in coupling α. Intuitively, however, it is certainly not expected that observability be independent of coupling. It seems the lack of observability is based entirely on the underflow problem of numerical illposedness. Before concluding that system observability is indeed dramatically poor based on this underflow problem, we must ask if we have configured our system to be as well posed as possible, in the sense that we wish to consider observability under the best possible conditions. Is there an alternative representation of this system where the singular-values do not decay as dramatically? In the next section, we find that an undamped and digitised problem formalisation gives us a more well-posed problem.

5.4.2 Digital Representation

By converting to a digital representation and looking particularly at marginally stable oscillations (undamped oscillations, $\zeta = 0$) we can constrain the eigenvalues of the system matrix $\mathbf{A}$ to a compact set. Now any ill-conditioning in the observability matrix, $\mathcal{O}(\mathbf{C}, \mathbf{A})$, can be isolated from the machine underflow and overflow problems in individual matrix entries and instead attributed to poor observability. Using a digital undamped representation, observability will be found later in Section 5.5 to be effected by *(i)* the coupling geometry, *(ii)* the number of measurement bits and *(iii)* scale of the network. Firstly, however, in the remainder of this section we show why the digital undamped representation is well conditioned.

For the original analogue system with companion format $(\mathbf{A}, \mathbf{B}, \mathbf{C})$ as per 5.4.2 after setting $\zeta = 0$ (undamped form) we have:

$$\mathbf{A}_i = \begin{pmatrix} 0 & 1 \\ -\omega_i^2 & 0 \end{pmatrix}, \mathbf{B}_i = \begin{pmatrix} 1 \\ 0 \end{pmatrix}, \mathbf{C}_i = (0, -\delta_i)\,. \tag{5.4.12}$$

The transformation matrix 5.4.3 for $\zeta = 0$ becomes:

$$T = \begin{pmatrix} \omega_i^2 & 0 \\ 0 & -1 \end{pmatrix}, \tag{5.4.13}$$

with the resulting transformed system having a rotational matrix $\mathbf{A}_i$,

$$\mathbf{A}_i = \begin{pmatrix} 0 & -\omega_i \\ \omega_i & 0 \end{pmatrix}, \tag{5.4.14}$$

$$\mathbf{B}_i = \begin{pmatrix} \omega_i \\ 0 \end{pmatrix}, \mathbf{C}_i = (0, \delta_i)\,. \tag{5.4.15}$$

This corresponds to (5.4.5) after setting $\zeta = 0$ as expected.

The advantage in system well-posedness with $\zeta = 0$ is that all the system eigenvalues lie conveniently on the imaginary axis, $\lambda(\mathbf{A}_i) = \pm\omega_i j$. This is convenient as by transferring to the digital domain the underflow problem is eliminated. To transfer to the digital domain the continuous system matrix $\mathbf{A}$ is mapped to $e^{A\Delta T}$, where ΔT is the digital sample time in seconds. For simplicity $\Delta T = 1$ here, the implication of this is discussed in more detail later in this section. The imaginary axis is transformed to the unit circle in the digital domain, therefore, the eigenvalues of our digital system lie on the unit circle and have unit magnitude. Real EEG measurement necessitates the conversion of signals to digital form for machine storage, so transferring to the digital domain in our model of EEG is entirely appropriate here.

With the system eigenvalues thus confined to a compact set on the unit circle, what now of the singular values of the digital system? The transformation matrix T in equation 5.4.13 is a rotational matrix such that $\mathbf{A}_i^{'} + \mathbf{A}_i = 0$. The singular values of the each individual (uncoupled) clock, $\sigma(\mathbf{A}_{idigital})$ are therefore exactly unity for all frequencies ω_i.

$$\begin{aligned}
\mathbf{A}_{i_{digital}} &= e^{\mathbf{A}_i}, \\
\Rightarrow \sigma(\mathbf{A}_{i_{digital}}) &= \sigma(e^{\mathbf{A}_i}), \\
\text{and } \sigma(\mathbf{K}) = \sqrt{\lambda(\mathbf{K}'\mathbf{K})} \text{ for any matrix } \mathbf{K} & \\
\Rightarrow \sigma(e_i^{\mathbf{A}}) &= \sqrt{\lambda((e_i^{\mathbf{A}})'e_i^{\mathbf{A}})} \\
&= \sqrt{\lambda(e^{\mathbf{A}_i'}e^{\mathbf{A}_i})} \\
&= \sqrt{\lambda(e^{\mathbf{A}_i'+\mathbf{A}_i})} \ \because \ \mathbf{A}_i'\mathbf{A}_i = \mathbf{A}_i\mathbf{A}_i' \\
&= \sqrt{\lambda(e^{\mathbf{0}})} \ \because \ \mathbf{A}_i' + \mathbf{A}_i = \mathbf{0}. \\
&= \sqrt{\lambda(\mathbf{I})} = \{1, 1\}\,. \qquad (5.4.16)
\end{aligned}$$

However, the system matrix consists not just of the block diagonals of $\{\mathbf{A}_1, \mathbf{A}_2, \mathbf{A}_3\ etc\}$, we also have off-diagonal coupling perturbation terms as described in equation 5.4.6. These perturbations are specifically designed such that the coupled network system remains purely oscillatory after coupling, i.e. eigenvalues of the coupled system remain on the imaginary axis (analogue) or exactly on the unit circle (digital). Therefore the previous analysis for the uncoupled case also applies here.

The proposed coupling between the clocks can be physically interpreted as representing springs attached between the clocks' pendula. Coupling therefore only reshapes the potential energy of the mechanical system and does not introduce any damping. Hence the new physical system, after the addition of the springs, is still a purely oscillatory one, but where the eigen-frequencies have shifted because of the addition of the springs. The stronger the coupling the more the eigen-frequencies shift.

Moreover, these springs transfer some energy between the clocks. It is therefore intuitive that as long as there is a pathway consisting of a series of springs linking one clock to another that observing the motion of any one clock in such a network will indeed contain information of all the clocks that are linked to it via a pathway of springs. Intuitively, this explains why such systems are in principal (and generically) observable.

Recall that for a network of 2 clocks, the networked system would have an $\mathbf{A}$ matrix of form,

$$\mathbf{A} = \begin{pmatrix} \mathbf{A}_1 + \varepsilon_{11} & \varepsilon_{12} \\ \varepsilon_{21} & \mathbf{A}_2 + \varepsilon_{22} \end{pmatrix} = \begin{pmatrix} 0 & -\omega_1 & 0 & 0 \\ \omega_1 + \alpha_{12} & 0 & -\alpha_{12} & 0 \\ 0 & 0 & 0 & -\omega_2 \\ -\alpha_{21} & 0 & \omega_2 + \alpha_{21} & 0 \end{pmatrix} \tag{5.4.17}$$

$\mathbf{A}_i$ is defined in (5.4.14). The perturbation terms ε_{ij} are defined in Equations 5.3.4 & 5.3.4 in Section 5.3. In general, given symmetric coupling ($\alpha_{ij} = \alpha_{ji}$) and no self-coupling ($\alpha_{ii} = 0 \ \forall\, i$), we have a system matrix $\mathbf{A}$ that is block-symmetric[5].

In a general for an $n \times n$ symmetric matrix $\mathbf{A}$, given n linearly independent columns (or equally rows), as was shown to be generically the case in Section 5.3, we can find an orthogonal matrix $\mathbf{T}$ to diagonalise $\mathbf{A}$ obtaining $\mathbf{D} = \mathbf{TAT}^{-1}$, where $\mathbf{D}$ is a diagonal matrix $\mathbf{D} = diag(\lambda_1, \ldots, \lambda_n)$ and where $\lambda_1, \ldots, \lambda_n$ are the eigenvalues of $\mathbf{A}$. It follows that we can also block diagonalise $\mathbf{A}$, since the 2×2 block columns (that is column pairs i and $i+1$ for i odd), or equally the 2×2 block rows, of $\mathbf{A}$ are linearly independent from each other by construction. Therefore a transformation $\mathbf{T}$ can be found to block-diagonalise $\mathbf{A}$, such that $\mathbf{D} = \mathbf{TAT}^{-1}$ is a block diagonal matrix, $\mathbf{D} = diag(\mathbf{D}_1, \ldots, \mathbf{D}_{\frac{n}{2}})$, where $\mathbf{D}_i$ is a 2×2 matrix. If we elect to choose our coupling such that $\mathbf{A}$ is a block-wise positive-definite matrix[6](as is the case for 5.4.17 given $\alpha_{ij} > 0 \ \forall\, i, j$), then we have that the block diagonal elements $\mathbf{D}_i$ have eigenvalues of $\pm\theta j$, where $\theta \in \mathbb{R}$.

The proof that coupled clocks remain purely oscillatory clocks can be elegantly demonstrated by reverting to the second order differential equation format. Consider that the dynamics of a network of uncoupled and unforced clocks can be written as,

$$\ddot{\mathbf{x}} + \mathbf{W}\mathbf{x} = 0. \tag{5.4.18}$$

where $\ddot{\mathbf{x}} = [\ddot{x}_1, \ddot{x}_2, \ldots, \ddot{x}_N]'$, $\mathbf{x} = [x_1, x_2, \ldots, x_N]'$, where x_i is the angular displacement of the i^{th} clock and $\mathbf{W}$ is a diagonal matrix, $\mathbf{W} = diag(\omega_1^2, \omega_2^2, \ldots, \omega_N^2)$.

---

[5] A matrix $\mathbf{M}$ with sub-matrices $\mathbf{A}, \mathbf{B}, \mathbf{C}, \mathbf{D}$ where $\mathbf{M} = \begin{pmatrix} \mathbf{A} & \mathbf{B} \\ \mathbf{C} & \mathbf{D} \end{pmatrix}$ is block-symmetric if $\mathbf{M}' = \mathbf{M}$ where the transpose is in block format: $\mathbf{M}' = \begin{pmatrix} \mathbf{A} & \mathbf{C} \\ \mathbf{B} & \mathbf{D} \end{pmatrix}$.

It follows that the coupled system (without external inputs) can be expressed in similar form as (5.4.18), with a new **W** matrix containing additional diagonal and off-diagonal terms,

$$\mathbf{W} = \begin{pmatrix} \omega_1^2 + \sum_j \alpha_{1j} & -\alpha_{12} & -\alpha_{13} & \cdots & -\alpha_{1N} \\ -\alpha_{12} & \omega_2^2 + \sum_j \alpha_{2j} & -\alpha_{23} & \cdots & -\alpha_{2N} \\ -\alpha_{13} & -\alpha_{23} & \omega_3^2 + \sum_j \alpha_{3j} & \cdots & -\alpha_{3N} \\ \vdots & \vdots & \vdots & \ddots & \vdots \\ -\alpha_{1N} & -\alpha_{2N} & -\alpha_{3N} & \cdots & \omega_N^2 + \sum_j \alpha_{Nj} \end{pmatrix} \tag{5.4.19}$$

The matrix **W** in (5.4.19) is a positive definite matrix for $\alpha_{ij} > 0 \ \forall \ i, j$, since it is a symmetric matrix where (i) All the diagonal entries are positive and (ii) **W** is a diagonally dominant matrix (Each diagonal entry is greater than the sum of the absolute values of all other row entries). Since **W** is positive definite, there exists N positive eigenvalues of **W** (**W** is full rank). Thus we can always find a transformation **T**, where we obtain a transformed state system $\mathbf{z} = \mathbf{T}\mathbf{x}$ with $\ddot{\mathbf{z}} = \mathbf{D}\mathbf{z}$, where $\mathbf{D} = \mathbf{T}\mathbf{B}\mathbf{T}^{-1}$ is a diagonal matrix,

$$\mathbf{D} = \begin{pmatrix} \widetilde{\omega}_1^2 & 0 & 0 & \cdots & 0 \\ 0 & \widetilde{\omega}_2^2 & 0 & \cdots & 0 \\ 0 & 0 & \widetilde{\omega}_3^2 & \cdots & 0 \\ \vdots & \vdots & \vdots & \ddots & \vdots \\ 0 & 0 & 0 & \cdots & \widetilde{\omega}_N^2, \end{pmatrix} \tag{5.4.20}$$

Thus, given coupling that is chosen to be symmetric ($\alpha_{ij} = \alpha_{jj}$) and positive ($\alpha_{ij} > 0 \ \forall \ i, j$) we can always mathematically reconfigure a coupled oscillator system with a **W** matrix such as Equation (5.4.19) to that of an uncoupled system of pure oscillators in Equation (5.4.20). The $\widetilde{\omega}_i$ in (5.4.20)are the natural frequencies of the reconfigured purely oscillatory coupled network, which are simply shifted or perturbed in frequency from the uncoupled clock frequencies ω_i.

Therefore, returning to the standard state space co-ordinate system of $2N$ 1^{st} order differential equations, we can transform the pendulum clock positions $\mathbf{x} \rightarrow \mathbf{T}\mathbf{x}$, giving

---

[6] **M** is a block-wise positive-definite matrix if each of the block-wise leading minors have a determinant greater than zero. (For the **M** defined in the previous footnote this equates to: $det(\mathbf{A}) > 0$ and $det(\mathbf{M}) > 0$).

$(\dot{\mathbf{Tx}}) = \mathbf{D}(\mathbf{Tx})$. In these new co-ordinates we have N independent purely oscillatory clocks with positions $\mathbf{Tx}$ and frequencies θ. The new frequency at clock i, θ_i, is shifted or perturbed from the original ω_i by the coupling terms α_{ij}. With our coupled system transformed to a purely oscillator network, the analysis in Equation 5.4.16 equally applies in the coupled case (with $\mathbf{D}_i$ replacing $\mathbf{A}_i$ here) and the singular values of the digital coupled system matrix should remain unity.

In addition we can now use the theoretical argument of generic observability based on independent clocks (see Section 5.3), with practical observability here becoming a question of whether our new clock frequencies θ_i are distinct and that there is sufficient read-out at the output to overcome any system information loss in quantisation noise.

We next consider the impact of practical observability with a biologically compatible model of coupling. This coupling would be a relatively weak coupling between close neighbours and very weak coupling between oscillators that have a long distance connection. Index difference can be used as a surrogate distance. Additionally, there is no requirement that each oscillator is connected to every other oscillator. In contrast, selective and organised network connection is equally biologically plausible. This is discussed in more detail in the following Section 5.5. Here in Figure 5.2 the spread of singular values of a network matrix $\mathbf{A}$ is shown for a more biologically appropriate nearest-neighbour-type organisation of connection strength, as illustrated in Figure 5.6(a). The maximum coupling strength α (strength between nearest neighbours) is 10^{-3}, frequencies were chosen in the normalised range $[0.001, 1]$ rad/s.

Through the use of an undamped system model together with digitalisation we have ensured that the *magnitude* of the singular values of the system matrix $\mathbf{A}_{digital}$ remains unity. The concern in this chapter, however, is observability, which involves not only the structure of the system matrix $\mathbf{A}_{digital}$ but rather the projection of output matrix $\mathbf{C}$ onto $\mathbf{A}_{digital}, \mathbf{A}^2_{digital}, \mathbf{A}^3_{digital} \cdots \mathbf{A}^{N-1}_{digital}$. The spread of singular values the observability matrix $\mathcal{O}$ is shown in Figure 5.3 for the digital system with no damping. The digital version enjoys much better observability properties, but fundamentally the problems with practical observability persist. Figure 5.3 depicts the case where C is connected to each oscillator in the network, $\mathbf{C} = \left[0, \frac{1}{N}, 0, \frac{1}{N} \cdots, 0, \frac{1}{N}\right]$, and the frequencies are chosen with uniform separation within the range $[0.001, 1]$. The plot also shows that a significant number of the singular values remain below the numerical noise floor for this simulation of 10^{-16},

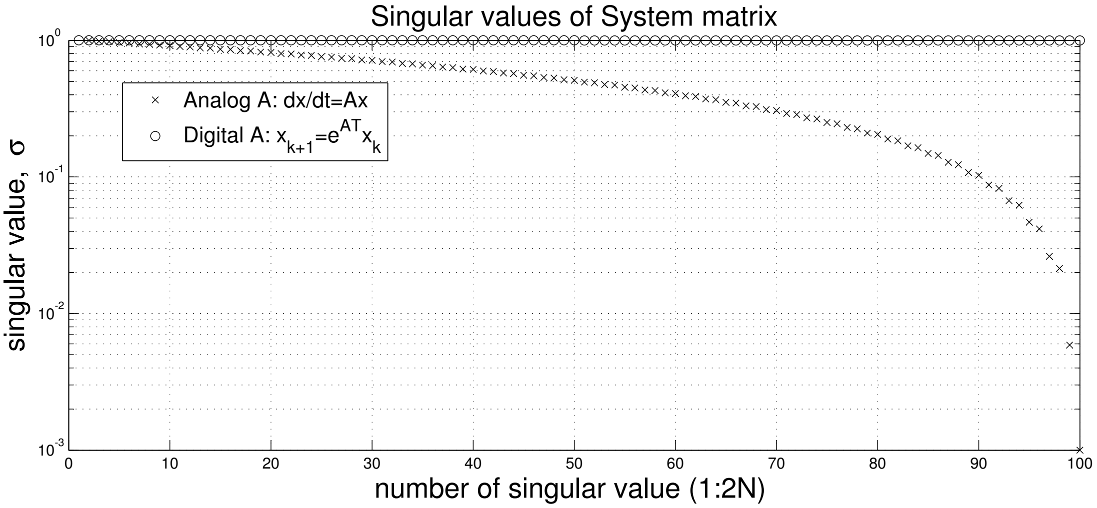

Figure 5.2: Singular values of system matrix **A**: Comparing digital and analogue system representations. $N = 50$ is the number of clocks in the system.

indicating practical difficulties with observability.

The earlier analysis of this section uses a digital sample time ΔT set to unit time. In addition, the results of Figure 5.3 use time-scaled clock frequencies. There is a correlation of reasoning here.

Firstly, consider the choice of ΔT. It is to be expected that the digital sampling frequency, $\frac{1}{\Delta T}$, has a significant effect on observability. Indeed, it does. For the frequency-normalised system in Figure 5.3, the effect of increasing and decreasing ΔT is shown in Figure 5.4.

Secondly, consider time-scaling. For the digitised system formulation it is no longer necessary to normalise frequency such that the maximum singular values of $\mathcal{O}$ are contained. Figure 5.5 shows the singular values for various frequency ranges to support this (all conditions apart from frequency are identical to the simulation in Figure 5.3). This modelling effort relates to real measurements so clock frequencies and sample time are somewhat fixed. For a standard EEG recording we can expect the sampling frequency to be 512Hz increasing to 1024Hz for specialised research machines. The “oscillator frequency range” of brain activity is typically assumed to be in the range from 0.2Hz to 200Hz. This

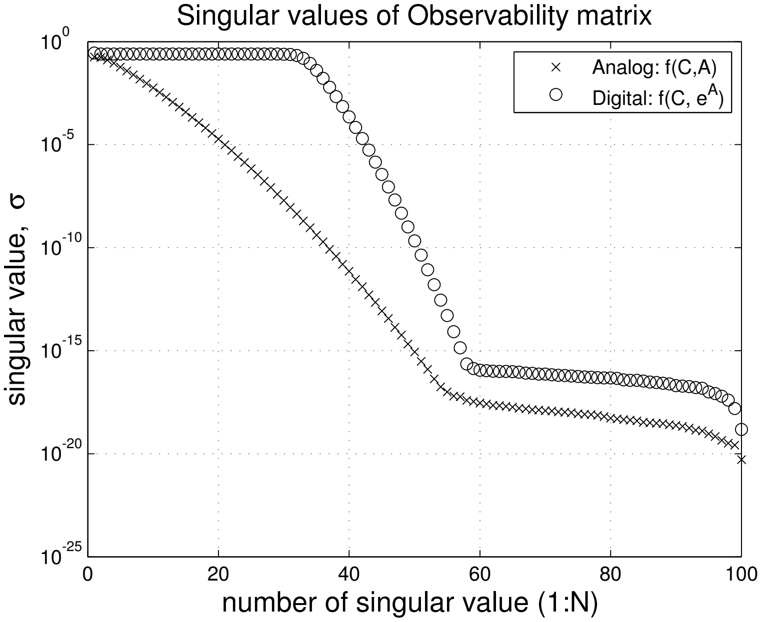

Figure 5.3: Singular values of the Observability matrix $\mathcal{O}$: Comparing digital and analogue system representations. $N = 50$ is the number of clocks in the system.

range pushes towards the Nyquist bound for a sampling frequency of 512Hz and sits nicely at just under twice the Nyquist bound for 1024Hz sampling. The transformation matrix T in equation 5.4.13 has provided not only a rotational system with the numerical magnitude benefits discussed earlier, but also allows for a time-scalable system. Normalising with the maximum frequency, the oscillation range becomes $f = [0.2/200, 1]$. Under the time-scale mapping $t \longrightarrow \frac{\tau}{\omega}$, simulating 1 second of τ time equates to $\frac{1}{\omega_{max}}$ seconds of real t time. For $\omega_{max} = 2\pi f_{max} = 2\pi f_{max} = 2\pi 200 rad/s$,

$$t = \frac{1}{\omega_{max}} = 0.796ms \approx \frac{1}{1024} \tag{5.4.21}$$

Therefore simulating the measurement of EEG frequencies in the range [0.2, 200] Hz sampled at 1024Hz can be equivalently achieved by simulating the normalised frequency range [0.001, 1]Hz with a sampling time of $\Delta T = 1$, as illustrated in Figure 5.5. This choice of time scaling with unity digital sampling is employed throughout the remainder of this thesis.

We now have a well-conditioned system representation to investigate observability

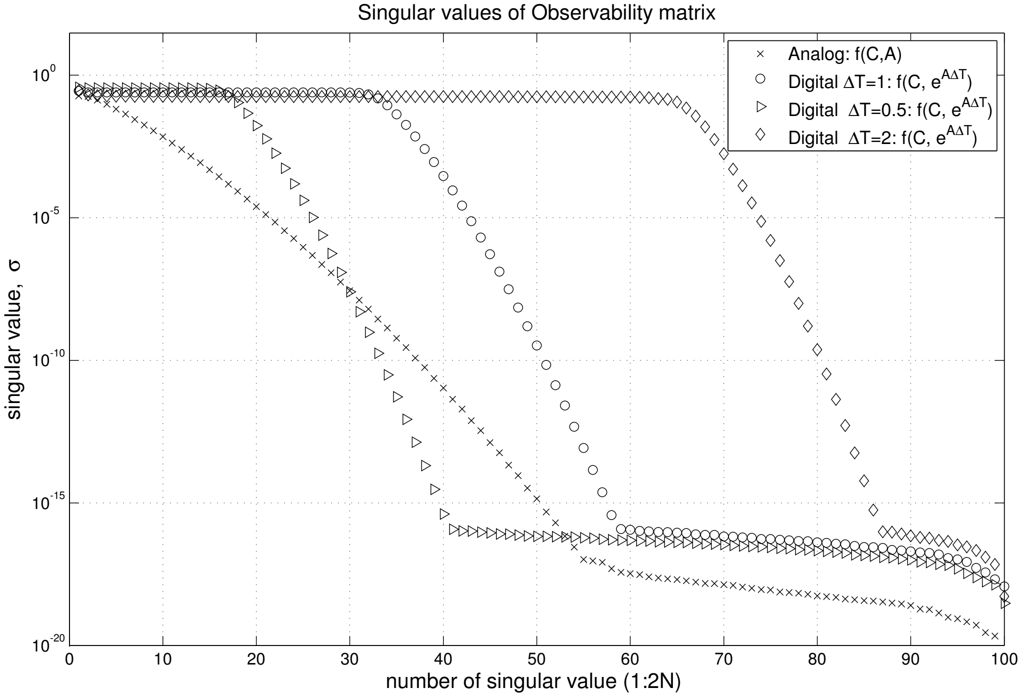

Figure 5.4: Singular values of the Observability matrix $\mathcal{O}$: Exploring the effect of digital sample time ΔT. $N = 50$ is the number of clocks.

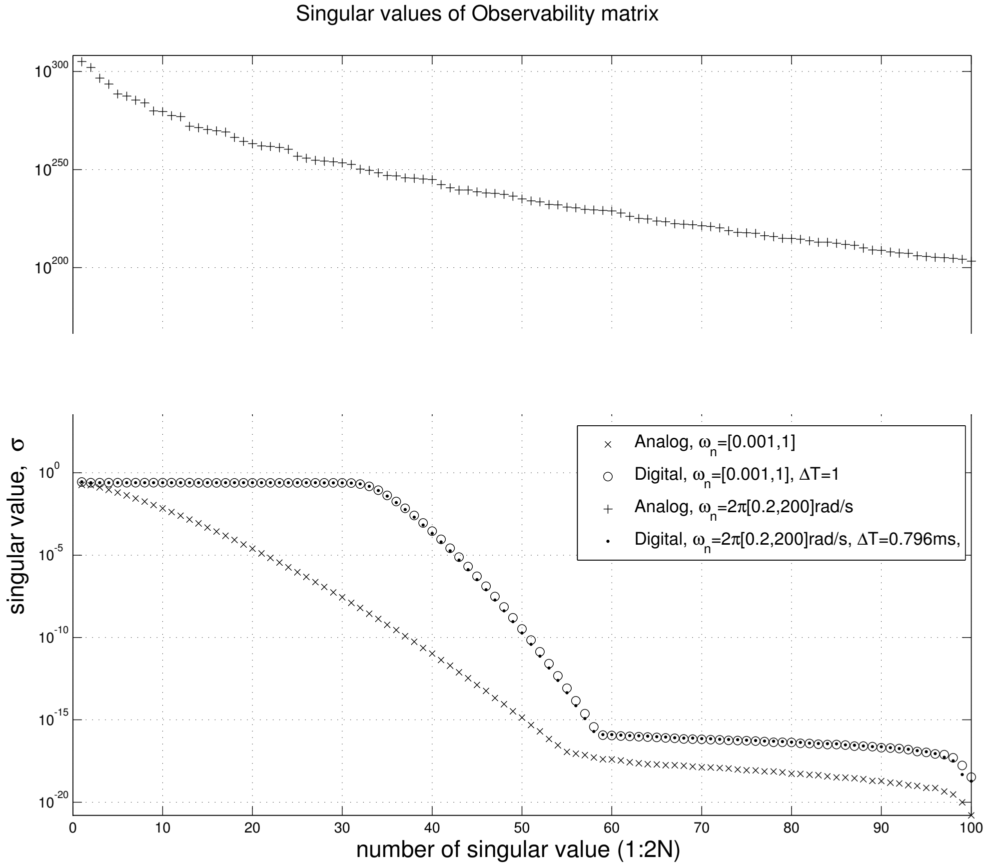

Figure 5.5: Singular values of the observability matrix $\mathcal{O}$. For a digital system with normalised frequencies $\omega_n \in [0.001, 1]$, using a sampling time, $\Delta T = 1s$, as shown with the marker (o) is equivalent to the system with frequencies $\omega_n \in 2\pi[0.2, 200]rad/s$ with a sample time $\Delta T = 0.796ms$, as shown with marker (.). The analogue equivalents for each frequency range, normalised and non-normalised, are marked as (x) and (+) respectively.

of networked clocks: Digital, undamped representation with normalised frequencies and unity sampling period. Despite this well conditioned system, we can see from Figure 5.5 (o or . symbols) that the magnitude of singular values of the observability matrix falls off dramatically after a certain percentage of near unity singular values. Our earlier analysis in this section has established that magnitude conditioning of $\mathbf{A}$ is not to blame. Instead, the loss of rank in the observability matrix, $\mathcal{O}$, relates to the inability to distinguish between the *angles* of $\lambda(\mathbf{A}_{digital})$. This translates to the inability to distinguish between e^{lA} and e^{kA} between row pairs l and k within the observability matrix $\mathcal{O}(\mathbf{C}, \mathbf{A}_{digital})$. Essentially we are running out of space on our unit-circle compact set. In avoiding the machine underflow and overflow problems we have constrained the system eigenvalues to a compact set on the unit circle, however the unit circle is a small set to fit information for N clocks such that we can distinguish between the angle of each clock with a finite number of bits. This indicates that practical observability in a large scale system is limited by the measurement resolution. There is clearly no reason to believe why we could, from an EEG record, recover anything like the number of states that may be required to describe the brain dynamics.

A Biologically Appropriate Model

To consider a digital, discretised analysis is completely in-line with the normal EEG measurement set-up. Moreover, the restriction to pure oscillators is equally biologically justifiable. The alternatives to marginal stability are either *(i)* damped oscillation or *(ii)* unstable oscillation. For the electro-magnetic activity of normal brain activity *(i)* and *(ii)* would indicate pathological states of activity, for example decay of neural activity until brain death and increasing neural excitability until a seizure state respectively. Therefore, operating the coupled oscillator model on the boundary of stability is bio-realistic for normal brain function. The consequence of most interest by employing an undamped and digitised model formalisation, is that, observability now varies as a function of coupling, α. The impact of coupling on observability is the topic of the next section.

5.5 Simulation Results for an EEG-like Measure

5.5.1 Observability as a Function of Network Connectivity

It is interesting to look at observability results as a function of network connection. We will investigate this under two connection regimes. Firstly, *nearest neighbour coupling*, where clocks are strongly coupled to their nearest neighbours and coupling magnitude decreases with connection distance, such that far away connections are weak. Secondly, a *probabilistically coupled network*, where a clock is coupled to any other clock with a certain probability while coupling magnitudes remain uniform. Both of these network structures have biological correlates. On the scale of a localised network consisting of tens of neurons, for nearest neighbour coupling the extracellular electrical fields arising from the oscillation activity of a few neurons will couple strongly to nearby neurons. The case of probabilistic coupling in localised networks can be attributed to the functional connectivity structure of that network. On the larger cortical scale, with a network of several cortical columns, for nearest neighbour coupling the synaptic connections will be strongest in the local region within a column. The case of probabilistic coupling has a biological basis in large inter-column functional networks of neurons where connectivity is more specific than distance-based decay through specific dendrite connections and synaptic coupling. Such connections span both median and long range scales and directly couple the spiking activity of neurons in one area of the brain to another.

Nearest-neighbour Coupling

For the nearest neighbour connection structure shown in Figure 5.6(a), the percentage of observable states as a function of increasing coupling strength, α, is shown in Figure 5.6(b). The clock network has normalised frequencies. The oscillator frequencies were chosen at random from a uniform distribution in the range (0.001, 1). Fifty samples of frequency distribution were simulated and the plotted observability percentage is the mean value over these trials. The standard deviation from the mean was quite small, especially for small alpha, therefore, only the mean values are shown in the plot.

Coupling was chosen here to have a geometrically decaying structure with strongest coupling strength to the nearest neighbouring oscillator. Oscillator i is coupled to its nearest neighbours (oscillators $i \pm 1$) with strength α and to oscillators $i \pm n$ with strength

α^n where $\alpha < 1$. (Note: The code is provided in Appendix A.5 for reference).

The percentage of observable states is calculated as the number of singular values of $\mathcal{O}$ that can be represented by 2^{10} digital number levels, where 10 is the number of measurement bits. We carefully posed our system so that the maximum singular value was of unity order. It then follows that the smallest singular value we can observe for $k = 10$ bits has a magnitude of $1/2^{10} \approx 10^{-3}$. We find almost full observability for $\alpha = 1$. Observability is almost, but not exactly, 100% due to the stochastic nature of the frequency distribution. However, coupling strength in the brain between neurons and indeed between groups of neurons is certainly much less than one.

One crude estimate to illustrate the likely order of coupling strength is based on numbers of connections. Take for example a mini-column of cortical tissue (0.03mm radius, 3mm height), one of the approximate 2×10^8 mini-column volumes in the whole cortex, each containing about 100 neurons with around 10,000 synapses per neuron [1, page 21]. Say that we require 5 synapses to establish a connection between mini-columns. Then the number of available corticocortical connections out from a single mini-column is 200,000 $(10,000 \times 100 \div 5)$. Given this limit, based on the number of biologically present synapses, we can find the ratio of biologically available connections to the total number of connections for a network of mini-columns that was fully interconnected (in the sense of each mini-column connecting to all the others) [122]. That connection ratio is just 1/1000.

$$\frac{\text{Biologically Available Connections}}{\text{Total Possible Connections}} = \frac{200,000 \times 2.10^8}{(2.10^8)^2} = \frac{1}{1000} \tag{5.5.1}$$

An $\alpha = \frac{1}{1000}$ corresponds to a very low level of observability as shown on the left hand side of plot (b) in Figure 5.6.

The results shown in Figure 5.6 depict the case of a measurement electrode connected only to the first oscillator, $\mathbf{C} = [0, 1, 0, 0, 0..., 0, 0]$. This configuration is applicable to a large-scale brain activity measurement, where from each electrode we wish to build a picture of a large area of cortical activity. In effect, under exploration is the ability to observe oscillations sourced far away from the electrode site through their influence on the local network under the probe.

Next we expand the scope of $\mathbf{C}$ to a more realistic model for measuring local EEG

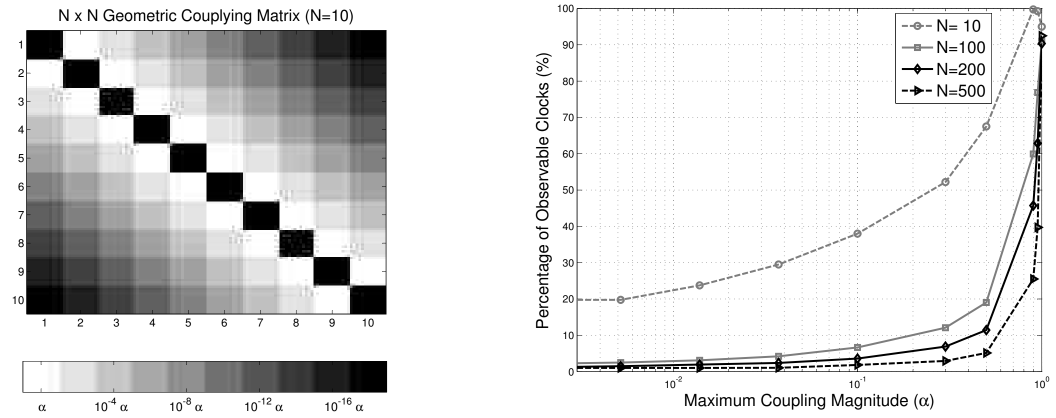

(a) Distance-based Geometric Decay Coupling Structure

(b) Observability as a function of coupling strength for the coupling structure in (a)

Figure 5.6: (a) An image showing the structure of the coupling matrix for a 2-D network of 10 clocks. The white boxes indicate that each clock is coupled to its nearest neighbours with the maximum coupling magnitude of α. Coupling strength to other clocks is geometrically decaying by distance of clock i to clock j as indicated by the accompanying grayscale bar. The black boxes indicate that each clock is not coupled to itself. (b) The percentage of observable clocks as a function of coupling strength, for various networks of N clocks. For large coupling strengths, α , the system is quite observable, however, realistic strength of connection between brain areas is of the order of 10^{-3} where observability is poor.

activity with distance-based measurement. Here the elements in $\mathbf{C}$ follow an exponential function centred with maximum gain on a single clock as illustrated in Figure 5.7. The multi-electrode case is also explored with $\mathbf{C}_5$ of Figure 5.7. These results certainly show a marginally improved picture of what we may glean from EEG measurements. In the biologically appropriate coupling range of $\alpha = 10^{-2} - 10^{-3}$, only just over a third of the network is observable for $\mathbf{C_1}$. The sobering picture that emerges from these results is that observability is independent of coupling strength for $\alpha < 10^{-2}$ in a network of 250 clocks. This is very limiting from an observability perspective as for a network of such modest order we can really only expect to see 33% of the network as an upper bound. This bound is limited by the number of angles distinguishable across the range of $\lambda(\mathbf{A})$ with 10 bits or 2^{10} levels. Increasing α towards unity (biologically incompatible levels) only improves observability as it significantly shifts the bounds of eigenvalues from $\lambda_n \in [\pm 0.001j, \pm 1\ j]$ for the uncoupled network to $\lambda_n \in [(\pm 0.001 \pm f(\alpha))j, (\pm 1 \pm f(\alpha))\, j]$ so there is a larger range with which to attempt fitting N eigenvalues with separation above quantisation noise. In Section 5.5.2 we show that observability from EEG is an illusive prospect for realistic, larger network orders.

Probabilistic Coupling

Observability as a function of increasing coupling probability yields similar results to those of increasing coupling strength discussed in the previous section. The nature of randomly coupled networks is to generate rather strange behaviour on first look. This fascinating behaviour is the topic of random graph theory and small world networks. We can use the ideas from these fields to evaluate the effect of long range probabilistic coupling on observability.

Initially it would seem that we could evaluate the effect of probabilistic coupling by plotting the percentage of observable clocks against the probability of connection between any two clocks, p_{ij}. However, the results of this are difficult to interpret. To illustrate this, take the example network of $N = 10$ clocks with $p_{ij} = 0.1$, where the coupling strength for connected nodes is uniformly set to $\alpha = 0.01$. Coupling is chosen to be symmetric $\alpha_{ij} = \alpha_{ji}$. Two examples of randomly generated networks which satisfy this are shown in Figure 5.8. For the first network, Figure 5.8(a), given a measurement at clock 1, $\mathbf{C} = [0, 1, 0, 0 \cdots, 0, 0]$ the number of observable clocks with infinite measurement resolution is 1 (10% Observable). Clock 1 is simply not connected to any other clocks, so

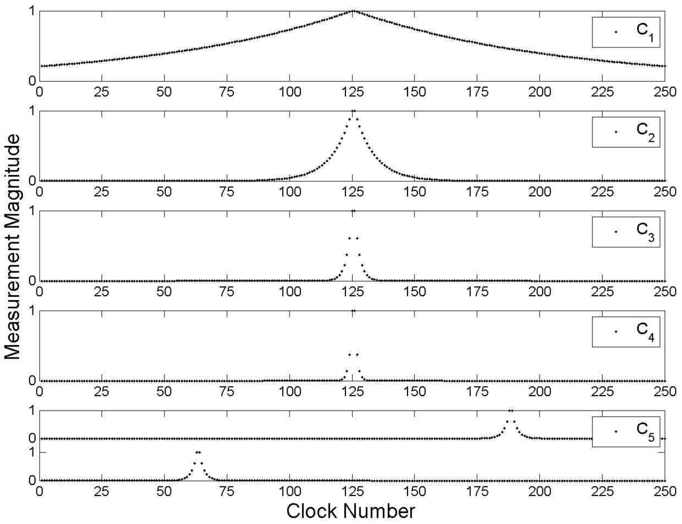

(a) Measurement matrices C_1 to C_5

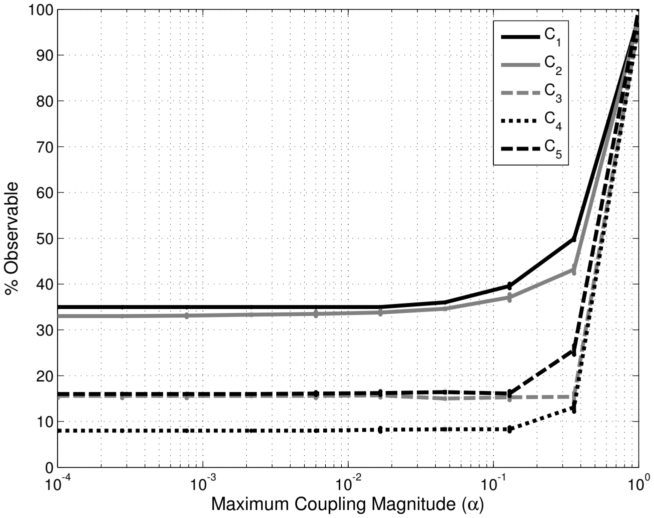

(b) Observability as a function of coupling strength for the measurement vectors in (a)

Figure 5.7: (a) Several possible configurations of measurement **C**. **C**$_1$ to **C**$_4$ are vectors modelling the strength of measurement from each of the 250 clocks at a single electrode site. **C**$_5$ is a matrix of two rows, modelling the simultaneous measurement from two electrodes. (b) The percentage of observable clocks for each of the measurement configurations in (a). Coupling was modelled as per Figure 5.6(a).

there is no information in the measurement about them. For the second network, Figure 5.8(a), the percentage of observable clocks under infinite resolution is 80%. We can only see a maximum of 8 out of 10 clocks as clock 2 and 4 are completely disconnected from the rest of the network. If we were to use these specific two trials we would have a mean observability percentage of 45% at probability of connection $p_{ij} = 0.1$. This statistic conveys little about the expected nature of observability in either trial.

By adding the effect of finite measurement resolution to 10 bits, or 10^{-3} levels the level of observability is dramatically reduced in the second network. For a normalised system with maximum numerical magnitude of order 1, any numbers smaller than 10^{-3} are lost in quantisation noise. Our revised observability estimated for the networks in Figure 5.8 (a) and (b) are now 10% and 40%. The variable of significance here is not so much p_{ij} but rather the *hop number* also referred to as the *shortest path length.* This refers to the number of hops needed to make a connection path between clock i and j. For example to connect clock 1 to clock 7 with the graph in Figure 5.8(a) we have a hop number of 2.

$$\boxed{\text{clock 1}} \xrightarrow{\qquad 1^{st} hop \qquad} \boxed{\text{clock 9}} \xrightarrow{\qquad 2^{nd} hop \qquad} \boxed{\text{clock 7}}$$

The information fed into clock 1 about clock 7 is attenuated by $\alpha^2 = 10^{-4}$. This is already less than the quantisation level, so for the quantised measurement at clock 1 can only see clock 9 and not clock 7 in this path. In general, clocks are only observable if:

$$\alpha^h \geq \frac{1}{2^K}, \tag{5.5.2}$$

for K number of bits and h, the hop number.

The implications of this for the measurement for the real cortical network can be explored by considering some anatomical statistics. If we consider single neurons to be the nodes of our graph, i.e the clocks in our network, what would our expected range of hop numbers be? For purely random connection if each neuron in the cortex has in the order of 10^4 synapses [1, page 21] it can potentially connect with 10^4 other neurons with a hop number of 1. If those neurons with a hop number of 1 from our initial neuron each connect to another 10^4 neurons, we have already amassed a network of 10^8 with just a hop number of 2. By taking an additional hop to 3 we potentially have a network of 10^{12} neurons which would completely account for the expected 10^{10} neurons [1] in the cortex.

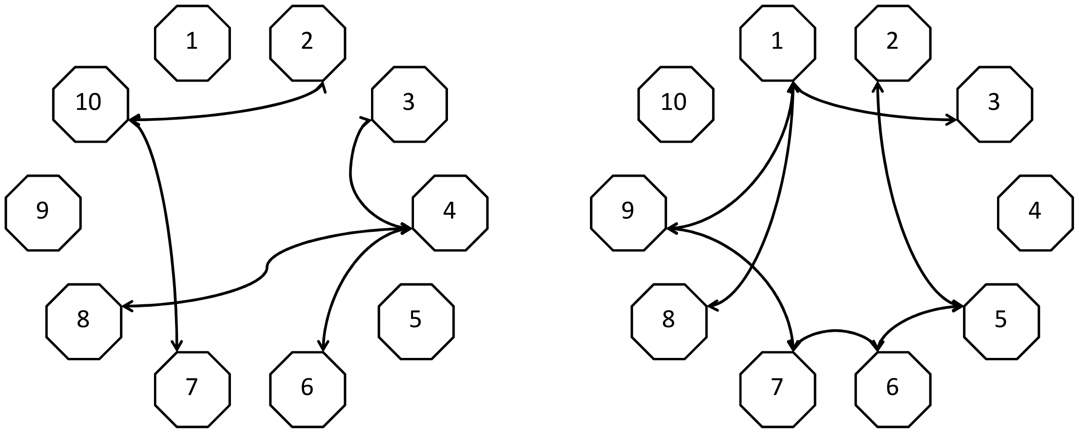

(a) First Connection graph, $N = 10$ oscillators (b) Second Connection graph, $N = 10$ oscillators

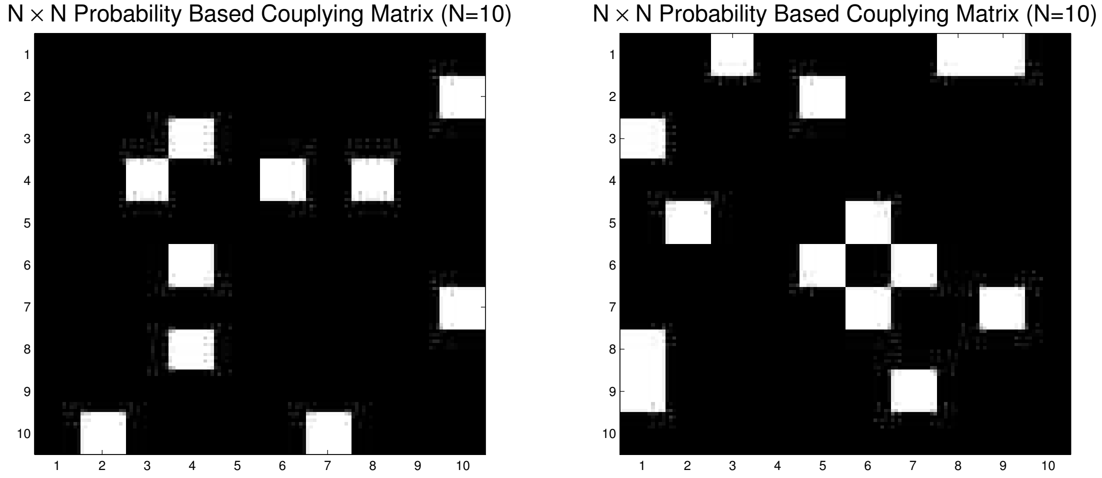

(c) Connection matrix for graph in 5.8(a) (d) Connection matrix for graph in 5.8(b)

Figure 5.8: Probabilistic connection matrices and associated graphs for networks of $N = 10$ clocks with probability of connection between clock i and clock j, $p_{ij} = 0.1$

α	α^3	Number of bits
0.1	10^{-3}	10
0.01	10^{-6}	20
0.001	10^{-9}	30

Table 5.5.1: Number of bits required to observe a network node at 3 hops from measurement site, dependent on coupling strength per hop, α

Certainly there is likely to be overlap, the 10^4 neurons with a hop number of 2 would be unlikely to connect to 10^4 unconnected neurons in the graph, and rather connect to some in the existing connected pool, however, this illustrates that the hop number for the brain is likely to be low.

The literature on graph theory analysis of cortical networks supports this. Interestingly, the universal finding from the literature is that cerebral cortical areas across mammal species are not randomly linked. Instead, cortical networks exhibit small world network characteristics [123]. That is, they do have short path lengths (hop number) in comparison to a network with regular ordered connection, however, these short path lengths are close to those found by purely random network connection as considered in the earlier analysis. The additional defining characteristic of small world networks is that they are more intricate than random in that they have a high *clustering coefficient* [124]. Cortical networks are strongly connected locally with fewer long range connections by comparison, creating densely connected local *clusters*. Yet the hop number between cortical regions is surprisingly small. Cortical connection behaves much like the classic example of small world network behaviour: the web of human acquaintances. This web has geographically local dense clusters and fewer long distance connections, yet the hop number between any two people is surprisingly small through a path of mutual acquaintances. An a indicator of order, a 2006 study on human brains suggests a mean global hop number of 2.49 as inferred using fMRI[125]. For an expected maximum hop number of 3, what would be the required number of bits to “see” all the nodes? Using 5.5.2 the findings are presented in Table 5.5.1 for various coupling magnitudes.

Table 5.5.1 presents practical numbers of bits for EEG machines, however it is important to note that these numbers of bits are based on what is necessary to see *each* node with path length of 3 *in isolation*. The prospect of attempting to see all 10^{10} nodes simultaneously is highly unlikely as we cannot possibly distinguish 10^{10} distinct angles within 2π with resolution 2^{10} or 2^{20} bits following on from the discussion in the preceding section. With 30 bits, 10^{10} equally separated angles would just fit in the range 2π with separation $\frac{1}{2^{30}}$, but this would not be the case in any real network where the eigenvalues (oscillation frequencies ± coupling perturbation) would not be exactly uniformly spaced and noise is present. The impact of noise on what we can observe is considered later in Chapter 6. The severity in loss of observability with increasing network order is discussed in the next section. We find that increased number of bits does not buy much observability when the size of the network is large.

5.5.2 Observability as a Function of Number of Bits

In this section we complete our observability analysis by considering the effect of the number of available bits. In our earlier simulations we used a conservative number of 10 bits. In a typical EEG machine for clinical usage, the signal is digitised with a resolution of 14 bits [34]. This would indicate that there is a range of 2^{14} levels available to represent the singular values from largest to smallest. Some recent research-oriented EEG machines have an A/D resolution of 24 bits [126]. Both these cases result in relatively few observable states as shown in Figure 5.9 particularly for larger network order. A geometrically decaying nearest neighbours coupling paradigm is chosen with maximum coupling strength of 0.1, clock frequencies are taken uniformly from the normalised range $0.001 - 1$. The measurement vector $\mathbf{C}$ is exponentially decaying, similar to those in Figure 5.7, with a decay of $e^{0.75n}$ where n is the distance (in number of clocks) from the measurement electrode.

Figure 5.9 has shown that the system is non-observable for all practical purposes due to the scale of the brain network. The two distinct slopes in the plot show that (a) for small network orders, observability halves per decade increase in the number of clocks in the network (b) for networks larger than 100 clocks, observability dramatically falls with a $\frac{1}{N}$ scaling law. This demonstrates that for all practical purposes observability from networked clocks is an illusion. It is important to note that the consequences of real measurement with a typical EEG machine are more severe than the limited observability with the clock model - the real brain-EEG interface suffers from the additional difficulty of noise. One can conservatively simulate the effect of noise as a reduction of the number of effective bits available. The plots shown also include the case of 10 bits to model the case of reduced apparent accuracy due to the presence of noise.

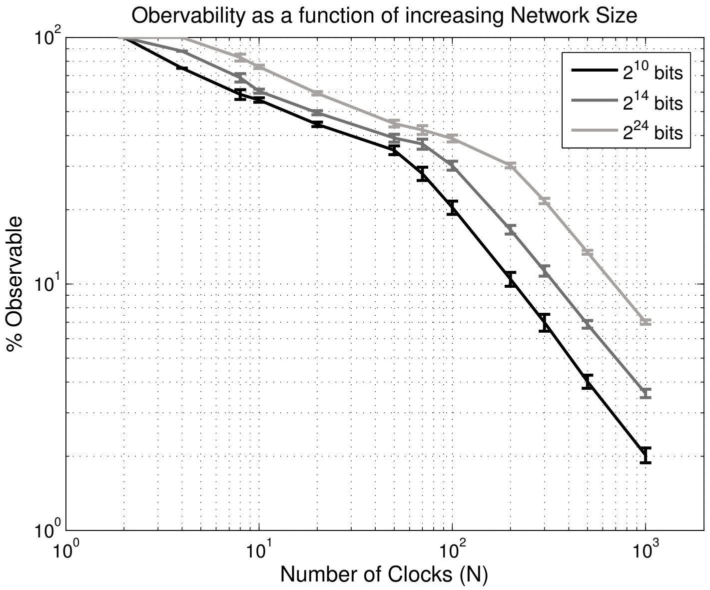

Figure 5.9: Percentage of states observable plotted against increasing networked size N. For networks larger than 100 clocks observability falls dramatically, with a $\frac{1}{N}$ scaling law, as the number of clocks increases.

The analysis in this section has been centred around observability based on the observability matrix $\mathcal{O}$. This only reveals what can be observed in the minimum time frame of N observations. The eigenvalues of the infinite observability gramian could be used to determine limits of observability for infinitely long observation time windows, however, as highlighted in Section 2.4, the EEG is inherently non-stationary and only short segments can be considered quasi-stationary for analysis. Having considered the effect of a finite resolution measurement, in the next section we look at the time constraints. The implications of observing longer time windows to attempt to average over the quantisation noise are discussed later in Chapter 6.

5.5.3 A Question of Time

Observation time is often discussed in the context of seizure prediction because brain dynamics are non-stationary [72, 127]. Certainly, any attempt to track the activity or dynamics of a system over time, based on a set of measurements, requires the underlying laws of nature not to change significantly over that analysis window. Here we wish to look at suitable time window durations from the point of view of bits of information.

One interpretation of the observation problem that is being highlighted in this section can be arrived at from purely counting what we actually measure. The brain is a system with, say, 10^{11} neurons [1]. For a standard EEG machine [34] with 10 bits per sample and 512 samples per second, the measurement rate is 5120 bits per second (bits/s) assuming the information is independent from sample to sample. If we had 64 electrodes or channels then the rate would increase by 5120×64 bits/s. Should we wish to observe just 1 bit of information about each neuron (i.e. 2 possible levels of activity per neuron - perhaps firing or not firing), then we would require 84 hours of EEG data. With estimates of EEG dynamical stationarity in the order of 10 seconds [68] this is clearly unrealistic. The fact that epilepsy is at all detectable from the EEG implies that it must correspond to a vastly simplified mode of behaviour in the brain, or be a localised brain issue with localised measurements.

We can also examine the reverse argument. Should we have 10 seconds of stationary data, and we use this to build a dynamical model for the current behaviour of the brain for the purpose of predicting its future behaviour, how many states can we detect? We use the term *state* in the dynamical systems sense, where each state variable describes the rate of change of a particular parameter. So a system with N states can be described by N first-order differential equations (or equally a single N^{th} order differential equation). By considering epilepsy to be a global network phenomenon perhaps our concern is to determine how many states we need to model the brain network. Of the 10^{11} neurons in the brain, 10^{10} reside in the cortex. Each neuron makes 10^4 connections [1], so the number of connections or network nodes in the brain is of the order 10^{14}. With our information rate of 5120×64 b/s we would have $5120 \times 64 \times 10$ bits in a 10 second quasi-stationary period. If we wish to describe the activity of each node over time (with only a single *state*!) to the accuracy of 10 bits (2^{10} discrete levels) then we could at most detect 5120×64 states. This is an upper bound as the effects of the inevitable noise and sample-to-sample dependence are not considered here. While this may seem a considerable number of 1^{st} order differential equations, it is sobering to think that this is just 0.0000003% of the total network. Can the brain activity network be adequately described by a model whose order is reduced by such a factor? Are the network dynamics of our brain indeed that simple? The prospect seems unlikely to us.

5.6 Discussion

We have shown that in the most ideal of situations, a very limited number of oscillators are observable from an EEG-like measure. Very few underlying oscillators are seen given the small coupling strengths we expect in the real brain. However, even for a reasonably large coupling strength we show how rapidly observability is lost as the size of our network increases. Figure 5.9 shows the percentage of observable states as a function of N, the number of clocks, when a single EEG measurement with resolutions K = 10,14 and 24 bits is used. This plot shows that observability rapidly falls off as the number of clocks in the network increases with approximately a $\frac{1}{N}$ scaling law. When K = 14, like in many typical EEG machines, less than 3% of all states can be reconstructed, even in a relatively small system with N = 1000 oscillators (2000 states). This is very limiting given that in a system such as the brain, where the number of neurons is in the order of 10^{11}, we expect to find a much larger number of oscillators than 1000! Thus the EEG does not unambiguously describe the generators of neural activity - even in an ideal situation where there is no noise, more than 97% of the oscillations cannot be identified. This is very much the best case scenario, introducing the challenges of a noisy measurement and the levels of observability will greatly decrease.

If the EEG was measured to infinite precision then the system would indeed be observable. However it is shown in Figure 5.9 that even with machinery that is sophisticated by today's standards (K = 24) the number of observable states only increases to just under 6%. Again this is an upper limit that declines significantly if noise is introduced into the model.

With relatively few states observable, the large scale measurements of EEG on both scalp and cortical surface are unlikely to reveal any underlying synchrony of oscillations as the number of underlying oscillators is far higher than the subset that is actually influencing the measure. Instead seizure prediction from synchrony increases would be better enabled via localised measurement, for example with micro-electrodes inserted into cortex or into deep brain structures.

In that case, why is epilepsy even detectable as a synchronous event via large scale EEG measures on the cortex and scalp? The results in this chapter imply the brain must be in an very advanced state of synchronisation across huge areas of cortex before we can see it in the EEG. By the time a sufficient number of oscillators have synchronised enough to observe this in the EEG it is most likely that the seizure would have already commenced. This may indicate why attempts at seizure detection have had more success with large scale EEG measures than was found for prediction [28].

The observability findings in this chapter are in stark contrast to the conventional assumptions that surround EEG measurement. Typical intracranial EEG electrodes or "macro-elecrodes" are assumed to have a recording domain in the order of 100μm [1, Ch. 4]. But for a large number of oscillations, only the largest amplitude and most spectrally distinct oscillations within this area will correspond to singular values above the measurement bit threshold. Therefore the results in this chapter indicate that we could see an oscillation located $100\mu m$ from an electrode *only if* all the other tissue was inactive. Thus, rather than observing all the activity in the 100μm radius, instead we observe only the dominant few percent of oscillations within this spatial area. Recent experimental results support these findings. A 2010 paper by Worrell *et. al.* [128] comparing the activity of micro-electrodes to nearby macro-electrode found that:

> *"Seizure-like events not detectable on clinical macroelectrodes were observed on isolated microelectrodes"*

and that

> *"clinical seizures begin from sub-millimetre scale epileptiform activity that spreads to neighbouring regions before a sufficient population of synchronously firing cells is recruited to be detectable on the macroelectrodes."*

These results were surprising and controversial results in clinical EEG as the amplitude of seizure like events on micro-electrodes was deemed to be sufficiently large to see on the nearby macro-electrode. These experimental findings provide experimental support to the theoretical work in the chapter.

Therefore we conclude that tracking the build up of synchronisation in the brain from scalp or cortical scale EEG is an ill-posed problem. The brain is not going to reveal its secrets by looking at large-scale EEG measures. More localised micro-electrode recordings may prove both a more useful measurement and open the possibility of intervention to prevent seizures, however, this presents a paradox in requiring precise knowledge of where to locate the electrodes.

5.7 Conclusion

With observability of a simple linear clock system proving an impossible task, it is highly unlikely that the more complex, real oscillatory system of the brain could be observable. To extend the observability argument beyond the simple linear systems case discussed in this chapter, both a stochastic argument and a non-linear argument follow in the next chapter.

5.7.1 Chapter Contribution

This chapter provides hitherto unavailable evidence that clinical EEG acquisition provides insufficient information for epileptic seizure prediction using linear observability theory. This is an important contribution to the field of epilepsy as it signals that the current approach to seizure prediction may well be mathematically invalid. This indicates the likelihood of need for a major paradigm change in seizure prediction efforts, however, encouragingly the results of this chapter do support *detection* for large scale epileptic events. Early detection may prove sufficient for a closed loop seizure prevention device.

Chapter 6

Stochastic and Non-linear Approaches to Observability in Network Clocks

Linear deterministic approaches to observability in networked clocks provided exceptionally poor results in Chapter 5. Can a linear stochastic or non-linear approach demonstrate more promise for observability in brain-like dynamics? We find this not to be the case in this chapter. The stocastic approach is considered using a Kalman Filter in Section 6.1, while the non-linear approach is considered with measure preserving maps in Section 6.3.

6.1 A Kalman Filter Approach to Observability in Network Clocks

The observability analysis in the previous chapter is centred on the observability matrix, $\mathcal{O}$. This tells us the extent of information observable from EEG given the minimum number of datapoints - given exactly N scalar measurements, can we solve for N states? The results indicate poor observability with only a fraction of the N states distinguishable given the expected constraints of biology and equipment.

The usual model of measurement that accompanies such observability matrix analysis is

$$y(t) = \mathbf{C}\mathbf{x}(t), \tag{6.1.1}$$

for time, t, an output measurement vector y, a linear weighting vector $\mathbf{C}$ and a state vector x. Note that $\mathbf{C}$ and y can be of matrix form to model multiple simultaneous measurements. Our earlier analysis in Chapter 5 also factored in quantisation as the addition of noise to the output. Thus equation 6.1.1 became,

$$y(t) = \mathbf{C}\mathbf{x}(t) + \nu(t), \tag{6.1.2}$$

where ν is the quantisation noise.

Perhaps we can do better with more data points? Any practical attempt to recover dynamics would never explicitly use the observability matrix with just N simultaneous equations to solve for N states given N measurements. Additional equations will not, however, supply new degrees of freedom. The $(N+1)^{st}$, $(N+2)^{nd}$ and $N+n^{th}$ equations will be somehow related to the existing N equations of the observability matrix. Therefore the observability matrix does tell us the fundamental limitations to observability in a system. The issue with just using N equations is that measurement noise may well cripple any practical ability to estimate the states. Instead, assuming some degree of stationarity in the system, a Kalman filter could be applied, using more than N datapoints to average over the noise.

The question for this section is: Can time-averaging be used to suppress noise in EEG? The results show, perhaps surprisingly, that a Kalman filter buys no significant improvement in observability for this particular class of systems. Filtering does not provide a more reliable state estimate.

6.2 The Measurement Model

To begin the classical system and measurement model in a Kalman Filter can be expressed as,

$$\mathbf{x}_{k+1} = \mathbf{A}\mathbf{x}_k + \upsilon_k \tag{6.2.1}$$

$$y_k = \mathbf{C}\mathbf{x}_k + \nu_k, \tag{6.2.2}$$

for discrete time k, state vector $\mathbf{x}$, stable system matrix, $\mathbf{A}$, measurement vector y, measurement matrix, $\mathbf{C}$, state noise υ and measurement noise ν.

6.2.1 The Classical System Model Fails for a Network of Clocks

We consider the model of state evolution, $\mathbf{x}_{k+1}$ in equation (6.2.1) for the specific case of networked clocks. The main issue is that such systems, with habitation on the boundary of stability, are not strictly stable. For simplicity and to gain some insight, the scalar case is presented first, followed by an extension to the full vector model.

The Scalar Case

Consider the scalar system:

$$x_{k+1} = ax_k + \upsilon_k, \; E[x_0] = 0. \tag{6.2.3}$$

υ_k is the system noise with zero-mean, $E\left[\upsilon_k\right] = 0$, and variance, $E\left[\upsilon_k^2\right] = \sigma_\upsilon^2$. The noise at time k is not correlated to noise at any other sample time, $E\left[\upsilon_k \upsilon_{k-\ell}\right] = 0, \; \forall \; \ell \neq 0$. The variance associated with the $(k+1)^{th}$ state, $E\left[(x_{k+1})^2\right]$[1], evolves as:

$$\begin{aligned} E\left[(x_{k+1})^2\right] &= E\left[(ax_k + \upsilon_k)^2\right] \\ &= a^2 E\left[(x_k)^2\right] + 2aE\left[\upsilon_k x_k\right] + E\left[(\upsilon_k)^2\right] \\ &= a^2 E\left[(x_k)^2\right] + E\left[(\upsilon_k)^2\right] \; \because \; x_k \text{ and } \upsilon_k \text{ are uncorrelated.} \\ &= a^2 E\left[(x_k)^2\right] + \sigma_\upsilon^2. \end{aligned} \tag{6.2.4}$$

By recursion, the expected value of state variance after ℓ samples is

---

[1] Variance of $(k+1)^{th}$ state is $E\left[(x_{k+1} - E\left[x_{k+1}\right])^2\right] = E\left[(x_{k+1})^2\right]$ under the condition that $E\left[x_{k+1}\right] = 0$. For the vector case $E\left[x_{k+1}\right] = E\left[\mathbf{A}x_k + \upsilon_k\right] = E\left[\mathbf{a}x_k\right] + E\left[\upsilon_k\right] = E\left[\mathbf{A}x_k\right] = \mathbf{A}E\left[x_k\right] = 0$.

$$\begin{aligned} E\left[(x_{k+\ell})^2\right]|_{a\neq 1} &= a^{2\ell}E[(x_k)^2] + \left(\frac{1-a^{2\ell}}{1-a^2}\right)\sigma_\upsilon^2, \\ E\left[(x_{k+\ell})^2\right]|_{a=1} &= E[(x_k)^2] + \ell\sigma_\upsilon^2. \end{aligned} \tag{6.2.5}$$

For $|a| < 1$ the system is stable, $|a| > 1$ the system is unstable and $|a| = 1$ the system operates on the stability boundary. For large ℓ, the stable case has bounded variance while the variance of the unstable case grows exponentially to ∞.

Stable, $(|\mathbf{a}| < \mathbf{1})$ $\lim_{\ell\to\infty} E[(x_{k+\ell})^2] = \left(\frac{1}{1-a^2}\right)\sigma_\upsilon^2$.

Unstable, $(|\mathbf{a}| > \mathbf{1})$ $\lim_{\ell\to\infty} E[(x_{k+\ell})^2] = \infty$.

Marginally Stable, $(|\mathbf{a}| = \mathbf{1})$ $\lim_{\ell\to\infty} E[(x_{k+\ell})^2] = \lim_{\ell\to\infty} E[(x_k)^2] + \ell\sigma_\upsilon^2 = \infty$.

We are interested in the change of variance right on the stability boundary $|a| = 1$ as this is where the eigenvalues of networked clocks lie. Here, the state variance grows linearly with time with the rate of growth set to the noise variance σ_υ^2. An unbounded (in the limit) state variance indicates that we do not have a suitable model in 6.2.3. The brain system is stable so a state with unbounded variance does not describe brain dynamics adequately. Therefore we consider $\upsilon_k = 0$ and a non-standard model with only measurement noise:

$$x_{k+1} = ax_k \tag{6.2.6}$$

$$y_k = cx_k + \nu_k, \tag{6.2.7}$$

The State Noise Model: Extension to the Vector Case

Extending the model in (6.2.9)to the vector case gives:

$$\begin{aligned} \mathbf{x}_{k+1} &= \mathbf{A}\mathbf{x}_k,\ E[x_0] = 0,\ E[x_0x_0^{'}] = Q_0. && (6.2.8) \\ y_k &= \mathbf{C}\mathbf{x}_k + \nu_k, && (6.2.9) \end{aligned}$$

Kalman Filter

The true state, $\mathbf{x}$, is not accessible as this is the variable we are attempting to recover from EEG data. It follows that their variance $E\left[\mathbf{x_k}\mathbf{x_k}'\right]$ is equally inaccessible. Instead we can find the error between the true state $\mathbf{x}$ and our estimate, denoted $\hat{\mathbf{x}}$, and its associated error covariance, $E\left[(\mathbf{x}-\hat{\mathbf{x}})(\mathbf{x}-\hat{\mathbf{x}})'\right]$.

Our system and measurement model is:

$$\mathbf{x}_{k+1} = \mathbf{A}\mathbf{x}_k \tag{6.2.10}$$

$$y_k = \mathbf{C}\mathbf{x}_k + \nu_k. \tag{6.2.11}$$

The simplest estimate of $\mathbf{x}$ is to use the model in equation 6.2.10, and tweak our estimate result with the corresponding output error.

$$\hat{\mathbf{x}}_{k+1} = \mathbf{A}\hat{\mathbf{x}}_k + \mathbf{H}_k(y - \hat{y}), \tag{6.2.12}$$

where $\mathbf{H}_k$ is any appropriate gain. A Kalman filter is one where $\mathbf{H}_k$ is designed to be optimal in minimising the trace of the error covariance, this optimal $\mathbf{H}_k$ will be denoted $\mathbf{K}_{f,k}$.

The Kalman filter [129] operates in a recursive manner to solve the Riccati equation for the covariance matrix. $\mathbf{P}_{k|k}$ is the *a posteriori* covariance at time k given all the data up to time k. It obeys the following recursion:

$$\begin{aligned}\mathbf{P}_{k|k} &= E[(\mathbf{x}_k - \hat{\mathbf{x}}_{k|k})(\mathbf{x}_k - \hat{\mathbf{x}}_{k|k})'] \\ &= \mathbf{P}_{k|k-1} - \mathbf{P}_{k|k-1}\mathbf{C}^{'}\left[\mathbf{C}\mathbf{P}_{k|k-1}\mathbf{C}^{'} + \mathbf{R}_\nu\right]^{-1}\mathbf{C}\mathbf{P}_{k|k-1}\end{aligned} \tag{6.2.13}$$

$\mathbf{R}_\nu$ is the covariance of the measurement error, $\nu_k \in N(0, \mathbf{R}_\nu)$. The predicted estimate of $\mathbf{x}$ at time k is denoted $\hat{\mathbf{x}}_{k+1|k}$, indicating that this is an *a priori* estimate of the state at the next time step, $(k+1)$, given the data up to and including time step k. This *a priori* estimate is related to $\hat{\mathbf{x}}_{k|k}$ through the state model in 6.2.36,

$$\hat{\mathbf{x}}_{k+1|k} = \mathbf{A}\hat{\mathbf{x}}_{k|k}. \tag{6.2.14}$$

The associated *a priori* error covariance, $\mathbf{P}_{k+1|k} = E[(\mathbf{x}_{k+1} - \hat{\mathbf{x}}_{k+1|k})(\mathbf{x}_{k+1} - \hat{\mathbf{x}}_{k+1|k})']$, is related to $\mathbf{P}_{k|k}$ through:

$$\mathbf{P}_{k+1|k} = \mathbf{A}\mathbf{P}_{k|k}\mathbf{A}'. \tag{6.2.15}$$

where $\mathbf{P}_{k|k}$ is the *a posteriori* error covariance in 6.2.13 and with $\hat{\mathbf{x}}_{k|k}$ denoting the updated state estimate. This updated estimate of $\mathbf{x}$ at time k is an *a posteriori* estimate of the state at the current time step, k, given the data up to and including time k. The update is formed with the last predicted state estimate plus a correction term based on the residual error found with the last predicted state estimate.

$$\hat{\mathbf{x}}_{k|k} = \hat{\mathbf{x}}_{k|k-1} + \mathbf{K}_{f,k}\underbrace{\left(y_k - \mathbf{C}\hat{\mathbf{x}}_{(k|k-1)}\right)}_{\text{“innovation”}}, \tag{6.2.16}$$

where $\mathbf{K}_{f,k}$ is the Kalman gain. The Kalman gain adjusts the relative importance of the innovation.

$$\mathbf{K}_{f,k} = \mathbf{P}_{k|k-1}\mathbf{C}'\left(\mathbf{C}\mathbf{P}_{k|k-1}\mathbf{C}' + \mathbf{R}_\nu\right)^{-1}. \tag{6.2.17}$$

Expressing the covariance entirely in an *a posteriori* fashion can be achieved by substituting equation 6.2.15 in 6.2.13, giving:

$$\mathbf{P}_{k|k} = \mathbf{A}\mathbf{P}_{k-1|k-1}\mathbf{A}' - \mathbf{A}\mathbf{P}_{k-1|k-1}\mathbf{A}'\mathbf{C}'\left[\mathbf{C}\mathbf{A}\mathbf{P}_{k-1|k-1}\mathbf{A}'\mathbf{C}' + \mathbf{R}_\nu\right]^{-1}\mathbf{C}\mathbf{A}\mathbf{P}_{k-1|k-1}\mathbf{A}'. \tag{6.2.18}$$

Assuming the limit for $k \to \infty$ exists, $\mathbf{P}_{k-1|k-1} \approx \mathbf{P}_{k|k} \approx \mathbf{P}_\infty$. Using $\mathbf{P}_{k-1|k-1} = \mathbf{P}_{k|k} = \mathbf{P}_\infty$ we can rewrite (6.2.18) as:

$$\mathbf{P}_\infty = \mathbf{A}\mathbf{P}_\infty\mathbf{A}' - \mathbf{A}\mathbf{P}_\infty\mathbf{A}'\mathbf{C}'\left[\mathbf{C}\mathbf{A}\mathbf{P}_\infty\mathbf{A}'\mathbf{C}' + \mathbf{R}_\nu\right]^{-1}\mathbf{C}\mathbf{A}\mathbf{P}_\infty\mathbf{A}'. \tag{6.2.19}$$

To gain some insight, let us consider the scalar case. We can consider the solution for a first order system ($\mathbf{A} = a = 1, \mathbf{C} = c = 1$). Using,

$$x_{k+1} = x_k = x_0,\ E[x_0] = 0,\ E[x_0^2] = Var[x_0] = \sigma_0^2 > 0 \tag{6.2.20}$$

$$y_k = x_k + \nu_k, \tag{6.2.21}$$

the covariance matrix in (6.2.18) reduces to:

$$P_{k|k} \quad = \quad P_{k-1|k-1} - P_{k-1|k-1}\left[P_{k-1|k-1} + R_\nu\right]^{-1} P_{k-1|k-1}. \tag{6.2.22}$$

If we let $P_{0|k} = 1$, the recursion of equation (6.2.22) results in:

$$P_{k+\ell|k+\ell} = \frac{R_\nu}{R_\nu + \ell} = \frac{1}{1 + \frac{\ell}{R_\nu}}. \tag{6.2.23}$$

For quantised noise,

$$R_\nu = \frac{\Delta^2}{12}, \tag{6.2.24}$$

where Δ is the maximum quantisation error [130, p 29]. For a 10−bit normalised measurement, $\Delta = \frac{1}{2^{10}}$. Therefore R_ν is a small number in the order of 10^{-7}. It follows that $P_{k+\ell|k+\ell}$ will decay to zero and the state is well estimated in this case.

For additional insight, consider the vector case for a single clock (2 states) with a single output measurement which has similar properties to the scalar case. For a normalised frequency, $\omega = 1$ we have,

$$\mathbf{A} = \begin{pmatrix} 0 & -1 \\ 1 & 0 \end{pmatrix}, \tag{6.2.25}$$

and

$$\mathbf{C} = \begin{pmatrix} 0 & -1 \end{pmatrix}, \tag{6.2.26}$$

If we let $P_{k|k} = \mathbf{I}$ (where $\mathbf{I}$ is the identity), the recursion of the covariance matrix in (6.2.18) reduces to:

$$\mathbf{P}_{k+2\ell|k+2\ell} \quad = \quad \mathbf{I}\left(\frac{1}{1 + \frac{\ell}{R_\nu}}\right), \tag{6.2.27}$$

for all ℓ. Given equation 6.2.24, it follows that for the two-state vector case, similarly to the scalar case, $P_{k+\ell|k+\ell}$ will decay to zero as $\ell \to \infty$ and the pair of states are well estimated in this case [2]. Although this vector example is for a single uncoupled clock, importantly, given that the coupled oscillator network can be transformed to an equivalent diagonalised system that is also purely oscillatory (eigenvalues of coupled system remain purely imaginary), as detailed in Section 5.4.2, the analysis of this 2-dimensional vector case for a pure clock can allow for reasonable inferences towards the higher dimensional coupled oscillator network.

Having considered how well one measurement with low R_ν can be used to find both (*i*) a single state (in the scalar example) and (*ii*) a small number of states (in the vector example for a two state clock), the natural next step is to consider how one measurement with low R_ν can be used to find a large number of states. The fundamental concern here is how the powers of a Kalman filter scale with increasing number of states while the measurement remains scalar (or at least low dimensional). This will be explored through simulation in the next section, however, here an analogous situations can be considered analytically in the scalar case. That is the case where R_ν is no longer much less than the order of the state we are attempting to estimate for a scalar constant state and scalar measurement. Consider:

$$x_{k+1} \equiv a \tag{6.2.29}$$

$$y_k = x_k + \nu_k, \tag{6.2.30}$$

where the variance of ν_k is $R_\nu = a^2$ and $E(\nu_k) = 0$. Therefore, the standard deviation of the measurement noise, a, is of the same order of the state. The Kalman estimate, $\hat{x}$ in this case simply reduces to the standard mean:

---

[2] Note that more generally for

$$\mathbf{A} = \begin{pmatrix} 0 & -\omega \\ \omega & 0 \end{pmatrix}, \tag{6.2.28}$$

we have the following: By converting to a digital sampled system with normalised sample period $T = 1$ (refer to Section 5.4.2 for sample period justification) we obtain $\mathbf{A} \to e^{\mathbf{A}T}$. Letting, $\mathbf{A}_{digital} = e^{\mathbf{A}T} = \begin{pmatrix} cos(\omega) & -sin(\omega) \\ sin(\omega) & cos(\omega) \end{pmatrix}$, and using the recursion equation in 6.2.18 we find for $\omega = \frac{\pi}{n}$ that with every ℓ a multiple of n we have, for an initial $\mathbf{P}_{0|0} = \mathbf{I}$, that $P_{k+\ell|k+\ell}$ is again a scalar times the identity: $P_{k+\ell|k+\ell} = \mathbf{I}\left(\frac{1}{1+\frac{\ell}{R_\nu}}\right)$.

$$\begin{aligned} \hat{x}_k &= \frac{1}{N}\sum_{k=1}^{N} y_k && (6.2.31) \\ &= a + \frac{1}{N}\sum_{k=1}^{N} \nu_k && (6.2.32) \end{aligned}$$

The expected value of the estimate gives the true state:

$$E\left[\hat{x}_k\right] = a \qquad (6.2.33)$$

since $E(\nu_k) = 0$. However the variance of the estimate is dependent on the number of samples N.

$$\begin{aligned} Var\left[\hat{x}_k\right] &= E\left[\left(\frac{1}{N}\sum_{k=1}^{N}\nu_k\right)^2\right] \\ &= E\left[\left(\frac{1}{N}\right)^2\right] E\left[\left(\sum_{k=1}^{N}\nu_k\right)^2\right] \\ &= \left(\frac{1}{N^2}\right)(NR_\nu) \\ &= \frac{R_\nu}{N} \\ &= \frac{a^2}{N} && (6.2.34) \end{aligned}$$

and it follows that the standard deviation of $\hat{x}_k$ is $\frac{a}{\sqrt{N}}$. With N limited to around 5000 due to stationarity considerations we are limited in how well we can recover the states. With 5000 samples, the standard deviation of the state estimate error only reduces by a factor of $\sqrt{(}5000) \approx 70$. Extrapolating to the vector state case, reducing the standard deviation of the measurement error by a factor of 70 will not make significant inroads in estimating across a large number of states.

We are particularly interested in the gain between $\mathbf{P}_{k|k}$ (or $Var\left[\hat{x}_k\right]$ for the previous scalar example) and $\mathbf{R}_\nu$. In matrix form this could be represented as a gain $\mathbf{G}$ such that, $\mathbf{P}_{k|k} = \mathbf{G}\mathbf{R}_\nu\mathbf{G}'$. $\mathbf{G}$ tells us how much better we can estimate the state than we can measure y. The EEG measurement y is limited due to quantisation noise. It is anticipated that when operating on the margins of stability with systems of large order, any measurement noise at the output will exasperate attempts to converge to a good state estimate. Extrapolating from the scalar case, it seems that our gain $\mathbf{G}$ is proportional to $\frac{1}{N}$ indicating that we can only estimate the states to within an error margin that is directly proportional to the number of sample points. As the number of states to be estimated increases this becomes a severely limiting factor. This implies that throwing more data at our Kalman filter to the limits of stationarity will not improve our state estimate and the limited observability results in Chapter 5 stand.

The performance of a Kalman Filter, $\mathbf{K}_f$ and associated variance gain, $\mathbf{G}$ is explored through simulation in section 6.2.2. As expected from the analysis in this section, these simulations show that while small networks can be reasonably well-estimated from a single measurement, this will not scale adequately. For large networks the poor gain in reduction of error variance over recursions of the Kalman filter become problematic and it is impossible to obtain reasonable estimates of the states without vast quantities of data, far exceeding what is available.

6.2.2 Simulation Results

The ability of a Kalman Filter to estimate states in a coupled clock network is investigated in this section. The Kalman filter is tasked with estimating the associated amplitude and phase for each oscillator. The results show that a Kalman Filter can reliably estimate the states in small networks. For a network of 10 clocks, the Kalman filter struggles to obtain reasonably accurate estimates within the stationarity window for EEG, taken to be 10 seconds of data. By network orders in the range of 100 clocks, the variance of the estimate is of similar order to the amplitude variation of the states we are trying to measure, and the Kalman estimator fails.

Simulation Set-up

To simulate the ability to estimate the states of a networked clock system, the iterative Kalman Filter is employed. The system model used the following formulation, as justified in Section 6.2,

$$\mathbf{x}_{k+1} = \mathbf{A}\mathbf{x}_k \tag{6.2.35}$$

$$y_k = \mathbf{C}\mathbf{x}_k + \nu_k. \tag{6.2.36}$$

In order to maintain continuity with analysis of Chapter 5, while simultaneously generating normalised EEG (with signal magnitude of 1) the following system parameters were applied. The natural frequencies of the undamped clocks were uniformly distributed across a normalised range of $0.01 - 1$, with a system matrix $\mathbf{A}$, converted to digital form from equation 5.4.17 in Chapter 5. Coupling was chosen to be distance-based geometrically decaying as illustrated in Figure 5.6 of Chapter 5. This generates uncoupled clock signals that oscillate with a maximum amplitude of 1, with coupled oscillations fluctuating minimally from this while remaining of order 1. The entries of the measurement vector $\mathbf{C}$ form a convex set as modelled by,

$$\mathbf{C} = \left[\begin{array}{cccccc} 0 & \delta_1 & 0 & \delta_2 \dots & 0 & \delta_N \end{array} \right]. \tag{6.2.37}$$

where $(\delta_i \geq 0, \sum_i \delta_i = 1)$. $\delta_i \geq 0$ indicates the relative contribution clock i makes in the EEG output signal. A uniform measurement of $\delta_i = \frac{1}{N}$ was assigned. Therefore the EEG signal has a maximum magnitude or order 1 and is easily quantised with $K = 10$ bits to $2^{10} = 1024$ levels between ± 1. ν_k is the quantisation noise.

In Chapter 5, we investigated the percentage of a network with N clocks we can expect to observe given the minimum number of measurements $(2N)$. Here simulations were run for measurements exceeding the $2N$ minimum, but the number of measurements was limited in line with EEG stationarity considerations. This upper limit was 5000 Kalman filter iterations, showing the performance of the filter within a stationarity time limits of approximately 10 seconds (with 512Hz sampling). Initial conditions were assigned randomly, in the range $[-1, 1]$, to each state.

Simulation Results

While the performance of the iterative Kalman filter provided near perfect estimation of the states for *small* networks, performance declined rapidly with increasing network order. Figure 6.1 shows a comparison of the true state x_k with Kalman estimate $\hat{x}_k$ at each iteration time step, k, for various network sizes. For a network of 2 clocks ($N = 2$) the estimate aligns almost perfectly with the true state after a small number of Kalman filter iterations. When the network is expanded to just 10 clocks ($N = 10$), the number of iterations for the Kalman filter required to arrive at an accurate estimate is longer than the $N = 2$ case as expected, with some error remaining after 5000 iterations. By further expanding the network to 100 clocks ($N = 100$) there is a marked degradation in performance, while the error between true state and estimate is reducing slowly over iterations of the filter, the error remains quite large by $k = 5000$. Note that the higher frequency oscillation as visible in the state shown from the $N = 10$ simulation is simply due to coupling from nearby clocks.

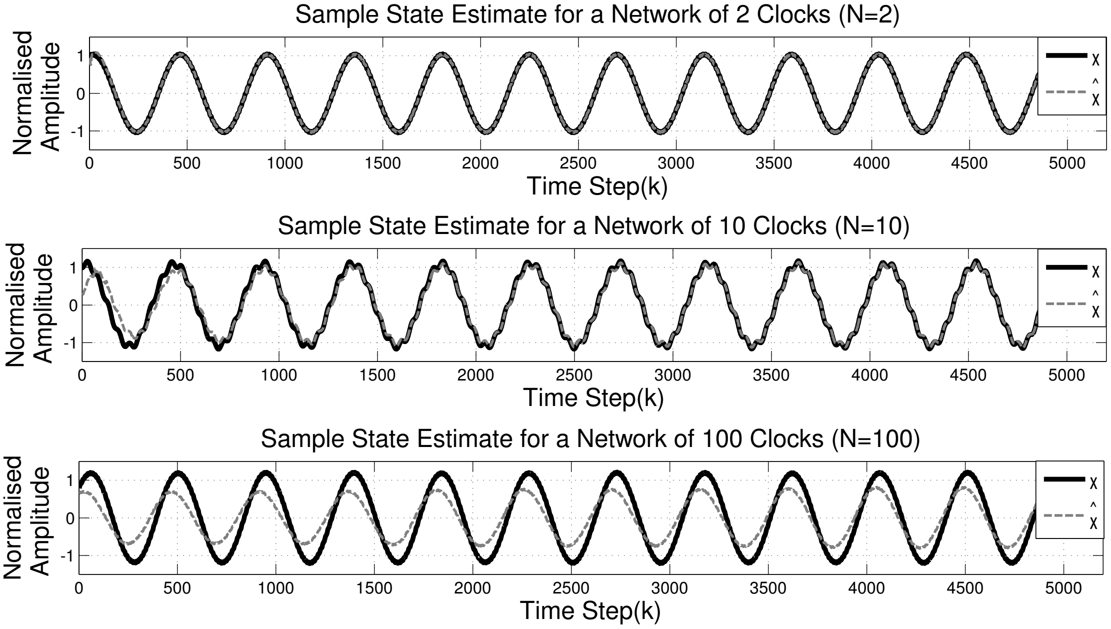

Figure 6.1: Comparison of true state x_k with Kalman estimate $\hat{x}_k$ at each iteration time step, k. Plots showing networks of 2, 10 and 100 clocks are shown as $N = 2, N = 10, N = 100$.

The comparison of the true state x_k with Kalman estimate $\hat{x}_k$ just discussed and illustrated in 6.1 looks at just one state (of $2N$ possible states) from the network. While this provides sample results it does not convey the distribution across the states in the Kalman filter. As expected in larger networks from Chapter 5, some states are well-observed in the EEG (and therefore well estimated by the Kalman Filter) while others are less so. The specific set of states that find themselves well-observed is a function of the initial conditions. This distribution is illustrated in Figure 6.2 between two states in a network of 100 clocks.

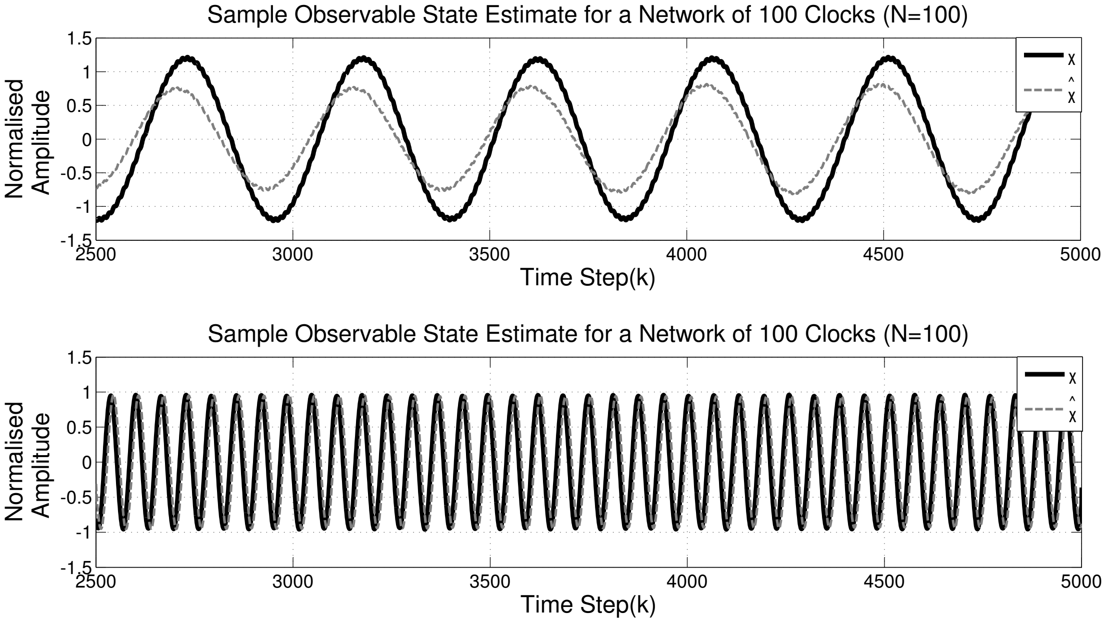

Figure 6.2: Comparison of true state x_k with Kalman estimate $\hat{x}_k$ at each iteration time step, k, in a network of $N = 100$ clocks. The upper trace shows a poorly estimated state, contrasting with a well estimated state in the lower trace.

The overall Kalman Filter performance as a function of increasing network order can be gauged by considering the *average* performance across states. The trace[3]of the covariance matrix $\mathbf{P}_{(k|k)}$ provides a good measure of this average behaviour. The diagonal elements of the covariance matrix indicate how well the Kalman filter is estimating the states. The i^{th} diagonal entry is the error variance for the i^{th} state. Small diagonal elements correspond to well-estimated states. The off diagonal elements represent the error cross variances between states which should become close to zero after a few iterations of the Kalman equations as the state errors are uncorrelated to each other.

---

[3] The trace of a matrix is the sum of its diagonal elements.

To visualise the Kalman filter at work, the progression of the trace of the covariance matrix together with the Kalman gain over iterations, k, are shown in Figure 6.3. The upper plot shows the normalised traces, $(Trace(\mathbf{P})/2N)$, while the lower plot shows the Kalman gain, K_f of the 1^{st} state for network orders of 2, 10 and 100 clocks. Note the Kalman gain for $N = 100$ is a moving average to aid visualisation by showing the trend without rapid local variations in signal. For a two clock network $(N = 2)$ the Kalman gain adjusts in the early timesteps such that the signal is well estimated (small trace) in just 200 iterations of the Kalman equations. In contrast, the 10 clock network, $(N = 10)$, takes the full 10 seconds of EEG data to reduce the trace to the same level. For the larger network of 100 clocks, the Kalman filter estimates the 200 states in the network very poorly with a very limited reduction in trace over the 10 seconds of EEG data and a Kalman gain that is very slowly increasing.

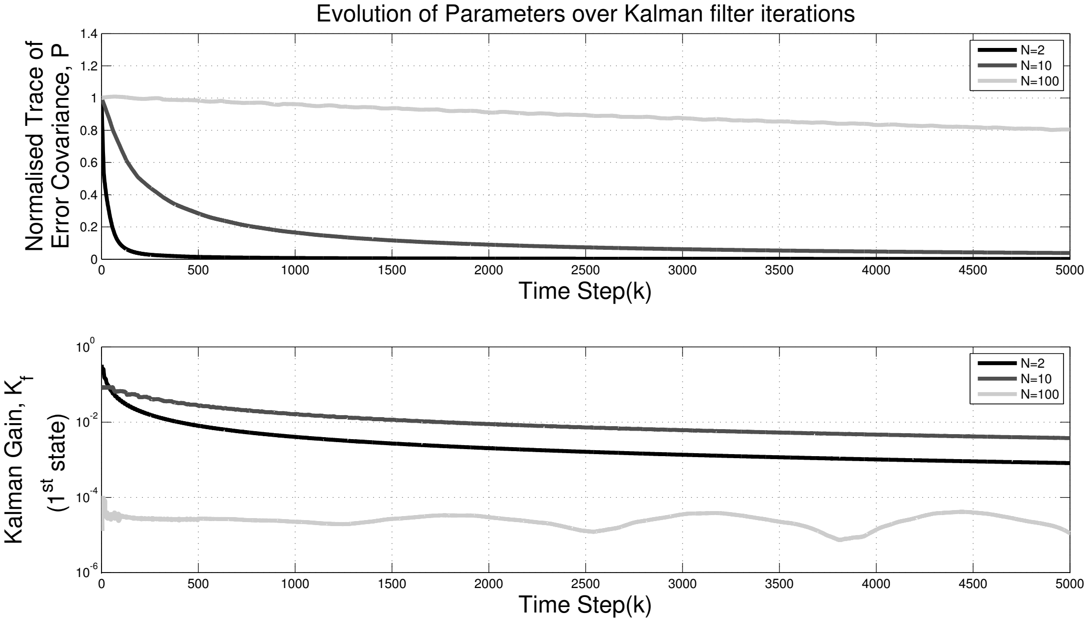

Figure 6.3: The Kalman Filter at work over k iterations. The upper trace shows the normalised trace of covariance matrix for networks with $N = 2, 10, 100$ clocks, illustrating the average performance of the filter over all states. The lower trace provides a snapshot of corresponding gain behaviour with the Kalman gain for just the 1^{st} state plotted for each network size.

From Figure 6.3 there is a clear degradation of estimation performance as the size of the system, N grows. This is as expected, however, the transition at which the network is largely unobservable is startling. This is shown in the sigmoidal behaviour of Figure 6.4. This plot shows that for networks of order greater than 100, the average state error variance approaches 1 after numbers of data samples appropriate to the stationarity limit of EEG. The system was constructed in a normalised fashion such that the states we are attempting to estimate are oscillations between limits of approximately ±1. An estimate with a variance of 1 for a signal with an amplitude of 1 is a complete failure as an estimate.

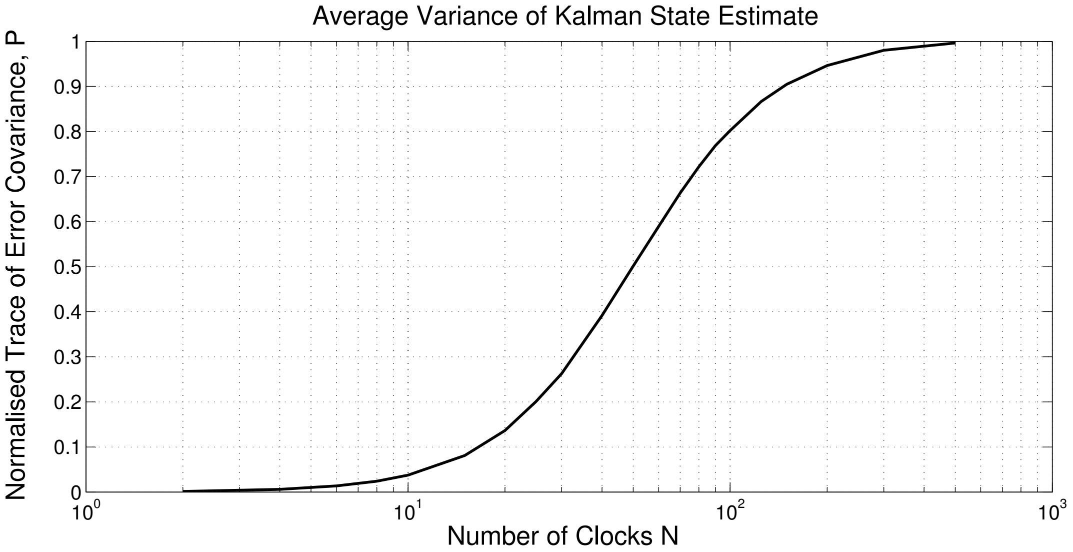

Figure 6.4: The normalised trace of the covariance matrix, P after iterating through 10 seconds of EEG data (5000 samples) against increasing network order, N

Statistics of Quantisation Noise

It is important to note that the findings in this chapter are based on using the Kalman filter in an environment very close to the optimal environment for which it was designed. The Kalman filter is optimally designed under the assumption that the observation noise, ν_k, is zero mean Gaussian white noise. In this chapter ν_k is purely quantisation noise. Quantisation noise approximates zero mean Gaussian white noise for sufficiently high quality quantised signals. Here 3-bit quantisation (2^3 levels) and 10-bit quantisation (2^{10} levels) are compared.

Figure 6.5 illustrates the quantisation of a sinusoid. For 3-bit quantisation the error signal is a structed time-series resulting in distinct peaks in the frequency spectrum above the white noise floor. For 10-bits, however, the error appears “random” and the frequency spectrum is almost unaffected. For our purposes the EEG is quantised with between 10-24 bits, therefore the quantisation error closely approximates zero mean Gaussian white noise and the Kalman filter is aptly applied.

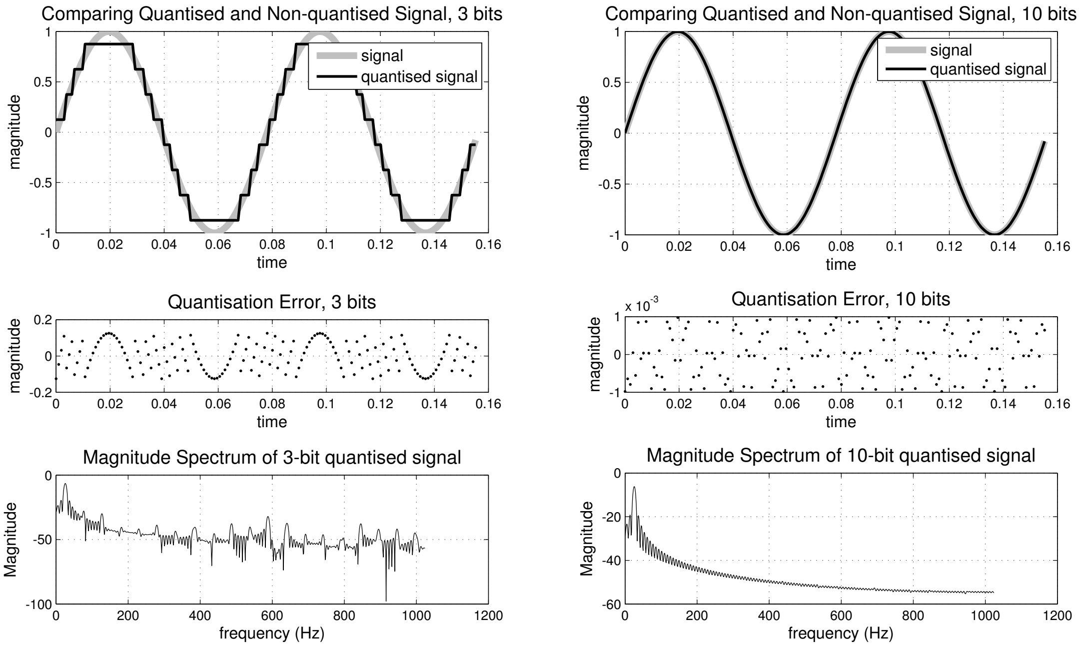

Figure 6.5: Comparing 3-bit and 10-bit quantisation noise. For 10-bits the noise looks “random” unlike at 3 bits where a very structured error time-series is formed. The spectrum for the quantised 10-bit signal is near identical to the original non-quantised signal, while for 3-bits there are distinct peaks in the spectrum above the noise floor.

Lessons from Kalman Estimation

The overriding conclusion from attempts at Kalman estimation is that more data brings little improvement to the amount of information extracted about the underlying system.

Operating at the margins of stability, the gain in how well we can estimate the states $\mathbf{x}$ from the measurement y is particularly poor. It is so poor that throwing more data at our filter fails to make effective inroads in error covariance reduction. Certainly, within the constraints of stationarity a Kalman filter will not reveal the secrets of an oscillatory system with state dimension significantly larger than the dimension of the measurement.

Having considered the stochastic approach, we next consider a non-linear argument.

6.3 Non-linear Extensions - Measure Preserving Maps

Having considered the inability of a Kalman filter to overcome measurement noise to estimate the underlying states of the system, in this section we use tools from ergodic theory (measure preserving maps) and information theory (entropy) to establish if there is something we have overlooked in the linear models and stochastic approaches discussed so far. In effect what is under investigation here is the "gain" in error reduction over the mapping function for both linear clocks and non-linear oscillators. The findings are consistent with the earlier analyses of Chapter 5 and in Section 6.2.2: extended analysis of EEG signals will not estimate the underlying states of brain oscillations, even if the underlying system was stationary for an extended period. Most importantly, while the observability matrix analysis applied only to linear system, ergodic theory can be extended to the non-linear case.

6.3.1 Entropy of Measure Preserving Maps

Ergodic theory is concerned with dynamical systems with an *invariant* measure [131]. Consider a measurable set, X, and a sigma-algebra, Σ[4]. For our purposes $X \in \mathbb{R}^N$ is the set of all possible states, and Σ is a collection of subsets of the state space. A measure μ on (X, Σ) is invariant under the mapping function $f(X \rightarrow X)$ if for every measurable set S in Σ:

$$\mu\left(f^{-1}\left(S\right)\right) = \mu\left(S\right). \tag{6.3.1}$$

We will concentrate on *Lebesgue* measures which correspond to the "standard" measures of space within Euclidean geometry: length in $\mathbb{R}^1$, area in $\mathbb{R}^2$, volume in $\mathbb{R}^3$ and so on.

---

[4] A sigma-algebra, Σ, over X is a collection of subsets of X where *(i)* for $S \in \Sigma$, its complement, $\overline{S}$, is also in Σ, *(ii)* the countable unions of sets in Σ are also in Σ, i.e. for $S_1, S_2 \in \Sigma \Rightarrow S_1 \cup S_2 \in \Sigma$ and *(iii)*

A mapping function f,

$$\mathbf{x}_{k+1} = f(\mathbf{x}_k), \tag{6.3.2}$$

for a vector of states $\mathbf{x} \in \mathbb{R}^N$, is considered to be *measure preserving* if a measure on set $\mathbf{x}_k \in S_k \subset \mathbb{R}^N$ is equivalent to the measure on the set $\mathbf{x}_{k+1} \in S_{k+1} \subset \mathbb{R}^N$ after mapping.

Entropy of a map, f, is the gain in state uncertainty over iterations of the map. If we take a measure y_k where,

$$\begin{aligned} \mathbf{x}_{k+1} &= f(\mathbf{x}_k) & (6.3.3) \\ y_k &= g(\mathbf{x_k}) + \nu, & (6.3.4) \end{aligned}$$

for some function g and we measure y with some uncertainty or error ν, entropy of the map f tells us how much the uncertainty reduces as we consider multiple mappings $\{x_k \to x_{k+1} \to \ldots\}$. Should we have a single state system, $\mathbf{x} = x$, with a single measurement y_k we can estimate x within an error of ν. If ν corresponds to a resolution of b_ν bits, for a two state system, $\mathbf{x}_k = [x_1(k), x_2(k)]'$, with a single measurement y_k we can estimate each state to an accuracy of $\frac{b_\nu}{2}$ bits. Additional time-series measurements can be used to build up the number of bits we have at our disposal to estimate the underlying states. Using entropy measures we wish to evaluate the additional gain in bits we can obtain from the mapping function. Particularly for systems like EEG with a low-dimensional measurement ($\mathbf{y} \in \mathbb{R}^M$) upon a high dimensional system ($\mathbf{x} \in \mathbb{R}^N$, where $N >> M$) we require positive entropy, otherwise Kalman Filtering and similar estimation techniques will only be able to provide us with information directly proportional to the number of measurements.

In terms of bits, consider the situation where we have M measurements, each over the observation window $k = 1 \ldots n$ and recorded with K bits at our disposal to estimate an underlying system with N states. Through just observation alone we have on average $\frac{KMn}{N}$ bits per state. As we are dealing with the scenario where $N \gg M$ (and indeed $N \gg Mn$) this will not provide sufficient information, as has been discussed in detail in Section 5.5.2. Here we consider the mapping function, f, in addition to the observation data. Note that this is explicitly using dynamics (the mapping function f) that are unavailable to us in the real EEG-seizure prediction problem. Nonetheless, let the mapping function, f, have positive entropy, $h_f > 0$ in bits per map iteration. Our improved estimate of the states

---

Σ must contain at least one non-empty subset of X

at each time step, k, with the addition of entropy from going n_f mappings back in time is: $\frac{(h_f n_f + K)M}{N}$ bits. This gives us an improved $\frac{(h_f n_f + K)Mn}{N}$ bits over the $\frac{KMn}{N}$ bits from observation alone as illustrated in the upcoming linear example with $M = 1$.

For linear systems,

$$\begin{aligned} \mathbf{x}_{k+1} &= \mathbf{A}\mathbf{x}_k & (6.3.5) \\ y_k &= C\mathbf{x_k} + \nu. & (6.3.6) \end{aligned}$$

For $\mathbf{A}$ an invertible mapping, with determinant $d = det(\mathbf{A})$, then for a Lebesgue measure μ:

$$\mu\left(\mathbf{A}^{-1}S\right) = \frac{\mu\left(S\right)}{|d|}. \tag{6.3.7}$$

Therefore, linear mappings, $\mathbf{A}$ with a unity determinant are measure preserving.

The entropy in a discrete, invertible $N \times N$ map $\mathbf{A}$ with eigenvalues λ_i is [132]:

$$h_\mu\left(\mathbf{A}\right) = \begin{cases} \sum\limits_{i:|\lambda_i|>1} log(|\lambda_i|) & \text{, forward in time} \\ & or \\ \sum\limits_{i:|\lambda_i|<1} log(\frac{1}{|\lambda_i|}) & \text{, backwards in time} \end{cases} \tag{6.3.8}$$

The choice of “unstable” ($|\lambda_i| > 1$) or “stable” ($|\lambda_i| < 1$) eigenvalues correspond to entropy gained by moving forward or backwards in the timeseries respectively.

Note that marginally stable eigenvalues ($|\lambda_i| = 1$) generate zero entropy. This follows intuitively considering that unity magnitude eigenvalues correspond to clock oscillations that neither decay nor expand in amplitude over time. After one period of a constant amplitude oscillation, there is essentially no new information to be gained by observing further periods of timeseries data as the same information is repeated. Hence, the information gain or entropy is zero. These concepts are demonstrated in the following linear example.

A linear example

The linear system,

$$\mathbf{x}_{k+1} = \mathbf{A}\mathbf{x}_k \tag{6.3.9}$$

$$y_k = C\mathbf{x_k} + \nu, \tag{6.3.10}$$

where,

$$\mathbf{A} = \begin{pmatrix} 2 & 0 \\ 0 & \frac{1}{2} \end{pmatrix}, \tag{6.3.11}$$

and

$$\mathbf{C} = \begin{pmatrix} 1 & 1 \end{pmatrix}, \tag{6.3.12}$$

is observable ($\mathcal{O}(\mathbf{C},\mathbf{A}) = [\mathbf{C},\mathbf{CA}]'$ is full rank) and $\mathbf{A}$ is a measure preserving map ($det\,(\mathbf{A}) = 1$).

Lets suppose that y is measured with 2 bits and that we are dealing with a normalised state $x_i \in (0,1]$. Normalisation provides simplicity for this example, but the analysis holds beyond normalised systems. For a single measurement y this provides us with just 1 bit of measurement about each state x_1 and x_2. Therefore our state estimate will have an error bound of $\frac{1}{2}$ (since the quantisation error is $\frac{1}{2^K}$, for K bits per state). Suppose we estimate that our state is $\mathbf{x} = [0.5, 0.5]$ and assume that our space including the error is the unit square, or set S_0 as shown in Figure 6.6. Mapping this unit square gives, $S_0 \rightarrow \mathbf{A}(S_0) = S_1$. The map is clearly measure preserving under a Lebesgue measure as area is preserved. Our new set, S_1 is centred at $\mathbf{x} = [0.25, 0.5]$. Consider for the moment that $\mathbf{x}$=[0.25,0.5] is the mapped state at time $k+1$ from the true estimate at time k. With the knowledge that our error is bounded at $\frac{1}{2}$, we can "update" S_1 to the criss-cross patterned area as illustrated in Figure 6.7. By now inverting the map we find a refined area $Z_0 = S_0 \cap \left(\mathbf{A}^{-1}\left(S_1\right)\right)$. With one iteration of the map $\mathbf{A}^{-1}$ between time $k+1$ and k the error boundary on the state estimate at time k is reduced. We now have x_1 estimated with a error of 0.25 (to a resolution of 2 bits) and the error on x_2 remains the same at 0.5

(to a resolution of 1 bits). This is 3 bits per two states (an average of 1.5 bits per state) from 2 bits of measurement. We have a entropy gain of 1 bit per iteration of the map.

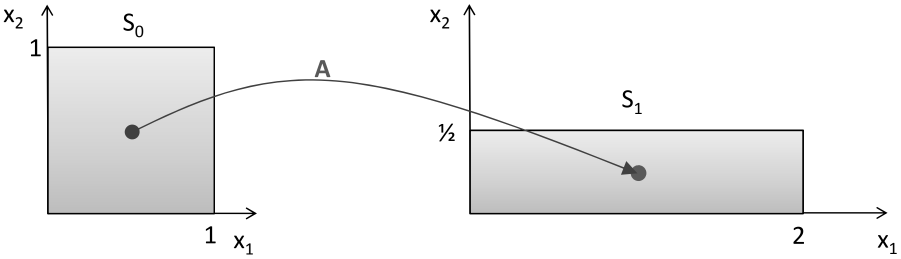

Figure 6.6: Illustration of the mapping of the space S_0, the state estimate at time k including the error on this estimate based on quantisation, to space S_1 at time $k+1$. Area is preserved under this mapping.

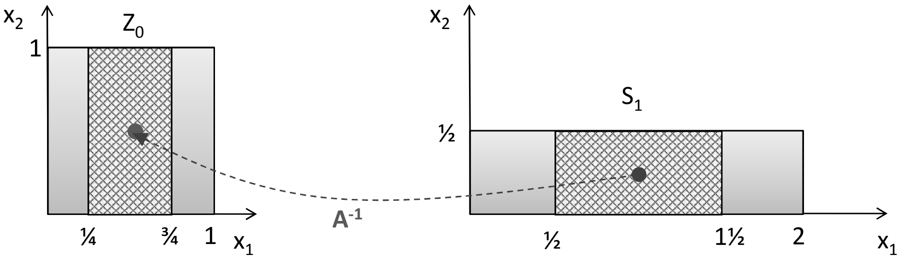

Figure 6.7: Illustration of the refinement of space S_0 to $Z_0 = S_0 \cap \left(\mathbf{A}^{-1}\left(S_1\right)\right)$, using two datapoints. The estimate area is shrunk by a factor of two.

Entropy can equally be found from the eigenvalue method, using equation 6.3.8:

$$h_\mu\left(\mathbf{A}\right) = \sum_{i:|\lambda_i|>1} log_2(|\lambda_i|) = log(2) = 1bit \tag{6.3.13}$$

and by considering the areas directly:

$$h_\mu\left(\mathbf{A}\right) = log_2\left(\frac{\mu(S_0)}{\mu(Z_0)}\right) = log_2\left(\frac{1}{\frac{1}{2}}\right) = log(2) = 1bit. \tag{6.3.14}$$

Using two iterations of the map, we can further refine S_0 to $Z_0^2 = S_0 \cap \left(\mathbf{A}^{-1}\left(S_1\right)\right) \cap \left(\mathbf{A}^{-1}\left(\mathbf{A}^{-1}\left(S_2\right) \cap S_1\right)\right)$. In general, the notation Z_0^n is the refinement of area S_0 by n iterations of the map. In this example we have used the map iterations forward in time (where the map $\mathbf{A}$ stretches state x_1 allowing refinement of S_0 with inverse mapping by revising the mapped area according to our quantisation error bounds. Equally this argument holds in inverse time using the inverse mapping first where x_2 is stretched, then allowing refinement with the original (non-inverse) mapping, as illustrated in Figures 6.8 and 6.9. The facility to use the timeseries in both directions is why the entropy from eigenvalues is the piecewise function in equation 6.3.8, split along the stability boundary (unstable systems in reverse time are conveniently "stable" for our data mining purposes).

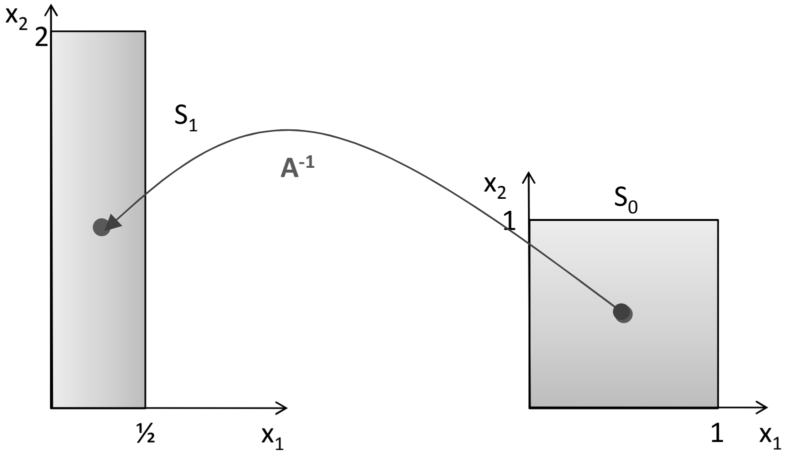

Figure 6.8: Illustration of the inverse mapping of the space S_0, the state estimate at time $k+1$ including the error on this estimate based on quantisation, to space S_1 at time k. Area is preserved under this mapping.

Now what of our earlier assumption that the true state lived exactly at the centre of the error set S_1? This can be considered to be true *on average*. Over a quantised timeseries, the quantisation error will be zero on average. Therefore, the above entropy of a measure preserving map is the entropy *on average* per one iteration of the map.

Entropy of a map f in terms of reduction in state estimation error, using a Lebesgue measure, μ, is:

$$E\left[h_\mu\left(f\left(\mathbf{x}_k\right)\right)\right] = \frac{1}{n} log_2 \left(\frac{\mu(S_0)}{\mu(Z_0^n)}\right), \tag{6.3.15}$$

where n is the number of iterations of the map, E is the expected value and the units of $h_\mu\left(f\left(\mathbf{x}\right)\right)$ are *bits per map iteration.*

For linear systems, the map f can take the form of a matrix $\mathbf{A}$ with eigenvalues

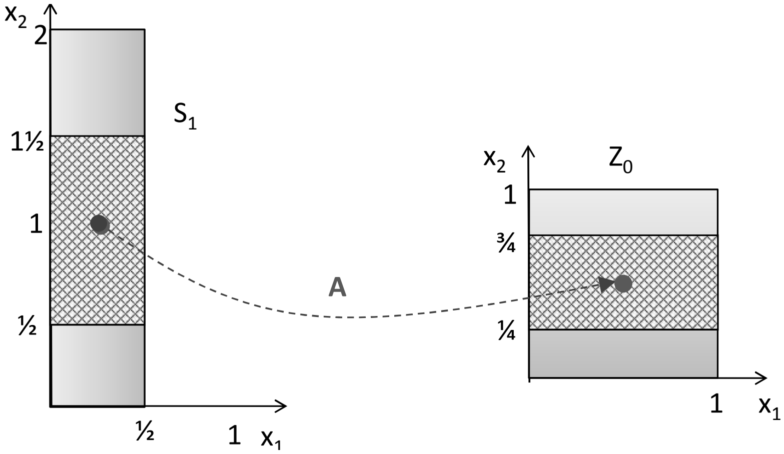

Figure 6.9: Illustration of the refinement of space S_0 to $Z_0 = S_0 \cap (\mathbf{A}(S_1))$, using two datapoints. The estimate area is shrunk by a factor of two.

$\lambda(\mathbf{A}) = \lambda_1, \lambda_2 \dots \lambda_N$ and,

$$h_\mu(\mathbf{A}) = \begin{cases} \sum_{i:|\lambda_i|>1} log(|\lambda_i|) & \text{, forwards in time} \\ \sum_{i:|\lambda_i|<1} log(\frac{1}{|\lambda_i|}) & \text{, backwards in time} \end{cases} \tag{6.3.16}$$

For non-linear systems with oscillatory dynamics, Equation 6.3.16 can also be used with the Jacobian, $\mathbf{J}$, of the system replacing the system matrix $\mathbf{A}$. The Jacobian is shown to provide a good estimate of entropy in the case of non-linear oscillatory systems in [133].

6.3.2 Entropy of Coupled Oscillations

Our model for the brain system and its measurement by EEG is the coupled oscillator model as introduced in Chapter 4 and further explored in Chapter 5 and Section 6.2. The mapping for coupled oscillators that are marginally stable has zero entropy. This is a fundamental limitation to what we can expect to observe about the high-dimensional underlying brain system from low-dimensional EEG signals.

The case of linear clocks

For a single uncoupled clock with continuous system matrix,

$$\mathbf{A} = \begin{pmatrix} 0 & -\omega_i \\ \omega_i & 0 \end{pmatrix}, \tag{6.3.17}$$

and corresponding digital system matrix, $\mathbf{A} \rightarrow e^{\mathbf{A}}$ for unity sample time,

$$\mathbf{A}_d = \begin{pmatrix} cos(\omega_i) & -sin(\omega_i) \\ sin(\omega_i) & cos(\omega_i) \end{pmatrix}, \tag{6.3.18}$$

These linear clocks are measure preserving, $det(\mathbf{A}_d) = 1$ and have zero entropy, given Equation 6.3.16 with $|\lambda_i(\mathbf{A}_d)| = 1, \forall i$. An illustration of these properties is given in Figure 6.10 based on a 1-dimensional measurement with 2 bits ($y \in \mathbb{R}^1, K = 2$) similar to the previous examples and $\omega_i = 1$rad/s.

The case of non-linear coupled oscillations

From an entropy viewpoint measurements of linear clocks reveal system information in a very sparing manner. What of non-linear oscillators? We find that the non-linear undamped pendulum oscillator system can also be shown to be a zero entropy mapping.

For a single uncoupled oscillator with differential equation, $\ddot{x} + \omega_i^2 sin(x) = 0$, we have the following continuous state mapping functions:

$$\dot{x_1} = f_1(\mathbf{x}) = x_2 \tag{6.3.19}$$

$$\dot{x_2} = f_2(\mathbf{x}) = -\omega_i^2 sin(x_1) \tag{6.3.20}$$

This can be expressed in matrix form using the Jacobian,

$$\mathbf{J} = \begin{pmatrix} \frac{df_1}{dx_1} & \frac{df_1}{dx_2} \\ \frac{df_2}{dx_1} & \frac{df_2}{dx_2} \end{pmatrix} = \begin{pmatrix} 0 & 1 \\ -\omega_i^2 cos(x_1) & 0 \end{pmatrix}. \tag{6.3.21}$$

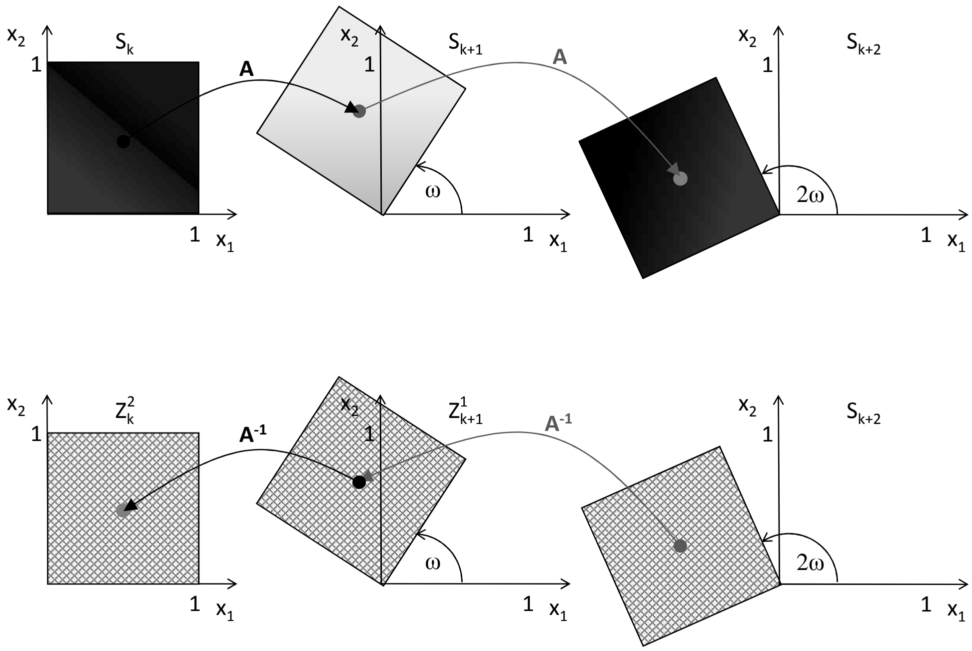

Figure 6.10: Illustration of the mapping of the space S_k, contain an estimate of two states from a single clock at time k including the error on this estimate based on quantisation, to space S_{k+1} at time $k+1$ and space S_{k+2} at time $k+2$. At S_{k+2} the revised area accounting for quantisation remains the same, therefore there is no refinement between space S_k and $Z_k^2 = S_k \cap \left(\mathbf{A}^{-1}\left(S_{k+1}\right)\right) \cap \left(\mathbf{A}^{-1}\left(\mathbf{A}^{-1}\left(S_{k+2}\right) \cap S_{k+1}\right)\right)$ and the entropy of the linear clock map is zero.

Transforming to a balanced matrix using **T**:

$$\mathbf{T} = \begin{pmatrix} \omega_i & 0 \\ 0 & -1 \end{pmatrix}, \tag{6.3.22}$$

we obtain,

$$\mathbf{TJT}^{-1} = \begin{pmatrix} 0 & -\omega_i \\ \omega_i cos(x_1) & 0 \end{pmatrix}. \tag{6.3.23}$$

Now converting to digital format ($\mathbf{J}_d \rightarrow e^{\mathbf{TJT}^{-1}}$) for unity sample time,

$$\mathbf{J}_d = \begin{pmatrix} cos(\sqrt{cos(x_1)}\omega_i) & -\frac{1}{\sqrt{cos(x_1)}} sin(\sqrt{cos(x_1)}\omega_i) \\ \sqrt{cos(x_1)} sin(\sqrt{cos(x_1)}\omega_i) & cos(\sqrt{cos(x_1)}\omega_i) \end{pmatrix}, \tag{6.3.24}$$

Using equation 6.3.7, these non-linear oscillations are measure preserving since $det(\mathbf{J}_d) = 1$ and would also appear to have zero entropy at first sight, given Equation 6.3.16 with $|\lambda_i(\mathbf{J}_d)| = 1, \forall i$. The time-varying nature of $\mathbf{J}_d$ along trajectories does not explicitly allow for an analytical estimate of the entropy such as this, however, through simulation, and averaging over trajectories, we show that the entropy of zero is indeed a very good approximation for this non-linear system.

An illustration of these properties is given in Figure 6.11 with $\omega_i = \frac{2\pi}{10}$rad/s. For an initial state estimate including error boundary of the unit square, subsequent mappings rotate the states by an approximate $\omega_i = \frac{2\pi}{10}$rad/s, while also mapping the shape in a non-linear fashion which distorts the initial area. The mapped areas remain unity (measure preserving). For any given discrete time k it may be possible to refine the area according to the boundaries of error, ± 0.5, however, due to the rotational nature of the system, any refinement is cancelled on average over mappings as we rotate through 2π. Since, regardless of non-linearity, the state is not known to be exactly at the centre of the unit square, but instead the expected value of x is the centre point, our entropy is an expected value over many measurements. Thus the secondary need for averaging in this non-linear case is superfluous and entropy is still zero (in the same expected value sense that it was defined for the linear case).

Numerical simulation assessing entropy in terms of area refinement shows that the

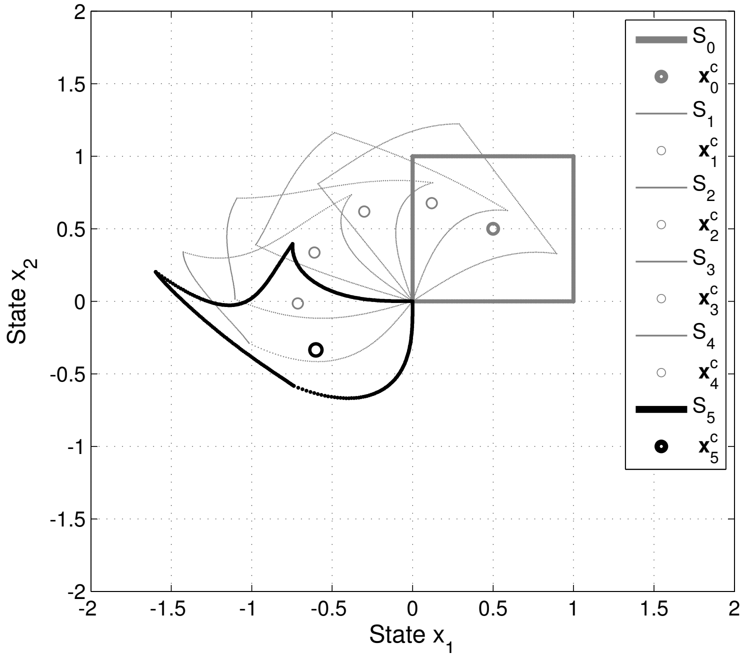

Figure 6.11: Illustration of the mapping of the set S_0, containing an initial estimate of two states from a single non-linear oscillation at time 0 including the error on this estimate based on quantisation. The map in Equation 6.3.24 is employed with a frequency $\omega_i = \frac{2\pi}{10}$ to map S_k to S_{k+1} for $k = 0, 1, 2, 3, 4$.

expected value of entropy is zero, using the Jacobian of the mapping function in Equation 6.3.24. Unity digital sample time is used in combination with a oscillator natural frequency of $\omega_i = \frac{2\pi}{1000}$. As discussed in Section 5.4.2 normalised frequency and sample time are equivalent using time-scaling to the natural frequency range of brain oscillations combined with EEG sampling period. As we are operating on the stability boundary, small approximation errors in the Jacobian can quickly lead to unstable results. A particular small normalised frequency ($\frac{2\pi}{1000}$) is chosen here so as to minimise numerical error impacting the stability of the simulation. The simulation results confirm that the expected value of entropy is zero. As the state set is rotated round the origin the average distance between the mapping of the centre point ($\mathbf{x}_k^c = [x_k^{c,1}, x_k^{c,2}]$, where the initial centre point is $\mathbf{x}_0^c = [\frac{1}{2}, \frac{1}{2}]$) and the area boundaries remains 0. Figure 6.12 illustrates that the expected distance between the set boundaries and the centre point is zero in both the $\mathbf{x}^1$ and $\mathbf{x}^2$ state directions. As expected, the distance from boundary to centre for the error area at each sample time k is periodic with period 1000, and averages over k (cumulative means) to zero. Therefore the simulations support that there is no refinement of the error state set to be gained with inverse mapping *on average* and the entropy of the non-linear oscillator map is zero.

The case of a Van Der Pol oscillator

Another non-linear oscillator example is the Van Der Pol oscillator. It is described by the equation,

$$\ddot{\mathbf{x}} - \epsilon(1 - \mathbf{x}^2)\dot{\mathbf{x}} + \omega_i^2 \mathbf{x} = 0 \qquad (6.3.25)$$

With oscillatory dynamics it would be expected that the mapping has zero entropy. Indeed that is the case. An illustration of the Van Der Pol mapping is given in Figure 6.13 with $\omega_i = \frac{2\pi}{10}$rad/s, for two choices of parameter ϵ.

Similar to the non-linear clock in the previous section we can find the Jacobian to analyse the measure preserving capabilities of the Van Der Pol oscillator. For a single uncoupled Van Der Pol oscillator with differential equation 6.3.25 we have the following continuous state mapping functions:

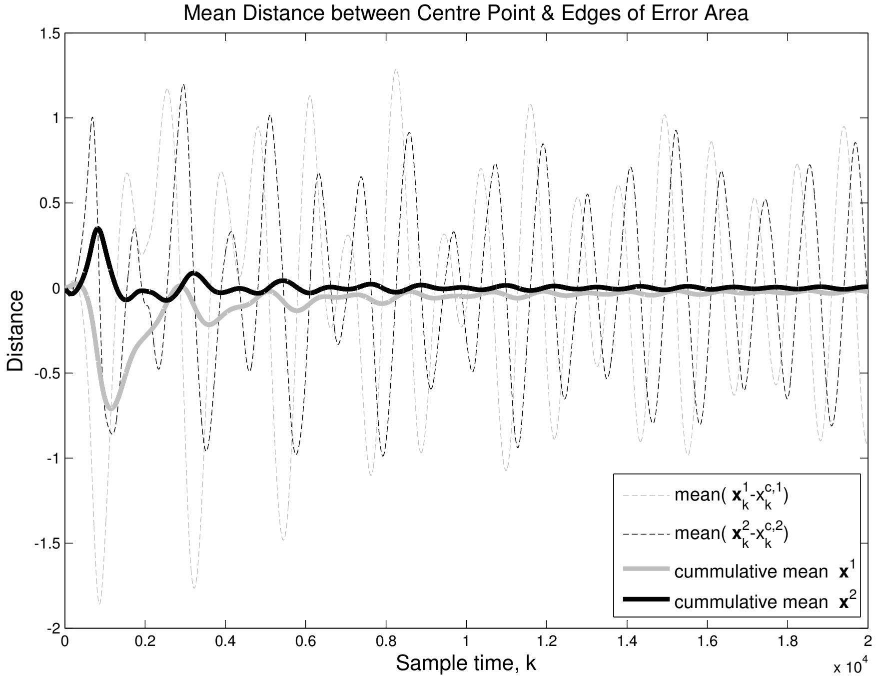

Figure 6.12: Evaluating an error area mapped by a non-linear oscillator. For each state direction, $\mathbf{x}^1$ (grey line) and $\mathbf{x}^2$ (black line): The dashed lines show the mean distances between the centre point of the error area and the error boundary points at each sample time k, and the solid lines shows the cumulative mean of the same distance over k.

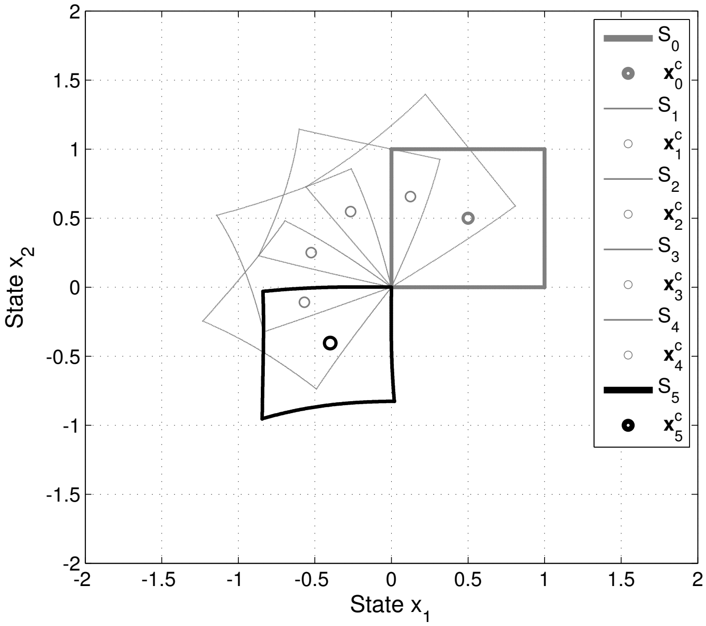

(a) Van Der Pol equation with $\epsilon = 0.1$

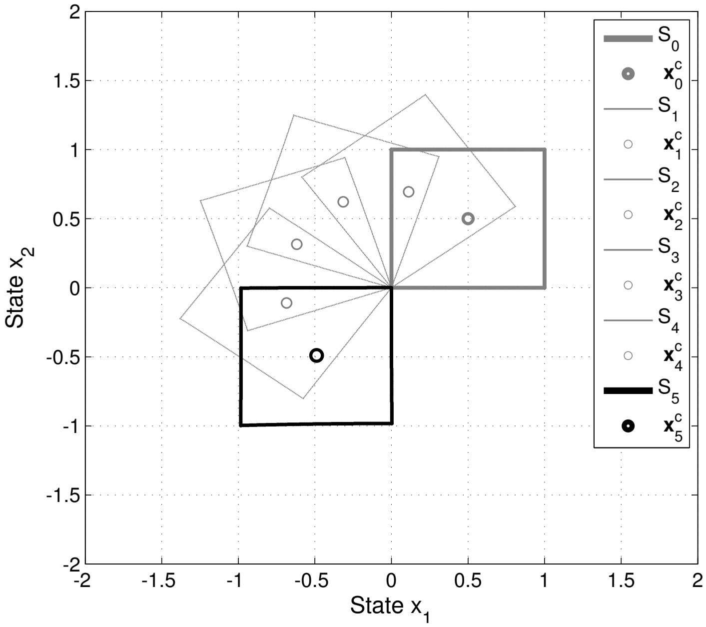

(b) Van Der Pol equation with $\epsilon = 0.01$

Figure 6.13: Illustration of the mapping of the set S_0, containing an initial estimate of two states from a single Van Der Pol oscillator at time 0 including the error on this estimate based on quantisation. The map in Equation 6.3.25 is employed with a frequency $\omega_i = \frac{2\pi}{10}$ to map S_k to S_{k+1} for $k = 0, 1, 2, 3, 4$.

$$\dot{x_1} = f_1(\mathbf{x}) = x_2 \tag{6.3.26}$$

$$\dot{x_2} = f_2(\mathbf{x}) = -\omega_i^2 x_1 + \epsilon(1 - x_1^2)x_2 \tag{6.3.27}$$

This can be expressed in matrix form using the Jacobian,

$$\mathbf{J} = \begin{pmatrix} \frac{df_1}{dx_1} & \frac{df_1}{dx_2} \\ \frac{df_2}{dx_1} & \frac{df_2}{dx_2} \end{pmatrix} = \begin{pmatrix} 0 & 1 \\ -\omega_i^2 & \epsilon(1 - x_1^2) \end{pmatrix}. \tag{6.3.28}$$

Transforming to a balanced matrix using $\mathbf{T}$:

$$\mathbf{T} = \begin{pmatrix} \omega_i & 0 \\ 0 & -1 \end{pmatrix}, \tag{6.3.29}$$

we obtain,

$$\mathbf{TJT}^{-1} = \begin{pmatrix} 0 & -\omega_i \\ \omega_i & \epsilon(1 - x_1^2) \end{pmatrix}. \tag{6.3.30}$$

The equations can be converted to digital format using $\mathbf{J}_d \rightarrow e^{\mathbf{TJT}^{-1}}$ for unity sample time.

The Van der Pol system is not so convenient analytically as the non-linear pendulum oscillator, however, we can still find properties that closely observe measure preserving maps. The determinant of the digital Jacobian is approximately unity for small ϵ.

$$\mathbf{J}_d = e^{\epsilon(1-x_1^2)} \approx 1(\because \epsilon \approx 0). \tag{6.3.31}$$

Similarly the eigenvalues of $\mathbf{J}$ are approximately on the imaginary axis:

$$\lambda(\mathbf{J}) = \pm\omega_i j + \delta, \tag{6.3.32}$$

where δ is a function of ϵ and $\delta << \omega_i$.

Numerical simulation assessing entropy in terms of area refinement shows that the expected value of entropy is zero, as shown in Figure 6.14. Unity digital sample time is used in combination with a oscillator natural frequency of $\omega_i = \frac{2\pi}{1000}$ and Van Der Pol

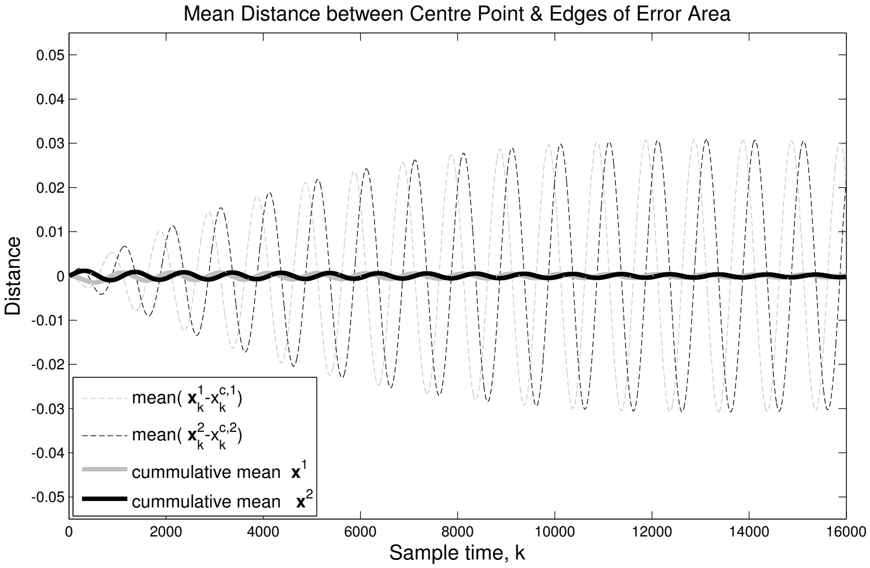

Figure 6.14: Evaluating an error area mapped by a Van Der Pol oscillator. For each state direction, $\mathbf{x}^1$ (grey line) and $\mathbf{x}^2$ (black line): The dashed lines show the mean distances between the centre point of the error area and the error boundary points at each sample time k, and the solid lines shows the cumulative mean of the same distance over k.

parameter $\epsilon = 0.0001$. As expected, the distance from boundary to centre for the error area at each sample time k is periodic with period 1000, and averages over k (cumulative means) to zero. Therefore the simulations support that there is negligible refinement of the error state set to be gained with inverse mapping *on average* and the entropy of the Van Der Pol oscillator is approximately zero.

One item for careful consideration for both the non-linear examples presented is that we are linearising with the Jacobian. Does this provide valid results for the underlying non-linear map? Indeed it does. Solutions for entropy of maps of linearised systems have been proven to closely approximate that of the non-linear system for these classes of oscillatory systems by Kawan [133].

6.4 Conclusions from Entropy

The results in the previous sections demonstrate that for both linear clocks and non-linear oscillators the amount of information we can glean from EEG signals of brain oscillations is severely limited by the number of EEG electrodes and their sampling rate.

Increasing the sampling rate is possible but not to the extent necessary to generate sufficient information. Is it not currently feasible to dramatically increase electrode numbers in an invasive device. Indeed the maximum of 64 electrodes for short-term in-hospital warning systems, already most likely far exceeds the number that could be implanted permanently given wiring constraints and safety considerations. Future electrode grids of 1000 to 10000 electrodes with wireless communication technology are under development at Bionic Vision Australia for a retinal prosthesis device, however, electrodes on these grids are densely organised and would likely be too localised for epileptic seizure prediction until such a time as we can reliably and finely localise the generation of seizures for a given patient.

Clearly, the passive observation of brain dynamics provides a limited flow of information. The results of this chapter show that oscillatory systems do not lend themselves to information extraction. The brain is certainly an oscillatory system and our ability to extract information from the brain is very limited in this case of low-dimensional EEG and furthermore, severely hampered by any noise. The noise kills any ability to estimate underlying states of an order significantly larger that the measurement. There is a real need to dramatically improve upon this, one feasible option is to include an input.

Including an input signal enables us to shine a strong light on a particular part of the dynamics. The amount of information we extract is still limited, but through use of an input we can focus the information we receive on a localised part of the dynamics. The inclusion of an input stimulus is explored in the next chapter.

6.4.1 Chapter Contribution

This chapter provides evidence that clinical EEG acquisition provides insufficient information for epileptic seizure prediction using stochastic Kalman estimation and entropy of measure preserving maps. These are significant findings following on from the previous chapter result that the system was not observable in the traditional sense with the minimum of measurements. Even with our best practical Kalman estimation attempt, using increased amounts of data to the stationarity limit, the system remains extremely unobservable. More fundamental is the contribution of the entropy of measure preserving maps result. Both linear and non-linear undamped oscillations are measure preserving maps with zero entropy. Therefore with brain dynamics appearing to be oscillatory in nature, and close to marginally stable, this result that the system does not lend itself to information extraction extends to all envisaged brain models and large-scale measures of EEG. This heralds the necessity for a significant deviation from traditional seizure prediction methodology. Regardless of model or analysis method, *passive* EEG observation of oscillatory brain dynamics lying on the boundary of stability will not be successful for epileptic seizure prediction.

Chapter 7

An Active Paradigm for Epileptic Seizure Prediction

This chapter presents a novel theoretical paradigm for epileptic seizure prediction based on a coupled oscillator model of brain dynamics. This model is used to investigate prediction methods capable of tracking the synchronisation changes that may lead to a seizure. The results of Chapter 5 and 6 indicate that state-space reconstruction of a coupled oscillator model from an EEG-like signal is ill-posed, therefore, monitoring system synchronisation via the EEG signal is unlikely to give advanced warning of imminent seizure activity. Through simulation, it is shown that synchronisation tracking may still be viable using an input probing stimulus to actively seek information from the coupled oscillator network.

Over the past 34 years many methods, including synchronisation measures, have been unsuccessfully applied to EEG recordings for seizure prediction [89]. Here we approach the epileptic seizure prediction problem with a very simplified coupled oscillator network. Despite this simplicity, such networks exhibit EEG like behaviour from a measurement point of view. Our previous results in Chapter 5 show that in the most ideal abstraction of the underlying problem, practical observability (assuming a finite precision EEG measurement instrument) is not an obvious property, even when the underlying system is observable in the normal sense (i.e. for ideal measurements). Coupled with the stochastic estimation and zero entropy map findings of Chapter 6 this offers explanation on why epilepsy prediction attempts based on passive observation of EEG signals fail - because sufficient information cannot be gleaned from the EEG signal. Due to the simplicity of our model, it is possible to explore active signal probing as a means to early-detection and prediction of epileptic events. This paradigm is explored here using simulation studies.

The remainder of this Chapter details an active paradigm for seizure prediction with the coupled-oscillator model introduced in Chapter 4 with supporting proof-of-concept simulations presented in Section 7.2. Section 7.4 follows with a discussion and conclusions on the relevance of these findings in a clinical setting.

7.1 The Coupled Oscillator Model

The coupled oscillator model used is that earlier described in Chapter 4. To briefly reiterate, EEG recordings from brain tissue are modelled as the output measurement from a system of networked clocks. Each individual oscillator is modelled as a pendulum clock with the oscillatory motion of the pendulum described as

$$\ddot{x}_i + 2\zeta_i\omega_i\dot{x}_i + \omega_i^2 x_i = F_i, \tag{7.1.1}$$

where x is the angular position of the pendulum, ζ is the damping parameter, ω is the natural frequency of oscillation and F is the forcing term. F will take the form $\sin(\omega_{in}t)$ for an external evoked input signal of frequency ω_{in} and F additionally includes $\sum_j \alpha_{ij}(x_i - x_j)$ for coupling of the position state from other pendulums.

The resulting state space model for an interacting system of two pendulums is $\dot{\mathbf{x}} = \mathbf{A}\mathbf{x} + \mathbf{B}u$, where u is the input signal and the $\mathbf{A}$ and $\mathbf{B}$ matrices are as follows:

$$\mathbf{A} = \begin{bmatrix} 0 & 1 & 0 & 0 \\ -\omega_1^2 + \alpha_{12} & -2\zeta_1\omega_1 & -\alpha_{12} & 0 \\ 0 & 0 & 0 & 1 \\ -\alpha_{21} & 0 & -\omega_2^2 + \alpha_{21} & -2\zeta_2\omega_2 \end{bmatrix} \tag{7.1.2}$$

$$\mathbf{B} = \begin{bmatrix} 1 & 0 & 1 & 0 \end{bmatrix}', \tag{7.1.3}$$

where prime($'$) denotes transpose and the input signal is, for example, $u = \sin(\omega_{in}t)$.

As earlier discussed in Chapter 4, this can be extended to an $2N$ state system, where there are N interconnected pendula subsystems as illustrated in Fig. 4.1. Each subsystem is allowed to connect to all the others and $\alpha_{ij} \equiv \alpha_{ji}$ (symmetric coupling). Random graphs

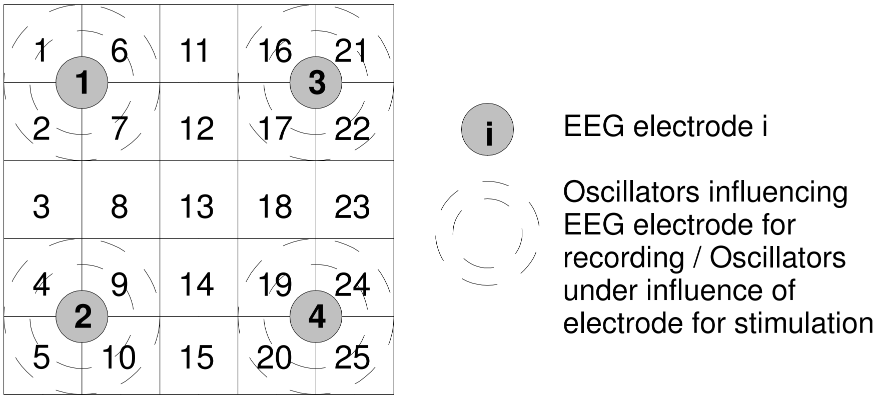

Figure 7.1: The simulation experimental set-up for a network of 25 coupled oscillators with 4 EEG channels.

can be constructed by choosing $\alpha_{ij} \geq 0$ from a distribution of values.

The output state equation for a single recorded EEG channel can be described by $\mathbf{y} = \mathbf{C}\mathbf{x}$, where

$$\mathbf{C} = \begin{bmatrix} 0 & -\delta_1 & 0 & -\delta_2 & \dots & 0 & -\delta_n \end{bmatrix}. \tag{7.1.4}$$

The output is a convex combination of the angular velocity states in the system ($\delta_i \geq 0, \sum_i \delta_i = 1$). This choice of $\mathbf{B}$ and $\mathbf{C}$ ensures that the transfer function, $G(s) = \mathbf{C}(s\mathbf{I} - \mathbf{A})^{-1}\mathbf{B}$, is normalized to 1 at DC. $\delta_i \geq 0$ indicates the relative contribution clock i makes in the EEG output signal.

7.2 A Paradigm for Seizure Prediction

A fully observably system would enable a reconstruction of the model to be estimated and tracked over time from the EEG. However, we find this unlikely to be feasible with the EEG signal. An alternative to parameter tracking and state-space estimation for seizure prediction is investigated in this section. In particular, we study what can be learned by probing the system with an input.

In our model we equate prediction of seizures with evidence of synchrony between many individual oscillators before synchrony is visible in our EEG electrode recordings. Synchrony is defined as sustained phase locking to a particular frequency and is computed as the least squares solution to the model

$$X(t) = A\cos(2\pi ft + \phi) + \mathrm{w}(t) \tag{7.2.1}$$

where f is the known frequency of the input stimulus, $\mathrm{w}(t)$ is zero mean white noise and the phase, ϕ and amplitude, $A = A(f)$, are estimated (see Appendix A.4 for details of this method). $X(t)$ can be either (1) the EEG signal used to estimate the phase-locking response to our probe stimulus, or (2) the internal states of the model to determine phase for individual clocks to establish if predictions from the EEG data correspond to a true picture of the underlying system activity. This definition of phase synchrony is used as it is more robust than the Hilbert transform (see Appendix A.4) in the presence of noise and can be used on broadband signals without any ambiguities.

The simulated coupled oscillator network was configured as shown in Fig. (7.1). There are 4 electrodes each influenced by the individual oscillators in their immediate vicinity. The network was interconnected with coupling parameters α_{ij}, chosen uniformly in the range 0-0.01. The system's natural frequencies, ω_i, were randomly chosen from a uniform distribution spanning from 0.5 Hz-100Hz. To stimulate the case of synchronisation build up throughout the network, the damping parameters, ζ_i, were chosen uniformly in the range 0.001 to 0.01. The generation of a seizure was modelled by expanding equation 7.1.1 for a single clock in the network to include a non-linear element, creating a Van der Pol oscillator with system equation $\ddot{x} + (\epsilon x^2 + 2\zeta\omega)\dot{x} + \omega^2 x = F$. By allowing a negative damping parameter, ζ, in this non-linear clock an unstable oscillator (becoming marginally stable in steady state) was formed which would slowly take over the entire network. Matlab Simulink Diagrams and associated code are provided in Appendix A.5.7.

The prediction paradigm was centred on the knowledge that a stable coupled oscillator network (modelling the normal brain state) only has significant responses to input frequencies in close proximity to the system natural frequencies ($\omega_1 \cdots \omega_n$). Investigative probing can enable the collection of normal system responses, $A(f)$, with a library of natural frequencies found as the peaks in this spectrum. In general we hypothesize that the seizure state will exhibit a significantly altered response to probe stimuli. One likely alteration to the system response is that subsequent probing with the system frequencies should elicit a measurable response in the EEG, except when the network propagates into a seizure state. In the seizure state, individual oscillators are synchronised to the frequency of the unstable oscillator and are therefore non-responsive to any probing stimulus (of sufficiently low stimulation level for patient safety). Sufficiently low stimulation implies that we would be operating in the subthreshold region to avoid inducing a seizure. Subthreshold stimulations are routinely used in epilepsy surgery for mapping purposes.

Our approach to seizure prediction is to monitor when the response to probe stimuli, $A(f)$, is significantly altered from the library of normal responses. If we get such an altered response on several adjoining electrode stimulation sites we can infer that the underlying brain matter may be in a seizure state. We hypothesize that the early seizure state will exhibit an altered response in advance of the seizure state being visible as synchronisation across EEG channels. This hypothesis is based on the knowledge that the signal at the EEG channel is a function of much fewer oscillators than are present in the system, thus an oscillation would have to be widespread across the network before it is visible at the EEG level.

Sample EEG signals generated from the coupled oscillator model are shown in Fig. (7.3). Simulation results providing proof-of-concept are illustrated in Fig. (7.2). In this simulation, a poor response to normally-resonant probe stimuli was found in advance of visible synchronisation (seizure activity) at the EEG level. This paradigm acts as a predictor of very immediate seizures and could be considered a form of early detection. However, early detection could prove sufficient to provide a therapeutic window for seizure abating stimuli in an implantable seizure control device. Note the time of the therapeutic window was 0.58 seconds for this simulation, which was entirely dependent on the choice of damping and coupling parameters in the model. A realistic estimate of therapeutic window time in real brain matter would require clinical data from probe stimuli.

7.3 Coupled Oscillator Model: A Conveniently Balanced System

It is interesting to observe that the oscillator clock model used in this Chapter is reasonably balanced between observability and its dual controllability. This is a convenience worth noting when we are considering the addition of inputs to the system framework.

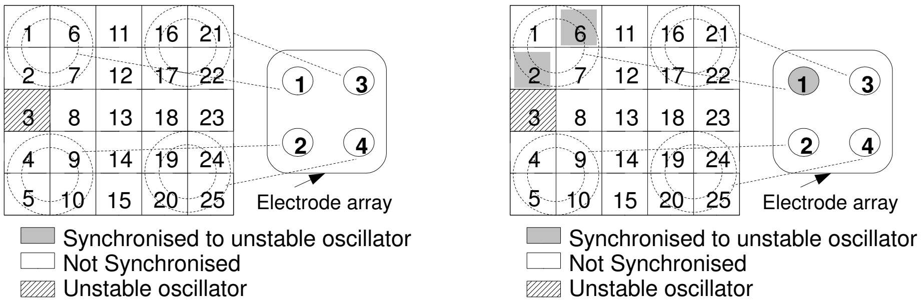

(a) Time t=0.2 sec

(b) Time t=2.9 sec

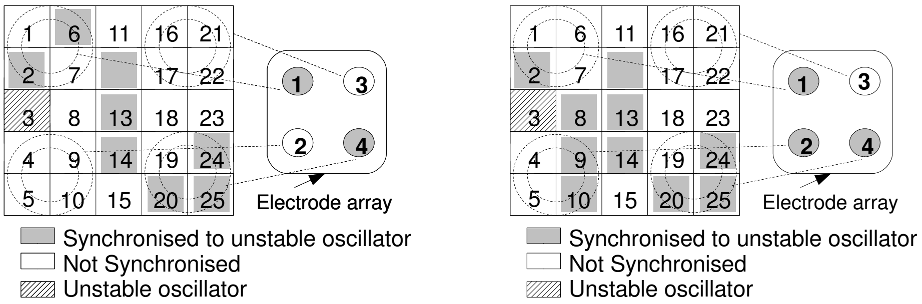

(c) Time t=3.28 sec

(d) Time t=3.48 sec

Figure 7.2: The simulated time evolution of a synchronisation (or seizure event) in the coupled oscillator model. Note that from t=0 seconds clock number 3 was unstable, by 2.9 seconds there was no longer a response to input probe stimuli in electrode one. However, it was not until t=3.48 seconds that synchronisation to the unstable natural frequency was measurable in the majority of EEG electrodes. Prediction therapy time window = 3.48-2.9= 0.58 seconds.

We are interested in what we could learn by probing the system with an input, as per the active model of EEG analysis described earlier in this Chapter. The ultimate goal of seizure prediction/ early detection, however, is to couple the advanced warning system with a seizure prevention mechanism. Such an mechanism to prevent the spread of seizure activity could perhaps involve further input signals to quench seizures rather than just probe for information. To this end a balanced transformation of the system is considered for the single output and input channel case.

A balanced transformation is one where the states of the transformed system are constructed such that the degree of controllability and the degree of observability of each state is the same. This implies that states that are difficult to observe are equally diffi-

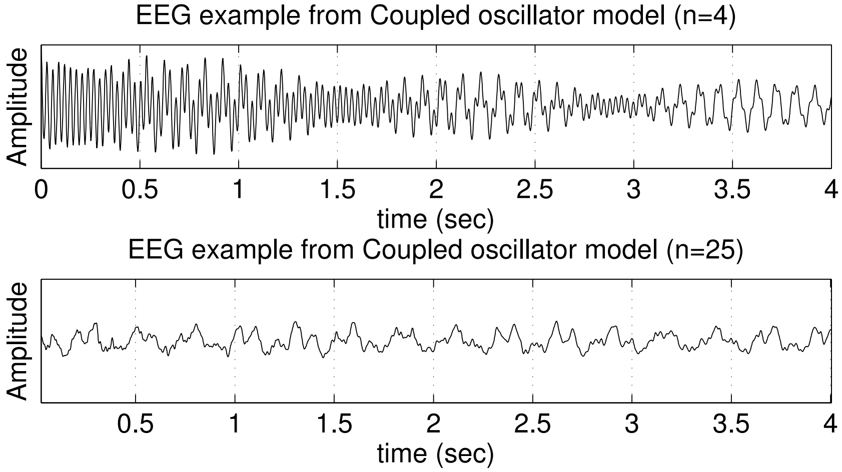

Figure 7.3: Sample EEG signals generated from the coupled oscillator model. The upper-trace shows the EEG signal corresponding to electrode number 2 in Figure 7.2. This is the weighted sum of the states from 4 clocks (n=4). The trace becomes synchronised to the unstable oscillator at 3.48 seconds. The lower trace is an example of the weighted sum of all 25 clocks (n=25) in the "normal" (stable) system, illustrating the increase of signal complexity with model order.

cult to control and vice versa. Those states that are easily controllable and observable have a significant component in the direction of the largest eigenvalues of the reachability gramian $\mathcal{P}$. Note the reachability gramian equals the observability gramian $\mathcal{Q}$ for a balanced system [118].

The time-scaled clock network as earlier discussed in Figure 5.1 of Chapter 5 was transformed to a balanced representation using the methods described in [118, Ch 7] (code is provided Appendix A.5.8). The range of singular values in the resultant system is almost identical to the non-transformed system as illustrated in Figure 7.4. This indicates that the time-scaled transform generates a system close to the optimal representation, in so far as, the limited number of states we can easily observe (those with large singular values) are conveniently also those states we can most easily control. This is promising for future development in design of input signals to desynchronise brain tissue for seizure control.

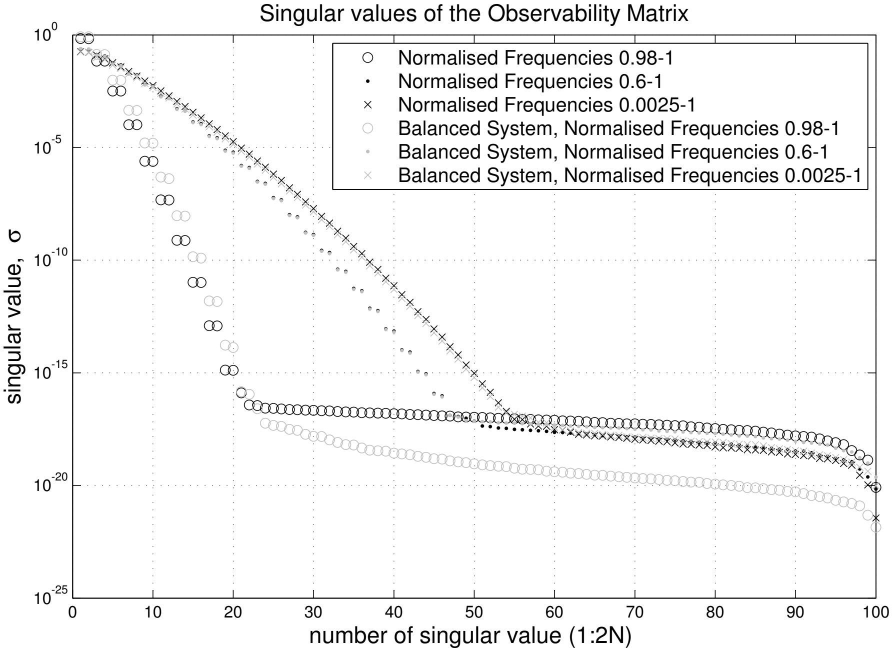

Figure 7.4: The Singular values of the observability matrix, $\mathcal{O} = \left[\mathbf{C}', \mathbf{CA}', \mathbf{CA}^{2'}, \ldots, \mathbf{CA}^{N-1'}\right]'$, are plotted for a network of 50 clocks (100 states) whose natural frequencies were uniformly chosen from the normalised frequency range of either 0.98-1 (plotted as symbol o), 0.6-1 (plotted as symbol .) or 0.0025-1 (plotted as symbol x). The results for the unbalanced system are shown in black (as previously provided in Figure 5.1 of Chapter 5), while the grey trace denotes the results of **A** and **C** from a balanced transform. Note the black and grey traces almost entirely overlap in the (x) and (.) datasets and are closely aligned for (o).

7.4 Discussion and Conclusion

We have provided, for a very simplistic abstraction of the real problem, a seizure prediction paradigm based on synchrony for use with EEG measurement using input probe stimuli. While the therapeutic window following prediction may be small, strategically placed electrodes at the seizure focus may enable synchronous activity to be found and abated prior to the emergence of clinical symptoms of epilepsy.

For this paradigm to be a viable clinical option stationarity and repeatability issues need to be addressed. The EEG is inherently non-stationary, however, the EEG may remain quasi-stationary for periods long enough to build up a library of “normal” responses to stimuli. Also, it needs to be established if the real brain system responses to probe stimuli are repeatable to some degree.

7.4.1 Chapter Contribution

This chapter demonstrates that evoked EEG following an active probing input signal has potential as an information rich signal for the therapeutic advanced warning of imminent seizure activity. While prediction may well remain illusive, the early detection of synchronous seizure events may be sufficient for intervention in a closed loop seizure prevention device. This is an important contribution providing initial theoretical justification for the very recently emerging clinical experimentation in active EEG for seizure warning.

Chapter 8

Conclusions

8.1 Conclusions

Can we predict epileptic seizures from EEG data? The overriding conclusion from the findings of this thesis is no.

The brain system is undoubtedly oscillatory with information commutated across neural networks due to oscillatory electric field potentials. Any brain model (and indeed all existing models) attempting to characterise the link between brain tissue and EEG will exhibit oscillatory dynamics. It follows that the coupled oscillator model used in this thesis is very suitable for the express purpose of investigating observability properties. Its suitability is based on the reasoning that if the most basic coupled oscillator model (that of coupled pendulum clocks) has limited observability with a basic measurement of spatially averaged oscillator activity, then the prospects of any improved observability in more complex and bio-realistic oscillator models is highly unlikely. The observability difficulties found in the work of this thesis stem from fundamental properties of oscillators themselves, that is dynamics which lie on the margins of stability. Therefore these results can naturally be extended to encompass any and all variations to oscillatory networked dynamics with an EEG-like measurement. We cannot predict the trajectories of a system when, with limited observability, we are only privy to a small fraction of the underlying dynamics. Seizure prediction from conventional large-scale EEG data is an exceedingly unlikely prospect.

A purely linear clock system is theoretically observable, however, by considering the uncertainty induced due to digitisation alone, that is, the simple quantisation of the measurement, it is not possible to estimate more than scantily few of the system's N states given N measurement data points. Essentially, as a simultaneous equation problem, the level of linear independence between equations falls below the level of measurement quantisation noise and indeed, for many of the equations, falls below standard computational quantisation limits. Importantly, this is with both the oscillation frequencies and the connectivity structure and strength completely known. Even in the scenario that the basic coupled clock model was sufficient to model brain dynamics, the level of complexity in the real-problem would be much increased to find not only the states but also frequencies and system structure. Furthermore, these limitations to observability were found in the absence of all noise sources apart from quantisation noise. Real EEG measurement is rampant with noise artefact, so again the real-problem is far more challenging. Given such poor observability in our simple noiseless model is is hard to envisage that real brain dynamics could be more observable.

The application of attempting to use more data to improve estimation capabilities by averaging over the quantisation noise was explored through iterative Kalman filtering. It was found, however, that when taking stationarity limitations into account, the estimation attempt ran out of time samples far in advance of gaining access to much system information due to the difficulties of system habitation on the stability boundary. Most significantly, the analysis of marginally stable oscillatory dynamics as measure preserving maps revealed that the effective expected map entropy over map iterations was zero. That is, no information in terms of refinement of error margins on a estimated state can be gained by iterating over oscillator map dynamics. Therefore, even if the brain remained stationary for a long period, additional data points would not bring about significant reduction of error area on our estimate. This entropy result is especially significant as it is a result which encompassed both linear and non-linear oscillatory systems.

On the restriction of the model to pure or marginally stable oscillators: It is biologically justifiable given the alternatives to marginal stability are either *(i)* damped oscillation or *(ii)* unstable oscillation. For the electro-magnetic activity of normal brain activity *(i)* and *(ii)* would indicate pathological states of activity, for example decay of neural activity until brain death and increasing neural excitability until a seizure state respectively. Therefore, operating the coupled oscillator model on the boundary of stability is bio-realistic for both normal brain function and for the pre-ictal period during which we aim to predict upcoming seizures. While certainly the brain will naturally deviate into both slightly underdamped and slightly damped modes of oscillation, it is envisioned that the natural balance of excitatory and inhibitory activity in the brain will constrain this damped and underdamped activity to dynamics that lie near to the critically damped (marginally stable) boundary. The entropy results of this thesis find that information extraction from marginally stable systems is difficult given limited amounts of data. The information extraction capabilities from dynamics that lie within a small distance on either side of the marginal stability boundary will naturally be similarly bleak.

In any case, mathematically speaking, the alternatives to pure or marginally stable oscillators are equally problematic for system observability. Both damped and undamped systems quickly become numerically unstable since the rows of the observability matrix, $(\mathbf{CA}^n)$, diverge exponentially to zero (in the case of damped oscillations) and to infinity (for unstable oscillations). The implication of this numerical divergence is that we quickly run out of the dynamic range with which to represent singular values of the observability matrix and observability is again poor. Restriction to pure oscillators allows us to stay within the dynamic range, however as the entropy results show, this is at the expense of no longer being able to average over any noise. Therefore, oscillators in general do not lend themselves well to practical observability.

We have considered observability in light of deterministic linear and non-linear dynamics, using linear, stochastic and non-linear analysis methods and found observability to be illposed. Other outstanding possibilities are stochastic dynamics or chaotic dynamics. For the stochastic case it is envisaged that any such dynamics could exhibit more deterministic emergent mean-field phenomena on large-scale EEG levels and therefore be incorporated into the existing analysis of this thesis. On chaotic dynamics, while this has been hypothesised for the brain, there are neither sufficiently bio-realistic models nor observations to support this. Nonetheless, should chaotic dynamics exist, the problem of identifying exponents would add to the problem of identifying states with chaotic dynamics having one or more positive Lyapunov exponents. Fitting data to sums of exponentials requires significant amounts of data, so again it is envisaged that we will run out of time and or reach a complexity barrier well before gaining significant access to information.

These observability limitations imply that, in a practical sense, we can only expect to fit EEG data to extremely simple models of brain activity with a limit of a a few tens of states. At the moment, no such brain models exist currently that can realistically and reliably model large-scale EEG measures of brain dynamics for the purpose of seizure prediction.

Why are simple models of brain dynamics, with limited numbers of states, insufficient for use in predicting seizures? In much of the seizure prediction work over the past decade the hypothesis that seizure events had low dimensional dynamics was employed with the idea that prediction efforts would be best concentrated towards tracking this transition from chaotic high dimensional dynamics to a low dimensional brain state. This has been unsuccessful and the observability results in this thesis may well explain why this is the case. The window of information that EEG provides is skewed to show only the most dominant and spectrally distinct oscillatory activity. It follows that seizure dynamics are visible in the EEG as abnormally excessive or synchronous activity only because they are the most dominant activity at that time. In the build up to a seizure, other dynamics such as those involved in motor or thinking tasks related to the persons current activity are more likely to dominate. Therefore the dynamics that would enable us to track transition to seizure are unlikely to make it through to be observed at the EEG until such a time as the seizure activity is dominant. By the time seizure activity is the dominant activity, the clinical manifestations of seizure activity will be present and it is far too late to “predict”. While brain-to-EEG models for epilepsy with small numbers of states could be used to classify seizures, they are insufficient to capture any build up to a seizure for prediction purposes as the EEG data applied to them will most likely not contain any of the seizure generating dynamics. Applying EEG data that is completed unrelated to seizure activity to an epilepsy model will not predict seizures, that is, unless we are extremely lucky and our electrodes happen to be in the exact right place. With current technology, however, it is not feasible to isolate a precise area in the brain where seizures originate from for electrode placement.

Certainly there is no logical requirement to be able to observe all the dynamics for tracking changes in brain state towards prediction. The issue is the extent to which EEG is a poor observer of brain activity. We would at least require the majority of the oscillations within a local radius of our electrode to be observable for predicting forthcoming seizure activity in that locality. The finding of this thesis indicate that this is not possible. The observability findings in Chapter 5 are in stark contrast to the conventional assumptions that surround EEG measurement. Typical intracranial EEG electrodes or "macro-elecrodes" are assumed to have a recording domain in the order of 100μm [1, Ch. 4]. But for a large number of oscillations, only the largest amplitude and most spectrally distinct oscillations within this area will correspond to singular values above the measurement bit threshold. This tells us that we could see an oscillation located $100\mu m$ from an electrode *only if* all the other tissue was inactive. Thus, rather than observing all the activity in the 100μm radius, instead we observe only the dominant few percent of oscillations within this spatial area. As discussed at the end of Chapter 5 recent experimental results support these findings. If we can only observe a few percent of the underlying oscillators within the conventionally assumed measurable range of our electrode - lets take 3% - then we would require over 97% of the underlying activity to be involved in the seizure state before we would be guaranteed to observe the seizure activity in the EEG. To "predict" we would need to be able to indicate that seizure activity was being generated far in advance of that activity taking over 97% the network domain we are attempting measuring. By the time 97% of that network is engaged in seizure activity the seizure is well-underway and there is no longer any need for prediction.

These results do not contradict the viability of seizure detection. The results in this thesis imply the brain must be in an very advanced state of synchronisation across huge areas of cortex before we can see seizures in the EEG. By the time a sufficient number of oscillators have synchronised enough to observe this in the EEG it is most likely that the seizure would be in an established state. This indicates why research findings in seizure detection have had more success with large scale EEG measures than was found for prediction. However, sufficiently early seizure detection to enable intervention that prevents any clinical manifestation of seizures for patients has not yet been achieved.

So what can be done to "detect" seizure activity in advance of the clinical manifestations of seizures? Future promise centres on conversion to the active EEG measurement paradigm, utilising inputs with specific frequency content to shine a selective light on a known portion of the oscillatory dynamics. If we can only observe a few percent of the dynamics, steering dynamics of known frequency content to be above the observability threshold could provide the ability to determine something about the underlying brain state in a reliable and repeatable manner. That said, while using evoked EEG for seizure prediction is at least a theoretically *possible* option (unlike with non-evoked conventional EEG), it is no less a daunting task.

8.2 Future Work

8.2.1 Clinical Evoked Prediction/ Early Seizure Detection

The findings of this thesis indicate that success in future development of seizure prediction from EEG signals should certainly be focused on the active approach to EEG acquisition. To this end data from evoked potentials in the epileptic brain must be analysed to inform further oscillator model development. We hope that such development can in turn inform the experimental procedure of active EEG towards successful clinical seizure prediction. Clinical trials of evoked EEG for seizure prediction are currently ongoing at St. Vincent's Hospital Melbourne. The brain has a range of existing inputs to complicate matters including: sensory input; modulation by hormones, metabolism and other chemicals. The advantage of including an evoked potential input is that most of these existing inputs can be tolerated as well, since we are only looking for correlation with our *known input*.

8.2.2 Seizure Control

Following the development of a reliable evoked EEG seizure prediction method, the natural extension of this work is towards seizure control. The balanced system property of the coupled oscillator model, in terms of matched observability and controllability in the few states that are accessible to our EEG electrodes, as discussed in Section 7.3, is promising for future development in design of input signals to desynchronise brain tissue for seizure control. Questions that remain for future work include: Can suitable input signals be found to prevent the spread of synchrony towards a seizure? Can perturbing signals disrupt the natural synchronisation cycle in brain tissue in such a manner as to not effect consciousness?

8.2.3 Observability of Synchronised Systems

Future avenues for research within observability of oscillatory systems remain for the seizure prediction and early onset detection problems, particularly concerning synchronisation of these systems.

- How synchronised must the underlying oscillators be to allow for the detection of that synchronisation at the EEG?
- Is it possible to identify a lower dimension sub-manifold of states that are clustered and synchronised?

Chapter A

Appendix

A.1 Comparison of Montages

This appendix section serves to provide further details on the choice of montage used for the EEG data used in Chapter 3 to explore time and frequency information in EEG.

This data set was take from patient 2 of the Freiburg data set (refer to table 1.3.2) and has a very strong 50Hz artefact as shown in the plot of raw data for channel 5 in Figure A.2 and channel 6 in Figure A.3. To try to remove this strong common mode artefact (an artefact present to an approximately equal degree on all channels), two montages are proposed: Bipolar and Common Average. The location of these electrodes on the cortex surface is shown in Figure A.1.

- **Bipolar Montage**
  For this montage the difference is taken between two adjacent electrode recordings. A zero mean function was also employed to mitigate DC offset problems as evident in raw recording of channel 6 at time 34 seconds (see Figure A.3). The resulting signal is a representation of the difference in activity between these two closely located areas. It can therefore be viewed as a representation of local brain activity under these electrodes. The contribution of the reference channel is excluded. Excluding the reference is advantageous for two reasons. Firstly, the reference is not an isolated reference. Secondly, the reference can be located in many different locations depending on local hospital convention. These locations vary from the use of a grid electrode

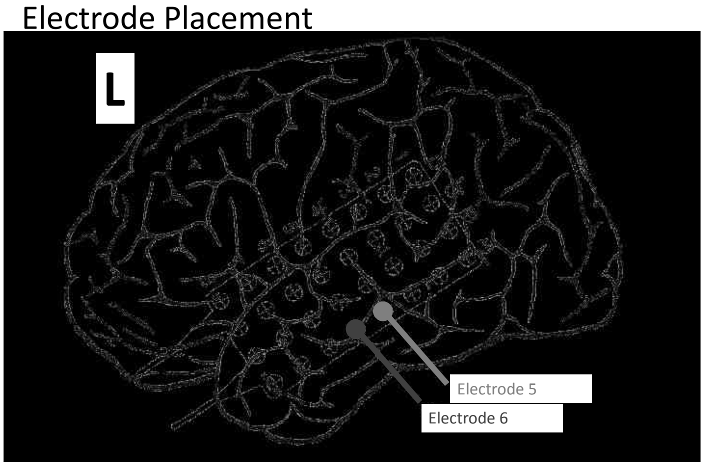

Figure A.1: Electrode placement, patient 2, Freiburg Data set

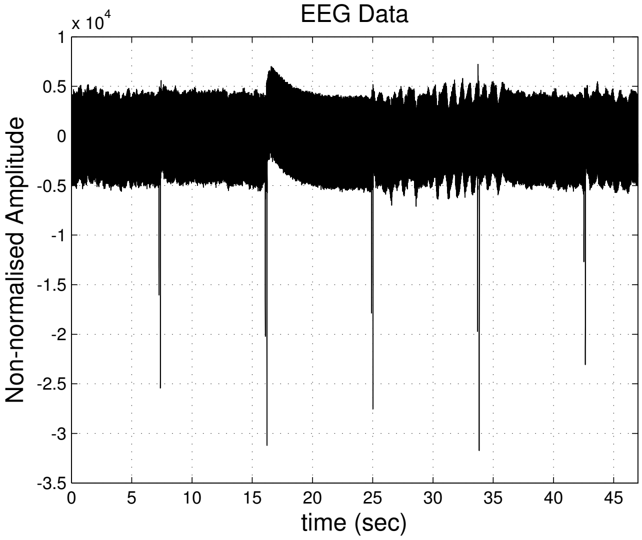

Figure A.2: Raw EEG recording, channel 5, patient 2, Freiburg Data set as reference to the use of an external scalp reference. Therefore, the reference is not necessarily indicative of the brain dynamics of interest and its effect is best removed from the signal under analysis. A plot of a Bipolar recording between channel 5 and channel 6 is shown in Figure A.4. One disadvantage of bipolar montaging is that if the channel pair cross a large sulcus or fold in the cortical tissue, the bipolar signal may no longer provide a representation of the local underlying brain function.

- **Common Average Montage**
  For this montage the average of all the other channels (not including the reference channels) is subtracted from the channel of interest. A zero mean function was also employed to mitigate DC offset problems as evident in in raw recording of channel 6 at time 34 seconds (see Figure A.3). The common average of the channels represents the reference information common to all channels. Subtracting this reference information means the resulting signal is a representation of the activity in the cortical area under the electrode. A plot of Common Average referenced recordings for channel 5 and channel 6 are shown in Figure A.5 and A.6 respectively. One disadvantage of common average referencing is that channels that become disconnected during recordings and exhibit a high level of noise can adversely skew the common average and effect all channels montaged in this manner. A solution to this is carefully continued monitoring of all channels and adjustment to the channels that make up the common average when necessary.

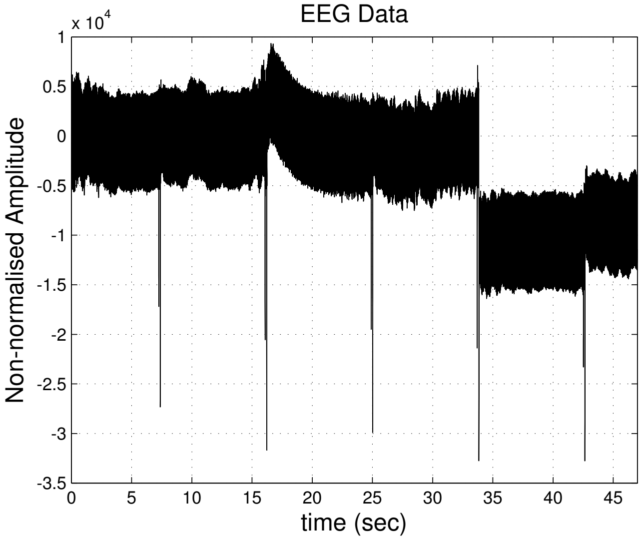

Figure A.3: Raw EEG recording, channel 6, patient 2, Freiburg Data set

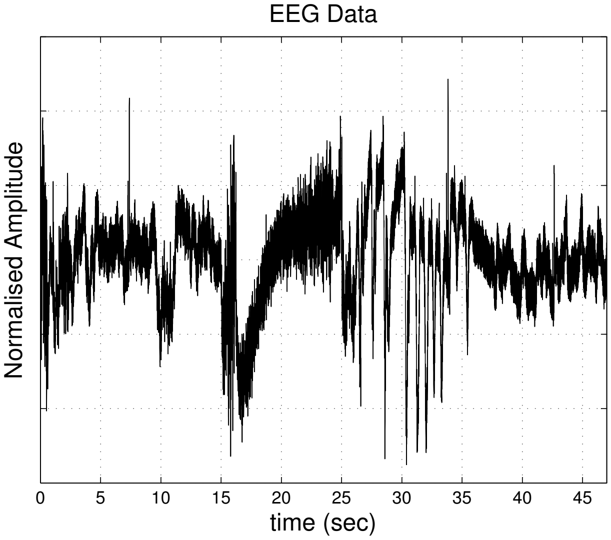

Figure A.4: Bipolar montaged EEG recording, channel 5-6, patient 2, Freiburg Data set

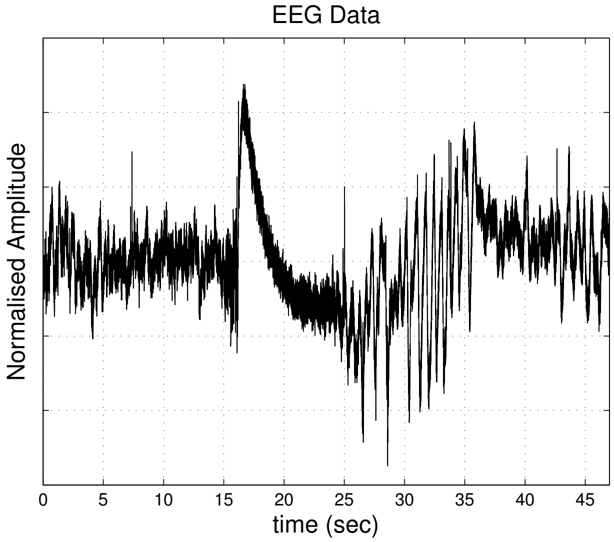

Figure A.5: Common Average montaged EEG recording, channel 5, patient 2, Freiburg Data set

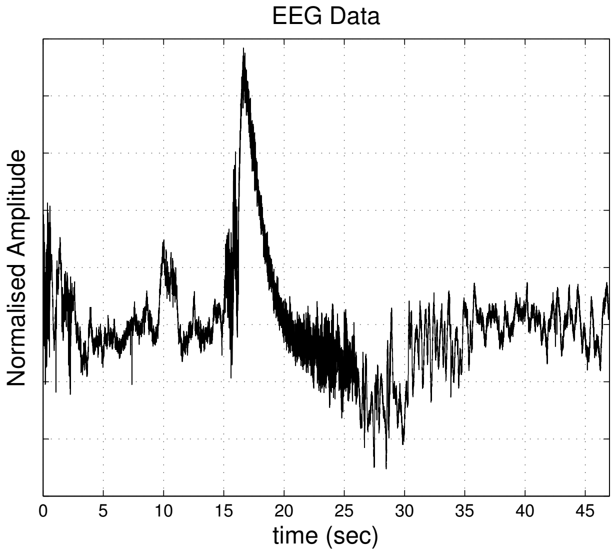

Figure A.6: Common Average montaged EEG recording, channel 6, patient 2, Freiburg Data set

A.2 Observability Conditions using Popov-Belevitch-Hautus (PBH) Test

This appendix section serves to provide further details on observability conditions using Popov-Belevitch-Hautus (PBH) test.

In section 5.3 it was found that row rank can only be lost in a coupled oscillator system matrix **A** if the row pairs k and $k+1$, for k odd, are themselves linearly dependent i.e. if,

$$\frac{-\lambda}{-\omega_k^2} = \frac{1}{-2\zeta_k\omega_k - \lambda}. \tag{A.2.1}$$

It was also found in section 5.3 that the λ in equation A.2.1 was the set of eigenvalues that can be found by solving the characteristic polynomials of each individual clock, $\lambda^2 + 2\zeta_i\omega_i + \omega_i^2 = 0$. The $2N$ eigenvalues, λ of the N uncoupled systems are

$$\lambda_{i\pm} = -\zeta_i\omega_i \pm \omega_i\sqrt{\zeta_i^2 - 1}, \text{ for } i = 1 \ldots N. \tag{A.2.2}$$

Considering the k^{th} clock with the i^{th} eigenvalue pair we can substitute $\lambda = \lambda_{i\pm}$ in equation A.2.1. This gives us,

$$\frac{\zeta_i\omega_i \pm \omega_i\sqrt{\zeta_i^2 - 1}}{-\omega_k^2} = \frac{1}{-2\zeta_k\omega_k + (\zeta_i\omega_i \pm \omega_i\sqrt{\zeta_i^2 - 1})} \tag{A.2.3}$$

which can be manipulated to,

$$(\zeta_i\omega_i \pm \omega_i\sqrt{\zeta_i^2 - 1})^2 - 2\zeta_k\omega_k(\zeta_i\omega_i \pm \omega_i\sqrt{\zeta_i^2 - 1}) + \omega_k^2 = 0. \tag{A.2.4}$$

By letting $x = \zeta_i\omega_i \pm \omega_i\sqrt{\zeta_i^2 - 1}$, equation A.2.4 becomes a quadratic in x with solution $x = \zeta_k\omega_k \pm \omega_k\sqrt{\zeta_k^2 - 1}$. The equality determining linear dependence, and thus rank deficiency is then,

$$x = \zeta_i\omega_i \pm \omega_i\sqrt{\zeta_i^2 - 1} = \zeta_k\omega_k \pm \omega_k\sqrt{\zeta_k^2 - 1}. \tag{A.2.5}$$

The system is observable via the PBH test provided the condition of A.2.5 does not occur. (i.e. provided the system natural frequencies and damping parameters do not overlap $\omega_i \neq \omega_j, \zeta_i \neq \zeta_j \ \forall i, j$)

A.3 Observability Conditions using Bezout Identity

As discussed in Chapter 5, the Bezout Identity tells us that polynomial matrices $\mathbf{D}(\lambda)$ and $\mathbf{N}(\lambda)$, will be right coprime if and only if there exists polynomial matrices $\mathbf{X}(\lambda)$ and $\mathbf{Y}(\lambda)$, such that,

$$\mathbf{X}(\lambda)\mathbf{N}(\lambda) + \mathbf{Y}(\lambda)\mathbf{D}(\lambda) = I, \tag{A.3.1}$$

where I is the Identity. Here we derive the necessary conditions for $\mathbf{D}(\lambda) = \lambda I - \mathbf{A}$ and $\mathbf{N}(\lambda) = \mathbf{C}$ to be right coprime and therefore the system pair $(\mathbf{A}, \mathbf{C})$ to be observable. The aim is to reduce the original matrix $[D(\lambda), N(\lambda)]'$ to $[I, \mathbf{0}]'$ where $'$ denotes prime, I is the identity matrix and $\mathbf{0}$ is a vector of zeros.

This can be achieved by applying successive elementary row operations to $[D(\lambda), N(\lambda)]'$. Elementary row operations, U_i, include either

1. Interchanging any 2 rows, $r_j \overset{swap}{\leftrightarrow} r_j$
2. Adding to a row, a polynomial multiple of another row, $r_i \rightarrow r_j + f(\lambda) r_j$
3. Scaling a row by any real or complex number, $r_i \rightarrow k r_j,\ for\ k \in \mathbb{C}$

The objective is to show for an arbitrary network of clocks that the conditions on parameters for which the system is observable would be quite unusual. Here this is illustrated for a network of 3 clocks under the following algebra-simplifying assumptions.

1. Uniform connection strength: $\alpha_{ij} = \alpha \; \forall \; i, j$
2. Each clock has the same damping parameter ζ
3. The system output is measured from a single clock: $\mathbf{C} = [0, c_1, 0, 0, \cdots, 0, 0]$ for $c_1 \in \Re$

Using the system matrix $\mathbf{A}$ from (4.3), we have,

$$\begin{pmatrix} D(\lambda) \\ N(\lambda) \end{pmatrix} = \begin{pmatrix} \lambda & -1 & 0 & 0 & 0 & 0 \\ \omega_1^2 + 2\alpha & \lambda + 2\zeta\omega_1 & -\alpha & 0 & -\alpha & 0 \\ 0 & 0 & \lambda & -1 & 0 & 0 \\ -\alpha & 0 & \omega_2^2 + 2\alpha & \lambda + 2\zeta\omega_2 & -\alpha & 0 \\ 0 & 0 & 0 & 0 & \lambda & -1 \\ -\alpha & 0 & -\alpha & 0 & \omega_3^2 + 2\alpha & \lambda + 2\zeta\omega_3 \\ 0 & c_1 & 0 & 0 & 0 & 0 \end{pmatrix}. \tag{A.3.2}$$

The structure of our coupled network has sufficient zero entries across $\mathbf{A} - \lambda I$ and $\mathbf{C}$ such that each column of $[\mathbf{A} - \lambda I, \mathbf{C}]'$ is independent of all the others except for a small non-generic set of unlikely (ω, ζ, α) combinations. The details of one possible path, $\mathbf{U}$, from $[\mathbf{A} - \lambda I, \mathbf{C}]'$ to $[I, \mathbf{0}]'$ are shown in table A.3.1. The system is observable provided that our $\mathbf{U}$ is a unimodular matrix. A polynomial matrix is unimodular if it's inverse is also a polynomial. This is the case if $det(\mathbf{U})$ equals a constant (i.e. $det(\mathbf{U}(\lambda)) \neq 0$ and $det(\mathbf{U}(\lambda)) \neq f(\lambda)$ for a polynomial function f). By solving $num(det(\mathbf{U})) = 0$ for the connection strength α, where num denotes the numerator, the resultant non-generic set was:

$$\begin{aligned} \alpha \in \{ & - & \frac{1}{3}\omega_1^2, \\ & - & \frac{\zeta^2}{24(-\omega_3 + \omega_2)} \left(f_1(\omega_1, \omega_2, \omega_3, \zeta) - \sqrt{f_2(\omega_1, \omega_2, \omega_3, \zeta)} \right), \\ & - & \frac{\zeta^2}{24(-\omega_3 + \omega_2)} \left(f_1(\omega_1, \omega_2, \omega_3, \zeta) + \sqrt{f_2(\omega_1, \omega_2, \omega_3, \zeta)} \right) \}, \end{aligned}$$

where

$$f_1(\omega_1, \omega_2, \omega_3, \zeta) = -8\omega_2^2\zeta^2\omega_3 + \omega_2\omega_1^2 + \omega_1^2\omega_3 - 8\zeta^2\omega_3\omega_1^2 + 2\omega_2^2\omega_3 + 4\omega_2\omega_1^2\zeta^2 + 2\omega_2^3,$$

$$\begin{aligned} f_2(\omega_1, \omega_2, \omega_3, \zeta) &= & 4\omega_2^6 - 32\omega_2^5\zeta^2\omega_3 + 8\omega_2^5\omega_3 - 32\omega_2^4\zeta^2\omega_3^2 + 4\omega_2^4\omega_1^2 \\ & - & 32\omega_2^4\omega_1^2\zeta^2 + 64\omega_2^4\zeta^4\omega_3^2 + 4\omega_2^4\omega_3^2 + 128\omega_2^3\omega_1^2\zeta^4\omega_3 \\ & - & 32\omega_2^3\zeta^2\omega_3\omega_1^2 + 8\omega_2^3\omega_1^2\omega_3 + 4\omega_2^2\omega_3^2\omega_1^2 + \omega_2^2\omega_1^4 \\ & + & 8\omega_2^2\omega_1^4\zeta^2 - 64\omega_2^2\zeta^4\omega_3^2\omega_1^2 + 16\omega_2^2\omega_1^4\zeta^4 - 64\omega_2\omega_1^4\zeta^4\omega_3 \\ & - & 8\omega_2\zeta^2\omega_1^4\omega_3 + 2\omega_1^4\omega_3\omega_2 + \omega_3^2\omega_1^4 + 64\zeta^4\omega_3^2\omega_1^4 - 16\omega_1^4\zeta^2\omega_3^2. \end{aligned} \quad \text{(A.3.3)}$$

Elementary row operation	$\mathbf{U}(\lambda)\begin{pmatrix} D(\lambda) \\ N(\lambda) \end{pmatrix}$ where $(\mathbf{U}(\lambda) = U_n \ldots U_2 U_1)$
U_1 : $r_1 - > r_1 + \frac{\lambda}{\alpha} r_4$ $U_1 = \begin{pmatrix} 1 & 0 & 0 & \frac{\lambda}{\alpha} & 0 & 0 & 0 \\ 0 & 1 & 0 & 0 & 0 & 0 & 0 \\ 0 & 0 & 1 & 0 & 0 & 0 & 0 \\ 0 & 0 & 0 & 1 & 0 & 0 & 0 \\ 0 & 0 & 0 & 0 & 1 & 0 & 0 \\ 0 & 0 & 0 & 0 & 0 & 1 & 0 \\ 0 & 0 & 0 & 0 & 0 & 0 & 1 \end{pmatrix}$	$\begin{pmatrix} 0 & -1 & \frac{\lambda}{\alpha}(w_2^2 + 2\alpha) & \frac{\lambda}{\alpha}(\lambda + 2\zeta\omega_2) & -\lambda & 0 \\ \omega_1^2 + 2\alpha & \lambda + 2\zeta\omega_1 & -\alpha & 0 & -\alpha & 0 \\ 0 & 0 & \lambda & -1 & 0 & 0 \\ -\alpha & 0 & \omega_2^2 + 2\alpha & \lambda + 2\zeta\omega_2 & -\alpha & 0 \\ 0 & 0 & 0 & 0 & \lambda & -1 \\ -\alpha & 0 & -\alpha & 0 & \omega_3^2 + 2\alpha & \lambda + 2\zeta\omega_3 \\ 0 & c_1 & 0 & 0 & 0 & 0 \end{pmatrix}$
U_2 : $r_1 \overset{swap}{\leftrightarrow} r_2$ $U_2 = \begin{pmatrix} 0 & 1 & 0 & 0 & 0 & 0 & 0 \\ 1 & 0 & 0 & 0 & 0 & 0 & 0 \\ 0 & 0 & 1 & 0 & 0 & 0 & 0 \\ 0 & 0 & 0 & 1 & 0 & 0 & 0 \\ 0 & 0 & 0 & 0 & 1 & 0 & 0 \\ 0 & 0 & 0 & 0 & 0 & 1 & 0 \\ 0 & 0 & 0 & 0 & 0 & 0 & 1 \end{pmatrix}$	$\begin{pmatrix} \omega_1^2 + 2\alpha & \lambda + 2\zeta\omega_1 & -\alpha & 0 & -\alpha & 0 \\ 0 & -1 & \frac{\lambda}{\alpha}(w_2^2 + 2\alpha) & \frac{\lambda}{\alpha}(\lambda + 2\zeta\omega_2) & -\lambda & 0 \\ 0 & 0 & \lambda & -1 & 0 & 0 \\ -\alpha & 0 & \omega_2^2 + 2\alpha & \lambda + 2\zeta\omega_2 & -\alpha & 0 \\ 0 & 0 & 0 & 0 & \lambda & -1 \\ -\alpha & 0 & -\alpha & 0 & \omega_3^2 + 2\alpha & \lambda + 2\zeta\omega_3 \\ 0 & c_1 & 0 & 0 & 0 & 0 \end{pmatrix}$
$U_3 \& U_4$: $r_3 \overset{swap}{\leftrightarrow} r_4$ $r_5 \overset{swap}{\leftrightarrow} r_6$ $U_4 U_3 = \begin{pmatrix} 1 & 0 & 0 & 0 & 0 & 0 & 0 \\ 0 & 1 & 0 & 0 & 0 & 0 & 0 \\ 0 & 0 & 0 & 1 & 0 & 0 & 0 \\ 0 & 0 & 1 & 0 & 0 & 0 & 0 \\ 0 & 0 & 0 & 0 & 0 & 1 & 0 \\ 0 & 0 & 0 & 0 & 1 & 0 & 0 \\ 0 & 0 & 0 & 0 & 0 & 0 & 1 \end{pmatrix}$	$\begin{pmatrix} \omega_1^2 + 2\alpha & \lambda + 2\zeta\omega_1 & -\alpha & 0 & -\alpha & 0 \\ 0 & -1 & \frac{\lambda}{\alpha}(w_2^2 + 2\alpha) & \frac{\lambda}{\alpha}(\lambda + 2\zeta\omega_2) & -\lambda & 0 \\ -\alpha & 0 & \omega_2^2 + 2\alpha & \lambda + 2\zeta\omega_2 & -\alpha & 0 \\ 0 & 0 & \lambda & -1 & 0 & 0 \\ -\alpha & 0 & -\alpha & 0 & \omega_3^2 + 2\alpha & \lambda + 2\zeta\omega_3 \\ 0 & 0 & 0 & 0 & \lambda & -1 \\ 0 & c_1 & 0 & 0 & 0 & 0 \end{pmatrix}$
U_5 : $r_1 \longrightarrow \frac{r_1}{\omega_1^2 + 2\alpha}$ $U_5 = \begin{pmatrix} \frac{1}{w_1^2 + 2\alpha} & 0 & 0 & 0 & 0 & 0 & 0 \\ 0 & 1 & 0 & 0 & 0 & 0 & 0 \\ 0 & 0 & 1 & 0 & 0 & 0 & 0 \\ 0 & 0 & 0 & 1 & 0 & 0 & 0 \\ 0 & 0 & 0 & 0 & 1 & 0 & 0 \\ 0 & 0 & 0 & 0 & 0 & 1 & 0 \\ 0 & 0 & 0 & 0 & 0 & 0 & 1 \end{pmatrix}$	$\begin{pmatrix} 1 & \frac{\lambda + 2\zeta\omega_1}{\omega_1^2 + 2\alpha} & \frac{-\alpha}{\omega_1^2 + 2\alpha} & 0 & \frac{-\alpha}{\omega_1^2 + 2\alpha} & 0 \\ 0 & -1 & \frac{\lambda}{\alpha}(w_2^2 + 2\alpha) & \frac{\lambda}{\alpha}(\lambda + 2\zeta\omega_2) & -\lambda & 0 \\ -\alpha & 0 & \omega_2^2 + 2\alpha & \lambda + 2\zeta\omega_2 & -\alpha & 0 \\ 0 & 0 & \lambda & -1 & 0 & 0 \\ -\alpha & 0 & -\alpha & 0 & \omega_3^2 + 2\alpha & \lambda + 2\zeta\omega_3 \\ 0 & 0 & 0 & 0 & \lambda & -1 \\ 0 & c_1 & 0 & 0 & 0 & 0 \end{pmatrix}$
U_6 : $r_3 \longrightarrow r_3 - r_5$ $U_6 = \begin{pmatrix} 1 & 0 & 0 & 0 & 0 & 0 & 0 \\ 0 & 1 & 0 & 0 & 0 & 0 & 0 \\ 0 & 0 & 1 & 0 & -1 & 0 & 0 \\ 0 & 0 & 0 & 1 & 0 & 0 & 0 \\ 0 & 0 & 0 & 0 & 1 & 0 & 0 \\ 0 & 0 & 0 & 0 & 0 & 1 & 0 \\ 0 & 0 & 0 & 0 & 0 & 0 & 1 \end{pmatrix}$	$\begin{pmatrix} 1 & \frac{\lambda + 2\zeta\omega_1}{\omega_1^2 + 2\alpha} & \frac{-\alpha}{\omega_1^2 + 2\alpha} & 0 & \frac{-\alpha}{\omega_1^2 + 2\alpha} & 0 \\ 0 & -1 & \frac{\lambda}{\alpha}(w_2^2 + 2\alpha) & \frac{\lambda}{\alpha}(\lambda + 2\zeta\omega_2) & -\lambda & 0 \\ 0 & 0 & \omega_2^2 + 3\alpha & \lambda + 2\zeta\omega_2 & -(\omega_3^2 - 3\alpha) & -(\lambda + 2\zeta\omega_3) \\ 0 & 0 & \lambda & -1 & 0 & 0 \\ -\alpha & 0 & -\alpha & 0 & \omega_3^2 + 2\alpha & \lambda + 2\zeta\omega_3 \\ 0 & 0 & 0 & 0 & \lambda & -1 \\ 0 & c_1 & 0 & 0 & 0 & 0 \end{pmatrix}$
U_7 : $r_5 \longrightarrow r_5 + \alpha r_1$ $U_7 = \begin{pmatrix} 1 & 0 & 0 & 0 & 0 & 0 & 0 \\ 0 & 1 & 0 & 0 & 0 & 0 & 0 \\ 0 & 0 & 1 & 0 & 0 & 0 & 0 \\ 0 & 0 & 0 & 1 & 0 & 0 & 0 \\ \alpha & 0 & 0 & 0 & 1 & 0 & 0 \\ 0 & 0 & 0 & 0 & 0 & 1 & 0 \\ 0 & 0 & 0 & 0 & 0 & 0 & 1 \end{pmatrix}$	$k_1 \in \Re : k_1 = w_3^2 + 2\alpha - \frac{\alpha^2}{\omega_1^2 + 2\alpha}$ $k_2 \in \Re : k_2 = -\alpha - \frac{\alpha^2}{\omega_1^2 + 2\alpha}$ $\begin{pmatrix} 1 & \frac{\lambda + 2\zeta\omega_1}{\omega_1^2 + 2\alpha} & \frac{-\alpha}{\omega_1^2 + 2\alpha} & 0 & \frac{-\alpha}{\omega_1^2 + 2\alpha} & 0 \\ 0 & -1 & \frac{\lambda}{\alpha}(w_2^2 + 2\alpha) & \frac{\lambda}{\alpha}(\lambda + 2\zeta\omega_2) & -\lambda & 0 \\ 0 & 0 & \omega_2^2 + 3\alpha & \lambda + 2\zeta\omega_2 & -(\omega_3^2 - 3\alpha) & -(\lambda + 2\zeta\omega_3) \\ 0 & 0 & \lambda & -1 & 0 & 0 \\ 0 & \frac{\alpha(\lambda + 2\zeta\omega_1)}{w_1^2 + 2\alpha} & k_2 & 0 & k_1 & \lambda + 2\zeta\omega_3 \\ 0 & 0 & 0 & 0 & \lambda & -1 \\ 0 & c_1 & 0 & 0 & 0 & 0 \end{pmatrix}$

Table A.3.1: Finding the set (α, ω, ζ) for which networked clocks are not fully observable

Table continued $\cdots$

Elementary row operation	$\mathbf{U}(\lambda)\begin{pmatrix} D(\lambda) \\ N(\lambda) \end{pmatrix}$ where $(\mathbf{U}(\lambda) = U_n \dots U_2 U_1)$
U_8 : $r_5 \rightarrow r_5 - \frac{1}{c_1}\frac{\alpha}{w_1^2+2\alpha}(\lambda + 2\zeta\omega_1)r_7$ $U_8 = \begin{pmatrix} 1 & 0 & 0 & 0 & 0 & 0 & 0 \\ 0 & 1 & 0 & 0 & 0 & 0 & 0 \\ 0 & 0 & 1 & 0 & 0 & 0 & 0 \\ 0 & 0 & 0 & 1 & 0 & 0 & 0 \\ 0 & 0 & 0 & 0 & 1 & 0 & \frac{1}{c_1}\frac{\alpha(\lambda+2\zeta\omega_1)}{w_1^2+2\alpha} \\ 0 & 0 & 0 & 0 & 0 & 1 & 0 \\ 0 & 0 & 0 & 0 & 0 & 0 & 1 \end{pmatrix}$	$\begin{pmatrix} 1 & \frac{\lambda+2\zeta\omega_1}{\omega_1^2+2\alpha} & \frac{-\alpha}{\omega_1^2+2\alpha} & 0 & \frac{-\alpha}{\omega_1^2+2\alpha} & 0 \\ 0 & -1 & \frac{\lambda}{\alpha}(w_2^2+2\alpha) & \frac{\lambda}{\alpha}(\lambda+2\zeta\omega_2) & -\lambda & 0 \\ 0 & 0 & \omega_2^2+3\alpha & \lambda+2\zeta\omega_2 & -(\omega_3^2-3\alpha) & -(\lambda+2\zeta\omega_3) \\ 0 & 0 & \lambda & -1 & 0 & 0 \\ 0 & 0 & k_2 & 0 & k_1 & \lambda+2\zeta\omega_3 \\ 0 & 0 & 0 & 0 & \lambda & -1 \\ 0 & c_1 & 0 & 0 & 0 & 0 \end{pmatrix}$
U_9 : $r_1 \rightarrow r_1 - \frac{1}{c_1}\frac{\lambda+2\zeta\omega_1}{w_1^2+2\alpha}r_7$ $U_9 = \begin{pmatrix} 1 & 0 & 0 & 0 & 0 & 0 & \frac{1}{c_1}\frac{\lambda+2\zeta\omega_1}{w_1^2+2\alpha} \\ 0 & 1 & 0 & 0 & 0 & 0 & 0 \\ 0 & 0 & 1 & 0 & 0 & 0 & 0 \\ 0 & 0 & 0 & 1 & 0 & 0 & 0 \\ 0 & 0 & 0 & 0 & 1 & 0 & 0 \\ 0 & 0 & 0 & 0 & 0 & 1 & 0 \\ 0 & 0 & 0 & 0 & 0 & 0 & 1 \end{pmatrix}$	$\begin{pmatrix} 1 & 0 & \frac{-\alpha}{\omega_1^2+2\alpha} & 0 & \frac{-\alpha}{\omega_1^2+2\alpha} & 0 \\ 0 & -1 & \frac{\lambda}{\alpha}(w_2^2+2\alpha) & \frac{\lambda}{\alpha}(\lambda+2\zeta\omega_2) & -\lambda & 0 \\ 0 & 0 & \omega_2^2+3\alpha & \lambda+2\zeta\omega_2 & -(\omega_3^2-3\alpha) & -(\lambda+2\zeta\omega_3) \\ 0 & 0 & \lambda & -1 & 0 & 0 \\ 0 & 0 & k_2 & 0 & k_1 & \lambda+2\zeta\omega_3 \\ 0 & 0 & 0 & 0 & \lambda & -1 \\ 0 & c_1 & 0 & 0 & 0 & 0 \end{pmatrix}$
U_{10} : $r_4 \rightarrow r_4 - \frac{\lambda}{k_2}r_5$ $U_{10} = \begin{pmatrix} 1 & 0 & 0 & 0 & 0 & 0 & 0 \\ 0 & 1 & 0 & 0 & 0 & 0 & 0 \\ 0 & 0 & 1 & 0 & 0 & 0 & 0 \\ 0 & 0 & 0 & 1 & -\frac{\lambda}{k_2} & 0 & 0 \\ 0 & 0 & 0 & 0 & 1 & 0 & 0 \\ 0 & 0 & 0 & 0 & 0 & 1 & 0 \\ 0 & 0 & 0 & 0 & 0 & 0 & 1 \end{pmatrix}$	$\begin{pmatrix} 1 & 0 & \frac{-\alpha}{\omega_1^2+2\alpha} & 0 & \frac{-\alpha}{\omega_1^2+2\alpha} & 0 \\ 0 & -1 & \frac{\lambda}{\alpha}(w_2^2+2\alpha) & \frac{\lambda}{\alpha}(\lambda+2\zeta\omega_2) & -\lambda & 0 \\ 0 & 0 & \omega_2^2+3\alpha & \lambda+2\zeta\omega_2 & -(\omega_3^2-3\alpha) & -(\lambda+2\zeta\omega_3) \\ 0 & 0 & 0 & -1 & -\frac{k_1\lambda}{k_2} & -\frac{\lambda(\lambda+2\zeta\omega_3)}{k_2} \\ 0 & 0 & k_2 & 0 & k_1 & \lambda+2\zeta\omega_3 \\ 0 & 0 & 0 & 0 & \lambda & -1 \\ 0 & c_1 & 0 & 0 & 0 & 0 \end{pmatrix}$
U_{11} : $r_5 \rightarrow r_5 - \frac{k_2}{(\omega_2^2+3\alpha)}r_3$ $U_{11} = \begin{pmatrix} 1 & 0 & 0 & 0 & 0 & 0 & 0 \\ 0 & 1 & 0 & 0 & 0 & 0 & 0 \\ 0 & 0 & 1 & 0 & 0 & 0 & 0 \\ 0 & 0 & 0 & 1 & 0 & 0 & 0 \\ 0 & 0 & -\frac{k_2}{(\omega_2^2+3\alpha)} & 0 & 1 & 0 & 0 \\ 0 & 0 & 0 & 0 & 0 & 1 & 0 \\ 0 & 0 & 0 & 0 & 0 & 0 & 1 \end{pmatrix}$	P_2, a polynomial function in λ, $P_2(\lambda) = \frac{k_2(\lambda+2\zeta\omega_2)}{(\omega_2^2+3\alpha)}$ P_3, a polynomial function in λ, $P_3(\lambda) = \frac{k_2(\lambda+2\zeta\omega_3)}{(\omega_2^2+3\alpha)}$ $\begin{pmatrix} 1 & 0 & \frac{-\alpha}{\omega_1^2+2\alpha} & 0 & \frac{-\alpha}{\omega_1^2+2\alpha} & 0 \\ 0 & -1 & \frac{\lambda}{\alpha}(w_2^2+2\alpha) & \frac{\lambda}{\alpha}(\lambda+2\zeta\omega_2) & -\lambda & 0 \\ 0 & 0 & \omega_2^2+3\alpha & \lambda+2\zeta\omega_2 & -(\omega_3^2-3\alpha) & -(\lambda+2\zeta\omega_3) \\ 0 & 0 & 0 & -1 & -\frac{k_1\lambda}{k_2} & -\frac{\lambda(\lambda+2\zeta\omega_3)}{k_2} \\ 0 & 0 & 0 & P_2 & k_1 - \frac{\lambda k_2}{(\omega_2^2+3\alpha)} & P_3 \\ 0 & 0 & 0 & 0 & \lambda & -1 \\ 0 & c_1 & 0 & 0 & 0 & 0 \end{pmatrix}$
U_{12} : $r_2 \rightarrow r_2 + r_6$ $U_{12} = \begin{pmatrix} 1 & 0 & 0 & 0 & 0 & 0 & 0 \\ 0 & 1 & 0 & 0 & 0 & 1 & 0 \\ 0 & 0 & 1 & 0 & 0 & 0 & 0 \\ 0 & 0 & 0 & 1 & 0 & 0 & 0 \\ 0 & 0 & 0 & 0 & 1 & 0 & 0 \\ 0 & 0 & 0 & 0 & 0 & 1 & 0 \\ 0 & 0 & 0 & 0 & 0 & 0 & 1 \end{pmatrix}$	$\begin{pmatrix} 1 & 0 & \frac{-\alpha}{\omega_1^2+2\alpha} & 0 & \frac{-\alpha}{\omega_1^2+2\alpha} & 0 \\ 0 & -1 & \frac{\lambda}{\alpha}(w_2^2+2\alpha) & \frac{\lambda}{\alpha}(\lambda+2\zeta\omega_2) & 0 & -1 \\ 0 & 0 & \omega_2^2+3\alpha & \lambda+2\zeta\omega_2 & -(\omega_3^2-3\alpha) & -(\lambda+2\zeta\omega_3) \\ 0 & 0 & 0 & -1 & -\frac{k_1\lambda}{k_2} & -\frac{\lambda(\lambda+2\zeta\omega_3)}{k_2} \\ 0 & 0 & 0 & P_2 & k_1 - \frac{\lambda k_2}{(\omega_2^2+3\alpha)} & P_3 \\ 0 & 0 & 0 & 0 & \lambda & -1 \\ 0 & c_1 & 0 & 0 & 0 & 0 \end{pmatrix}$
U_{13} : $r_4 \rightarrow r_4 + \frac{k_1}{k_2}r_6$ $U_{13} = \begin{pmatrix} 1 & 0 & 0 & 0 & 0 & 0 & 0 \\ 0 & 1 & 0 & 0 & 0 & 0 & 0 \\ 0 & 0 & 1 & 0 & 0 & 0 & 0 \\ 0 & 0 & 0 & 1 & 0 & \frac{k_1}{k_2} & 0 \\ 0 & 0 & 0 & 0 & 1 & 0 & 0 \\ 0 & 0 & 0 & 0 & 0 & 1 & 0 \\ 0 & 0 & 0 & 0 & 0 & 0 & 1 \end{pmatrix}$	$P_0(\lambda) = -\frac{k_1}{k_2} - \frac{\lambda(\lambda+2\zeta\omega_3)}{k_2}$ $\begin{pmatrix} 1 & 0 & \frac{-\alpha}{\omega_1^2+2\alpha} & 0 & \frac{-\alpha}{\omega_1^2+2\alpha} & 0 \\ 0 & -1 & \frac{\lambda}{\alpha}(w_2^2+2\alpha) & \frac{\lambda}{\alpha}(\lambda+2\zeta\omega_2) & 0 & -1 \\ 0 & 0 & \omega_2^2+3\alpha & \lambda+2\zeta\omega_2 & -(\omega_3^2-3\alpha) & -(\lambda+2\zeta\omega_3) \\ 0 & 0 & 0 & -1 & 0 & P_0 \\ 0 & 0 & 0 & P_2 & k_1 - \frac{\lambda k_2}{(\omega_2^2+3\alpha)} & P_3 \\ 0 & 0 & 0 & 0 & \lambda & -1 \\ 0 & c_1 & 0 & 0 & 0 & 0 \end{pmatrix}$

Table A.3.1: Finding the set (α, ω, ζ) for which networked clocks are not fully observable

Table continued $\cdots$ Elementary row operation	$\mathbf{U}(\lambda)\begin{pmatrix} D(\lambda) \\ N(\lambda) \end{pmatrix}$ where $(\mathbf{U}(\lambda) = U_n \ldots U_2 U_1)$
$U_{14}:$ $r_2 \rightarrow r_2 + \frac{\lambda(\lambda+2\zeta\omega_2)}{\alpha} r_4$ $U_{14} = \begin{pmatrix} 1 & 0 & 0 & \frac{\lambda(\lambda+2\zeta\omega_2)}{\alpha} & 0 & 0 & 0 \\ 0 & 1 & 0 & 0 & 0 & 0 & 0 \\ 0 & 0 & 1 & 0 & 0 & 0 & 0 \\ 0 & 0 & 0 & 1 & 0 & 0 & 0 \\ 0 & 0 & 0 & 0 & 1 & 0 & 0 \\ 0 & 0 & 0 & 0 & 0 & 1 & 0 \\ 0 & 0 & 0 & 0 & 0 & 0 & 1 \end{pmatrix}$	$P_1(\lambda) = -1 - \frac{k_1}{k_2}\frac{\lambda(\lambda+2\zeta\omega_2)}{\alpha}$ $\begin{pmatrix} 1 & 0 & \frac{-\alpha}{\omega_1^2+2\alpha} & 0 & \frac{-\alpha}{\omega_1^2+2\alpha} & 0 \\ 0 & -1 & \frac{\lambda}{\alpha}(w_2^2+2\alpha) & 0 & 0 & P_1 \\ 0 & 0 & \omega_2^2+3\alpha & \lambda+2\zeta\omega_2 & -(\omega_3^2-3\alpha) & -(\lambda+2\zeta\omega_3) \\ 0 & 0 & 0 & -1 & 0 & P_0 \\ 0 & 0 & 0 & P_2 & k_1 - \frac{\lambda k_2}{(\omega_2^2+3\alpha)} & P_3 \\ 0 & 0 & 0 & 0 & \lambda & -1 \\ 0 & c_1 & 0 & 0 & 0 & 0 \end{pmatrix}$
$U_{15}:$ $r_7 \rightarrow r_7 + c_1 r_2$ $U_{15} = \begin{pmatrix} 1 & 0 & 0 & 0 & 0 & 0 & 0 \\ 0 & 1 & 0 & 0 & 0 & 0 & 0 \\ 0 & 0 & 1 & 0 & 0 & 0 & 0 \\ 0 & 0 & 0 & 1 & 0 & 0 & 0 \\ 0 & 0 & 0 & 0 & 1 & 0 & 0 \\ 0 & 0 & 0 & 0 & 0 & 1 & 0 \\ 0 & c_1 & 0 & 0 & 0 & 0 & 1 \end{pmatrix}$	$\begin{pmatrix} 1 & 0 & \frac{-\alpha}{\omega_1^2+2\alpha} & 0 & \frac{-\alpha}{\omega_1^2+2\alpha} & 0 \\ 0 & -1 & \frac{\lambda}{\alpha}(w_2^2+2\alpha) & 0 & 0 & P_1 \\ 0 & 0 & \omega_2^2+3\alpha & \lambda+2\zeta\omega_2 & -(\omega_3^2-3\alpha) & -(\lambda+2\zeta\omega_3) \\ 0 & 0 & 0 & -1 & 0 & P_0 \\ 0 & 0 & 0 & P_2 & k_1 - \frac{\lambda k_2}{(\omega_2^2+3\alpha)} & P_3 \\ 0 & 0 & 0 & 0 & \lambda & -1 \\ 0 & 0 & \frac{c_1\lambda(\omega_2^2+2\alpha)}{\alpha} & 0 & 0 & 0 \end{pmatrix}$
$U_{16}:$ $r_2 \rightarrow r_2 - \frac{1}{c_1} r_7$ $U_{16} = \begin{pmatrix} 1 & 0 & 0 & 0 & 0 & 0 & -\frac{1}{c_1} \\ 0 & 1 & 0 & 0 & 0 & 0 & 0 \\ 0 & 0 & 1 & 0 & 0 & 0 & 0 \\ 0 & 0 & 0 & 1 & 0 & 0 & 0 \\ 0 & 0 & 0 & 0 & 1 & 0 & 0 \\ 0 & 0 & 0 & 0 & 0 & 1 & 0 \\ 0 & 0 & 0 & 0 & 0 & 0 & 1 \end{pmatrix}$	$\begin{pmatrix} 1 & 0 & \frac{-\alpha}{\omega_1^2+2\alpha} & 0 & \frac{-\alpha}{\omega_1^2+2\alpha} & 0 \\ 0 & -1 & 0 & 0 & 0 & 0 \\ 0 & 0 & \omega_2^2+3\alpha & \lambda+2\zeta\omega_2 & -(\omega_3^2-3\alpha) & -(\lambda+2\zeta\omega_3) \\ 0 & 0 & 0 & -1 & 0 & P_0 \\ 0 & 0 & 0 & P_2 & k_1 - \frac{\lambda k_2}{(\omega_2^2+3\alpha)} & P_3 \\ 0 & 0 & 0 & 0 & \lambda & -1 \\ 0 & 0 & \frac{c_1\lambda(\omega_2^2+2\alpha)}{\alpha} & 0 & 0 & 0 \end{pmatrix}$
$U_{17}:$ $r_3 \rightarrow r_3 + (\lambda+2\zeta\omega_2) r_4$ $U_{17} = \begin{pmatrix} 1 & 0 & 0 & 0 & 0 & 0 & 0 \\ 0 & 1 & 0 & 0 & 0 & 0 & 0 \\ 0 & 0 & 1 & (\lambda+2\zeta\omega_2) & 0 & 0 & 0 \\ 0 & 0 & 0 & 1 & 0 & 0 & 0 \\ 0 & 0 & 0 & 0 & 1 & 0 & 0 \\ 0 & 0 & 0 & 0 & 0 & 1 & 0 \\ 0 & 0 & 0 & 0 & 0 & 0 & 1 \end{pmatrix}$	$P_4(\lambda) = -(\lambda+2\zeta\omega_3) - \frac{k_1(\lambda+2\zeta\omega_2)}{k_2}$ $\begin{pmatrix} 1 & 0 & \frac{-\alpha}{\omega_1^2+2\alpha} & 0 & \frac{-\alpha}{\omega_1^2+2\alpha} & 0 \\ 0 & -1 & 0 & 0 & 0 & 0 \\ 0 & 0 & \omega_2^2+3\alpha & 0 & -(\omega_3^2-3\alpha) & P_4 \\ 0 & 0 & 0 & -1 & 0 & P_0 \\ 0 & 0 & 0 & P_2 & k_1 - \frac{\lambda k_2}{(\omega_2^2+3\alpha)} & P_3 \\ 0 & 0 & 0 & 0 & \lambda & -1 \\ 0 & 0 & \frac{c_1\lambda(\omega_2^2+2\alpha)}{\alpha} & 0 & 0 & 0 \end{pmatrix}$
$U_{18}:$ $r_5 \rightarrow r_5 + P_2 r_4$ $U_{18} = \begin{pmatrix} 1 & 0 & 0 & 0 & 0 & 0 & 0 \\ 0 & 1 & 0 & 0 & 0 & 0 & 0 \\ 0 & 0 & 1 & 0 & 0 & 0 & 0 \\ 0 & 0 & 0 & 1 & 0 & 0 & 0 \\ 0 & 0 & 0 & P_2 & 1 & 0 & 0 \\ 0 & 0 & 0 & 0 & 0 & 1 & 0 \\ 0 & 0 & 0 & 0 & 0 & 0 & 1 \end{pmatrix}$	$\begin{pmatrix} 1 & 0 & \frac{-\alpha}{\omega_1^2+2\alpha} & 0 & \frac{-\alpha}{\omega_1^2+2\alpha} & 0 \\ 0 & -1 & 0 & 0 & 0 & 0 \\ 0 & 0 & \omega_2^2+3\alpha & 0 & -(\omega_3^2-3\alpha) & P_4 \\ 0 & 0 & 0 & -1 & 0 & P_0 \\ 0 & 0 & 0 & 0 & k_1 - \frac{\lambda k_2}{(\omega_2^2+3\alpha)} & P_3 + P_0 P_2 \\ 0 & 0 & 0 & 0 & \lambda & -1 \\ 0 & 0 & \frac{c_1\lambda(\omega_2^2+2\alpha)}{\alpha} & 0 & 0 & 0 \end{pmatrix}$
$U_{19}:$ $r_7 \rightarrow r_7 - \frac{c_1\lambda}{\alpha}\frac{\omega_2^2+2\alpha}{\omega_2^2+3\alpha} r_3$ $U_{19} = \begin{pmatrix} 1 & 0 & 0 & 0 & 0 & 0 & 0 \\ 0 & 1 & 0 & 0 & 0 & 0 & 0 \\ 0 & 0 & 1 & 0 & 0 & 0 & 0 \\ 0 & 0 & 0 & 1 & 0 & 0 & 0 \\ 0 & 0 & 0 & 0 & 1 & 0 & 0 \\ 0 & 0 & 0 & 0 & 0 & 1 & 0 \\ 0 & 0 & -\frac{c_1\lambda}{\alpha}\frac{\omega_2^2+2\alpha}{\omega_2^2+3\alpha} & 0 & 0 & 0 & 1 \end{pmatrix}$	$\begin{pmatrix} 1 & 0 & \frac{-\alpha}{\omega_1^2+2\alpha} & 0 & \frac{-\alpha}{\omega_1^2+2\alpha} & 0 \\ 0 & -1 & 0 & 0 & 0 & 0 \\ 0 & 0 & \omega_2^2+3\alpha & 0 & -(\omega_3^2-3\alpha) & P_4 \\ 0 & 0 & 0 & -1 & 0 & P_0 \\ 0 & 0 & 0 & 0 & k_1 - \frac{\lambda k_2}{(\omega_2^2+3\alpha)} & P_3 + P_0 P_2 \\ 0 & 0 & 0 & 0 & \lambda & -1 \\ 0 & 0 & 0 & 0 & \frac{-c_1\lambda(\omega_3^2+3\alpha)}{\alpha}\frac{\omega_2^2+2\alpha}{\omega_2^2+3\alpha} & c_1 P_1 - \frac{c_1\lambda(\omega_2^2+2\alpha)P_4}{\alpha(\omega_2^2+3\alpha)} \end{pmatrix}$

Table A.3.1: Finding the set (α, ω, ζ) for which networked clocks are not fully observable

Table continued $\cdots$ Elementary row operation	$\mathbf{U}(\lambda)\begin{pmatrix} D(\lambda) \\ N(\lambda) \end{pmatrix}$ where $(\mathbf{U}(\lambda) = U_n \ldots U_2 U_1)$
$U_{20}:$ $r_7 \rightarrow r_7 \frac{\alpha(\omega_2^2+3\alpha)}{c_1(\omega_2^2+2\alpha)}$ $U_{20} = \begin{pmatrix} 1 & 0 & 0 & 0 & 0 & 0 & 0 \\ 0 & 1 & 0 & 0 & 0 & 0 & 0 \\ 0 & 0 & 1 & 0 & 0 & 0 & 0 \\ 0 & 0 & 0 & 1 & 0 & 0 & 0 \\ 0 & 0 & 0 & 0 & 1 & 0 & 0 \\ 0 & 0 & 0 & 0 & 0 & 1 & 0 \\ 0 & 0 & 0 & 0 & 0 & 0 & \frac{\alpha(\omega_2^2+3\alpha)}{c_1(\omega_2^2+2\alpha)} \end{pmatrix}$	$P_6 = -\lambda P_4 + \frac{P_1(\omega_2^2+3\alpha)}{\alpha(\omega_2^2+2\alpha)}$ $\begin{pmatrix} 1 & 0 & \frac{-\alpha}{\omega_1^2+2\alpha} & 0 & \frac{-\alpha}{\omega_1^2+2\alpha} & 0 \\ 0 & -1 & 0 & 0 & 0 & 0 \\ 0 & 0 & \omega_2^2+3\alpha & 0 & -(\omega_3^2-3\alpha) & P_4 \\ 0 & 0 & 0 & -1 & 0 & P_0 \\ 0 & 0 & 0 & 0 & k_1 - \frac{\lambda k_2}{(\omega_2^2+3\alpha)} & P_3 + P_0 P_2 \\ 0 & 0 & 0 & 0 & \lambda & -1 \\ 0 & 0 & 0 & 0 & \lambda(\omega_3^2+3\alpha) & P_6 \end{pmatrix}$
$U_{21}:$ $r_1 \rightarrow r_1 + \frac{\alpha}{(\omega_2^2+3\alpha)(\omega_1^2+2\alpha)} r_3$ $U_{21} = \begin{pmatrix} 1 & 0 & \frac{\alpha}{(\omega_2^2+3\alpha)(\omega_1^2+2\alpha)} & 0 & 0 & 0 & 0 \\ 0 & 1 & 0 & 0 & 0 & 0 & 0 \\ 0 & 0 & 1 & 0 & 0 & 0 & 0 \\ 0 & 0 & 0 & 1 & 0 & 0 & 0 \\ 0 & 0 & 0 & 0 & 1 & 0 & 0 \\ 0 & 0 & 0 & 0 & 0 & 1 & 0 \\ 0 & 0 & 0 & 0 & 0 & 0 & 0 \end{pmatrix}$	$P_5 = -\frac{\lambda}{\omega_1^2+2\alpha} + \frac{\alpha(\omega_3^2+3\alpha)}{(\omega_2^2+3\alpha)(\omega_1^2+2\alpha)}$ $\begin{pmatrix} 1 & 0 & 0 & 0 & P_5 & \frac{\alpha P_4}{(\omega_2^2+3\alpha)(\omega_1^2+2\alpha)} \\ 0 & -1 & 0 & 0 & 0 & 0 \\ 0 & 0 & \omega_2^2+3\alpha & 0 & -(\omega_3^2-3\alpha) & P_4 \\ 0 & 0 & 0 & -1 & 0 & P_0 \\ 0 & 0 & 0 & 0 & k_1 - \frac{\lambda k_2}{(\omega_2^2+3\alpha)} & P_3 + P_0 P_2 \\ 0 & 0 & 0 & 0 & \lambda & -1 \\ 0 & 0 & 0 & 0 & \lambda(\omega_3^2+3\alpha) & P_6 \end{pmatrix}$
$U_{22}:$ $r_7 \rightarrow r_7 + P_6 r_6$ $U_{22} = \begin{pmatrix} 1 & 0 & 0 & 0 & 0 & 0 & 0 \\ 0 & 1 & 0 & 0 & 0 & 0 & 0 \\ 0 & 0 & 1 & 0 & 0 & 0 & 0 \\ 0 & 0 & 0 & 1 & 0 & 0 & 0 \\ 0 & 0 & 0 & 0 & 1 & 0 & 0 \\ 0 & 0 & 0 & 0 & 0 & 1 & 0 \\ 0 & 0 & 0 & 0 & 0 & P_6 & 1 \end{pmatrix}$	$\begin{pmatrix} 1 & 0 & 0 & 0 & P_5 & \frac{\alpha P_4}{(\omega_2^2+3\alpha)(\omega_1^2+2\alpha)} \\ 0 & -1 & 0 & 0 & 0 & 0 \\ 0 & 0 & \omega_2^2+3\alpha & 0 & -(\omega_3^2-3\alpha) & P_4 \\ 0 & 0 & 0 & -1 & 0 & P_0 \\ 0 & 0 & 0 & 0 & k_1 - \frac{\lambda k_2}{(\omega_2^2+3\alpha)} & P_3 + P_0 P_2 \\ 0 & 0 & 0 & 0 & \lambda & -1 \\ 0 & 0 & 0 & 0 & \lambda(\omega_3^2+3\alpha) + P_6 & 0 \end{pmatrix}$
$U_{23}:$ $r_5 \rightarrow r_5 + \frac{k_2}{(\omega_2^2+3\alpha)} r_6$ $U_{23} = \begin{pmatrix} 1 & 0 & 0 & 0 & 0 & 0 & 0 \\ 0 & 1 & 0 & 0 & 0 & 0 & 0 \\ 0 & 0 & 1 & 0 & 0 & 0 & 0 \\ 0 & 0 & 0 & 1 & 0 & 0 & 0 \\ 0 & 0 & 0 & 0 & 1 & \frac{k_2}{(\omega_2^2+3\alpha)} & 0 \\ 0 & 0 & 0 & 0 & 0 & 1 & 0 \\ 0 & 0 & 0 & 0 & 0 & 0 & 1 \end{pmatrix}$	$P_7 = P_3 + Z_6 Z_2 - \frac{k_2}{(\omega_2^2+3\alpha)}$ $\begin{pmatrix} 1 & 0 & 0 & 0 & P_5 & \frac{\alpha P_4}{(\omega_2^2+3\alpha)(\omega_1^2+2\alpha)} \\ 0 & -1 & 0 & 0 & 0 & 0 \\ 0 & 0 & \omega_2^2+3\alpha & 0 & -(\omega_3^2-3\alpha) & P_4 \\ 0 & 0 & 0 & -1 & 0 & P_0 \\ 0 & 0 & 0 & 0 & k_1 & P_7 \\ 0 & 0 & 0 & 0 & \lambda & -1 \\ 0 & 0 & 0 & 0 & \lambda(\omega_3^2+3\alpha) + P_6 & 0 \end{pmatrix}$
$U_{24}:$ $r_5 \rightarrow r_5 + P_7 r_6$ $U_{24} = \begin{pmatrix} 1 & 0 & 0 & 0 & 0 & 0 & 0 \\ 0 & 1 & 0 & 0 & 0 & 0 & 0 \\ 0 & 0 & 1 & 0 & 0 & 0 & 0 \\ 0 & 0 & 0 & 1 & 0 & 0 & 0 \\ 0 & 0 & 0 & 0 & 1 & 0 & P_7 \\ 0 & 0 & 0 & 0 & 0 & 1 & 0 \\ 0 & 0 & 0 & 0 & 0 & 0 & 1 \end{pmatrix}$	$P_8 = k_1 + \lambda P_7$ $P_9 = \lambda(\omega_3^2+3\alpha) + P_6$ $\begin{pmatrix} 1 & 0 & 0 & 0 & P_5 & \frac{\alpha P_4}{(\omega_2^2+3\alpha)(\omega_1^2+2\alpha)} \\ 0 & -1 & 0 & 0 & 0 & 0 \\ 0 & 0 & \omega_2^2+3\alpha & 0 & -(\omega_3^2-3\alpha) & P_4 \\ 0 & 0 & 0 & -1 & 0 & P_0 \\ 0 & 0 & 0 & 0 & P_8 & 0 \\ 0 & 0 & 0 & 0 & \lambda & -1 \\ 0 & 0 & 0 & 0 & P_9 & 0 \end{pmatrix}$
$U_{25}:$ $r_7 \rightarrow r_7 - \frac{b_1\lambda}{a_1} r_5$ $U_{25} = \begin{pmatrix} 1 & 0 & 0 & 0 & 0 & 0 & 0 \\ 0 & 1 & 0 & 0 & 0 & 0 & 0 \\ 0 & 0 & 1 & 0 & 0 & 0 & 0 \\ 0 & 0 & 0 & 1 & 0 & 0 & 0 \\ 0 & 0 & 0 & 0 & 1 & 0 & 0 \\ 0 & 0 & 0 & 0 & 0 & 1 & 0 \\ 0 & 0 & 0 & 0 & -\frac{b_1\lambda}{a_1} & 0 & 1 \end{pmatrix}$	$P_8(\lambda) = a_1\lambda^4 + a_2\lambda^3 + a_3\lambda^2 + a_4\lambda + 1, a_i \in \Re\ \forall\ i$ $P_9(\lambda) = b_1\lambda^5 + b_2\lambda^4 + b_3\lambda^3 + b_4\lambda^2 + b_5\lambda,\ b_i \in \Re\ \forall\ i$ $\beta_i \in \Re\ \forall\ i$ $\begin{pmatrix} 1 & 0 & 0 & 0 & P_5 & \frac{\alpha P_4}{(\omega_2^2+3\alpha)(\omega_1^2+2\alpha)} \\ 0 & -1 & 0 & 0 & 0 & 0 \\ 0 & 0 & \omega_2^2+3\alpha & 0 & -(\omega_3^2-3\alpha) & P_4 \\ 0 & 0 & 0 & -1 & 0 & P_0 \\ 0 & 0 & 0 & 0 & P_8 & 0 \\ 0 & 0 & 0 & 0 & \lambda & -1 \\ 0 & 0 & 0 & 0 & \beta_1\lambda^3 + \beta_2\lambda^2 + \beta_3\lambda & 0 \end{pmatrix}$

Table A.3.1: Finding the set (α, ω, ζ) for which networked clocks are not fully observable

Table continued $\cdots$ Elementary row operation	$\mathbf{U}(\lambda)\begin{pmatrix} D(\lambda) \\ N(\lambda) \end{pmatrix}$ where $(\mathbf{U}(\lambda) = U_n \ldots U_2 U_1)$
U_{26} : $r_5 \longrightarrow r_5 - \frac{a_1\lambda}{\beta_1} r_7$ $U_{26} = \begin{pmatrix} 1 & 0 & 0 & 0 & 0 & 0 & 0 \\ 0 & 1 & 0 & 0 & 0 & 0 & 0 \\ 0 & 0 & 1 & 0 & 0 & 0 & 0 \\ 0 & 0 & 0 & 1 & 0 & 0 & 0 \\ 0 & 0 & 0 & 0 & 1 & 0 & -\frac{a_1\lambda}{\beta_1} \\ 0 & 0 & 0 & 0 & 0 & 1 & 0 \\ 0 & 0 & 0 & 0 & 0 & 0 & 1 \end{pmatrix}$	$d_i \in \Re \; \forall \; i$ $\begin{pmatrix} 1 & 0 & 0 & 0 & P_5 & \frac{\alpha P_4}{(\omega_2^2+3\alpha)(\omega_1^2+2\alpha)} \\ 0 & -1 & 0 & 0 & 0 & 0 \\ 0 & 0 & \omega_2^2+3\alpha & 0 & -(\omega_3^2-3\alpha) & P_4 \\ 0 & 0 & 0 & -1 & 0 & P_0 \\ 0 & 0 & 0 & 0 & d_1\lambda^3+d_2\lambda^2+d_3\lambda+d_4 & 0 \\ 0 & 0 & 0 & 0 & \lambda & -1 \\ 0 & 0 & 0 & 0 & \beta_1\lambda^3+\beta_2\lambda^2+\beta_3\lambda & 0 \end{pmatrix}$
U_{27} : $r_7 \longrightarrow r_7 - \frac{\beta_1}{a_2} r_5$ $U_{27} = \begin{pmatrix} 1 & 0 & 0 & 0 & 0 & 0 & 0 \\ 0 & 1 & 0 & 0 & 0 & 0 & 0 \\ 0 & 0 & 1 & 0 & 0 & 0 & 0 \\ 0 & 0 & 0 & 1 & 0 & 0 & 0 \\ 0 & 0 & 0 & 0 & 1 & 0 & 0 \\ 0 & 0 & 0 & 0 & 0 & 1 & 0 \\ 0 & 0 & 0 & 0 & -\frac{\beta_1}{a_2} & 0 & 1 \end{pmatrix}$	$e_i \in \Re \; \forall \; i$ $\begin{pmatrix} 1 & 0 & 0 & 0 & P_5 & \frac{\alpha P_4}{(\omega_2^2+3\alpha)(\omega_1^2+2\alpha)} \\ 0 & -1 & 0 & 0 & 0 & 0 \\ 0 & 0 & \omega_2^2+3\alpha & 0 & -(\omega_3^2-3\alpha) & P_4 \\ 0 & 0 & 0 & -1 & 0 & P_0 \\ 0 & 0 & 0 & 0 & d_1\lambda^3+d_2\lambda^2+d_3\lambda+d_4 & 0 \\ 0 & 0 & 0 & 0 & \lambda & -1 \\ 0 & 0 & 0 & 0 & e_1\lambda^2+e_2\lambda+e_3 & 0 \end{pmatrix}$
U_{28} : $r_5 \longrightarrow r_5 - \frac{d_1\lambda}{e_1} r_7$ $U_{28} = \begin{pmatrix} 1 & 0 & 0 & 0 & 0 & 0 & 0 \\ 0 & 1 & 0 & 0 & 0 & 0 & 0 \\ 0 & 0 & 1 & 0 & 0 & 0 & 0 \\ 0 & 0 & 0 & 1 & 0 & 0 & 0 \\ 0 & 0 & 0 & 0 & 1 & 0 & -\frac{d_1\lambda}{e_1} \\ 0 & 0 & 0 & 0 & 0 & 1 & 0 \\ 0 & 0 & 0 & 0 & 0 & 0 & 1 \end{pmatrix}$	$f_i \in \Re \; \forall \; i$ $\begin{pmatrix} 1 & 0 & 0 & 0 & P_5 & \frac{\alpha P_4}{(\omega_2^2+3\alpha)(\omega_1^2+2\alpha)} \\ 0 & -1 & 0 & 0 & 0 & 0 \\ 0 & 0 & \omega_2^2+3\alpha & 0 & -(\omega_3^2-3\alpha) & P_4 \\ 0 & 0 & 0 & -1 & 0 & P_0 \\ 0 & 0 & 0 & 0 & f_1\lambda^2+f_2\lambda+f_3 & 0 \\ 0 & 0 & 0 & 0 & \lambda & -1 \\ 0 & 0 & 0 & 0 & e_1\lambda^2+e_2\lambda+e_3 & 0 \end{pmatrix}$
U_{29} : $r_5 \longrightarrow r_5 - \frac{f_1}{e_1} r_7$ $U_{29} = \begin{pmatrix} 1 & 0 & 0 & 0 & 0 & 0 & 0 \\ 0 & 1 & 0 & 0 & 0 & 0 & 0 \\ 0 & 0 & 1 & 0 & 0 & 0 & 0 \\ 0 & 0 & 0 & 1 & 0 & 0 & 0 \\ 0 & 0 & 0 & 0 & 1 & 0 & -\frac{f_1}{e_1} \\ 0 & 0 & 0 & 0 & 0 & 1 & 0 \\ 0 & 0 & 0 & 0 & 0 & 0 & 1 \end{pmatrix}$	$g_i \in \Re \; \forall \; i$ $\begin{pmatrix} 1 & 0 & 0 & 0 & P_5 & \frac{\alpha P_4}{(\omega_2^2+3\alpha)(\omega_1^2+2\alpha)} \\ 0 & -1 & 0 & 0 & 0 & 0 \\ 0 & 0 & \omega_2^2+3\alpha & 0 & -(\omega_3^2-3\alpha) & P_4 \\ 0 & 0 & 0 & -1 & 0 & P_0 \\ 0 & 0 & 0 & 0 & g_1\lambda+g_2 & 0 \\ 0 & 0 & 0 & 0 & \lambda & -1 \\ 0 & 0 & 0 & 0 & e_1\lambda^2+e_2\lambda+e_3 & 0 \end{pmatrix}$
U_{30} : $r_7 \longrightarrow r_7 - \frac{e_1\lambda}{g_1} r_5$ $U_{30} = \begin{pmatrix} 1 & 0 & 0 & 0 & 0 & 0 & 0 \\ 0 & 1 & 0 & 0 & 0 & 0 & 0 \\ 0 & 0 & 1 & 0 & 0 & 0 & 0 \\ 0 & 0 & 0 & 1 & 0 & 0 & 0 \\ 0 & 0 & 0 & 0 & 1 & 0 & 0 \\ 0 & 0 & 0 & 0 & 0 & 1 & 0 \\ 0 & 0 & 0 & 0 & -\frac{e_1\lambda}{g_1} & 0 & 1 \end{pmatrix}$	$h_i \in \Re \; \forall \; i$ $\begin{pmatrix} 1 & 0 & 0 & 0 & P_5 & \frac{\alpha P_4}{(\omega_2^2+3\alpha)(\omega_1^2+2\alpha)} \\ 0 & -1 & 0 & 0 & 0 & 0 \\ 0 & 0 & \omega_2^2+3\alpha & 0 & -(\omega_3^2-3\alpha) & P_4 \\ 0 & 0 & 0 & -1 & 0 & P_0 \\ 0 & 0 & 0 & 0 & g_1\lambda+g_2 & 0 \\ 0 & 0 & 0 & 0 & \lambda & -1 \\ 0 & 0 & 0 & 0 & h_1\lambda+h_2 & 0 \end{pmatrix}$
U_{31} : $r_7 \longrightarrow r_7 - \frac{h_1}{g_1} r_5$ $U_{31} = \begin{pmatrix} 1 & 0 & 0 & 0 & 0 & 0 & 0 \\ 0 & 1 & 0 & 0 & 0 & 0 & 0 \\ 0 & 0 & 1 & 0 & 0 & 0 & 0 \\ 0 & 0 & 0 & 1 & 0 & 0 & 0 \\ 0 & 0 & 0 & 0 & 1 & 0 & 0 \\ 0 & 0 & 0 & 0 & 0 & 1 & 0 \\ 0 & 0 & 0 & 0 & -\frac{h_1}{g_1} & 0 & 1 \end{pmatrix}$	$m_i \in \Re \; \forall \; i$ $\begin{pmatrix} 1 & 0 & 0 & 0 & P_5 & \frac{\alpha P_4}{(\omega_2^2+3\alpha)(\omega_1^2+2\alpha)} \\ 0 & -1 & 0 & 0 & 0 & 0 \\ 0 & 0 & \omega_2^2+3\alpha & 0 & -(\omega_3^2-3\alpha) & P_4 \\ 0 & 0 & 0 & -1 & 0 & P_0 \\ 0 & 0 & 0 & 0 & g_1\lambda+g_2 & 0 \\ 0 & 0 & 0 & 0 & \lambda & -1 \\ 0 & 0 & 0 & 0 & m_1 & 0 \end{pmatrix}$

Table A.3.1: Finding the set (α, ω, ζ) for which networked clocks are not fully observable

Table continued ⋯ Elementary row operation	$\mathbf{U}(\lambda)\begin{pmatrix} D(\lambda) \\ N(\lambda) \end{pmatrix}$ where ($\mathbf{U}(\lambda) = U_n \dots U_2 U_1$)
U_{32} : $r_7 \rightarrow r_7/m_1$ $U_{32} = \begin{pmatrix} 1 & 0 & 0 & 0 & 0 & 0 & 0 \\ 0 & 1 & 0 & 0 & 0 & 0 & 0 \\ 0 & 0 & 1 & 0 & 0 & 0 & 0 \\ 0 & 0 & 0 & 1 & 0 & 0 & 0 \\ 0 & 0 & 0 & 0 & 1 & 0 & 0 \\ 0 & 0 & 0 & 0 & 0 & 1 & 0 \\ 0 & 0 & 0 & 0 & 0 & 0 & \frac{1}{m_1} \end{pmatrix}$	$\begin{pmatrix} 1 & 0 & 0 & 0 & P_5 & \frac{\alpha P_4}{(\omega_2^2+3\alpha)(\omega_1^2+2\alpha)} \\ 0 & -1 & 0 & 0 & 0 & 0 \\ 0 & 0 & \omega_2^2+3\alpha & 0 & -(\omega_3^2-3\alpha) & P_4 \\ 0 & 0 & 0 & -1 & 0 & P_0 \\ 0 & 0 & 0 & 0 & g_1\lambda+g_2 & 0 \\ 0 & 0 & 0 & 0 & \lambda & -1 \\ 0 & 0 & 0 & 0 & 1 & 0 \end{pmatrix}$
U_{33} : $r_5 \rightarrow r_5 - (g_1\lambda + g_2)r_7$ $U_{33} = \begin{pmatrix} 1 & 0 & 0 & 0 & 0 & 0 & 0 \\ 0 & 1 & 0 & 0 & 0 & 0 & 0 \\ 0 & 0 & 1 & 0 & 0 & 0 & 0 \\ 0 & 0 & 0 & 1 & 0 & 0 & 0 \\ 0 & 0 & 0 & 0 & 1 & 0 & -(g_1\lambda+g_2) \\ 0 & 0 & 0 & 0 & 0 & 1 & 0 \\ 0 & 0 & 0 & 0 & 0 & 0 & 1 \end{pmatrix}$	$\begin{pmatrix} 1 & 0 & 0 & 0 & P_5 & \frac{\alpha P_4}{(\omega_2^2+3\alpha)(\omega_1^2+2\alpha)} \\ 0 & -1 & 0 & 0 & 0 & 0 \\ 0 & 0 & \omega_2^2+3\alpha & 0 & -(\omega_3^2-3\alpha) & P_4 \\ 0 & 0 & 0 & -1 & 0 & P_0 \\ 0 & 0 & 0 & 0 & 0 & 0 \\ 0 & 0 & 0 & 0 & \lambda & -1 \\ 0 & 0 & 0 & 0 & 1 & 0 \end{pmatrix}$
U_{34} : $r_6 \rightarrow r_6 - sr_7$ $U_{34} = \begin{pmatrix} 1 & 0 & 0 & 0 & 0 & 0 & 0 \\ 0 & 1 & 0 & 0 & 0 & 0 & 0 \\ 0 & 0 & 1 & 0 & 0 & 0 & 0 \\ 0 & 0 & 0 & 1 & 0 & 0 & 0 \\ 0 & 0 & 0 & 0 & 1 & 0 & 0 \\ 0 & 0 & 0 & 0 & 0 & 1 & -\lambda \\ 0 & 0 & 0 & 0 & 0 & 0 & 1 \end{pmatrix}$	$\begin{pmatrix} 1 & 0 & 0 & 0 & P_5 & \frac{\alpha P_4}{(\omega_2^2+3\alpha)(\omega_1^2+2\alpha)} \\ 0 & -1 & 0 & 0 & 0 & 0 \\ 0 & 0 & \omega_2^2+3\alpha & 0 & -(\omega_3^2-3\alpha) & P_4 \\ 0 & 0 & 0 & -1 & 0 & P_0 \\ 0 & 0 & 0 & 0 & 0 & 0 \\ 0 & 0 & 0 & 0 & 0 & -1 \\ 0 & 0 & 0 & 0 & 1 & 0 \end{pmatrix}$
U_{35} : $r_3 \rightarrow r_3 + (\omega_3^2 + 3\alpha)r_7$ $U_{35} = \begin{pmatrix} 1 & 0 & 0 & 0 & 0 & 0 & 0 \\ 0 & 1 & 0 & 0 & 0 & 0 & 0 \\ 0 & 0 & 1 & 0 & 0 & 0 & (\omega_3^2+3\alpha) \\ 0 & 0 & 0 & 1 & 0 & 0 & 0 \\ 0 & 0 & 0 & 0 & 1 & 0 & 0 \\ 0 & 0 & 0 & 0 & 0 & 1 & 0 \\ 0 & 0 & 0 & 0 & 0 & 0 & 1 \end{pmatrix}$	$\begin{pmatrix} 1 & 0 & 0 & 0 & P_5 & \frac{\alpha P_4}{(\omega_2^2+3\alpha)(\omega_1^2+2\alpha)} \\ 0 & -1 & 0 & 0 & 0 & 0 \\ 0 & 0 & \omega_2^2+3\alpha & 0 & 0 & P_4 \\ 0 & 0 & 0 & -1 & 0 & P_0 \\ 0 & 0 & 0 & 0 & 0 & 0 \\ 0 & 0 & 0 & 0 & 0 & -1 \\ 0 & 0 & 0 & 0 & 1 & 0 \end{pmatrix}$
U_{36} : $r_1 \rightarrow r_3 - P_5 r_7$ $U_{36} = \begin{pmatrix} 1 & 0 & 0 & 0 & 0 & 0 & -P_5 \\ 0 & 1 & 0 & 0 & 0 & 0 & 0 \\ 0 & 0 & 1 & 0 & 0 & 0 & 0 \\ 0 & 0 & 0 & 1 & 0 & 0 & 0 \\ 0 & 0 & 0 & 0 & 1 & 0 & 0 \\ 0 & 0 & 0 & 0 & 0 & 1 & 0 \\ 0 & 0 & 0 & 0 & 0 & 0 & 1 \end{pmatrix}$	$\begin{pmatrix} 1 & 0 & 0 & 0 & 0 & \frac{\alpha P_4}{(\omega_2^2+3\alpha)(\omega_1^2+2\alpha)} \\ 0 & -1 & 0 & 0 & 0 & 0 \\ 0 & 0 & \omega_2^2+3\alpha & 0 & 0 & P_4 \\ 0 & 0 & 0 & -1 & 0 & P_0 \\ 0 & 0 & 0 & 0 & 0 & 0 \\ 0 & 0 & 0 & 0 & 0 & -1 \\ 0 & 0 & 0 & 0 & 1 & 0 \end{pmatrix}$
U_{37} : $r_4 \rightarrow r_4 + P_0 r_6$ $U_{37} = \begin{pmatrix} 1 & 0 & 0 & 0 & 0 & 0 & 0 \\ 0 & 1 & 0 & 0 & 0 & 0 & 0 \\ 0 & 0 & 1 & 0 & 0 & 0 & 0 \\ 0 & 0 & 0 & 1 & 0 & P_0 & 0 \\ 0 & 0 & 0 & 0 & 1 & 0 & 0 \\ 0 & 0 & 0 & 0 & 0 & 1 & 0 \\ 0 & 0 & 0 & 0 & 0 & 0 & 1 \end{pmatrix}$	$\begin{pmatrix} 1 & 0 & 0 & 0 & 0 & \frac{\alpha P_4}{(\omega_2^2+3\alpha)(\omega_1^2+2\alpha)} \\ 0 & -1 & 0 & 0 & 0 & 0 \\ 0 & 0 & \omega_2^2+3\alpha & 0 & 0 & P_4 \\ 0 & 0 & 0 & -1 & 0 & 0 \\ 0 & 0 & 0 & 0 & 0 & 0 \\ 0 & 0 & 0 & 0 & 0 & -1 \\ 0 & 0 & 0 & 0 & 1 & 0 \end{pmatrix}$

Table A.3.1: Finding the set (α, ω, ζ) for which networked clocks are not fully observable

Table continued $\cdots$ Elementary row operation	$\mathbf{U}(\lambda)\begin{pmatrix} D(\lambda) \\ N(\lambda) \end{pmatrix}$ where ($\mathbf{U}(\lambda) = U_n \dots U_2 U_1$)
U_{38} : $r_3 \rightarrow r_3 + P_4 r_6$ $U_{38} = \begin{pmatrix} 1 & 0 & 0 & 0 & 0 & 0 & 0 \\ 0 & 1 & 0 & 0 & 0 & 0 & 0 \\ 0 & 0 & 1 & 0 & 0 & P_4 & 0 \\ 0 & 0 & 0 & 1 & 0 & 0 & 0 \\ 0 & 0 & 0 & 0 & 1 & 0 & 0 \\ 0 & 0 & 0 & 0 & 0 & 1 & 0 \\ 0 & 0 & 0 & 0 & 0 & 0 & 1 \end{pmatrix}$	$\begin{pmatrix} 1 & 0 & 0 & 0 & 0 & \frac{\alpha P_4}{(\omega_2^2+3\alpha)(\omega_1^2+2\alpha)} \\ 0 & -1 & 0 & 0 & 0 & 0 \\ 0 & 0 & \omega_2^2+3\alpha & 0 & 0 & 0 \\ 0 & 0 & 0 & -1 & 0 & 0 \\ 0 & 0 & 0 & 0 & 0 & 0 \\ 0 & 0 & 0 & 0 & 0 & -1 \\ 0 & 0 & 0 & 0 & 1 & 0 \end{pmatrix}$
U_{39} : $r_1 \rightarrow r_1 + \frac{\alpha}{(\omega_2^2+3\alpha)(\omega_1^2+2\alpha)} P_4 r_6$ $U_{39} = \begin{pmatrix} 1 & 0 & 0 & 0 & 0 & 0 & 0 \\ 0 & 1 & 0 & 0 & 0 & 0 & 0 \\ 0 & 0 & 1 & 0 & 0 & 0 & 0 \\ 0 & 0 & 0 & 1 & 0 & 0 & 0 \\ 0 & 0 & 0 & 0 & 1 & 0 & 0 \\ 0 & 0 & 0 & 0 & 0 & 1 & 0 \\ 0 & 0 & 0 & 0 & 0 & 0 & 1 \end{pmatrix}$	$\begin{pmatrix} 1 & 0 & 0 & 0 & 0 & 0 \\ 0 & -1 & 0 & 0 & 0 & 0 \\ 0 & 0 & \omega_2^2+3\alpha & 0 & 0 & 0 \\ 0 & 0 & 0 & -1 & 0 & 0 \\ 0 & 0 & 0 & 0 & 0 & 0 \\ 0 & 0 & 0 & 0 & 0 & -1 \\ 0 & 0 & 0 & 0 & 1 & 0 \end{pmatrix}$
$U_{40}, U_{41}, U_{42} \& U_{43}$: $r_6 \rightarrow -r_6$ $r_2 \rightarrow -r_2$ $r_3 \rightarrow r_3/(\omega_2^2+3\alpha)$ $r_4 \rightarrow -r_4$ $U_{43}U_{42}U_{41}U_{40} = \begin{pmatrix} 1 & 0 & 0 & 0 & 0 & 0 & 0 \\ 0 & -1 & 0 & 0 & 0 & 0 & 0 \\ 0 & 0 & \frac{1}{(\omega_2^2+3\alpha)} & 0 & 0 & 0 & 0 \\ 0 & 0 & 0 & -1 & 0 & 0 & 0 \\ 0 & 0 & 0 & 0 & 1 & 0 & 0 \\ 0 & 0 & 0 & 0 & 0 & -1 & 0 \\ 0 & 0 & 0 & 0 & 0 & 0 & 1 \end{pmatrix}$	$\begin{pmatrix} 1 & 0 & 0 & 0 & 0 & 0 \\ 0 & 1 & 0 & 0 & 0 & 0 \\ 0 & 0 & 1 & 0 & 0 & 0 \\ 0 & 0 & 0 & 1 & 0 & 0 \\ 0 & 0 & 0 & 0 & 0 & 0 \\ 0 & 0 & 0 & 0 & 0 & 1 \\ 0 & 0 & 0 & 0 & 1 & 0 \end{pmatrix}$
U_{44} : $r_5 \overset{swap}{\leftrightarrow} r_7$ $U_{44} = \begin{pmatrix} 1 & 0 & 0 & 0 & 0 & 0 & 0 \\ 0 & 1 & 0 & 0 & 0 & 0 & 0 \\ 0 & 0 & 1 & 0 & 0 & 0 & 0 \\ 0 & 0 & 0 & 1 & 0 & 0 & 0 \\ 0 & 0 & 0 & 0 & 0 & 1 & 0 \\ 0 & 0 & 0 & 0 & 1 & 0 & 0 \\ 0 & 0 & 0 & 0 & 0 & 0 & 1 \end{pmatrix}$	$\begin{pmatrix} 1 & 0 & 0 & 0 & 0 & 0 \\ 0 & 1 & 0 & 0 & 0 & 0 \\ 0 & 0 & 1 & 0 & 0 & 0 \\ 0 & 0 & 0 & 1 & 0 & 0 \\ 0 & 0 & 0 & 0 & 1 & 0 \\ 0 & 0 & 0 & 0 & 0 & 1 \\ 0 & 0 & 0 & 0 & 0 & 0 \end{pmatrix} = \begin{pmatrix} I \\ \mathbf{0} \end{pmatrix}$

Table A.3.1: Finding the set (α, ω, ζ) for which networked clocks are not fully observable

A.4 Phase Estimation: Comparison of Least Squares Method and Hilbert Transform

In Chapter 7 it is required to estimate the phase associated with a particular frequency in order to determine the synchronisation of oscillators within a clock network and/or the synchronisation of measurement signals. Synchronisation here is defined as the sustained phase locking to a particular signal of frequency f, where this signal may be *(i)* that of an input probing signal or *(ii)* an unstable ("seizure inducing") oscillation within the clock network.

The chosen method for phase estimation is to find the least squares solution to the model:

$$X(t) = A\cos(2\pi f t + \phi) + \mathrm{w}(t) \tag{A.4.1}$$

where f is the known frequency of the input stimulus, $\mathrm{w}(t)$ is zero mean white noise and the phase, ϕ and amplitude, $A = A(f)$ [134, Ch. 7]. $X(t)$ can be either *(i)* the EEG signal used to estimate the phase-locking response to our probe stimulus, or *(ii)* the internal states of the model to determine phase for individual clocks to establish if predictions from the EEG data correspond to a true picture of the underlying system activity. This definition of phase synchrony is used as it is more robust than the Hilbert transform in the presence of noise and can be used on broadband signals without any ambiguities. Details of the least squares solutions are provided next in this appendix followed with a comparison of this method and the commonly used Hilbert transform to illustrate the superiority of this method in the presence of noise.

Equation A.4.1 can be rewritten in discrete form as:

$$\begin{aligned} x(n) &= A\cos(2\pi f n + \phi) + \mathrm{w}(n) \tag{A.4.2}\\ &= A\cos(2\pi f n)\cos(\phi) - A\sin(2\pi f n)\sin(\phi) + \mathrm{w}(n)\text{using the cos(A+B) trigonometry rule} \tag{A.4.3}\\ &= \underbrace{A\cos(\phi)}_{\alpha_1}\cos(2\pi f n) - \underbrace{A\sin(\phi)}_{\alpha_2}\sin(2\pi f n) + \mathrm{w}(n) \tag{A.4.4} \end{aligned}$$

Since f is known, equation A.4.4 results in a linear function of unknown α_1 and α_2, where

$$A = \sqrt{\alpha_1^2 + \alpha_2^2} \tag{A.4.5}$$

$$\phi = \tan^{-1}\left(\frac{-\alpha_2}{\alpha_1}\right) \tag{A.4.6}$$

We can now write the estimation problem in matrix form as:

$$\mathbf{X} \;=\; \mathbf{H\Theta} + \mathrm{W}, \tag{A.4.7}$$

where $\mathbf{X} = \begin{bmatrix} x(0) & x(1) & \ldots & x(N-1) \end{bmatrix}^{'}$, $\mathbf{\Theta} = \begin{bmatrix} \alpha_1 & \alpha_2 \end{bmatrix}^{'}$, $\mathrm{W} = \begin{bmatrix} \mathrm{w}(0) & \mathrm{w}(1) & \ldots & \mathrm{w}(N-1) \end{bmatrix}^{'}$ and

$$\mathbf{H} = \begin{bmatrix} 1 & 0 \\ \cos(2\pi f) & \sin(2\pi f) \\ \vdots & \vdots \\ \cos\left(2\pi f\left(N-1\right)\right) & \sin\left(2\pi f\left(N-1\right)\right) \end{bmatrix}. \tag{A.4.8}$$

Since the noise is assumed to be Gaussian, the least squares estimator, $\hat{\mathbf{\Theta}}$, is the maximum likelihood estimator. The term to minimise is:

$$\begin{aligned} J(\mathbf{\Theta}) &= \sum_{n=0}^{N-1} \left(x(n) - E[x(n)]\right)^2 \\ &= (\mathbf{X} - \mathbf{H\Theta})^{'}(\mathbf{X} - \mathbf{H\Theta}), \end{aligned} \tag{A.4.9}$$

since $E[x(n)] = \mathbf{H\Theta}$. The cost function can be written as a quadratic function in $\mathbf{\Theta}$.

$$\begin{aligned} J(\mathbf{\Theta}) &= (\mathbf{X}^{'} - \mathbf{\Theta}^{'}\mathbf{H}^{'})(\mathbf{X} - \mathbf{H\Theta}) \\ &= \mathbf{X}^{'}\mathbf{X} - \mathbf{X}^{'}\mathbf{H\Theta} - \mathbf{\Theta}^{'}\mathbf{H}^{'}\mathbf{X} + \mathbf{\Theta}^{'}\mathbf{H}^{'}\mathbf{H\Theta} \\ &= \mathbf{H}^{'}\mathbf{H\Theta}^{'}\mathbf{\Theta} - 2\mathbf{\Theta}^{'}\mathbf{H}^{'}\mathbf{X} + \mathbf{X}^{'}\mathbf{X}. \end{aligned} \tag{A.4.10}$$

The estimate $\hat{\Theta}$ is found where $\partial J/\partial\mathbf{\Theta} = 0$:

$$\frac{\partial J}{\partial \mathbf{\Theta}} = 2\mathbf{H}^{'}\mathbf{H}\hat{\Theta} - 2\mathbf{H}^{'}\mathbf{X} = 0 \tag{A.4.11}$$

$$\hat{\Theta} = (\mathbf{H}^{'}\mathbf{H})^{-1}\mathbf{H}^{'}\mathbf{X}. \tag{A.4.12}$$

As $N \to \infty$,

$$\mathbf{H}^{'}\mathbf{H} = \begin{pmatrix} \frac{N}{2} & 0 \\ 0 & \frac{N}{2} \end{pmatrix}, \tag{A.4.13}$$

and

$$\boxed{\hat{\Theta} = \begin{bmatrix} \alpha_1 \\ \alpha_2 \end{bmatrix} = \begin{bmatrix} A\cos(\phi) \\ -A\sin(\phi) \end{bmatrix} = \begin{bmatrix} \frac{2}{N}\sum_{n=0}^{N-1} x(n)\cos(2\pi fn) \\ \frac{2}{N}\sum_{n=0}^{N-1} x(n)\sin(2\pi fn) \end{bmatrix}.} \tag{A.4.14}$$

Figure A.7 and Figure A.8 show comparisons between the robustness of the least squares solutions described above and the Hilbert transform as described in Section 2.3.1 of Chapter 2. Figure A.7 plots phase error against signal to noise ration (SNR) for a single frequency with phase offset in Gaussian noise as per the model in equation A.4.1. The least squares method dramatically out performs the Hilbert transform with least squares providing comparable accuracy in phase estimation to the Hilbert transform when the signal has 10 times more noise.

The noise in a evoked EEG set-up, however, will not necessarily be Gaussian. Instead we expect the evoked EEG signal to be a multifrequency signal which may contain the evoked input frequency, f_{in}. We wish find the phase is the EEG signal associated with f_{in} to determine if there is sustained phase-locking to the input signal. Figure A.8 compares the phase estimating powers of both methods for a signal where the noise is an additional frequency:

$$X(t) = A\cos(2\pi f_1 t + \phi_1) + A_n\cos(2\pi f_2 t + \phi_2) \tag{A.4.15}$$

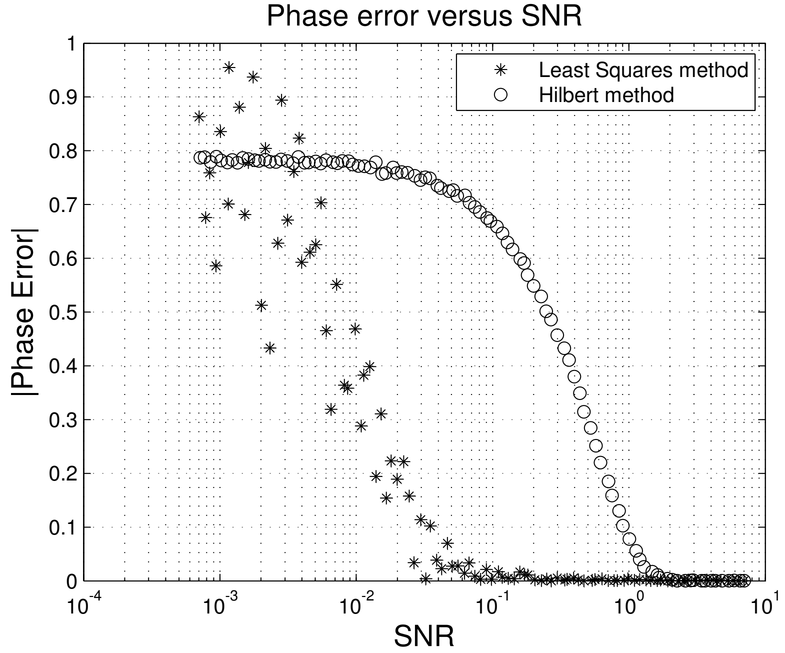

Figure A.7: Comparing phase estimator performance between least Squares method and Hilbert transform method for a single sinusoid in Gaussian noise. The absolute value of phase error is plotted against signal to noise ration (SNR).

where f_1 is the frequency for which we are estimating the associated phase ϕ_1. A_n is the noise amplitude and the signal component $A_n \cos(2\pi f_2 t + \phi_2)$ is considered to be noise. Again the least sqaures algorithm far exceeds the performance of the Hilbert transform. Therefore, in Chapter 7 as the evoked input frequencies (and internal model frequencies) are exactly known, the least squares method is used to evaluate phase synchronisation. The MATLAB code used to generate Figure A.7 and A.8 is provided in Appendix A.5.9.

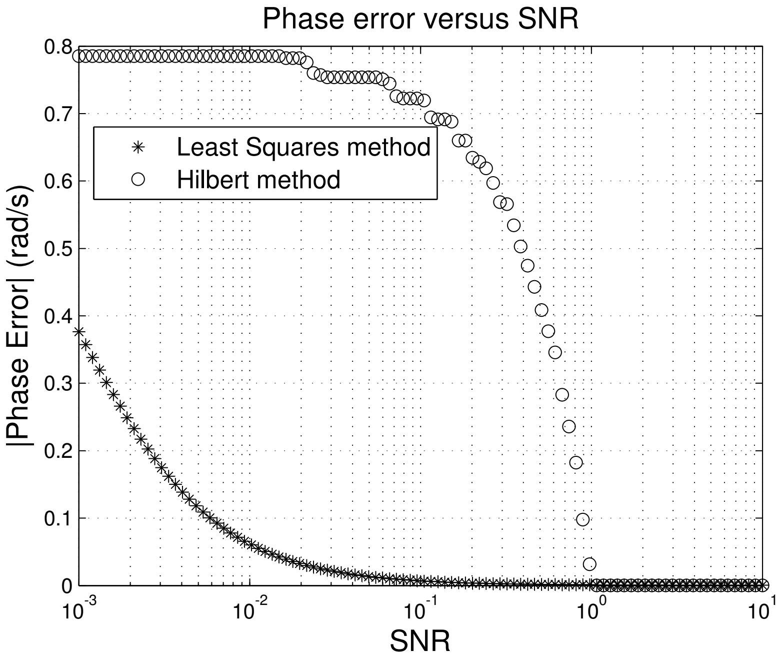

Figure A.8: Comparing phase estimator performance between Least Squares method and Hilbert transform method for a single sinusoid within a multi-frequency signal. The absolute value of phase error is plotted against signal to noise ration (SNR).

A.5 Additional information to enable complete reproducibility of key results

This Appendix contains additional technical particulars including Matlab Code to enable complete reproducibility of the key results plotted in this thesis.

A.5.1 Figure 5.1: Singular Values of the Observability Matrix

Figure 5.1 compares effect of frequency range on the singular values of the time-scaled continuous representation of the system matrix **A** for a network of 50 clocks (100 states).

```
%% Ploting singular values of Observability Matrix
% Feb 2009
% Generate time scaled model
% Plot singular values

%Define constants
N=50; %number of subsystems (=¿ 2*N number of states)
Fmax=1; %normalised maxium frequency
option=[1,2,3]; %set up for loop for each trace

for opt=1:length(option)

if opt==1
        Fmin=0.98; %normalised minimum frequency
elseif opt==2
        Fmin=0.6; %normalised minimum frequency
elseif opt==3
        Fmin=0.0025; %normalised minimum frequency
end


F=Fmin+(Fmax-Fmin)*[1:1:N]/N; %equi-spaced freqs, uniform distribution over range
Wn=2*pi*F;
Wnorm=max(Wn);
D=repmat(0.001,1,N); %Define damping parameters

alpha=0.01; %Define Couping Parameters
alp=alpha*triu(ones(N),1);

A=generateDampedA(N, alp,D,Wn);
A=A/Wnorm; %Timescale

%Transformed C
C=zeros(1,2*N); %pre-memory allocate
C(1:2:2*N)=0;
C(2:2:(2*N))=-1;
```

```
C=C/abs(sum(C)); %Make C a convex combination, so that max singular value is of order 1

obseby=obsv(A,C); %Observability Matrix
singular_values=svd(obseby);
sing_array(opt,:)=singular_values;
end

% Plot Singular values
figure(3)
semilogy(sing_array(1,:), “ko”)
hold on
grid on
title(“Singular values of the Observability Matrix”, “fontsize”, 14)
semilogy(sing_array(2,:), “k.”)
semilogy(sing_array(3,:), “kx”)

xlabel(“number of singular value (1:2N)”, “fontsize”, 14 )
ylabel(“singular value, σ”, “fontsize”, 14)
legend(“Normalised Frequencies 0.98-1”, “Normalised Frequencies 0.6-1”, “Normalised Frequencies
0.0025-1”)
hold off




function A=generateDampedA(N, alp,D,Wn)
%Function to generate the A matrix (dx/dt=Ax+Bu) for a large system of
%interconnected pendulum sub-systems each connected via alp (alp(i,j)
%connects sys i to sys j)
%A=generateContinuousA(N, alp,D,Wn)
%N=number of sub systems
%D= vector of damping in each subsystem
%Wn=vector of natural frequencies for each subsystem (in Rad/s)

%for N pendulum subsystems each of 2nd order=¿ 2*N states in state space
A=zeros(2*N,2*N); %Allocate memory

%define elementary matrices
AJ=[0 -1;+1 0]; %elementary rotation matrix
AC=[0 0;1 0]; %elementary coupling matrix
ACr=[1 0;0 0]; %elementary coupling matrix
ACl=[0 0;0 1]; %elementary coupling matrix
AD=[+1 0;0 +1]; %elementary diagonal matrix
AJp=[0 1;1 0]; %positive elementary rotation matrix
Ar=[+1 +1;+1 +1]; %replicate expand matrix

%Generate uncoupled A - block diagonal
A_block_offdiag=kron(diag(Wn.*sqrt(1-D.^2)), AJ);
A_block_ondiag=kron(diag(-D.*Wn), AD);
A_uncoupled=A_block_offdiag+A_block_ondiag;

%Generate Coupling matrix
```

```
% Each 2x2 Block matrix Epsilon_ij=T_i *[0,0;a,0]*inv(T_j)
% Where a is the coupling term
D_term_array=sqrt(1-(D).^2);
SumAlpha=diag(sum(alp, 2)); % the sum of each row is the diagonal coupling term
Alpha_diag=-kron(SumAlpha,Ar);
Alpha_offdiag=kron(alp,Ar);
%Wscaling=repmat(kron(1./Wn,Ar), N, 1); not needed with normalised freqs
Wscaling=ones(2*N); %replacement for normalised freqs
D_j=kron(D,ones(N,1));
D_i=kron(D’,ones(1,N));
D_divD_term_j=kron(D./D_term_array,ones(N,1));
D_term_i=kron(D_term_array’,ones(1,N));
Epsilon_11=kron(D_i,ACr) ;
Epilson_12=kron(D_i,AC’) .* kron(D_divD_term_j,AC’);
Epilson_21=kron(D_term_i,-AC);
Epilson_22=kron(D_term_i,ACl) .* kron(D_divD_term_j,-ACl);
Epsilon=(Alpha_diag+Alpha_offdiag).*Wscaling.*(Epsilon_11+Epilson_12+Epilson_21+Epilson_22);

A=A_uncoupled+Epsilon;

end
```

A.5.2 Figure 5.2: Singular Values of the System Matrix

Figure 5.2 compares the singular values of continuous and discrete representations of the system matrix **A** for a network of 50 clocks (100 states).

```
% PLOTING SINGULAR VALUES
% Comparing Digital & Continuous Representations
% 2010

% Defining Constants
N=50; % number of subsystems (clocks) ( 2*N number of states)
Wmax=1; % Max Normalised Clock Frequency
Wmin=0.001; % Max Normalised Clock Frequency
Wn=Wmin+(Wmax-Wmin)*[0:1:N-1]/(N-1); % equi-spaced freqs, uniform distribution over range
Wn=Wn([randperm(length(Wn))]);
mag=0.001; % Maximum coupling magnitude

% Defining Couplying, see function details for further info
alp=makecouplingmatrix(N,mag,0,2);
% Creating system Matrix, see function “generateA” details for further info
A=generateA(N, alp,Wn);

% Finding Singular Values
singular_valuesAnal=svd(A); % Analog or continuous
singular_valuesDig=svd(expm(A)); % Digital
% plotting
figure(1)
```

```
semilogy(singular_valuesAnal,’xk’)
hold on
grid on
title(“Singular values of System matrix”,“fontsize”, 18)
semilogy(singular_valuesDig,“ok”)
xlabel(“number of singular value (1:2N)”,“fontsize”, 18 )
ylabel(“singular value, $\sigma$”,“fontsize”, 18)
legend(“Analog A: $dx/dt = Ax$”,“Digital A: $x_{k+1} = e^{AT}x_k$”)
hold off


function A=generateA(N,alp,Wn)
%2009
%Function to generate the A matrix (dx/dt=Ax+Bu) for a large system of
%interconnected pendulum sub-systems
%[A]=generateA(N, alp,Wn)
%N=number of clock sub systems
%alp=alpha matrix of coupling parameters; alp(i,j)=0 for i==j;
%alp(i,j) connects sys i to sys j
%Wn=vector of natural frequencies for each subsystem

A=zeros(2*N,2*N); %Allocate memory

%define elementary matrices
AJ=[0 -1;+1 0]; %elementary rotation matrix
AC=[0 0;1 0]; %elementary coupling matrix
AO=[-1 -1;1 -1]; %elementary damped oscillation matrix
AJp=[0 1;1 0]; %positive elementary rotation matrix
Aa=[+1 -1;+1 -1]; %alpha expand matrix
Ar=[+1 +1;+1 +1]; %replicate expand matrix

%Block diagonal elements of A
A_osc=kron(diag(Wn), AJ); %block diagonal oscillation part

%The couplying term Epsilon
%Epsilon(i,i) are small pertubabtions to the diagonal
%Epsilon(i,j) are the off diagonal terms

%Given the alp matrix, the sum of each row is the diagonal coupling term
Alpha=diag(sum(alp, 2));
Epsilon_diag=kron(Alpha,AC);
Epilson_off_diag=kron(alp,-AC);
Epsilon=(Epsilon_diag+Epilson_off_diag);

A=A_osc+Epsilon;


function alp=makecouplingmatrix(n,mag,prob,option)

% 01/10/09
% Generate various couplying matrices, alp
```

```
% Matrix element alp(i,j) denotes coupling strength between clock i and clock j
% Option=1:5; Various coupling structure options
% n is the number of Clocks in network
% mag is the magitude of couplying
% prob is the probability that any 2 clocks are connected

% Option=1; Toplitz connection structure, linearly decaying nearest neighbour
%mag=max couplying strength, prob is n/a (can let prob=0)
% Option=2; Decaying couplying strength
%mag=max couplying strength, prob is n/a (can let prob=0)
% Option=3; Probabilitic Coupling (random long range connection)
%mag=couplying strength, prob is in range [0:1]
% Option=4; Immediate nearest neighbour
%mag=couplying strength, prob is n/a (can let prob=0)
% Option=5; Toeplitz connection structure, geometrically decaying nearest neighbours
%mag=max couplying strength, prob is n/a (can let prob=0)

if (option == 1) %Toplitz connection structure, linearly decaying nearest neighbour
%Creating matrix alp with zeros on diagonal and decreaing magnitudes on
%off-diagonal, so that any given clock is couplyed strongly with those
%nearby and less with those far away, strongest couplying is
%determined by mag parameter
alpha=toeplitz((n-1)*0.1:-0.1:0);
alpha=alpha-diag(diag(alpha));
alpha=alpha/((n-1)*0.1-0.1);
alp=mag*alpha;
end


if (option ==2) %decaying couplying strength
% Creating matrix alp of coupling terms with exponential decay
% in distance away from the node
% Coupling is of the form mag*exp(-dec*distance)
% distance = difference in clock number
dec=0.5; %rate of exponential decay
alpha=toeplitz(0:-1:-n+1);
alpha=mag*exp(dec*alpha);
alpha=alpha-diag(diag(alpha)); %remove the diagonal in the coupling matrix
%alpha=alpha-diag(sum(alpha)); %would balance the diagonal in the coupling
%matrix, don't need as generate A does this instead
alp=alpha;
end



if option==3 % Probabilitic Coupling (random long range connection)
% Creating matrix alp of coupling terms with coupling terms modelling
% long range network connection with probability, prob
% strength of this coupling is mag (uniform across the entire field)
beta=rand(n); %create a matrix with elements between 0 and 1
beta=mag*floor(beta+prob); %select those elements greater than 1
```

```
beta=beta-diag(diag(beta)); %remove the diagonal of the coupling matrix
beta=triu(beta); %only keep the uppertriangular part
beta=beta+beta’; %make coupling symmetric
beta=beta-diag(diag(beta)); %remove diagonal elements
%balance the diagonal of the coupling matrix - no need as done later in
%generateA
alp=beta;
end

if (option==4) % Immediate nearest neighbour
% Creating matrix alp of couplying terms modelling nearest neighbour
% connection (each node is only connected to its nearest neighbours)
alp=circshift(diag(ones(1,n)),-1);
alp=triu(alp);
alp=alp+alp’;
alp=mag*alp;
end

if (option==5) %Toeplitz connection structure, geometrically decaying nearest neighbours
% Creating matrix alp of coupling terms with geometric decay
% in distance away from the node
alpha=mag.^toeplitz(0:+1:n-1);
alpha=alpha-diag(diag(alpha)); %remove the diagonal in the coupling matrix
alp=alpha;
end
```

A.5.3 Figure 5.6: Observability as a Function of Network Coupling

Figure 5.6 considers the percentage of the network that is observable as a function of network coupling for a networks of 10,100,200 and 500 clocks.

```
% Observabilty versus connection strength with a geometric toplitz stucture of
% coupling strongest at nearest neighbours (distance based geometric decay
% in coupling
% 12/12/2009

N_vect=[10,100,200,500]; %number of clocks
mag_vect=[logspace(-3,-1,8),0.3,0.5,0.9,0.95,1]; %strength of coupling
T=1; %sample time
TT=50; %number of trials
tolerance=1/(2^10);
r=zeros(length(mag_vect), length(N_vect)); %memory allocation
rp=zeros(length(N_vect),TT);%memory allocation
std_r=zeros(length(mag_vect), length(N_vect)); %memory allocation

for i=1:length(N_vect)
        N=N_vect(i)
        C=zeros(1,2*N);
```

```
    C(2)=1;%let C be connected to only one state
    for t=1:TT
        t=t
        Wmin=0.001;
        Wmax=1;
        Wn=Wmin+(Wmax-Wmin)*[0:1:N-1]/N;
        Wn=Wn([randperm(length(Wn))]);
        for k=1:length(mag_vect)
            mag=mag_vect(k);
            alp=makecouplingmatrix(N,mag,0,5);
            A=generateA(N,alp,Wn);
            %check observability
            O=obsv(expm(A*T),C);
            rp(k,t)=ceil(rank(O,tolerance)/2/N*100);
        end
    end
    r(:,i)=mean(rp’);
    std_r(:,i)=std(rp’,1);
    figure(2)
    h=subplot(1,1,1);
    string_colour=[’r’,’b’,’k’,’g’,’¿’,’k’,’y’,’x’];
    errorbar(mag_vect,r(:,i)’,std_r(:,i)’, string_colour(i));
    set(h,’XScale’,’log’)
    grid on
    hold on
end
vals=num2str(N_vect’);
string=repmat(’N=’, length(N_vect),1);
text4legend=strcat(string, vals);
legend(text4legend);
ylabel(“Percentage of Observable Clocks (%)”)
title(“Obervability as a function of increasing coupling magnitude’)
xlabel(“Maximum Coupling Magnitude \ alpha”)
```

A.5.4 Figure 5.9: Observability versus Network Order

Figure 5.9 illustrates the percentage of states observable plotted against increasing networked size N. For networks larger than 100 clocks observability falls dramatically, with a $\frac{1}{N}$ scaling law, as the number of clocks increases.

```
%% Percentage of States Observable versus Increasing Network Order, N
% Comparing Observability with different numbers of bits
% 2010

% Define Constants
N_vect=[2:2:10,20:10:100,200,300, 500, 1000]; %number of clocks
mag=0.1 %strength of coupling
```

```
T=1; %sample time
TT=50; %number of trials
tolerance_vect=[1/(2^10),1/(2^14),1/(2^24)]; %smallest number represented given (10, 14, 24) mea-
surment bits
dec=0.75; %rate of decay in generating C
Wmin=0.001; %minimum normalised Freq
Wmax=1; %maximum normalised Freq

%Pre-Memory Allocate
r=zeros(length(tolerance_vect), length(N_vect)); %allocation
rp=zeros(length(N_vect),TT);%allocation
std_r=zeros(length(tolerance_vect), length(N_vect)); %allocation


for i=1:length(N_vect)
    N=N_vect(i)
    %let output measurement C be connected to all states with maximum
    %connection strength at clock number N/2 and exponentally decaying
    %strength away from clock N/2 towards clocks 1 and N
    decay=exp([0:-dec:-(N-1)*dec/2]);
    C=[decay(end:-1:1), decay];
    C=kron(C,[0,1]);
    C=C/abs(sum(C)); %Normalise C such that it is a compact set
    for t=1:TT
        t=t
        %Frequencies over normalised range, Uniformly spaced
        Wn=Wmin+(Wmax-Wmin)*[0:1:N-1]/N;
        Wn=Wn([randperm(length(Wn))]);
        alp=makecouplingmatrix(N,mag,0,5); %Generate coupling strength matrix
        A=generateA(N,alp,Wn); %Generate system matrix

        %check observability
        O=obsv(expm(A*T),C); %Generate observability matrix
        for k=1:length(tolerance_vect)
            %smallest number represented given number of measurement bits
            tolerance=tolerance_vect(k);
            %Find number of singular values of O that are greater than tolerance
            rp(i,t,k)=ceil(rank(O,tolerance)/2/N*100);
        end
    end
end
figure(8)
h=subplot(1,1,1);
string_colour=[’r’,’b’,’k’];
for k=1:length(tolerance_vect)
    r(k,:)=mean(rp(:,:,k)’); %Find mean observability percentage over trials
    std_r(k,:)=std(rp(:,:,1)’,1); %Find standard deviation of observability percentage over trials
    errorbar(N_vect,r(k,:)’,std_r(k,:)’, string_colour(k));
    grid on
    hold on
end
```

```
set(h,’XScale’,’log’)
set(h,’YScale’,’log’)
legend(’2^10 bits’, ’2^14 bits’,’2^24 bits’);
ylabel(“% Observable”)
title(“Observability as a function of increasing Network Size” )
xlabel(“Number of Clocks (N)”)
```

A.5.5 Figure 6.4: Covariance Trace versus Network Order for Kalman Estimation

Figure 5.9 shows the normalised trace of the covariance matrix for Kalman estimation, **P** after iterating through 10 seconds of EEG data (5000 samples) against increasing network order, N.

```
%% Kalman Trace versus Network order plot
%03/06/2010
clear all
N_vect=[2,4,6,8,10,15,20,25,30,40,50,60,70,80,90,100,125,150,200,500]; %N=number of clocks

b_vect=[0]; %or example [2,10,0] %b= number of bits 0⇒ inf or continuous
Itt=5000; %number of kalman itterations


for n=1:length(N_vect)
        N=N_vect(n)
        [xhat,x, Kf, Observ_10bit, tr_Papr, tr_Papost, P_apri,O]=kalmanestimate(N,b,Itt);
        Trace_time=tr_Papr/(2*N);
        Trace(n)=Trace_time(end);
end

figure(6)
semilogx(N_vect, Trace)
grid on
title(“Average Variance of Kalman State Estimate”)
xlabel(“Number of Clocks N”)
ylabel(“Normalised Trace of Error Covariance”)
```

```
function [xhat,x, Kf, Observ_10bit, tr_Papr, tr_Papost, P_apri, O]=kalmanestimate(N,b,Itt)
%[xhat,x, Kf, Observ_10bit, tr_Papr, tr_Papost, P_apri,O]=kalmanestimate(N,b,Itt)
%INPUTS
%N num clocks
%b number of measurment bits b=0 for inf bits
%Itt number of kalman iterations
%OUTPUTS
%xhat:timseries of estimated states
```

```
%x: timeseries of trie states
%Kf: timeseries of Kalman gains for each state
%Observ_10bit: rank of observability matrix for a 10-bit tolerance
%tr_Papr: timeseries of trace of apriori covariance
%tr_Papost: timeseries of trace of aposteri covariance
%P_apri: final apriori covariance matrix
%O: observability matrix

%constant variables
Wmin=0.01; %min freq (normalised)
Wmax=1; %max freq (normalised)
T=1; %Ditital sample time
tolerance=1/2^b; %smallest quantisation step
mag=0.01; %max magnitude of couplying strength

%define clock frequencies
Wn=Wmin+(Wmax-Wmin)*[0:1:N-1]/N;
Wn=Wn([randperm(length(Wn))]);
%define coupling matrix
alp=makecouplingmatrix(N,mag,0,5);
A=generateA(N,alp,Wn); %generate unsampled rotational matrix A=[0,-w;+w,0] etc
C=kron(ones(1,N), [0,1]);
O=obsv(expm(A*T),C);

%What percent of states are visible according to the rank test
if (N > 50)
        Observ_10bit=0; %to avoid lengthy simulation time for non-main simulation result
else
        Observ_10bit=ceil(rank(O,tolerance)/2/N*100);
end


%Compare rank result with kalman model
%x(k+1)=Ax
%y=Cx+v where v is the error added by quantisation


%initise x
x=zeros(2*N,Itt+1);
x0_firststate=rand(1,N); %initial state
x0_secondstate=cos(asin(x0_firststate));
x0=kron(x0_firststate,[1,0])+kron(x0_secondstate,[0,1]);
x0=x0’;
%y(1)=quantizer(C*x0,b);

xhat=zeros(2*N,Itt+1); %initialing state extimate
Kf=zeros(2*N,Itt); %initialing kalman gain
xhat_predict(:,1)=rand(1,(2*N));
P_apri=eye(2*N); %initialising P_apriori
P_apost=eye(2*N); %initialising P_aposteri
R1=0; %variance of state noise
```

```
R2=1; %variance of measurement noise
G=zeros(1,2*N); %models case of x(k+1)=Ax +Gw for us G=0
T=1;%Sample time
A=expm(A*T); %digitise A
C=C/N; %normalise EEG, to between bewteen +1 and -1
%(need norm for ease of quantising as nesc for comparing measures on EEG)

for k=1:Itt
    if (k/50)==round(k/50)
        k
    end
    if k==1
        x(:,k)=A*x0;
    else
        x(:,k)=A*x(:,k-1);
    end

    if b==0
        y(k)=C*x(:,k);
    else
        y(k)=quantizer(C*x(:,k),b);
    end

    P_apri=A*P_apost*A'+G*R1*G';%update equation for new P_apriori=f(P_aposteri)
    tr_Papr(k) = trace(P_apri);

    Kf(:,k)=P_apri*C'*inv(R2+C*P_apri*C'); %Kalman gain = f(P_apriori)

    P_apost=P_apri-P_apri*C'*inv(C*P_apri*C' +R2)*C*P_apri; %P_aposteri=f(P_apriori)
    tr_Papost(k) =trace(P_apost);


    xhat_update(:,k)=xhat_predict(:,k)+Kf(:,k)*(y(k)-C*xhat_predict(:,k));

    xhat_predict(:,k+1)=A*xhat_update(:,k);%+G*u(k);

end

xhat= [xhat_update, xhat_update(:,end)];




function [xq]=quantizer(x,b)
%[xq]=quantizer(x,b)
%xq = quantized output
%x = unquatised signal
%b = number of bits
%quantising bewteen +1 and -1 with 2^b levels
x(x>=1)=1-eps; %make signals that are near 1 just less than 1;
x(x<=-1)=-1+eps; %make signals that are near -1 just greater than 1;
xq=floor((x+1)*2^(b-1)); %b-1
```

```
xq=xq/2^(b-1); %b-1
xq=xq-(2^(b)-1)/2^b; %xq-1; %(2^(b)-1)/2^b;
```

A.5.6 Figures 6.12 and 6.14: Distance Evaluation of Error Area for Entropy of Measure Preserving Maps

Figures 6.12 and 6.14 illustrate the error area mapped by a non-linear oscillator and Van Der Pol Oscillator respectively as a metric of entropy on measure preserving maps.

```
%% Entropy of Measure Preserving Oscillator Maps
% Visualising Mappings and evaluating entropy through distance based
% measures
% 2010

clear all
%Define initial unit square
NoPoints=10000;
x1(1,:)=rand(1,NoPoints); %state1 at initial time 1
x2(1,:)=rand(1,NoPoints); %state2 at initial time 1
x1mid(1)=0.5;
x2mid(1)=0.5;
%define unit square edge sets
Oto1=0:0.01:1;
x1edge(1,:)=[Oto1,Oto1,zeros(1,length(Oto1)),ones(1,length(Oto1))];%edge set, state1_edgetime0
x2edge(1,:)=[zeros(1,length(Oto1)),ones(1,length(Oto1)),Oto1,Oto1]; %edge set,state2_edgetime0



%% Plot example mappings
itt=7; %num of mappings
w=2*pi/10; %clock frequency

%CHOOSE MAP
%map='Linear';
%map='NonLinear';
map='VanDarPol';
for i=1:itt
        [x1mid(i+1),x2mid(i+1)]=mappoints(map,x1mid(i),x2mid(i),w);
        [x1edge(i+1,:),x2edge(i+1,:)]=mappoints(map,x1edge(i,:),x2edge(i,:),w);
end

figure(20)
legendsetup %sets up appropriate legend
plot(x1edge(1,:),x2edge(1,:),'.', 'MarkerSize',7, 'color',[0.5 0.5 0.5])
hold on
plot(x1mid(1),x2mid(1),'o','color',[0.5 0.5 0.5],'LineWidth',2)
for i=2:itt
```

```
        plot(x1edge(i,:),x2edge(i,:),’.’, ’MarkerSize’,2, ’color’,[0.5 0.5 0.5])
        hold on
        plot(x1mid(i),x2mid(i),’o’,’color’,[0.5 0.5 0.5],’LineWidth’,1)
end
side=length(Oto1);
plot(x1edge(itt+1,1:side),x2edge(itt+1,1:side),’k.’)
plot(x1edge(itt+1,1+side:2*side),x2edge(itt+1,1+side:2*side),’k.’)
plot(x1edge(itt+1,1+2*side:3*side),x2edge(itt+1,1+2*side:3*side),’k.’)
plot(x1edge(itt+1,1+3*side:4*side),x2edge(itt+1,1+3*side:4*side),’k.’)
plot(x1mid(itt+1),x2mid(itt+1),’ok’,’LineWidth’,2,’MarkerSize’,7)
xlabel(’State x_1’, ’fontsize’, 14)
ylabel(’State x_2’,’fontsize’, 14)
set(gca,’FontSize’,12)
set(gca,’XLim’,[-2 2])
set(gca,’YLim’,[-2 2])
grid on
legend(’S_0’,’x_0^c’,’S_1’,’x_1^c’,’S_2’,’x_2^c’,’S_3’,’x_3^c’,’S_4’,’x_4^c’,’S_5’,’x_5^c’)
hold off




%% Calculate average distance of edge from centre in all directions
itt=10000; %number of mappings

w=2*pi/1000; %clock frequency

%CHOOSE MAP
%map=’Linear’;
%map=’NonLinear’;
map=’VanDarPol’;
for i=1:itt
        [x1mid(i+1),x2mid(i+1)]=mappoints(map,x1mid(i),x2mid(i),w);
        [x1edge(i+1,:),x2edge(i+1,:)]=mappoints(map,x1edge(i,:),x2edge(i,:),w);
end

%Distance measured to show entropy =0
for i=1:itt
        DistancefromCentrex1_k(i,:)=x1edge(i+1,:)-x1mid(i+1); %distance form centre at each point k
        DistancefromCentrex2_k(i,:)=x2edge(i+1,:)-x2mid(i+1);
end

figure(8)
grey=[0.75,0.75,0.75];
%Mean at each time step
plot(mean((DistancefromCentrex1_k(:,:)’)),’–’, ’Color’, grey)
hold on
plot(mean((DistancefromCentrex2_k(:,:)’)),’–k’)
xlabel(’Sample time, k’, ’FontSize’, 14)
%Moving Mean
```

```
movingmean_x1=cumsum(mean((DistancefromCentrex1_k(:,:)’)))./[1:1:size(x1edge,1)-1];
movingmean_x2=cumsum(mean((DistancefromCentrex2_k(:,:)’)))./[1:1:size(x2edge,1)-1];
plot(movingmean_x1, ’Color’, grey, ’LineWidth’, 3)
hold on
plot(movingmean_x2,’k’, ’LineWidth’, 3)
legend(“mean(x_k^1-x_k^c,1)”, “mean(x^2_k-x_k^c,2)”, “cumulative mean x^1”, “cumulative mean
x^2”)
title(“Mean Distance between Centre Point & Edges of Error Area”, “FontSize”, 14)
ylabel(“Distance”, “FontSize”, 14)




function [x1new, x2new]=mappoints(Map, x1, x2, w)

T=1; %digital sampling time

if (strcmp(Map, ’Linear’))

        A=[0,-w;w,0]; %continuous map
        A=expm(A*T); %digital map
        eigA=abs(eig(A));
        x=[x1;x2];
        for i=1:length(x1)
                xnew(:,i)=A*x(:,i);
        end
        x1new=xnew(1,:);
        x2new=xnew(2,:);

end


if (strcmp(Map, ’NonLinear’))
        x=[x1;x2];
        for i=1:length(x1)
                A=[0,-w;w*cos(x1(i)),0]; %continuous map
                A=expm(A*T);%digital map
                %or could equally use the following to get equivalent result.
                %A=[cos(sqrt(cos(x1(i)))*w), (-1/sqrt(cos(x1(i))))*sin(sqrt(cos(x1(i)))*w);
                % (sqrt(cos(x1(i))))*sin(sqrt(cos(x1(i)))*w),cos(sqrt(cos(x1(i)))*w)]
                eigA(:,i)=abs(eig(A));
                xnew(:,i)=A*x(:,i);
        end
        x1new=xnew(1,:);
        x2new=xnew(2,:);
end


if (strcmp(Map, ’VanDarPol’))
        e=0.0001; %vanderpol parameter
        x=[x1;x2];
        for i=1:length(x1)
```

```
            A=[0,-w;w,-e*(1-(x1(i))^2)];%continuous map
            A=expm(A*T); %digital map
            xnew(:,i)=A*x(:,i);
        end
        x1new=xnew(1,:);
        x2new=xnew(2,:);
end
```

A.5.7 Figure 7.2: Evoked Network Clock Simulation

Figure 7.2 was generated using the Matlab Simulink simulation shown in Figure A.9 and A.10. The contents of each second order linear clock block (clock numbers 1-2 and 4-25) are shown in Figure A.11 with the contents of the non-linear clock (clock number 3) shown in Figure A.12. The associated set-up code in Matlab is also provided in this section.

```
%%Initialisation variables for clock system simulation Model 5by5_v6

%% Constants

Total_num_Clock_systems=25;
N=Total_num_Clock_systems;
feedback_difference=1; %set =zero for coupling to be = state of other
%systems or set=1 for the diff between current system and other systems


%% Evoked Input

Evoked_Amp=10;
Evoked_Freq=10;
%Switch vector E(k): 1=¿ Evoked signal is connected to system k
E=zeros(1,Total_num_Clock_systems);
E([1,2,6,7])=1;
E([16,17,21,22])=1;
E([4,9,5,10])=1;
E([19,24,20,25])=1;


%% Clock system
%Damp(i) sets damping parameter for clock i
Damp(1)=0.01;
Damp([2,6,7])=0.0075;
Damp([3,8,13,12,11])=0.005;
Damp([4,9,14,19,18,17,16])=0.0025;
Damp([5,10,15,20,25,24,23,22,22,21])=0.001;
Damp(3)=-0.01; %unstable element
epsilon=0.00000001; %parameter in Van dar Pole clock (clock number 3)
```

```
%uniformly distributed freq
percentage=100;
Fmid=0.5+(100-0.5)/2;
Fmax=Fmid*(1+percentage/100);
Fmin=Fmid*(1-percentage/100);
F = Fmin + (Fmax-Fmin) * rand(1,Total_num_Clock_systems);
F(1)=10;
F(3)=6;

%% EEG output
%C=weights eg=[w1^2, 0, w2^2, 0 ...etc]
%but simulink only has connections to angle state =¿
%weights eg=[w1^2, w2^2, ...etc]
weights=(2*pi*F).^2;


%% Clock System Coupling



%or alpha(1,1) is coupling strength of system 1 onto system 1
%alpha(1,:) the 1st row, is coupling strength row vector for all systems onto system 1
%alpha(2,:) the 2nd row, is coupling strength for all systems onto system 2
%more specifically alpha(2,5) is the coupling strength for system 5 onto system 2 etc

%Let coupling be anywhere in range 0-alp_max where e.g. alp_max=0.01
alp_max=0.01;
alp=rand(N,N)*alp_max;
alpha=alp;

alpha([1:N+1:N*N])=0; %set diagonal elements to zero (so self coupling)

%allows global connection (default)
%to mutually couple systems 1 & 2, sys_coup(1,1)=2 and sys_coup(2,1)=1;
%each row i corresponds to the systems to be connected to system i
sys_coup=zeros(Total_num_Clock_systems,Total_num_Clock_systems);
sys_coup(:,1)=-1*ones(1,Total_num_Clock_systems);


%% load results
load Xsimout.mat
load tsimout
load EEG.mat
%load pulse_input.mat

EEG_channel(1,:)=weights(1)*X(1+1,:)+weights(2)*X(1+2,:)+weights(6)*X(1+6,:)+weights(7)*X(1+7,:);
EEG_channel(2,:)=weights(4)*X(1+4,:)+weights(5)*X(1+5,:)+weights(9)*X(1+9,:)+weights(10)*X(1+10,:);
EEG_channel(3,:)=weights(16)*X(1+16,:)+weights(17)*X(1+17,:)+weights(21)*X(1+21,:)+weights(22)*X(1+22,:);
EEG_channel(4,:)=weights(19)*X(1+19,:)+weights(20)*X(1+20,:)+weights(24)*X(1+24,:)+weights(25)*X(1+25,:);


%% Testing of results, with evoked sig
```

```
clear phase
clear amp
clear amp_sig
clear phase_sig
data=X(1,:)

%Find which clocks are synchronised to evoked input via moving window
Fs=512;
window=Fs;
step=round(window/10);
freq=10;
time_whole=X(1,:);
steptime=1:step:round((length(data)-window));
phase=zeros(25,length(steptime));
amp=zeros(25, length(steptime));

phase_sig=zeros(4,length(steptime));
amp_sig=zeros(4,length(steptime));

for clock=1:25;
         clock
        data=X(clock+1,:);

        k=0;
        for i=1:step:round((length(data)-window))
                 k=k+1;
                timeseries=data(1+(i-1):window+(i-1))';
                tchunk=time_whole(1+(i-1):window+(i-1))';
                [phase(clock,k), amp(clock,k)]=is_sync(timeseries, Fs,tchunk, freq);
        end

end

for sig=1:4
        data=EEG_channel(sig,:);
         sig=sig
        steptime=1:step:round((length(data)-window));
        k=0;
        for i=1:step:round((length(data)-window))
                 k=k+1;
                timeseries=data(1+(i-1):window+(i-1))';
                tchunk=time_whole(1+(i-1):window+(i-1))';
                [phase_sig(sig,k), amp_sig(sig,k)]=is_sync(timeseries, Fs,tchunk, freq);
        end
end


%% plot results of previous cell
for clock=1:25
         clock
        subplot(3,1,1)
        plot(X(1,:),X(clock+1,:),'r')
```

```
        subplot(3,1,2)
        plot(steptime/Fs,phase(clock,:))
        subplot(3,1,3)
        pause
end

for sig=1:4
        subplot(3,1,1)
        plot(X(1,:),EEG_channel(sig,:),'r')
        subplot(3,1,2)
        plot(steptime/Fs,phase_sig(sig,:))
        subplot(3,1,3)
        pause
end


%% Testing of results, with Unstable osc
clear phaseBad
clear ampBad
clear amp_sigBad
clear phase_sigBad

data=X(1,:); %set up variable
%Find which clocks are synchronised to unstable osc,
%letting unstable ossillation be box number 3
Fs=512;
window=Fs;
freq=F(3);
time_whole=X(1,:);
step=round(window/10);

steptime=1:step:round((length(data)-window));
phaseBad=zeros(25,length(steptime));
ampBad=zeros(25, length(steptime));

phase_sigBad=zeros(4,length(steptime));
amp_sigBad=zeros(4,length(steptime));

for clock=1:25;
         clock
        data=X(clock+1,:);

        steptime=1:step:round((length(data)-window));
        k=0;
        for i=1:step:round((length(data)-window))
                k=k+1;
                timeseries=data(1+(i-1):window+(i-1))';
                tchunk=time_whole(1+(i-1):window+(i-1))';
                [phaseBad(clock,k), ampBad(clock,k)]=is_sync(timeseries, Fs,tchunk, freq);
         end
end
```

```
for sig=1:4
    data=EEG_channel(sig,:);
    sig=sig
    steptime=1:step:round((length(data)-window));
    k=0;
    for i=1:step:round((length(data)-window))
         k=k+1;
        timeseries=data(1+(i-1):window+(i-1))';
        tchunk=time_whole(1+(i-1):window+(i-1))';
        [phase_sigBad(sig,k), amp_sigBad(sig,k)]=is_sync(timeseries, Fs,tchunk, freq);
    end
end


%% plot results of previous cell
for clock=1:25
         clock
        subplot(3,1,1)
        plot(X(1,:),X(clock+1,:),'r')
        grid on
        subplot(3,1,2)
        plot(steptime/Fs,phaseBad(clock,:))
        grid on
        pause
end

for sig=1:4
         sig
        subplot(3,1,1)
        plot(X(1,:),EEG_channel(sig,:),'r')
        grid on
        grid on
        subplot(3,1,2)
        plot(steptime/Fs,phase_sigBad(sig,:))
        grid on
        grid on
        pause
end



function [phase, amp]=is_sync(timeseries, Fs,t, freq)

%[phase, amp]=is_sync(timeseries, Fs,t, freq)
%where Fs is sample time
%t= time vector
%freq is frequency you want to find phase offset of, can be a vector


%% Phase estimation based on least squares
for f=1:length(freq)
```

```
          F=freq(f);
          xfc=cos(2*pi*F*t);
          xfs=sin(2*pi*F*t);
          H=[xfc,xfs];
          x=timeseries;
          Theta_est=[2/length(x),0;0,2/length(x)]*(H'*x);
          phase(f)=atan(-Theta_est(2)/ Theta_est(1));
          amp(f)=sqrt(Theta_est(1).^2 +Theta_est(2).^2);
end
```

Figure A.9: Overall Block Digram of Network Clock Simulation in Simulink, part a

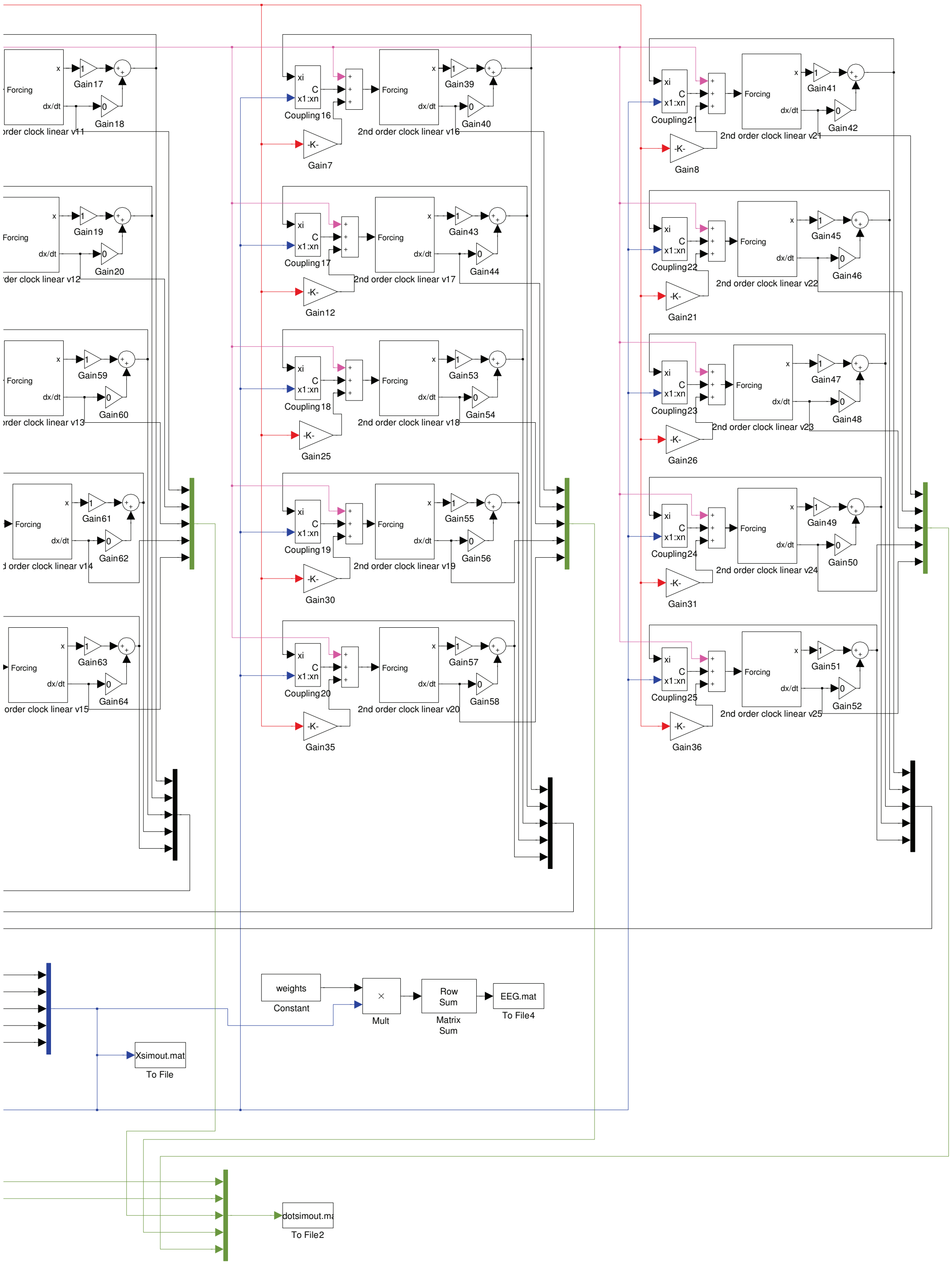

Figure A.10: Overall Block Digram of Network Clock Simulation in Simulink, part b

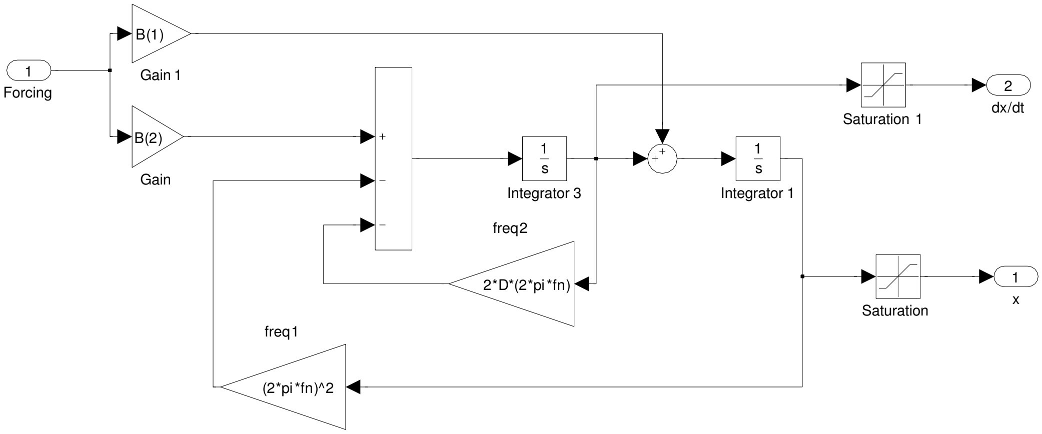

Figure A.11: The 2^{nd} order linear clock simulink block diagram. Corresponds to clock numbers 1-2 and 4-25 in A.9 and A.10

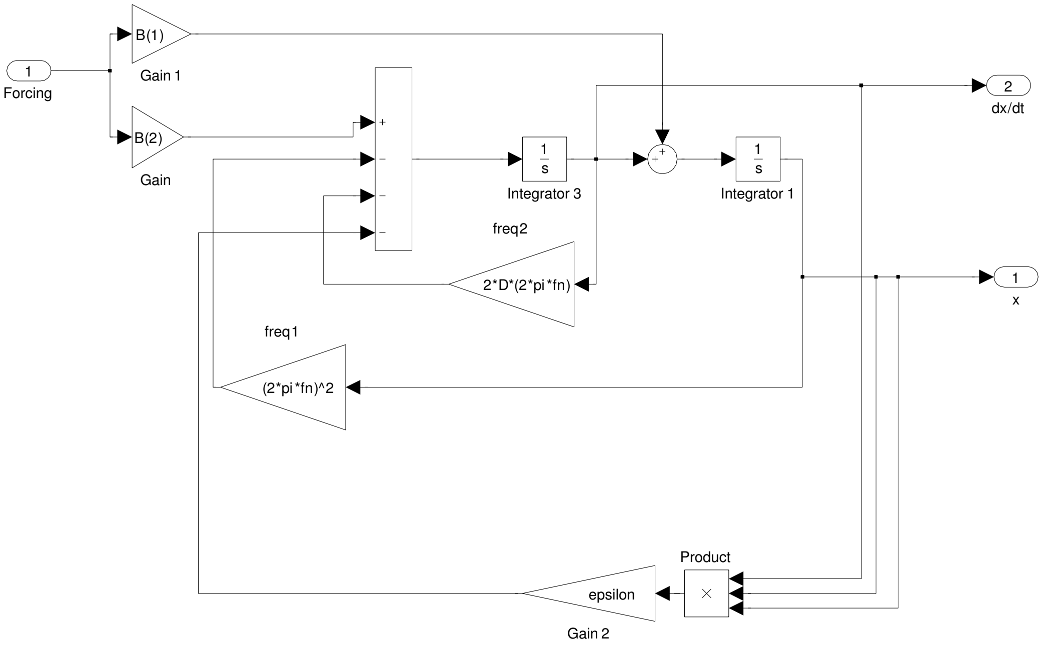

Figure A.12: The Van Der Pol Non-linear clock simulink block diagram. Corresponds to clock number 3 in A.9

A.5.8 Figure 7.4: Comparing Singular values of the Observability Matrix for Balanced and Original System State Representations.

Figure 7.4 considers the singular values of the time-scaled continuous representation of the system matrix **A** for a network of 50 clocks (100 states) comparing a balanced system state representations with the original representation used throughout this thesis.

```
%% Observability with the Balanced Transform

% (1) Generate transformed and time scaled model
% (2) Balanced transform
% (3) Optional Balanced system truncation
% (4) Plot singular values


% (1) Generate transformed and time scaled model

N=50; %number of subsystems (=¿ 2*N number of states)
Fmax=1; %non-normalised maximum frequency
option=[1,2,3]; %set up for loop for each trace

for opt=1:length(option)

    if opt==1
        Fmin=0.98; %normalised minimum frequency
    elseif opt==2
        Fmin=0.6; %normalised minimum frequency
    elseif opt==3
        Fmin=0.0025; %normalised minimum frequency
    end


    F=Fmin+(Fmax-Fmin)*[1:1:N]/N; %equi-spaced freqs, uniform distribution over range
    Wn=2*pi*F;
    Wnorm=max(Wn);
    D=repmat(0.001,1,N); %Define damping parameters

    alpha=0.001; %Define Couping Parameters
    alp=alpha*triu(ones(N),1);

    Aold=generateDampedA(N, alp,D,Wn);
    Aold=Aold/Wnorm; %Timescale

     %non-balanced B  C
    Bold=zeros(1,2*N)'; %pre-memory allocate
    Bold(1:2:(2*N)-1)=Wn/Wnorm;
    Bold(2:2:2*N)=0;

    Cold=zeros(1,2*N); %pre-memory allocate
    Cold(1:2:2*N)=0;
    Cold(2:2:(2*N))=-1;
```

```
        % (2) Balanced transform

        Q=lyap(Aold', Cold'*Cold);
        P=lyap(Aold,Bold*Bold');
        U=chol(P,'lower');
        [K,lam]=eig(U'*Q*U);
        sigma=sqrt(lam); %Singular values

        %Or equally using the eigean values
        T=sqrt(sigma)*K'*inv(U); %Balanced transformation
        Tinv=U*K*sigma^(-0.5);
        C=Cold*inv(T); %Balanced C
        B=T*Bold; %Balanced B
        A=T*Aold*inv(T); %Balanced A


        % (3) Optional Balanced system truncation

        truncate=0; %option to truncate system: 1 to truncate, 0 otherwise
        k=50; %order that i'm reducing system to
        if truncate==1
            %If I only had kth column of K
            Kro=K(:,1:k); %K reduced order
            Sigmaro=sigma(1:k,1:k);
            T_ro=sqrt(Sigmaro)*Kro'*inv(U);
            B=T_ro*Bold %Balanced B
            Tinv_ro=U*Kro*(Sigmaro)^(-0.5);
            C=Cold*Tinv_ro %Balanced C
            A=T_ro*Aold*Tinv_ro %Balanced A
        end

        obseby=obsv(A,C/N);
        %Normalised C above so C is a convex combination and max singular value is of order 1
        singular_values=svd(obseby);

        obsebyold=obsv(Aold,Cold/N);
        %Normalised C used to so C is a convex combination and max singular value is of order 1
        singular_valuesold=svd(obsebyold);

        sing_array(opt,:)=singular_values;
        sing_arrayold(opt,:)=singular_valuesold;



    end

    % (4) Plot singular values

    % Plot Singular values of non-Balanced model
    semilogy(sing_arrayold(1,:),'ok')
    hold on
```

```
grid on
semilogy(sing_arrayold(2,:), “.k”)
semilogy(sing_arrayold(3,:), “xk”)

% Plot Singular values of Balanced model
grey=[0.75,0.75,0.75];
semilogy(sing_array(1,:), “o”, “Color”, grey)
hold on
grid on
semilogy(sing_array(2,:), “.”, “Color”, grey)
semilogy(sing_array(3,:), “x”, “Color”, grey)

title(“Singular values of the Observability Matrix”, “fontsize”, 14)
xlabel(“number of singular value (1:2N)”, “fontsize”, 14 )
ylabel(“singular value, sigma”, “fontsize”, 14)
legend(“Normalised Frequencies 0.98-1”, “Normalised Frequencies 0.6-1”,
“Normalised Frequencies 0.0025-1”, “Balanced System, Normalised Frequencies 0.98-1”,
“Balanced System, Normalised Frequencies 0.6-1”, “Balanced System, Normalised Frequencies 0.0025-
1”)
hold off
```

Note the function *generateDampedA* is provided in A.5.1.

A.5.9 Figures A.7 and A.8: Comparing Phase Estimation Techniques

Figure A.7 compares the phase estimation performance of the least squares algorithm with the Hilbert transforms for a signal in Gaussian Noise, while Figure A.8 compares the phase estimation performance of the least squares algorithm with the Hilbert transforms for a multi-frequency signal.

```
%% COMPARE HILBERT AND LEAST SQUARES PHASE ESTIMATION: GAUSSIAN NOISE
%2008

Fs=1/0.001; %define sampling frequency
t=0:1/Fs:2; % define time vector
f1=10; %define sinusoid freqency

%least squares phase
Nvector=logspace(-1,3,100); %level of noise
for k=1:100 %loop over noise level
        for i=1:200 %loop over random generation of Gaussian noise vector
                N=Nvector(k);
                Noise=N*randn(1,length(t));
                Noise_rms=sqrt(mean(Noise. ∧ 2))’;
                %Define Signal
                x=cos(2*pi*f1*t +pi/4)′ + Noise′;
```

```
                %Least Squares Algorithm
                xfc=cos(2*pi*f1*t)';
                xfs=sin(2*pi*f1*t)';
                H=[xfc,xfs];
                Theta_est=[2/length(x),0;0,2/length(x)]*(H'*x);
                Phase(i)=atan2(-Theta_est(2),Theta_est(1));
        end
        Phase_error(k)=abs((mean(Phase-pi/4)));
        SNR(k)=(1/sqrt(2))/Noise_rms;
end

figure(1)
semilogx(SNR, Phase_error, “k*”)
title(“Phase error versus SNR”,“fontsize”, 14)
xlabel(“SNR”, “fontsize”, 14)
ylabel(“|Phase Error| (rad/s)”, “fontsize”, 14)
grid on
hold on

%hilbert phase
for k=1:100 %loop over noise level
        for i=1:200 %loop over random generation of Gaussian noise vector
                N=Nvector(k);
                Noise=N*randn(1,length(t));
                Noise_rms=sqrt(mean(Noise. ∧ 2))';
                %Define Signal
                x=cos(2*pi*f1*t +pi/4)' + Noise';                    %Compute Hilbert Phase
                Phi=angle(hilbert(x))-angle(hilbert(cos(2*pi*f1*t')));
                %Transpose phase
                index_neg=find(Phi<-pi);
                Phi(index_neg)=Phi(index_neg)+2*pi;
                index_neg=find(Phi>pi);
                Phi(index_neg)=Phi(index_neg)-2*pi;
                Phaseh(i)=mean(Phi);
        end
        Phase_errorh(k)=abs((mean(Phaseh-pi/4)));
        SNR(k)=(1/sqrt(2))/Noise_rms;
end

semilogx(SNR, Phase_errorh, “ko”)
legend(“Least Squares method”, “Hilbert method”)
hold off



%% COMPARE HILBERT AND LEAST SQUARES PHASE ESTIMATION: MULTIFREQUENCY
“NOISE”

Fs=1/0.001; %define sampling frequency
t=0:1/Fs:2; % define time vector
f1=10; %define sinusoid freqency
```

```
f2=15; %define second sinusoid freqency

%least squares phase
Nvector=logspace(-1,3,100); %level of noise
for k=1:100 %loop over noise level
    N=Nvector(k);
    Noise=N*cos(2*pi*f2*t +pi/8);
    Noise_rms=N/sqrt(2);
    %Least Squares Method
    x=cos(2*pi*f1*t +pi/4)' + Noise';
    xfc=cos(2*pi*f1*t)';
    xfs=sin(2*pi*f1*t)';
    H=[xfc,xfs];
    Theta_est=[2/length(x),0;0,2/length(x)]*(H'*x);
    Phase=atan2(-Theta_est(2),Theta_est(1));
   Phase_error(k)=abs(Phase-pi/4);
    SNR(k)=(1/sqrt(2))/Noise_rms;
end

figure(2)
semilogx(SNR, Phase_error, “k*”)
title(“Phase error versus SNR”,“fontsize”, 14)
xlabel(“SNR”, “fontsize”, 14)
ylabel(“|Phase Error| (rad/s)”, “fontsize”, 14)
grid on
hold on

%hilbert phase
for k=1:100 %loop over noise level
    N=Nvector(k);
    Noise=N*cos(2*pi*f2*t +pi/8);
    Noise_rms=N/sqrt(2);
    x=cos(2*pi*f1*t +pi/4)' + Noise';
    %Compute Hilbert Phase
    Phi=angle(hilbert(x))-angle(hilbert(cos(2*pi*f1*t')));
    index_neg=find(Phi<-pi);
    Phi(index_neg)=Phi(index_neg)+2*pi;
    index_neg=find(Phi>pi);
    Phi(index_neg)=Phi(index_neg)-2*pi;
    Phaseh=mean(Phi);
    Phase_errorh(k)=abs(Phaseh-pi/4);
    SNR(k)=(1/sqrt(2))/Noise_rms;
end

semilogx(SNR, Phase_errorh, “ko”)
legend(“Least Squares method”, “Hilbert method”)
hold off
```

Bibliography

[1] P.L. Nunez and R. Srinivasan. *Electric Fields of the Brain - The neurophysics of EEG*. Oxford University Press, 2nd edition, 2006.

[2] H. P. Zaveri, M. G. Frei, and I. Osorio. State of seizure prediction. In Schelter B., Trimmer J., and A. Schulze-Bonhage, editors, *Seizure Prediction in Epilepsy: From Basic Mechanisms to Clinical Applications*, pages 325–330. Wiley-VCH, 2008.

[3] ILAE IBE and WHO. *Atlas Epilepsy Care in the World 2005: Global Campaign Against Epilepsy*. World Health Organization, 2005.

[4] E.H. Reynolds. The ILAE[2] /IBE[1] /WHO[3] global campaign against epilepsy: Bringing epilepsy "out of the shadows" . *Epilepsy & Behaviour*, 1:S3–S8, 2000.

[5] R.G. Beran, L. Hall, and J. Michelazzi. An accurate assessment of the prevalence ratio of epilepsy adequately adjusted by influencing factors. *Neuroepidemiology*, 4(2):71–81, 1985.

[6] J. Rho and R. Sankar. Progress in epilepsy research: The pharmacological basis of antiepileptic drugs. *Epilepsia*, 40:1471–1483, 1999.

[7] B. Schmitz. Psychiatric syndromes related to antiepileptic drugs. *Epilepsia*, 40:S65–S70, 1999.

[8] W. Löscher and D. Schmidt. Critical review: Experimental and clinical evidence for loss of effect (tolerance) during prolonged treatment with antiepileptic drugs. *Epilepsia*, 47:1253–1284, 2006.

[9] L.D Iasemidis. Epileptic seizure prediction and control. *IEEE Transactions on Biomedical Engineering*, 50:549–558, 2003.

---

[1] IBE: International Bureau for Epilepsy

[2] ILAE: International League against Epilepsy

[3] WHO: World Health Organisation

[10] J. Milton and P. Jung (Eds.). *Epilepsy as a Dynamic Disease.* Springer-Verlag, 2003.

[11] K. Lehnertz, F. Mormann, T. Kreuz, R.G. Andrzejak, C. Reike, P. David, and C.E. Elger. Seizure prediction by nonlinear eeg analysis. *IEEE Engineering in Medicine and Biology Magazine*, 22(1):57–63, 2003.

[12] C.E. Elger. Future trends in epileptology. *Current Opinion in Neurology*, 14:185–186, 2001.

[13] F. Mormann, T. Kreuz, C. Reike, R. G. Andrzejak, A Kraskov, P. David, C. E. Elger, and K. Lehnertz. On the predictability of epileptic seizures. *Clinical Neurophysiology*, 116:569–587, 2005.

[14] G.H. Banks, K.J Regan, and R.G Beran. The prevalence and direct costs of epilepsy in australia. In R.G. Beran and C. Pachlatko, editors, *ILAE*^{2} *Commission on Economic Aspects of Epilepsy. Cost of epilepsy: Proceedings of the 20th International Epilepsy Congress.*, pages 39–48. Wehr-Baden: Ciba-Geigy Verlag, 1995.

[15] C. Mathers and R. Penm. Health system costs of cardiovascular diseases and diabetes in australia 1993-94. *Australian Institute of Health and Welfare, Australian Government: Health and welfare expenditure series no. 5*, 1999.

[16] I. A. W. Kotsopoulos, S.M.A. Evers, A. J. H. Ament, and M.C.T. de Krom. Estimating the costs of epilepsy: An international comparison of epilepsy cost studies. *Epilepsia*, 42(5):634–640, 2001.

[17] E.R. Kandel, J.H. Schwartz, and T.M. Jessel. *Principals of Neural Science.* McGraw-Hill, 4th edition, 2002.

[18] L. Sherwood. *Human physiology: from cells to systems.* Brooks Cole, 4th edition, 2001.

[19] http://www.doctorhugo.org/brainwaves/brainwaves.html.

[20] C.J. Stam. *Nonlinear Brain Dynamics.* Nova Science Publishers, 1st edition edition, 2006.

[21] R.S. Fisher, W. Blume W. Van Emde Boas, C. Elger, P. Genton, P. Lee, and Jr. J. Engel. Epileptic seizures and epilepsy. Definitions proposed by the ILAE^2 and the IBE^1. *Epilepsia*, 46:470–472, 2005.

[22] J.G. R. Jefferys. Models and mechanisms of experimental epilepsies. *Epilepsia*, 44(Suppl. 12):44–50, 2003.

[23] D.A. McCormick and D. Contreras. On the cellular and network bases of epileptic seizures. *Annual Review of Physiology*, 63:815–846, 2001.

[24] C. Bernard. Visions & reflections. dogma and dreams: Experimental lessons for epilepsy mechanism chasers. *Cellular and Molecular Life Sciences*, 62:1177–1181, 2005.

[25] E. Perucca. An introduction to antiepileptic drugs. *Epilepsia*, 46:21–37, 2005.

[26] Jr. J. Engel. Report of the ILAE^2 classification core group. *Epilepsia*, 47(9):1558–1568, 2006.

[27] E. Niedermeyer and R. Lopes Da Silva. *Electroencephalography: Basic Principles, Clinical Applications and Related Fields.* Lippincott Williams & Wilkins, 5th edition edition, 2005.

[28] A. Varsavsky, I. Mareels, and M. Cook. *Epileptic seizures and the eeg: measurement, models, detection and prediction.* CRC Press, 2010.

[29] W. J. Freeman. The physiology of perception. *Scientific America*, 264(2):78–85, 1991.

[30] J.J. Carr and J. M. Brown. *Introduction to biomedical equipment technology.* Prentice Hall, 3rd edition, 1998.

[31] M. Sam and E.L. So. Significance of epileptiform discharges in patients without epilepsy in the community. *Epilepsia*, 42(10):1273–1278, 2001.

[32] G. B.Cavazzuti, L. Cappella, and A. Nalin. Longitudinal study of epileptiform eeg patterns in normal children. *Epilepsia*, 21(1):43–55, 1980.

[33] National Electricity Market Management Company Limited. Frequency & time deviation monitoring in the nem (national electricity market). Technical report, National Electricity Market Management Company Limited, Feb 2007.

[34] Compumedics. Profusion eeg user guide. ©*Compumedics Limited, 30-40 Flockhart Street, Abbotsford 3067, Victoria*, 2002.

[35] H.H. Jasper. The ten-twenty electrode system of the international federation. *Electroencephalography and clinical neurophysiology*, 10:371–375, 1958.

[36] C. Schmid-Schönbein. Improvement of seizure control by psychological methods in patients with intractable epilepsies. *Seizure*, 7:261–270, 1998.

[37] P. Rajna, B Clemens, E. Esibri, E. Dobos, A. Geregely, M. Gottschal, I. György, Á. Horváth, F. Horváth, L. Mezöfi, I. Velkey, J. Veres, and E. Wagner. Hungarian multicentre epidemiologic study of the warning and initial symptoms (prodrome, aura) of epileptic seizures. *Seizure*, 6:361–368, 1997.

[38] B. Litt and K. Lehertz. Seizure prediction and the preseizure period. *Current Opinion in Neurology*, 15(2):173–177, 2002.

[39] C.C. Jouny, P.J. Franaszczuk, and G.K. Bergey. Signal complexity and synchrony of epileptic seizures: is there an identifiable preictal period? *Clinical Neurophysiology*, 116:552–558, 2005.

[40] F. Mormann, T. Kreuz, R. G Andrzejak, P. David, K. Lehnertz, and C.E. Elger. Epileptic seizures are preceeded by a decrease in synchronisation. *Epilepsy research*, 53:173–185, 2003.

[41] F. Mormann, R. G Andrzejak, T. Kreuz, P. David, C. Rieke, C.E. Elger, and K. Lehnertz. Automated detection of a preseizure state based on a decrease in synchronization in intracranial electroencephalogram recordings from epilepsy patients. *Physical Review E*, 57:021912, 2003.

[42] B. Litt, R. Esteller, J. Echauz, M. D'Allessandro, R. Stor, T. Henry, P. Pennell, C. Epstein, R. Bakay, M. Dichter, and G. Vachtsevanos. Epileptic seizures may begin hours in advance of clinical onset: A report of 5 patients. *Neuron*, pages 51–54, 30.

[43] K. Lehnertz and C.E. Elger. Can epileptic seizures be predicted? evidence from nonlinear time series analysis of brain electrical activity. *Physical Review Letters*, 80(22):5019–5022, 1998.

[44] M. Le Van Quyen, J. Martinerie, M. Baulac, and F. Varela. Anticipating epileptic seizures in real time by a non-linear analysis of similarity between eeg recordings. *NeuroReport*, 10(10):2149–2155, 1999.

[45] J. W. Polderman and J. C. Willems. *Introduction to mathematical systems theory.* Springer, 1991.

[46] W.J. Freeman. Tutorial in neurobiology: From single neurons to brain chaos. *International Journal of Bifurcation and Chaos*, 2(3):451–482, 1992.

[47] S. Blanco, H. Garcia, R. Quian Quiroga, L. Romanelli, and O.A. Rosso. Stationarity of the eeg series. *IEEE Engineering in Medicine and Biology*, 14(4):395–399, 1995.

[48] S.S. Viglione and G.O Walsh. Epileptic seizure prediction. *Electroencephalography and clinical neurophysiology*, 39:435, 1975.

[49] A. Siegel, C. L. Grady, and A. F. Mirsky. Prediction of spike-wave bursts in absence epilepsy by eeg power-spectrum signals. *Epilepsia*, 23:47–60, 1982.

[50] T. Inouye, Y. Matsumoto, K. Shinosaki, A. Iyama, and S. Toi. Increases in the power spectral slope of background electroencephalogram just prior to asymmetric spike and wave complexes in epileptic patients. *Neuroscience Letters*, 173:197–200, May 1994.

[51] M. E. Saab and J. Gotman. A system to detect the onset of epileptic seizures in scalp eeg. *Clinical Neurophysiology*, 116:427–442, 2005.

[52] A. Bragin, C.L Wilson, R.J Staba, M. Reddick, I. Fried, and J. Engel Jr. Interictal high-frequency oscillations (80-500hz) in the human epileptic brain: Entorhinal cortex. *Annals of Neurology*, 52:407–415, 2002.

[53] R.J. Staba, C.L. Wilson, A. Bragin, I. Freid, and J. Engel Jr. Quantitative analysis of high-frequency oscillations (80-500 hz) recorded in human epileptic hippocampus and entorhinal cortex. *Journal of Neurophysiology*, 88:1743–1752, 2002.

[54] Z. Rogowski, I. Gath, and E. Bental. On the prediction of epileptic seizures. *Biological Cybernetics*, 42:9–15, 1981.

[55] P.E. McSharry, L.A. Smith, and L. Tarassenko. Comparison of predictability of epileptic seixures by a linear and a non-linear method. *IEEE Transactions on Biomedical Engineering*, 50(5):628–633, 2003.

[56] R. Esteller, J. Echauz, M. D'Alessandro, G. Worrell, S. Cranstoun, G. Vachtsevanos, and B. Litt. Continuous energy variation during the seizure cycle: towards an on-line accumulated energy. *Clinical Neurophysiology*, 116:517–526, 2005.

[57] M. A. Harrison, M. G. Frei, and I. Osorio. Accumulated energy revisited. *Clinical Neurophysiology*, 116:527–531, 2005.

[58] F. Mormann, K. Lehnertz, P. David, and C. E. Elger. Mean phase coherance as a measure for phase synchronisation and its application to the eeg of epileptic patients. *Physica D*, 114:358–369, 2000.

[59] M. Le Van Quyen *et al.* Preictal state identification by synchronization changes in long-term intracranial EEG recordings. *Clinical Neurophysiology*, 116:559–568, 2005.

[60] H. Z. Stanislaw. *Systems and Control (Engineering & Technology).* Oxford University Press, 2007.

[61] F. Takens. Detecting strange attractors in turbulence. In D. A. Rand and L.-S. Young, editors, *Dynamical Systems and Turbulence*, volume 898 of *Lecture Notes in Mathematics*, pages 366–381. Springer-Verlag, 1981.

[62] D. Aeyels. Generic observability of differentiable systems. *SIAM J. Control and optimization*, 19(5), 1981.

[63] J. Stark. Observing complexity, seeing simplicity. *Philosophical Transactions of the Royal Society London A*, 358:41–61, 2000.

[64] F. H. Lopes da Silva, W. Blanes S.N. Kallitzin, J. Parra, P. Suffczynski, and D. N. Velis. Dynamical dieases of brain systems: Different routes to epileptic seizures. *IEEE Transactions on Biomedical Engineering*, 50(5), 2003.

[65] P.A. Robinson, C.J. Rennie, D.L. Rowe, S.C. O'Connor, J.J. Wright, E. Gordon, and R.W. Whitehouse. Neurophysical modeling of brain dynamics. *Neuropsychopharmacology*, 28:S74–S79, 2003.

[66] A. Jedynak, M. Bach, and J. Timmer. Failure of dimensional analysis in a simple five-dimensional system. *Physical Review E*, 50(3):1770–1781, 1994.

[67] J. Stark, D.S Broomhead, M.E. Davies, and J. Huke. Delay embedding for forced systems. ii. stochastic forcing. *Journal of Nonlinear Science*, 13:519–577, 2003.

[68] T. Dikanev, D. Smirnov, R.Wennberg, J.L Perez Valazquez, and B. Bezruchko. EEG nonstationarity during intracranially recorded seizures: statistical and dynamical analysis. *Clinical Neurophysiology*, 116:1796–1807, 2005.

[69] C. Reike, K. Sternickel, R. G. Andrzejak, C. E. Elger, P. David, and K. Lehnertz. Measuring nonstationarity by analysing loss of recurrance in dynamical systems. *Physical Review Letters*, 88(24), 2002.

[70] H. Kantz and T. Schreiber. *Nonlinear time series analysis.* Cambridge University Press, 2nd edition, 2006.

[71] T. Schreiber. Detecting and analyzing nonstationarity in a time series using nonlinear cross predictions. *Physical Review Letters*, 78(5):843–846, 1997.

[72] C. Reike, F. Mormann, R. G. Andrzejak, T. Kreuz, P. David, C. E. Elger, and K. Lehnertz. Discerning nonstationarity from nonlinearity in seizure-free and preseizure EEG recordings from epilepsy patients. *IEEE transactions on Biomedical Engineering*, 50(5):634–639, 2003.

[73] K. Lehnertz, R. G. Andrzejak, J. Arnhold, T. Kreuz, F. Mormann, C. Reike, G. Widman, and C. E. Elger. Nonlinear EEG analysis in epilepsy: Its possible use for interictal focus localization, seizure anticipation, and prevention. *Journal of Clinical Neurophysiology*, 18(3):209–222, 2001.

[74] R. Aschenbrenner-Scheibe, T. Maiwald, M. Winterhalder, H. U. Voss, J. Trimmer, and A. Schulze-Bonhage. How well can epileptic seizures be predicted? an evaluation of a nonlinear method. *Brain*, 126:2616–2626, 2003.

[75] T. Maiwald, M. Winterhalder, R. Aschenbrenner-Scheibe, H. U. Voss, A. Schulze-Bonhage, and J. Timmer. Comparison of three nonlinear seizure prediction methods by means of the seizure prediction characteristic. *Physica D*, 194:357–368, 2004.

[76] M. A. Harrison, I. Osorio, M. G. Frei, S. Asuri, and Y. Lai. Correlation dimension and integral do not predict epileptic seizures. *Chaos*, 15(033106), 2005.

[77] L. D. Iasemidis, J. C. Sackellares, H. P. Zaveri, and W. J. Williams. Phase space topography and the lyapunov exponent of electrocorticograms in partial seizures. *Brain Topography*, 2(3):187–201, 1990.

[78] A. Wolf, J. B. Swift, H. L. Swinney, and J. A Vastano. Determining lyapunov exponents from a time series. *Physica D*, 16(285), 1985.

[79] Y. C. Lai, M. A. Harrison, M. G. Frei, and I. Osorio. Inability of lyapunov exponents to predict epileptic seizures. *Physical review letters*, 91(6), 2003.

[80] Y. C. Lai, M. A. Harrison, M. G. Frei, and I. Osorio. Controlled test for predictive power of lyapunov exponents: their inability to predict epileptic seizures. *Chaos*, 14(3):630–642, 2004.

[81] L. D. Iasemidis, K. Tsakalis, J. C. Sackellares, and P. M. Pardalos. Comment on “inability of lyapunov exponents to predict epileptic seizures”. *Physical Review Letters*, 94(019801), 2005.

[82] R. C. Hilborn. *Chaos and Nonlinear Dynamics: An introduction for Scientists and Engineers*. Oxford University Press, 1994.

[83] W. Van Drongelen, S. Nayak, D. M. Frim, M. H. Kohrman, V. L. Towle, H. C. Lee, A. B. McGee, M. S. Chico, and K. E. Hecox. Seizure anticipation in pediatric epilepsy: Use of kolmogorov entropy. *Pediatric Neurology*, 29(3):207–213, 2003.

[84] M. Le Van Quyen, J. Martinerie, V. Navarro, P. Boon, M. D'Havé, C. Adam, and B. Renault. Anticipation of epileptic seizures from standard eeg recordings. *The Lancet*, 357:183–188, January 2001.

[85] V. Navarro, J. Martinerie, M. Le Van Quyen, S. Clemenceau, C. Adam, M. Baulac, and F. Varela. Seizure anticipation in human neocortical partial epilepsy. *Brain*, 125:640–655, 2002.

[86] W. De Clercq, P. Lemmerling, S. Van Huffel, and W. Van Paesschen. Evaluation of the methods for determining a pre-ictal state in scalp eeg measurement. *Proceedings of 2nd European Medical and Biological Engineering Conference EMBEC'02, Vienna, Austria*, 2002.

[87] C. J. Stam and B. W Van Dijk. Synchronization likelihood: an unbiased measure of generalized synchronisation in multivariate data sets. *Physica D*, 163:236–251, 2002.

[88] M. Le Van Quyen, C. Adam, M. Baulac, J. Martinerie, and F. J. Varela. Nonlinear interdependancies of eeg signals in human intracranically recorded temporal lobe seizures. *Brain Research*, 792:24–40, 1998.

[89] F. Mormann, R. G. Andrzejak, C. E. Elger, and K. Lehnertz. Seizure prediction: the long and winding road. *Brain*, 130(2):314–33, 2007.

[90] Schelter B., Trimmer J., and A. Schulze-Bonhage, editors. *Seizure Prediction in Epilepsy: From Basic Mechanisms to Clinical Applications*. Wiley-VCH, 2008.

[91] B. Schelter, M. Winterhalder, T. Maiwald, A. Brandt, A. Schad, A. Schulze-Bonhage, and J. Timmer. Testing statistical significance of multivariate time series analysis techniques for epileptic seizure prediction. *Chaos: An Interdisciplinary Journal of Nonlinear Science*, 16:013108, 2006.

[92] R.G. Andrzejak, F. Mormann, T. Kreuz, C. Rieke, A. Kraskov, C.E. Elger, and K. Lehnertz. Testing the null hypothesis of the nonexistence of a preseizure state. *Physical Review E*, 67(1):10901, 2003.

[93] P. Boon, K. Vonck, V. De Herdt, A. Van Dycke, M. Goethals, L. Goossens, M. Van Zandijcke, T. De Smedt, I. Dewaele, R. Achten, et al. Deep brain stimulation in patients with refractory temporal lobe epilepsy. *Epilepsia*, 48(8):1551–1560, 2007.

[94] J. Gotman. Automatic recognition of epileptic seizures in the EEG. *Electroencephalography and clinical Neurophysiology*, 54(5):530–540, 1982.

[95] J. Gotman. Automatic seizure detection: improvements and evaluation. *Electroencephalography and clinical Neurophysiology*, 76(4):317–324, 1990.

[96] A. Varsavsky and I. Mareels. A complete strategy for patient un-specific detection of epileptic seizures using crude estimations of entropy. *Proceedings of IEEE EMBS*, pages 6491–6494, August 2007.

[97] I. Osorio, M.G. Frei, J. Giftakis, T. Peters, J. Ingram, M. Turnbull, M. Herzog, M.T. Rise, S. Schaffner, R.A. Wennberg, et al. Performance reassessment of a real-time seizure-detection algorithm on long ECoG series. *Epilepsia*, 43(12):1522–1535, 2002.

[98] H. Qu and J. Gotman. A seizure warning system for long-term epilepsy monitoring. *Neurology*, 45(12):2250, 1995.

[99] D. T. Liley, P. J. Cadusch, and M.P Dafilis. A spatially continuous mean field theory of electrocortical activity. *Network*, 13, 2002.

[100] A.L. Hodgkin and A.F. Huxley. A quantitative description of membrane current and its application to conduction and excitation in nerve. *The Journal of physiology*, 117(4):500, 1952.

[101] H.R. Wilson and J.D. Cowan. Excitatory and inhibitory interactions in localized populations of model neurons. *Biophysical Journal*, 12(1):1–24, 1972.

[102] B.H. Jansen and V.G. Rit. Electroencephalogram and visual evoked potential generation in a mathematical model of coupled cortical columns. *Biological Cybernetics*, 73(4):357–366, 1995.

[103] F. Wendling, JJ Bellanger, F. Bartolomei, and P. Chauvel. Relevance of nonlinear lumped-parameter models in the analysis of depth-EEG epileptic signals. *Biological Cybernetics*, 83(4):367–378, 2000.

[104] F. Wendling, F. Bartolomei, JJ Bellanger, and P. Chauvel. Epileptic fast activity can be explained by a model of impaired GABAergic dendritic inhibition. *European Journal of Neuroscience*, 15(9):1499–1508, 2002.

[105] F. Wendling, A. Hernandez, J.J. Bellanger, P. Chauvel, and F. Bartolomei. Interictal to ictal transition in human temporal lobe epilepsy: insights from a computational model of intracerebral EEG. *Journal of Clinical Neurophysiology*, 22(5):343, 2005.

[106] P. Suffczynski, S. Kalitzin, and FH Lopes Da Silva. Dynamics of non-convulsive epileptic phenomena modeled by a bistable neuronal network. *Neuroscience*, 126(2):467–484, 2004.

[107] FH Lopes da Silva, A. Hoeks, H. Smits, and LH Zetterberg. Model of brain rhythmic activity. *Biological Cybernetics*, 15(1):27–37, 1974.

[108] PA Robinson, CJ Rennie, JJ Wright, H. Bahramali, E. Gordon, and DL Rowe. Prediction of electroencephalographic spectra from neurophysiology. *Physical Review E*, 63(2):21903, 2001.

[109] PA Robinson, CJ Rennie, and DL Rowe. Dynamics of large-scale brain activity in normal arousal states and epileptic seizures. *Physical Review E*, 65(4):41924, 2002.

[110] F. Takens. Detecting strange attractors in turbulence. In D. A. Rand and L.-S. Young, editors, *Dynamical Systems and Turbulence*, volume 898 of *Lecture Notes in Mathematics*, page 366. Springer-Verlag, 1981.

[111] Y. Kuramoto. *Chemical Oscillations, Waves, and Turbulence.* Springer-Verlag, New York, 1984.

[112] A Stefanovska. Coupled oscillators: Complex but not complicated cardiovascular and brain interactions. *Proceedings of 28th IEEE EMBS International Conference*, pages 437–440, September 2006.

[113] S. Boi, ID Couzin, N. Del Buono, NR Franks, and NF Britton. Coupled oscillators and activity waves in ant colonies. *Proceedings of the Royal Society B: Biological Sciences*, 266(1417):371, 1999.

[114] H. Haken. *Brain Dynamics: Synchronization and Activity Patterns in Pulse-coupled Neural Nets with Delays and Noise.* Springer, 2002.

[115] P. Suffczynski, S. Kalitzin, F.L. da Silva, J. Parra, D. Velis, and F. Wendling. Active paradigms of seizure anticipation: Computer model evidence for necessity of stimulation. *Phys. Rev. E*, 78, 2008.

[116] J. J. Wright, R. R. Kydd, and G. J. Lees. State-changes in the brain viewed as linear steady-states and non-linear transitions between steady-states. *Biological Cybernetics*, 53:11–17, 1985.

[117] M. Bennett, M.F. Schatz, H. Rockwood, and K. Wiesenfeld. Huygens's clocks. *Proceedings of The Royal Society A: Mathematics, Physical and Engineering Sciences*, 458(2019):563–579, 2002.

[118] A.C. Antoulas. *Approximation of Large-Scale Dynamical Systems (Advances in Design and Control).* Society for Industrial and Applied Mathematics Philadelphia, PA, USA, 2005.

[119] R. Koplon and E.D. Sontag. Linear systems with sign-observations. *SIAM Journal on Control and Optimization*, 31(5):1245–1266, 1993.

[120] T. Kailath, editor. *Linear systems.* Information & Science Series. Prentice-Hall, 1980.

[121] D Feingold and S Richard. Block diagonally dominant matrices and generalizations of the gerschgorin circle theorm. *Pacific Journal of Mathematics*, 12(4):1241–1250, 1962.

[122] A. C. Johansson and A. Lanser. Towards cortex sized attractor ANN. In A. J. Ijspeert, M. Masayuki, and N. Wakamiya, editors, *Biologically Inspired Approaches to Advanced Information Technology*, Lecture Notes in Computer Science. Springer, 2004.

[123] F. Crick and E. Jones. Backwardness of human neuroanatomy. *Nature*, 361:109 – 110, 1993.

[124] D.J. Watts and S.H. Strogatz. Collective dynamics of "small-world" networks. *Nature*, 393(6684):440–442, 1998.

[125] S. Achard, R. Salvador, B. Whitcher, J. Suckling, and E. Bullmore. A resilient, low-frequency, small-world human brain functional network with highly connected association cortical hubs. *Journal of Neuroscience*, 26(1):63, 2006.

[126] Compumedics Neuroscan, 6605 West W.T. Harris Blvd,Suite F,Charlotte, NC 28269,USA. ^{TM}*SynAmps*^{2} *Specifications*, 2009.

[127] J.S. Ebersole. In search of seizure prediction: a critique. *Clinical Neurophysiology*, 116(3):489–492, 2005.

[128] M. Stead, M. Bower, B. H. Brinkmann, K. Lee, F. B Richard Marsh, W Meyer, B. Litt, J. Van Gompel, and G. A. Worrell. Microseizures and the spatiotemporal scales of human partial epilepsy. *Brain*, 2010.

[129] Rudolph Emil Kalman. A new approach to linear filtering and prediction problems. *Transactions of the ASME–Journal of Basic Engineering*, 82(Series D):35–45, 1960.

[130] S.V. Vaseghi. *Advanced digital signal processing and noise reduction.* Wiley, 2009.

[131] Paul R. Halmos. *Lectures on Ergodic Theory.* Chelsea Publishing Company, 1956.

[132] B. Hasselblatt, B. Fiedler, and AB Katok. *Handbook of dynamical systems*, volume 1A & 1B. North Holland, Elsevier, 2002.

[133] C. Kawan. Invariance Entropy of Control Sets. *SIAM pre-print, http://opus.bibliothek.uni-augsburg.de/volltexte/2010/1510/pdf/mpreprint_10_001.pdf*, 2010.

[134] Steven M. Kay. *Fundamentals of Statistical Signal Processing: Estimation Theory*, volume I. Prentice Hall, 1998.

Author/s:
O'SULLIVAN-GREENE, ELMA

Title:
Reevaluating electroencephalography for epileptic seizure prediction

Date:
2011

Citation:
O'Sullivan-Greene, E. (2011). Reevaluating electroencephalography for epileptic seizure prediction. PhD thesis, Engineering, Department of Electrical & Electronic Engineering, Melbourne School of Engineering and National ICT Australia, The University of Melbourne.

Persistent Link:
http://hdl.handle.net/11343/36630

File Description:
Reevaluating electroencephalography for epileptic seizure prediction